

Structure and mechanism
of the heterodimeric ABC translocation complexes

TAP and TmrAB

Dissertation

zur Erlangung des Doktorgrades
der Naturwissenschaften

Vorgelegt beim Fachbereich
Biochemie, Chemie und Pharmazie
der Johann Wolfgang Goethe-Universität
in Frankfurt am Main

von

Susanne Hofmann

aus Darmstadt

Frankfurt am Main, 2019

(D30)

Vom Fachbereich Biochemie, Chemie und Pharmazie der Johann Wolfgang Goethe-Universität
als Dissertation angenommen.

Dekan: Prof. Dr. Clemens Glaubitz

Gutachter: Prof. Dr. Robert Tampé

Zweitgutachter: Prof. Dr. Klaas Martinus Pos

Datum der Disputation:

Results and parts of this work were published in:*

- 2019 **Hofmann S**, Janulienė D, Mehdipour AR, Thomas C, Stefan E, Brüchert S, Kuhn BT, Geertsma ER, Hummer G, Tampé R, Moeller A, Conformation space of a heterodimeric ABC exporter under turnover conditions, *manuscript submitted*
- 2019 Braner M, Koller N, Knauer J, Herbring V, **Hank S**, Wieneke R, Tampé R, Optical control of the antigen translocation by synthetic photo-conditional viral inhibitors, *Chem Sci* 2019, 10, 2001-2005
DOI: 10.1039/C8SC04863K
- 2018 Klein A, **Hank S**, Raulf A, Joest E, Tissen F, Heilemann M, Wieneke R, Tampé R, Live-cell labeling of endogenous proteins with nanometer precision by transduced nanobodies, *Chem Sci* 2018 (9) 7835-7842
DOI: 10.1039/C8SC02910E
- 2018 Barth K, **Hank S**, Spindler PE, Prisner TF, Tampé R, Joseph B, Conformational Coupling and trans-Inhibition in the Human Antigen Transporter Ortholog TmrAB Resolved with Dipolar EPR Spectroscopy, *J Am Chem Soc* 140(13):4527-4533
DOI: 10.1021/jacs.7b12409
- 2014 Lin J, Eggensperger S, **Hank S**, Wycisk AI, Wieneke R, Mayerhofer PU, Tampé R, A negative feedback modulator of antigen processing evolved from a frameshift in the cowpox virus genome, *PLoS Pathog* 10(12):e1004554
DOI: 10.1371/journal.ppat.1004554

* *Name at birth: Susanne Hank*

Table of contents

Table of contents	I
1. Declaration.....	V
2. Zusammenfassung	XI
3. Summary.....	XVII
4. Introduction	1
4.1 ATP-binding cassette transporters	1
4.1.1 TAP – a key player of the MHC class I dependent antigen processing pathway.....	4
4.1.2 TmrAB – a model system for heterodimeric ABC exporters	7
4.2 Scaffold proteins as lipid-bilayer mimics	10
4.3 Conformational trapping of membrane proteins	13
4.3.1 Synthetic antibody fragments	14
4.3.2 Nanobodies	16
4.3.3 Cyclic peptides.....	17
5. Aims and motivation.....	21
6. Material	23
6.1 Antibodies and antibody fragments.....	23
6.2 Bacterial strains	23
6.3 Buffers	24
6.4 Chemicals and reagents	29
6.5 Consumables and lab equipment.....	30
6.6 Detergents	30
6.7 Enzymes	31
6.8 Media.....	31
6.9 Oligonucleotides	33
6.10 Peptides	33
7. Methods.....	35
7.1 Molecular biology and microbiology.....	35
7.1.1. Preparation of competent <i>E. coli</i> cells.....	35
7.1.2 Design of DNA constructs.....	35
7.1.3.1 DNA amplification.....	35

7.1.3.2 Amplification and isolation of plasmid DNA	36
7.1.3.3 DNA sequencing	37
7.2 Biochemistry	37
7.2.1 Protein production and purification	37
7.2.1.1 Production and purification of TAP	37
7.2.1.2 Production and purification of TmrAB.....	38
7.2.1.3 Production and purification of synthetic antibodies	39
7.2.1.4 Production and purification of nanobodies	39
7.2.1.5 Production and purification of saposin A.....	40
7.2.1.6 Production and purification of membrane scaffold proteins	40
7.2.2 Reconstitution	41
7.2.2.1 Functional reconstitution of TAP and TmrAB into LUVs	41
7.2.2.2 Reconstitution of TAP and TmrAB in nanodiscs	42
7.2.2.3 Reconstitution of TmrAB using saposin A.....	43
7.2.3 Protein labeling	43
7.2.3.1 Biotinylation	43
7.2.4 Selection of synthetic antibodies	44
7.2.4.1 Library sorting by phage display.....	44
7.2.4.2 Enzyme-linked immunosorbent assay (ELISA)	45
7.2.4.3 Complex formation and isolation	45
7.2.5 Selection of nanobodies.....	46
7.2.5.1 Immunization	46
7.2.5.2 Library sorting by phage display.....	46
7.2.5.3 Single clone screening.....	48
7.2.5.4 Determination of binding constants by switchSENSE.....	48
7.2.6 Binding Assays	49
7.2.6.1 Filter binding	49
7.2.6.2 Fluorescence anisotropy	49
7.2.7 Peptide transport	49
7.2.8 ATPase assays.....	50
7.2.8.1 Malachite-Green based assay	50
7.2.8.2 Radioactive assay.....	51
7.2.9 Nucleotide occlusion.....	51
7.2.10 SDS-PAGE	51
7.2.11 Coomassie staining	52

7.2.12 Silver staining	52
7.2.13 Immunoblotting.....	52
7.2.14 Bradford assay	53
7.2.15 Size exclusion chromatography	53
7.2.16 Detergent exchange to amphipols	54
7.2.17 GraFix	54
7.3 Biophysics	55
7.3.1 Electron microscopy (EM)	55
7.3.1.1 Single-particle negative-stain EM.....	55
7.3.1.2 Cryo-EM sample preparation, data acquisition, and image processing	55
7.3.2 Model building	56
8. Results and Discussion	59
8.1 Structural analysis of human cTAP	59
8.1.1 Purified cTAP is functional in peptide binding and translocation	59
8.1.2 Antibodies as stabilizing chaperones of selected functional states of TAP	62
8.1.2.1 Selection of synthetic antibodies	62
8.1.2.2 Selection of nanobodies.....	66
8.1.3 Electron microscopy of human ^{ICP47} cTAP	70
8.1.4 Discussion.....	74
8.1.4.1 Selection of state-specific antibody fragments.....	74
8.1.4.2 Structural analysis of TAP by single-particle EM	77
8.2 Conformational cycle of TmrAB resolved by cryo-EM	79
8.2.1 Purification of TmrAB in catalytically active form	79
8.2.2 Generation of antibodies to trap selected functional states of TmrAB.....	80
8.2.2.1 Selection of synthetic antibodies	81
8.2.2.2 Selection of nanobodies.....	84
8.2.3 Structural analysis of TmrAB by single-particle cryo-EM	88
8.2.3.1 Conformational plasticity in IF conformations.....	94
8.2.3.2 ATP-triggered NBD dimerization induces the transition to the OF-open conformation	96
8.2.3.3 ATP hydrolysis and nucleotide release are necessary to reset TmrAB back into the IF conformation	100
8.2.3.4 Global conformational changes and helical shifts within the TMDs during the translocation cycle of TmrAB.....	103
8.2.4 Discussion.....	106

8.3 Alternative attempts to stabilize the outward-facing state of TmrAB.....	111
8.3.1 Selection of macrocyclic peptides as conformational arrestors	111
8.3.2 Discussion.....	115
9. Conclusion.....	117
10. References	119
11. Appendix.....	133
12. Abbreviations.....	135
13. List of figures.....	139
14. List of tables	141
15. Danksagung.....	143
16. Curriculum vitae	145
17. Erklärung.....	147
18. Versicherung	147

1. Declaration

Except where stated otherwise by reference or acknowledgment, the work presented was generated by myself under the supervision of my advisors during my doctoral studies. All contributions from colleagues are explicitly referenced in the thesis. The material listed below was obtained in the context of collaborative research:

Synthetic antibodies and nanobodies were generated in collaboration with Pawel Dominik (Kossiakoff laboratory, Department of Biochemistry and Molecular Biology, The University of Chicago, Chicago, IL, USA) and Els Pardon (Steyaert laboratory, VIB-VUB Center for Structural Biology in Brussels, Vrije Universiteit Brussel, Brussels, Belgium). The antibody selection was performed within the context of a research visit at the Kossiakoff laboratory and the Steyaert laboratory.

Simone Prinz (Kühlbrandt laboratory, Department of Structural Biology, Max Planck Institute of Biophysics, Frankfurt) recorded all micrographs of negatively-stained ^{ICP47}cTAP:

Fig. 17b: Negative-stain EM analysis of ^{ICP47}cTAP in GDN. Collaboration partner: Simone Prinz (Kühlbrandt laboratory, Department of Structural Biology, Max Planck Institute of Biophysics, Frankfurt). Simone Prinz recorded micrographs of negatively-stained ^{ICP47}cTAP. Sample preparation was done by me.

Fig. 18: EM analysis of ^{ICP47}cTAP upon fixation and detergent removal. Collaboration partner: Simone Prinz (Kühlbrandt laboratory, Department of Structural Biology, Max Planck Institute of Biophysics, Frankfurt). Simone Prinz recorded micrographs of negatively-stained ^{ICP47}cTAP. Sample preparation was done by me.

Fig. 19: GraFix treatment of ^{ICP47}cTAP. Collaboration partner: Simone Prinz (Kühlbrandt laboratory, Department of Structural Biology, Max Planck Institute of Biophysics, Frankfurt). Simone Prinz recorded micrographs of negatively-stained ^{ICP47}cTAP. Sample preparation was done by me.

Fig. 20b: Synthetic antibody C2 as fiducial marker for EM. Collaboration partner: Simone Prinz (Kühlbrandt laboratory, Department of Structural Biology, Max Planck Institute of Biophysics,

Frankfurt). Simone Prinz recorded micrographs of negatively-stained ^{ICP47}cTAP. Sample preparation was done by me.

Fig. 21b: Detergent exchange for amphipols. Collaboration partner: Simone Prinz (Kühlbrandt laboratory, Department of Structural Biology, Max Planck Institute of Biophysics, Frankfurt). Simone Prinz recorded micrographs of negatively-stained ^{ICP47}cTAP. Sample preparation was done by me.

Data collection of negatively-stained TmrAB was performed in collaboration with the Kühlbrandt laboratory at the Department of Structural Biology, Max Planck Institute of Biophysics, Frankfurt:

Fig. 31: Negative-stain EM analysis of TmrAB in β -DDM. Collaboration partner: Kühlbrandt laboratory (Department of Structural Biology, Max Planck Institute of Biophysics, Frankfurt). Sample preparation and data collection of negatively-stained TmrAB was done by me.

Fig. 32: Negative-stain EM analysis of reconstituted TmrAB. Collaboration partner: Kühlbrandt laboratory (Department of Structural Biology, Max Planck Institute of Biophysics, Frankfurt). The saposin A-encoding plasmid was kindly provided by Jens Frauenfeld (Salipro AB, Stockholm, Sweden) within the context of a material transfer agreement. pMSP1D1 and pMSP2N2 were a gift from Stephen Sligar (Addgene plasmids # 20061 and # 29520). Sample preparation and data collection of negatively-stained TmrAB was done by me.

Fig. 34: Antibodies as fiducial marker proteins. Collaboration partner: Kühlbrandt laboratory (Department of Structural Biology, Max Planck Institute of Biophysics, Frankfurt). Sample preparation and data collection of negatively-stained TmrAB/antibody complexes was done by me. Fig. 34d-f: Nb 9F10 was kindly provided by Stefan Brüchert (Tampé laboratory, Institute of Biochemistry, Goethe-University, Frankfurt) and Benedikt Kuhn (Geertsma laboratory, Institute of Biochemistry, Goethe-University, Frankfurt). The NBD^{TmrA}-/NBD^{TmrB}-encoding plasmids were thankfully provided by Benedikt Kuhn.

Arne Möller (Department of Structural Biology, Max Planck Institute of Biophysics, Frankfurt) and Dovile Janulienė (Möller laboratory, Department of Structural Biology, Max Planck Institute of Biophysics, Frankfurt) performed all cryo-EM data collection and data processing of TmrAB:

Fig. 35: Cryo-EM analysis of nanodisc-embedded TmrAB^{WT} under turnover conditions. Collaboration partner: Arne Möller and Dovile Janulienė (Möller laboratory, Department of Structural Biology, Max Planck Institute of Biophysics, Frankfurt). Cryo-EM data collection and data processing was performed by Arne Möller and Dovile Janulienė. Sample preparation was done by me.

Fig. 36: Conformational plasticity in IF conformations translates to substrate binding. Collaboration partner: Arne Möller and Dovile Janulienė (Möller laboratory, Department of Structural Biology, Max Planck Institute of Biophysics, Frankfurt). Cryo-EM data collection and data processing was performed by Arne Möller and Dovile Janulienė. Models of IF TmrAB were provided by Ahmad Reza Mehdipour (Hummer laboratory, Department of Theoretical Biophysics, Max Planck Institute of Biophysics, Frankfurt) and Christoph Thomas (Tampé laboratory, Institute of Biochemistry, Goethe-University, Frankfurt). TmrAB^{M139-}, TmrAB^{H246-}, TmrAB^{W297-}, TmrAB^{M139, H246-}, and TmrAB^{M139, W297-}-encoding plasmids were provided by Stefan Brüchert (Tampé laboratory, Institute of Biochemistry, Goethe-University, Frankfurt). Sample preparation, binding, and transport studies were done by me.

Fig. 37: Asymmetric post-hydrolysis state. Collaboration partner: Arne Möller and Dovile Janulienė (Möller laboratory, Department of Structural Biology, Max Planck Institute of Biophysics, Frankfurt). Cryo-EM data collection and data processing was performed by Arne Möller and Dovile Janulienė. Model of UR^{asym}/UR^{asym*} TmrAB was provided by Ahmad Reza Mehdipour (Hummer laboratory, Department of Theoretical Biophysics, Max Planck Institute of Biophysics, Frankfurt) and Christoph Thomas (Tampé laboratory, Institute of Biochemistry, Goethe-University, Frankfurt). Sample preparation was done by me.

Fig. 38: ATP binding induces the IF-OF-open transition. Collaboration partner: Arne Möller and Dovile Janulienė (Möller laboratory, Department of Structural Biology, Max Planck Institute of Biophysics, Frankfurt). Cryo-EM data collection and data processing was performed by Arne Möller and Dovile Janulienė. Models of OF (open/occluded) TmrAB were provided by Ahmad Reza Mehdipour (Hummer laboratory, Department of Theoretical Biophysics, Max Planck Institute of Biophysics, Frankfurt) and Christoph Thomas (Tampé laboratory, Institute of Biochemistry, Goethe-University, Frankfurt). Sample preparation and peptide binding assays were performed by me.

Fig. 39: TmrAB_{ATP-Vi} and TmrA^{EQ}B_{ATP} are equivalent. Collaboration partner: Arne Möller and Dovile Janulienė (Möller laboratory, Department of Structural Biology, Max Planck Institute of Biophysics, Frankfurt). Cryo-EM data collection and data processing was performed by Arne Möller and Dovile Janulienė. Models of OF (open/occluded) TmrAB were provided by Ahmad Reza Mehdipour (Hummer laboratory, Department of Theoretical Biophysics, Max Planck Institute of Biophysics, Frankfurt) and Christoph Thomas (Tampé laboratory, Institute of Biochemistry, Goethe-University, Frankfurt). Sample preparation and nucleotide occlusion assays were performed by me.

Fig. 40: Cryo-EM analysis of nanodisc-embedded TmrA^{EQ}B_{ATP-ADP}. Collaboration partner: Arne Möller and Dovile Janulienė (Möller laboratory, Department of Structural Biology, Max Planck Institute of Biophysics, Frankfurt). Cryo-EM data collection and data processing was performed by Arne Möller and Dovile Janulienė. Sample preparation was done by me.

Fig. 41: Helical shifts within the TMD of TmrA during substrate translocation. Models of TmrAB were provided by Ahmad Reza Mehdipour (Hummer laboratory, Department of Theoretical Biophysics, Max Planck Institute of Biophysics, Frankfurt) and Christoph Thomas (Tampé laboratory, Institute of Biochemistry, Goethe-University, Frankfurt).

Fig. 42: Helical shifts within the TMD of TmrB during substrate translocation. Models of TmrAB were provided by Ahmad Reza Mehdipour (Hummer laboratory, Department of Theoretical Biophysics, Max Planck Institute of Biophysics, Frankfurt) and Christoph Thomas (Tampé laboratory, Institute of Biochemistry, Goethe-University, Frankfurt).

Cyclic peptides were generated in collaboration with Richard Obexer (Suga laboratory, Department of Chemistry, The University of Tokyo, Tokyo, Japan). Richard Obexer selected and synthesized cyclic peptide VD3. The selection target was provided by me. The biochemical characterization of cyclic peptide VD3 was performed by me.

Fig. 46: VD3 binds to the periplasmic side of TmrAB. Monovalent streptavidin was provided by Nita Chang (Geertsma laboratory, Institute of Biochemistry, Goethe-University, Frankfurt).

Fig. 47: Fourier shell correlation (FSC) curves. Collaboration partner: Arne Möller and Dovile Janulienė (Möller laboratory, Department of Structural Biology, Max Planck Institute of

Biophysics, Frankfurt). Cryo-EM data collection and data processing was performed by Arne Möller and Dovile Januliene.

Whenever a figure, table or text is identical to a previous publication, it is stated explicitly in the thesis that copyright permission and/or co-author agreement has been obtained.

The following parts of the thesis have been previously published:

- Chapter “7.2.7 and 8.1.1” in
PLoS Pathogens 10(12): e1004554 as “A negative feedback modulator of antigen processing evolved from a frameshift in the cowpox virus genome” by Jiacheng Lin, Sabine Eggensperger, **Susanne Hank**, Agnes I. Wycisk, Ralph Wieneke, Peter U. Mayerhofer, and Robert Tampé
- Parts of Figure “9”
- Chapter “7.2.8.2” in
Journal of the American Chemical Society 140 (13) as “Conformational Coupling and trans-Inhibition in the Human Antigen Transporter Ortholog TmrAB Resolved with Dipolar EPR Spectroscopy” by Katja Barth, **Susanne Hank**, Philipp E. Spindler, Thomas F. Prisner, Robert Tampé, and Benesh Joseph
- Chapter “3, 5, 7.2.1.2, 7.2.1.6, 7.2.2.2, 7.2.6.2, 7.2.7, 7.2.8.2, 7.2.9, 7.3.1.2, 7.3.2, 8.2.3, 8.2.4” as “Conformation space of a heterodimeric ABC exporter under turnover conditions” by **Susanne Hofmann**, Dovile Janulienė, Ahmad R. Mehdipour, Christoph Thomas, Erich Stefan, Stefan Brüchert, Benedikt T. Kuhn, Eric R. Geertsma, Robert Tampé, and Arne Möller (manuscript is submitted)
- Parts of Figures “32, 33, 34, 35, 36, 37, 38, 39, 40, 43, 47”

2. Zusammenfassung

ABC- (*ATP-binding cassette*) Transporter repräsentieren eine omnipräsente Superfamilie integraler Membranproteine, die den Transport einer Vielzahl chemisch höchst diverser Substrate über biologische Membranen mittels ATP-Bindung und -Hydrolyse katalysieren und in allen drei Domänen des Lebens (Eukaryoten, Prokaryoten und Archaeen) zu finden sind. Alle eukaryotischen ABC-Transporter sind Exporter, die eine essentielle Rolle in unterschiedlichsten physiologischen Prozessen spielen – angefangen mit Schlüsselfunktionen bei der Aufnahme von Nährstoffen bis hin zum adaptiven Immunsystem. Aus diesem Grund werden Fehlfunktionen von ABC-Transportern mit einer Vielzahl schwerwiegender Krankheitsbilder wie zum Beispiel Hypercholesterinämie oder Mukoviszidose in Verbindung gebracht. Ein detailliertes Verständnis des Aufbaus und der Funktion von ABC-Transportern ist folglich ein wichtiges Ziel der klinischen Forschung. Im Rahmen dieser Doktorarbeit wurden daher zwei ABC-Transporter (TAP und TmrAB) aus unterschiedlichen Organismen (human und bakteriell) als Modellsysteme für heterodimere ABC-Transporter hinsichtlich ihrer konformationellen Heterogenität während des Substrat-Transportes untersucht und ein allgemein gültiger Transport-Mechanismus postuliert.

Tagtäglich wird der menschliche Körper mit zahlreichen Toxinen, Bakterien, Viren und Parasiten konfrontiert. Um dieser Vielzahl an Pathogenen entgegenzuwirken, hat der Körper ein komplexes Abwehrsystem entwickelt, das aus der angeborenen (innaten) und der erworbenen (adaptiven) Immunantwort besteht. Das adaptive Immunsystem basiert auf der Erkennung und Eliminierung infizierter oder entarteter Zellen vermittelt durch die Präsentation körpereigener und körperfremder Peptid-Antigene an der Zelloberfläche. Eine Schlüsselrolle in der adaptiven Immunantwort spielt der mit der Antigenprozessierung assoziierte ABC-Transporter (*transporter associated with antigen processing*, TAP). Als Teil des dynamischen makromolekularen Peptid-Beladungskomplexes (*peptide-loading complex*, PLC) transportiert TAP proteasomale Degradationsprodukte vom Zytosol ins Lumen des Endoplasmatischen Retikulums (ER), wo anschließend die Beladung dieser Peptide auf Moleküle des Hauptkompatibilitätskomplexes I (*major histocompatibility complex I*, MHC I) als weiterer Komponente des PLCs erfolgt. Nach der MHC I-Beladung migrieren kinetisch stabile MHC I-Peptid-Komplexe für die Antigenpräsentation über das *Golgi*-Netzwerk zur Plasmamembran. Durch die zentrale Rolle von TAP in der MHC I-vermittelten Antigenpräsentation können Dysfunktionen des ABC-Transporters schwerwiegende Auswirkungen auf die adaptive Immunantwort gegen infizierte oder maligne Zellen haben. Doch nicht nur Fehlfunktionen des Transporters können den Antigen-Transport und damit die MHC I-vermittelte

Antigenpräsentation stören. Eine große Anzahl an Viren hat spezielle Strategien zur Umgehung der adaptiven Immunantwort entwickelt - mit verheerenden Folgen für den menschlichen Körper.

Neben diversen Krankheitsbildern spielen ABC-Transporter auch in der Resistenzentwicklung von Bakterien gegen Antibiotika eine bedeutende Rolle. Aus diesem Grund wurde in dieser Studie zusätzlich zum humanen TAP-Komplex, auch der bakterielle ABC-Transporter TmrAB (*Thermus thermophilus multidrug resistance proteins A and B*) hinsichtlich seines Transportmechanismus untersucht. Bei TmrAB handelt es sich ebenfalls um einen heterodimeren ABC-Export-Komplex, der als funktionales Ortholog von TAP betrachtet werden kann.

In der Vergangenheit wurden viele funktionale und strukturelle Aspekte von ABC-Transportern mittels diverser biochemischer Methoden und strukturgebender Verfahren, wie der Kristallstrukturanalyse oder der Kryo-Elektronenmikroskopie, untersucht und aufgeklärt. Dennoch handelt es sich bei der Mehrzahl der publizierten Strukturen um einzelne *Schnappschüsse* aus einer Vielzahl an möglichen Konformeren, die ein ABC-Export-Komplex während des Transport-Prozesses einnehmen kann. Um jedoch einen allgemein gültigen Transport-Mechanismus zu postulieren, ist ein detailliertes Verständnis des kompletten konformationellen Spektrums in der nativen zellulären Umgebung essentiell. Ziel dieser Arbeit war daher die Untersuchung und Bestimmung des molekularen Aufbaus und des konformationellen Spektrums der heterodimeren ABC-Export-Komplexe TAP und TmrAB mittels Einzelpartikel-Kryo-Elektronenmikroskopie.

Um TAP und TmrAB für strukturelle Analysen in distinkten Konformationen zu arretieren, wurden drei unterschiedliche Ansätze verglichen: die Generierung synthetischer Antikörper (1), Nanobodies (2) oder zyklischer Peptide (3) als *Tools* für den konformationellen Arrest (die Selektion zyklischer Peptide wurde nur für TmrAB durchgeführt). Fragmente konventioneller heterotetramerer Antikörper werden bedingt durch ihre hohe Stabilität und die zielgerichtete Selektivität häufig als konformationelle Arrestoren von Membranproteinen in der Strukturbiologie eingesetzt. Die von Schwerketten-Antikörpern abstammenden Nanobodies der *Camelidae* haben zusätzlich den Vorteil, dass der ausgeprägte CDR3-loop (*complementarity-determining region*, CDR) bestimmte Epitope binden kann, welche die flachen, konkaven Antigenbindungsstellen konventioneller heterotetramerer Antikörper nicht erreichen können. Die mittels Phagen- (synthetische Antikörper, Nanobodies) oder mRNA-Display (zyklische

Peptide) isolierten Bindemoleküle wurden hinsichtlich ihrer biochemischen Eigenschaften charakterisiert. Es wurde gezeigt, dass sowohl die selektierten Antikörper als auch die zyklischen Peptide spezifisch mit Affinitäten im nanomolaren Bereich an ihr jeweiliges Antigen binden. Jedoch hat sich im Rahmen der weiteren biochemischen Charakterisierung und der initialen Elektronenmikroskopie-Experimente mittels Negativkontrastierung (*negative-stain*) herausgestellt, dass die generierten Antikörper (für TAP und TmrAB) und zyklischen Peptide (für TmrAB) nicht den gewünschten Effekt zeigen. Aus diesem Grund wurden für den weiteren Verlauf des Projektes Nanobodies verwendet, die Konformations-unabhängig binden und im Rahmen einer anderen Studie generiert wurden.

Parallel zur Selektion der Bindemoleküle wurden verschiedene Strategien (unterschiedliche Detergenzien, die Zugabe von Fixierung-Reagenzien, der Austausch von Detergens durch amphiphile Polymere) getestet, um die TAP und TmrAB Proben hinsichtlich ihrer Reinheit, Homogenität und Stabilität für die Einzelpartikel-Kryo-Elektronenmikroskopie zu optimieren. Die *via negative-stain* Elektronenmikroskopie analysierten TAP-Proben waren homogen hinsichtlich der Partikelgröße, jedoch waren keine sichtbaren, für ABC-Transporter charakteristischen Motive (wie zum Beispiel die NBDs) zu erkennen. Auch die Zugabe synthetischer Antikörper als Markerproteine führte zu keiner Verbesserung der Probenqualität, weshalb die TAP-Struktur im Rahmen dieser Studie nicht bestimmt werden konnte. Aus diesem Grund wurden alle weiterführenden Experimente mit TmrAB durchgeführt. Mittels Einzelpartikel-Kryo-Elektronenmikroskopie wurde das konformationelle Spektrum von TmrAB unter Transport-Bedingungen bestimmt. Dazu wurde TmrAB in ein synthetisches Modellmembransystem (Nanodisks) eingebettet, welches die lokale Lipidumgebung der Membran simuliert, und die TmrAB-Nanodisks direkt vor dem Einfrieren mit Nukleotid und Substrat versetzt. Die Analyse der Kryo-Elektronenmikroskopie-Daten ergab ein breites Spektrum an verschiedenen Konformeren mit nach innen (der intrazellulären Seite zugewandt, *inward-facing*) oder nach außen (der extrazellulären Seite zugewandt, *outward-facing*) gerichteter Orientierung.

Die *inward-facing* Partikel konnten zwei distinkten Konformationen zugeordnet werden, die sich durch die Öffnung des intrazellulären *Gates* unterscheiden. Speziell Transmembranhelix 6 (TMH6) beider Untereinheiten wies deutliche Veränderungen zwischen beiden Konformeren auf. Im Zuge des Konformationswechsels von *inward-* zur *outward-facing* Orientierung kommt es zu einer Verschiebung der TMH6 nach außen. Diese Verschiebung leitet den konformationellen Übergang ein und ist mit einer Vergrößerung der intrazellulären Kavität

verbunden. Die Vergrößerung der intrazellulären Kavität ermöglicht die Bindung von Substrat in der Substratbindekavität. Daher wurde auch nur in dieser Konformation eine Extra-Dichte beobachtet, die dem Substrat zugeordnet werden konnte. Mittels Alanin-Substitution nahe der Extra-Dichte liegender Aminosäure-Reste mit anschließenden Bindungs- und Transportstudien, wurde gezeigt, dass M139 und W297 von TmrB an der Bindung von Substrat in der Substratbindekavität beteiligt sind.

Die restlichen (nicht *inward-facing*) Partikel wurden zwei Konformationen mit dimerisierten NBDs zugeordnet, in denen der intrazelluläre Eintrittsweg für das Substrat verschlossen ist. Die atomare Auflösung der Datensätze erlaubte die Bestimmung der gebundenen Nukleotide in den Nukleotidbindestellen (NBS): ADP in der ATP-Hydrolyse aktiven NBS und ATP in der Hydrolyse inaktiven NBS. Die Identität der gebundenen Nukleotide belegt, dass es sich bei diesen Konformationen um den Zustand nach der ATP-Hydrolyse handelt.

Da in diesem Experiment keine Partikel mit zur extrazellulären Seite geöffneten (*outward-facing open*) TMDs beobachtet wurden, was eine Voraussetzung für die Freisetzung des Substrates auf der extrazellulären Seite darstellt, wurde für weitere Studien eine katalytisch inaktive Variante des Transport-Komplexes eingesetzt: TmrA^{E523Q}B. In dieser mutierten Form von TmrAB wurde das katalytische Glutamat der A-Untereinheit durch Glutamin substituiert, weshalb der Transport-Komplex ATP binden aber nicht hydrolysieren kann. Für die Einzelpartikel-Kryo-Elektronenmikroskopie wurde TmrAB in Nanodisks unmittelbar vor der Probenpräparation mit ATP versetzt. Die Analyse der aufgenommenen Daten ergab Transport-Partikel in zwei *outward-facing* Konformationen: in einer *outward-facing occluded* und einer *outward-facing open* Orientierung.

Ähnlich des zuvor beschriebenen (*turnover*) Experiments lagen die NBDs in der *outward-facing occluded* Konformation in dimerisierter Form vor – mit dem Unterschied, dass beide NBS ATP gebunden haben. Interessant für den Transport-Zyklus ist allerdings die zweite im Datensatz beobachtete Konformation: *outward-facing open*. Die NBDs sind geschlossen, die TMDs dafür Flügel-ähnlich nach außen (daher *outward-facing open*) geöffnet, um die Freisetzung eines potentiellen Substrates in den extrazellulären Raum zu ermöglichen. Diese Studie bestätigt die Hypothese, dass die durch ATP-Bindung induzierte Dimerisierung der NBDs die Öffnung der TMDs nach außen auslöst und damit die treibende Kraft für den Substrat-Transport über die Membran ist (nicht wie vielfach im ABC-Transporter-Feld diskutiert die ATP-Hydrolyse).

In einem dritten Ansatz wurde der Übergangszustand der ATP-Hydrolyse mittels Vanadat (V_i)-*trapping* von TmrAB in Nanodisks analysiert. Die Untersuchung der Einzelpartikel-Kryo-Elektronenmikroskopie-Daten ergab ausschließlich *outward-facing* orientierte Partikel mit zur extrazellulären Seite geöffneten oder geschlossenen TMDs (*outward-facing open* und *occluded*). Im Unterschied zur ATP-gebundenen TmrA^{E523Q}B-Probe wurde in der katalytisch-aktiven NBS jedoch ADP und V_i nachgewiesen und in der katalytisch-inaktiven NBDs gebundenes ATP. Um den Transport-Zyklus abzuschließen und den Transport-Komplex für einen neuen Zyklus vorzubereiten ist jedoch der Übergang der *outward-facing* zurück zur *inward-facing* Orientierung notwendig. Die Erklärung für diesen konformationellen Übergang ergab sich durch den Vergleich der hier beschriebenen *outward-facing occluded* Zustände mit den Post-Hydrolyse-Zuständen des *turnover* Experiments: Im Vergleich zum ATP-gebundenen Zustand der TmrA^{E523Q}B-Probe und dem ATP/ADP+ V_i -gebundenen Zustand der V_i -getrappten TmrAB-Probe sind die ADP-gebundene katalytisch-aktive NBS und das intrazelluläre *Gate* leicht geöffnet. Diese Asymmetrie in den NBS beweist, dass die Freisetzung des anorganischen Phosphates den NBD-Dimer schwächt, was wiederum dazu führt, dass sich das intrazelluläre *Gate* öffnet und der Transporter einen Konformationwechsel von *outward-facing* zu *inward-facing* durchläuft. Die Ergebnisse zeigen, dass die Freisetzung des anorganischen Phosphates für den Übergang der *outward-* zur *inward-facing* Konformation notwendig ist und damit den Geschwindigkeitsbestimmenden Schritt im Transport-Zyklus darstellt.

Zusammenfassend wurde im Rahmen dieser Studie das konformationelle Spektrum des heterodimeren ABC-Export-Komplexes TmrAB abgebildet und fundamentale bisher nicht beschriebene Schritte des Transport-Zyklus heterodimerer Exporter diskutiert. Basierend auf den Ergebnissen wurde ein allgemein gültiger Transport-Mechanismus für heterodimere ABC-Transport-Komplexe postuliert, der Antworten auf die wesentlichen Fragen im ABC-Transporter-Feld liefert (z.B. welcher Schritt des Transport-Zyklus die treibende Kraft für den Substrat-Transport über die Membran darstellt). Die Beschreibung der globalen und lokalen konformationellen Änderungen während des Transport-Zyklus trägt einen wichtigen Schritt zum Verständnis von ABC-Transporter-Dysfunktionen oder viraler *escape* Strategien bei und stellt damit einen wichtigen Schritt für die klinische Forschung zur Entwicklung potentieller neuer Therapeutika dar.

3. Summary

ATP-binding cassette (ABC) transporters constitute an omnipresent superfamily of integral membrane proteins, which catalyze the translocation of a multitude of chemically diverse substrates across biological membranes. In humans, ABC transporters typically act as highly promiscuous exporters, responsible for many physiological processes, multi-drug resistance, and severe diseases, such as hypercholesterolemia, lipid trafficking disorders, and immune deficiency. In all ABC transporters, ATP-driven movements within two highly conserved nucleotide-binding domains (NBDs) are coupled to conformational changes of two transmembrane domains (TMDs), which provide a framework for substrate binding and release on the opposite side of the membrane and enable the transporter to cycle between inward-facing and outward-facing orientations. Several structures of ABC transporters determined either by X-ray crystallography or single-particle electron cryo-microscopy (cryo-EM) have been reported, mostly exhibiting a variation of the inward-facing state, which highlights their dynamic behavior. However, for a complete understanding of the conformational dynamics, further structural information on intermediates is needed – especially for heterodimeric ABC transporters, which are predominant in humans and for which only limited structural information is available.

One prime example of such human heterodimeric ABC transport complexes is the transporter associated with antigen processing (TAP). TAP is a key player of the adaptive immune response, because it translocates proteasomal degradation products into the ER lumen for loading of MHC I molecules. Many functional aspects of TAP have been disclosed in recent years. However, structural information is lacking far behind and a major challenge in the field of medical relevant transporters. Recently, the heterodimeric ABC export system TmrAB (*Thermus thermophilus* multidrug resistance proteins A and B) was identified as an ortholog of TAP, by sharing structural homology with TAP and, intriguingly, being able to restore antigen presentation in human TAP-deficient cells. Thus, TmrAB is a biochemically well-characterized ABC exporter that can be regarded as a functional ortholog of TAP and serves as a model system for (heterodimeric) ABC export systems in general.

Thus, to illuminate the molecular basis of substrate translocation by single-particle cryo-EM, one of the main objectives of this work was the generation of stabilizing chaperones (synthetic

antibodies, nanobodies, cyclic peptides) to reduce the conformational heterogeneity of TAP and TmrAB. Selected antibodies were analyzed with respect to stable complex formation, conformational trapping, and the ability to serve as alignment tools for structural studies by single-particle cryo-EM. Both antibody types were shown to form sufficiently stable complexes to serve as a rigid body for EM analyses. However, all selected antibodies bound to the inward-facing state exclusively.

Hence, for EM studies, various ligands were added to elucidate the full spectrum of conformational states during the catalytic cycle. For TAP, first attempts by negative-stain EM revealed a homogenous distribution of particles on the grid. Surprisingly, no transporter-like features were observed although various attempts were applied to increase the overall sample quality.

For TmrAB, in contrast, the complete conformational space in a native-like lipid environment under turnover conditions was mapped. Cryo-EM analysis of TmrAB incubated with ATP-Mg²⁺ and substrate revealed two distinct inward-facing conformations (IF^{wide} and IF^{narrow}) as well as two asymmetric conformations with dimerized NBDs, which were markedly different from all previously reported structures. Here, the catalytically active site was slightly wider and contained ADP, while ATP was still bound at the catalytically-inactive site within the NBDs, demonstrating an asymmetric post-hydrolysis state. Intriguingly for the inward-facing conformations, a weak additional density close to residues M139^{TmrB} and W297^{TmrB} was observed in the inward-facing conformation, which displayed a higher degree of cytosolic gate opening (IF^{wide}) indicating the presence of substrate. To verify that this density corresponds to substrate, single alanine mutations of M139^{TmrB} and W297^{TmrB} were introduced, leading to a strong reduction in substrate binding and transport. Since substrate release requires the opening of the extracellular gate, the absence of an outward-facing open conformation indicated that the opening must be highly transient. In order to explore the outward-facing open conformation, a cryo-EM analysis of the catalytically-inactive TmrA^{E523Q}B mutant upon incubation with ATP-Mg²⁺ was performed. Remarkably, within the same dataset, two different outward-facing conformations (occluded and open) were resolved, both in an ATP-bound state, which indicated that binding of ATP is sufficient to drive the large-scale conformational transition from inward-facing to outward-facing open. To explore the effect of nucleotide hydrolysis, TmrAB was trapped by vanadate. Again, two populations were observed, representing the outward-facing open and outward-facing occluded conformation.

Based on several structures of key intermediates, determined under turnover conditions or trapped in the pre-hydrolysis and hydrolysis transition state, for the first time the complete description of the ATP hydrolysis and translocation cycle of a heterodimeric ABC transport complex was elucidated in one single study. By mapping the conformational landscape during active turnover, aided by mutational and chemical modulation of kinetic rates, fundamental and so-far hidden steps of the substrate translocation cycle of asymmetric ABC transporters were resolved and a general template for (heterodimeric) ABC exporter-catalyzed substrate translocation was provided.

4. Introduction

4.1 ATP-binding cassette transporters

ATP-binding cassette (ABC) transporters constitute an omnipresent superfamily of integral membrane proteins that utilize the energy of ATP binding and hydrolysis to translocate a multitude of chemically diverse substrates across cell membranes in all domains of life (1-5). ABC transporters thus play key roles in various cellular and physiological processes, ranging from nutrient uptake to adaptive immunity (6, 7). Although all ABC transporters share two conserved cytosolic nucleotide-binding domains (NBDs), which couple the chemical energy of ATP to conformational changes of two transmembrane domains (TMDs) aligning the translocation pathway (5, 6, 8), the structural organization and conformational spectrum are highly diversified. Based on the structural organization of their core TMDs and direction of substrate translocation, ABC proteins are stringently classified into seven distinct types (Figure 1) (9). Type I and II ABC transport systems are importers (9). They are characterized by a minimal core of five and ten transmembrane helices (TMHs) as shown for the maltose transporter MalFGK₂ or the vitamin B₁₂ transporter BtuCD from *Escherichia coli*, respectively (9-11). In contrast, type III ABC importers do not comprise the conserved architecture of two similar TMDs, but consist of one integral membrane protein (EcfT) and a membrane-embedded substrate-binding protein (EcfS) (9). These energy-coupling factor (ECF) importers are found in bacteria, Archaea, and some plant organelles (12, 13). The ABC transporter type IV fold is defined by six characteristically arranged TMHs as shown for the lipid A-flipping ABC transporter MsbA, the transporter associated with antigen processing (TAP) or its bacterial ortholog TmrAB (9, 14-18). Type V ABC transporters have TMD architectures, which differ strongly from the previously described ABC transporter fold, as shown by the 3.9-Å resolution X-ray structure of nucleotide-free *Aquifex aeolicus* Wzm-Wzt (19). The transmembrane helices and intracellular loops of Wzm-Wzt are shorter compared to type IV ABC exporters, resulting in a smaller distance between NBDs and membrane. Additionally, the NBDs of Wzm-Wzt remain in close contact to each other even in the absence of nucleotide (9, 19). The lipopolysaccharide-extracting ABC transporter LptB₂FG from *Pseudomonas aeruginosa* constitutes a novel class of ABC transporters: ABC transporter type VI (9). For the TMDs LptF and LptG, no helix swapping as in type IV transporters is observed but the twelve TMHs are all bent outwards, forming a large V-shaped cavity. Moreover, both TMDs harbor periplasmic β-jellyroll-like domains, which presumably release lipopolysaccharide upon ATP hydrolysis-induced conformational changes (20). The homodimeric

ABC transporter MacB, as part of the MacAB-TolC multidrug efflux pump, is an example for a type VII ABC transporter (9). The TMDs consist of four helices each, which form a tight dimer, while the NBDs are clearly separated. Thus, instead of a TMD substrate-binding cavity, the entry pathway for periplasmic substrates is thought to be located at the membrane-periplasm boundary (9, 21).

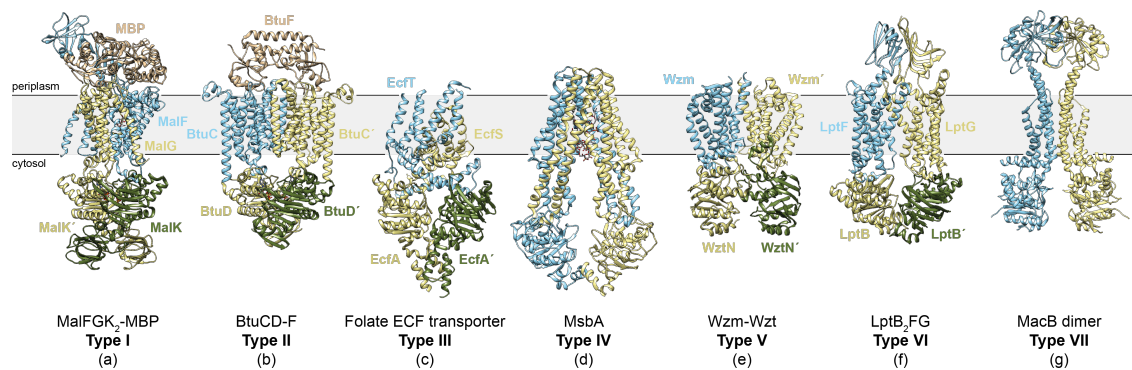


Figure 1: **Representative bacterial ABC transporters.** **a**, X-ray structure of the *Escherichia coli* maltose importer MalFGK₂ in complex with the maltose-binding protein (MBP), maltose, and ATP (PDB: 2R6G; (11)). **b**, Crystal structure of the transporter-binding protein complex BtuCD-F from *E. coli* trapped in an β - γ -imidoadenosine 5'-phosphate (AMP-PNP)-bound intermediate state (PDB: 4FI3; (10)). **c**, X-ray structure of the folate ECF transporter from *Lactobacillus brevis* determined in an inward-facing nucleotide-free conformation (PDB: 4HUQ; (13)). **d**, Cryo-EM reconstruction of nucleotide-free *E. coli* MsbA in lipid nanodiscs with bound lipopolysaccharide (PDB: 5TV4; (18)). **e**, X-ray structure of a channel-forming O-antigen polysaccharide ABC transporter Wzm-Wzt-homolog from *Aquifex aeolicus* (PDB: 6AN7; (19)). **f**, Crystal structure of lipopolysaccharide-extracting nucleotide-free LptB₂FG from *Pseudomonas aeruginosa* (PDB: 5X5Y; (20)). **g**, Cryo-EM reconstruction of the MacB dimer as part of the MacAB-TolC ABC-type tripartite multidrug efflux pump from *E. coli* (PDB: 5NIK; (21)). Adapted from (9).

Apart from above-mentioned differences in TMD architecture, a common feature of all seven classes of ABC transporters is the highly conserved structural domain organization of the NBDs (Figure 2). During catalysis, the NBDs form tight dimers in a head-to-tail arrangement, forming two nucleotide-binding sites (12, 22). Within the nucleotide-binding sites, several highly conserved sequence motifs are essential for coordinating ATP binding and hydrolysis, as well as for NBD-NBD and NBD-TMD communication (Figure 2) (12). The key motifs Walker A (P-loop) and Walker B coordinate the phosphates of ATP and supplement the catalytic base essential for ATP hydrolysis, the C-loop (signature motif) aligns the ATP molecule for ATP hydrolysis (22-25). Further hallmarks of the NBDs of ABC transporters are the D-loop, which ensures unidirectional transport across the membrane (26-28), and the Q- and X-loops, which are involved in inter-domain communication (29) and communication with the TMD coupling helices, respectively (30). In many ABC proteins (28 out of 48 in humans), one of the two ATP-binding sites is

catalytically inactive due to several amino acid substitutions, suggesting an asymmetric function of the two NBDs (12, 31).

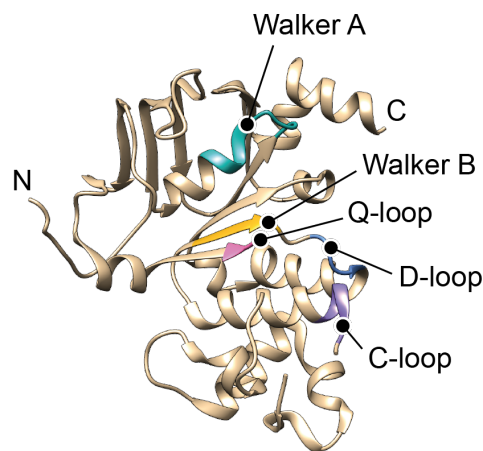


Figure 2: **Domain organization of TAP1 NBD.** Important sequence motifs within the NBDs of ABC transporters exemplarily shown for the NBD of rat TAP1 (PDB: 2IXE) (26, 27). Walker A and B motif: phosphate coordination of the ATP. Additionally, the Walker B motif provides the catalytic glutamate (24, 25). Q-loop: provides contacts to the TMD and is thus involved in the interdomain communication (29). D-loop: ensures unidirectional transport (26-28). C-loop (signature motif): aligns ATP for hydrolysis (22).

During ATP hydrolysis-driven substrate translocation, ABC transporters cycle between inward-open and outward-open states accompanied by conformational rearrangements within the NBDs and TMDs, suggesting a trajectory of numerous transient intermediates. In the current model, which is supported by several X-ray structures of ABC transporters, substrate translocation follows an *alternating access* mechanism (12, 15). ATP (and substrate) binding induce a tight dimerization of the two NBDs in a head-to-tail fashion leading to the assembly of two nucleotide-binding sites, each sandwiched between the Walker A/B motif of one NBD and the ABC signature motif of the other NBD (32-35). NBD dimerization causes a conformational change in the TMDs leading to a transition from an inward-open to an outward-open conformation to allow for release of the transported substrate. Hydrolysis of ATP and release of ADP and inorganic phosphate are essential to reset the transporter back into the inward-facing state (5, 12).

Over the last decades, several structures of ABC transporters determined either by X-ray crystallography or cryo-EM were reported, mostly exhibiting a variation of the inward-facing state with partially or fully separated NBDs (16, 32-34, 36-41). Single-particle cryo-EM has made it possible to visualize ABC transporters that were refractory to crystallization and enabled the elucidation of transient conformational states of various transporters (9, 42). The first structures

of transition intermediates were presented for the nucleotide-bound homodimeric antibacterial peptide ABC transporter McjD from *Escherichia coli* (43), the ATP γ S-bound homodimeric peptide exporter PCAT1 (44), the ADP-bound homodimeric lipid-linked oligosaccharide flippase PglK from *Campylobacter jejuni* (45), and the zosuquidar/UIC2-bound human-mouse chimeric ABCB1 (46). Lately, the molecular structures of human ATP-bound outward-facing ABCB1 and bovine MRP1 were solved by cryo-EM utilizing ATP hydrolysis-incompetent mutants in which the catalytic glutamates were replaced by glutamines (35, 47).

While these structures provided new insights into the structural dynamics of ABC transporters, the connection of different structural states of transporters during the catalytic cycle remains to be elucidated. This is specifically true for heterodimeric ABC transporters, which are predominant in humans and for which only limited structural information is available. Because of their involvement in various cellular functions, malfunctioning ABC transporters are the root cause of a variety of human pathologies, including hypercholesterolemia, lipid trafficking disorders, and immune deficiency (1, 5). Furthermore, human ABC exporters mediate chemotherapy resistance of cancer cells during chemotherapy, whereas bacterial ABC proteins are responsible for multidrug resistance in microorganisms, an emerging global public health threat (48, 49), highlighting the importance of a complete mechanistic understanding of ABC transporter-catalyzed substrate translocation.

4.1.1 TAP – a key player of the MHC class I dependent antigen processing pathway

The adaptive immune response of jawed vertebrates is based on a sophisticated protection system, with TAP as one of the key components (50). Cytosolic proteasomal degradation products are recognized and translocated by TAP into the lumen of the endoplasmic reticulum (ER) and are subsequently transferred onto major histocompatibility complex class I (MHC I) molecules in the macromolecular peptide-loading complex (PLC) (51, 52). The PLC is composed of the heterodimeric transport complex TAP, the chaperones tapasin and calreticulin, the ER-resident disulfide isomerase ERp57, the MHC class I heavy chain, and β_2 -microglobulin (53, 54). Thermodynamically stable peptide/MHC I complexes dissociate from the PLC and traffic *via* the secretory pathway to the cell surface for antigen presentation. Cytotoxic CD8⁺ T-lymphocytes (CTLs) recognize antigens presented on MHC I, leading to a CTL-mediated elimination of infected or malignantly transformed cells (50).

TAP is a heterodimer composed of the two half-transporters TAP1 (also known as ABCB2) and TAP2 (ABCB3) (5, 12, 55, 56). TAP shares the same architecture as other type IV ABC transporters, composed of a N-terminal TMD and a cytosolic NBD per ABC half-transporter, which is referred to as coreTAP (cTAP) complex. Additionally, human TAP1 and TAP2 harbor a specialized N-terminal transmembrane domain (TMD0), a four-TMH bundle, which provides the interaction platform for the recruitment and assembly of the PLC *via* the interaction with the MHC I-specific chaperone tapasin (12, 51, 57). With regards to peptide binding and translocation as well as the integration of TAP into the ER membrane, the TMD0s are dispensable (58-60).

As major component of the PLC, TAP recognizes proteasomal degradation products and translocates these peptides into the lumen of the endoplasmic reticulum (ER) for transfer onto MHC I molecules to trigger the adaptive immune response. This function implies that TAP is highly selective but has to translocate a wide spectrum of peptides across the ER membrane. Thus, TAP binds and shuttles preferentially hydrophilic peptides with a length of 8 to 16 amino acids into the ER, however, longer, even 40-mer peptides can also be transported, but with lower efficiency (12, 61-64). The N- and C-terminal residues determine the affinity of TAP, allowing the combination of high selectivity of the transporter and a broad variety of antigenic peptides. Positively charged residues are favored for the first two positions of the N-terminus, aromatic residues for the third N-terminal position and basic or hydrophobic residues at the C-terminus (63, 65, 66). By dynamic nuclear polarization (DNP)-enhanced solid-state nuclear magnetic resonance (ssNMR) spectroscopy, Lehnert and co-workers deciphered the backbone conformation of an antigenic peptide in complex with TAP. The high-affinity peptide KRYQNSTVY was found to bind to TAP in an overall extended conformation with an N-to-C terminus distance of approximately 2.5 nm, which was in perfect agreement with previously performed pulsed electron paramagnetic resonance (EPR) distance measurements on a peptide/TAP complex (66, 67). According to previous findings, the affinity and specificity were found to be mediated by multiple recognition sites in the N- and C-terminal regions of peptides (67). Besides peptide binding, also peptide translocation by TAP was heavily investigated. In 2014, Grossmann *et al.* showed that TAP acts as a molecular diode that translocates peptide substrates against the concentration gradient in a strict unidirectional way (27). By substitution of the conserved aspartate within the D-loop of TAP1 (D647), the importance of the D-loop in coupling ATP hydrolysis with peptide translocation was emphasized. The ATP hydrolysis-incompetent D647A/wt complex decreased the ATP-driven NBD dimerization affinity and thus turned the unidirectional primary active pump into a passive bidirectional nucleotide-gated facilitator upon binding of either ATP or ADP (27). In summary, Grossmann *et al.* showed within this study that

ATP hydrolysis is not required for peptide translocation *per se* but is essential for active and unidirectional transport.

TAP is a prime target for the inhibition by viral factors and is involved in tumor development and infectious diseases (5, 12). Several viruses have developed various mechanisms as immune escape strategies, including direct inhibition of TAP. The immediate early gene product ICP47 encoded by Herpes simplex virus (HSV-1/2), for example, inhibits binding of antigenic peptides by acting as a competitive inhibitor of TAP with nanomolar binding affinity (68-70). The type I membrane glycoprotein US6 encoded by human cytomegalovirus (HCMV) is an example for a viral glycoprotein, which affects TAP on the ER-luminal side. US6 causes a *trans*-inhibition of TAP by arresting the transporter in a conformational state incapable of ATP binding (71-74). Another type I membrane protein, which causes a conformational arrest of TAP and therefore inhibits peptide translocation by TAP, is UL49.5, a viral protein encoded by several varicelloviruses. UL49.5 has developed different strategies to inhibit peptide translocation *via* TAP. On one hand, UL49.5 induces proteasomal degradation of TAP, on the other hand, it arrests the transporter in a transport-incompetent state without affecting ATP and peptide binding (75, 76). BNLF2a, a tail-anchored protein encoded by Epstein-Barr-virus, abolishes both ATP and peptide binding (12, 77, 78). Finally, a short ER-luminal fragment of the type II membrane protein CPXV012, which results from a frameshift in the cowpox virus genome, inhibits TAP by mimicking a high ER-luminal peptide concentration provoking a *trans*-inhibition of antigen translocation (79).

Many functional aspects of the TAP complex were disclosed in recent years. However, structural information is lacking far behind. Until 2016, structural information was only based on homology models from the crystallized bacterial exporter Sav1866 from *Staphylococcus aureus* (32), TM287/288 from *Thermotoga maritima* (36), mouse ABCB1 (80), and the soluble NBD1 of TAP1 (31), while a high-resolution structure of the heterodimeric TAP complex was eagerly awaited. In 2016, Oldham *et al.* determined the structure of human TAP bound to the viral factor ICP47 by cryo-EM (16, 17). This 4.0-Å resolution structure revealed the exact position of ICP47 in the TAP complex and thus the mechanism of ICP47-mediated inhibition of TAP (Figure 3b). ICP47 was found to form a helical hairpin with the 55 N-terminal residues of ICP47 wedging in between two helical bundles of the TAP complex. ICP47 thus traps TAP in an inactive conformation distinct from the normal transport cycle by cracking the gating region at the ER-luminal side open to a width of approximately 4 Å in diameter. No density was observed for the 33 C-terminal residues of ICP47 due to the high flexibility. ICP47 was found to form strong contacts with TMH3 and

TMH6 of TAP2, whereas the interactions of ICP47 and TAP1 were less extensive (16). These results are in agreement with a study published by Herbring and co-workers highlighting the stabilizing properties of an ICP47 fragment (residues 1 to 65) when fused to TAP2, demonstrating a directionality for optimal ICP47 binding dictated by the asymmetry of the heterodimeric TAP complex (81). A fundamental step in the understanding of the underlying mechanistic principles of TAP function was provided by Bles and coworkers (51). Bles *et al.* isolated the human PLC from Burkitt's lymphoma cells stabilized by ICP47 and determined the structure of the fully assembled human endogenous PLC by single-particle cryo-EM to an overall resolution of 9.9 Å. This cryo-EM structure provided an integral framework for the understanding of the quality control of peptide/MHC I complexes in adaptive immunity (51).

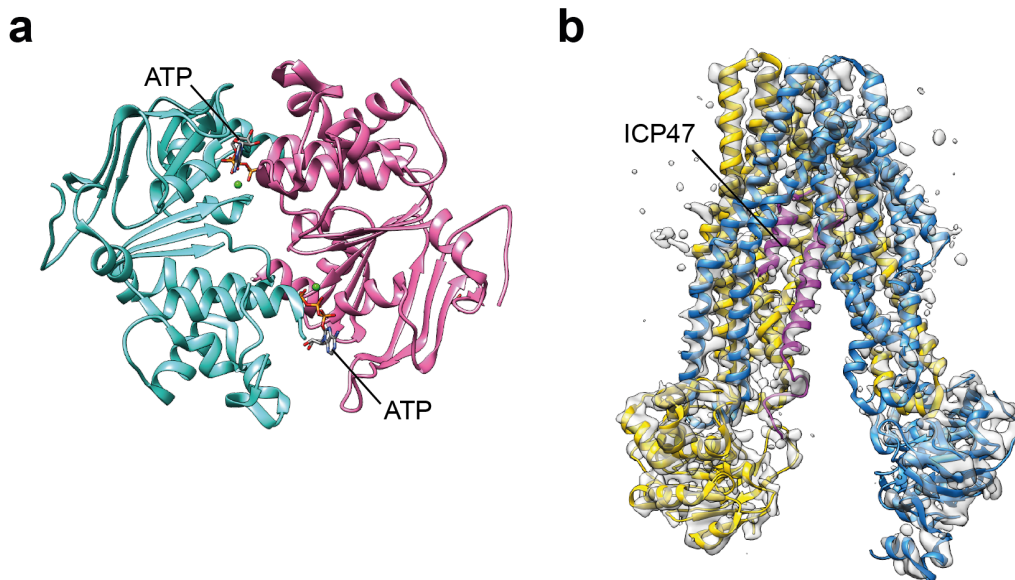


Figure 3: **TAP complex at atomic resolution.** **a**, 2.0-Å resolution structure of the rat TAP1-NBD homodimer (D645N mutant) with two ATP-Mg²⁺ at the dimer interface (PDB: 2IXE, (31)). **b**, Cryo-EM map of ICP47-bound TAP filtered to 4.0 Å resolution. The atomic model (cartoon representation) is fitted into the density map (EMD: 8482, PDB: 5U1D, (16)). ICP47 (magenta) is wedged between TAP1 (blue) and TAP2 (gold) trapping TAP in a unique inward-facing conformation.

4.1.2 TmrAB – a model system for heterodimeric ABC exporters

Over the last few years, several bacterial and eukaryotic export systems were identified, which mediate a multidrug resistance phenotype by translocating a wide range of structurally and chemically unrelated compounds out of cells (82-84). One prime example of such a bacterial multidrug export system is the heterodimeric transport complex TmrAB (*Thermus thermophilus* multidrug resistance proteins A and B) identified from the Gram-negative thermophilic

eubacterium *Thermus thermophilus* HB27, which was originally isolated from terrestrial hot springs in Japan (83, 85). In 2004, the whole genome of *T. thermophilus* was sequenced, revealing at least 42 complexes to be primary transporters belonging to the ABC protein family. However, TmrA (TTC0976) and TmrB (TTC0977) were the only two ABC half-transporters found (86). TmrAB shares the same conserved architecture as most ABC export systems, comprised of two half-transporters encoded by one polypeptide chain each, which are arranged in a pseudo-twofold symmetric manner. The transmembrane domain (TMD) of each half-transporter is composed of six transmembrane helices (TMHs), which are organized in a domain swapping arrangement, where each wing is composed of TMH1-TMH3 and TMH6 of one subunit and TMH4-5 of the other subunit (14, 83). The NBDs contain the conserved Walker A, Walker B, and ABC signature motif, as well as the Q-loop, D-loop, and H-loop, but one half-transporter contributes to a catalytically inactive, degenerate ATP-binding site. This functional asymmetry within the NBDs is the result of a substitution of the putative catalytic glutamate next to the Walker B motif by an aspartate (83).

TmrAB is an exceptionally versatile export system with an extremely broad substrate specificity. Already in 2011, Zutz *et al.* presented TmrAB-mediated Hoechst 33342 uptake in inside-out vesicles. Detergent-solubilized TmrAB was shown to turn over 9 molecules of ATP per second at a permissive temperature of 68 °C (83). Apart from drugs, TmrAB has been demonstrated to translocate and concentrate peptide substrates up to 4000-fold in an ATP-dependent manner into liposomes (15). Additionally, an involvement of TmrAB in glycolipid translocation is discussed, based on the liquid chromatography-mass spectrometry performed by Bechara *et al.* (87). Upon applying an extensive delipidation protocol, a selectivity of TmrAB for negatively charged lipid species was observed. Among various phosphatidylglycerol (PG) species, also hepta- and tetra-acylated lipid A species were found to be tightly attached to TmrAB. Only upon applying hydrolyzing conditions, retained lipid A species were displaced and no rebinding was observed. In contrast, upon incubation of TmrAB with the non-hydrolysable ATP analogue AMP-PNP or utilizing an ATPase-deficient mutant of TmrAB, the population of bound lipid A species remained the same. Based on these results, Bechara and co-workers concluded that conformational changes of the NBDs are necessary for lipid A displacement, and therefore proposed a role of TmrAB in glycolipid translocation (87).

Many functional aspects of substrate translocation by TmrAB were disclosed in recent years, showing that TmrAB can serve as a model system for (heterodimeric) ABC export systems in general. Additionally, it was shown that TmrAB can be regarded as an ortholog of human TAP,

because it does not only share structural homology with TAP, but is also able to restore antigen presentation in human TAP-deficient cells by translocating antigenic peptides (15).

In 2015, Kim and co-workers provided first insights into the structure of TmrAB by the determination of a subnanometer-resolution single-particle cryo-EM reconstruction of detergent-solubilized TmrAB in a nucleotide-free conformation, utilizing a Fab (fragment antigen binding) as fiducial marker (14). Within this study, TmrAB-binding Fabs were isolated from a human naïve B-cell Fab phage-displayed library and analyzed for their ability to form rigid complexes with TmrAB. Two Fabs (AH5 and BA6), which had the highest relative affinities, were used for cryo-EM, and three-dimensional reconstructions of TmrAB/Fab complexes were determined. The density map of the TmrAB/AH5 complex with an overall resolution of 8.2 Å was of sufficient quality to clearly resolve secondary structure features (Figure 4a) (14). In 2017, the nucleotide-free inward-facing state of TmrAB was further investigated by X-ray crystallography. Nöll *et al.* presented the 2.7-Å X-ray structure of detergent-solubilized TmrAB in a unique asymmetric nucleotide-free inward-facing state (Figure 4b). This structure, together with the X-ray structure of the ABC exporter TM287/288 from the thermophilic bacterium *Thermotoga maritima* are the only crystal structures of heterodimeric ABC exporters encompassing a degenerate nucleotide-binding site so far (36, 88). In the nucleotide-free state, TmrAB adopts a unique asymmetric conformation, with the extracellular gate tightly sealed, but a cavity within the TMDs open to the cytosol. Kim *et al.* observed significant extra density in this cavity bound to TMH5 of TmrB and speculated that this density is attributable to a co-purified lipid or detergent molecule (14). Additionally, a lateral gate is formed by TmrB at the intracellular side of the membrane, enabling the transporter to accommodate potential hydrophobic substrates (14, 15). Another remarkable structural feature of TmrAB are the C-terminal helices of the half-transporters, referred to as zipper helices. Nöll and co-workers investigated the importance of the rearrangement of the zipper helices during substrate translocation by disulfide cross-linking of an introduced cysteine pair, combined with subsequent transport studies and deletion of the zipper helices. In both cases, the translocation activity of TmrAB was shown to be drastically reduced, suggesting an important role of the zipper helices in guiding the conformational changes associated with substrate translocation (15).

In line with the understanding of the structural rearrangements of TmrAB during substrate translocation, Barth *et al.* investigated the transition from the inward-open to the outward-open conformation using pulsed electron-electron double resonance spectroscopy (PELDOR/DEER). Addition of increasing ATP concentrations resulted in a tunable equilibrium between the inward-

and outward-open conformation, indicating that ATP binding to TmrAB, rather than ATP hydrolysis, is sufficient to drive dimerization of the NBDs and opening of the extracellular gate (89).

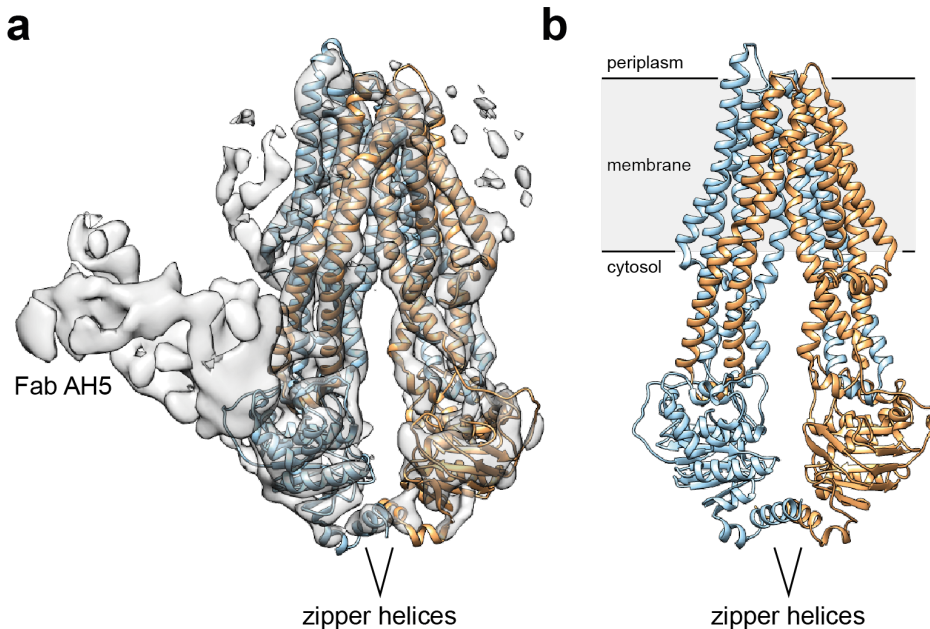


Figure 4: **Nucleotide-free inward-facing conformation of TmrAB.** **a**, Cryo-EM map of the TmrAB/AH5 complex filtered to a resolution of 8.2 Å. The atomic model of TmrA (blue) and TmrB (orange) is fitted into the density map (EMD: 6085, (14)). **b**, Cartoon representation of the 2.7-Å X-ray structure of TmrA (blue) and TmrB (orange) (PDB: 5MKK, (15)).

4.2 Scaffold proteins as lipid-bilayer mimics

20-30% of open reading frames of sequenced genomes account for membrane proteins (90), which play essential roles in many cellular processes, such as membrane transport, cell-to-cell communication, signal transduction, or lipid and energy metabolism (91). Due to their high abundance and key functions, membrane proteins are prime drug targets (92). In order to study membrane proteins *in vitro*, they have to be isolated from their native lipid environment. This membrane protein extraction is most commonly done using detergents. However, due to the dissociating properties of detergents, structurally and functionally important lipids might get lost, resulting in a loss of protein stability and function (93).

The impact of associated lipids on protein function has been highlighted for both ABC transporters investigated in the current study: In 2015, Bechara *et al.* monitored progressive delipidation of TmrAB by nano-electrospray mass spectrometry upon addition of an excess of

detergent and incubation at physiological temperatures (87). By applying this extensive delipidation protocol, only the most tightly bound lipids remained associated with TmrAB, resulting in a reduction of ATPase activity by about 60-70%. Additionally, when using shorter-chain detergents, such as octyl glucoside, TmrAB precipitated, which confirms the importance of bound lipids to the stability of the transporter (87). For TAP, Schölz *et al.* established a reconstitution protocol for functional TAP into proteoliposomes, which allowed the authors to systematically investigate the modulation of TAP function by specific lipids (94). Strikingly, upon reconstitution of TAP into large unilamellar vesicles composed of *E. coli* polar lipids, all functional parameters determined for TAP in membranes could be restored. By liquid chromatography Fourier transform mass spectrometry, phosphatidylethanolamine and phosphatidylinositol were identified as being essential for TAP function. The data indicate that loss of TAP function is directly associated with delipidation (94).

The drawbacks of detergents in membrane protein extraction have spurred the development of membrane model systems to study membrane proteins in a native-like lipid environment. One prime example of such a membrane mimetic system is the nanodisc technology developed by the laboratory of Stephen G. Sligar. With the introduction of the nanodisc system, Sligar and co-workers have provided a straightforward approach for the production of stable, discoidal bilayers of defined size and composition (95, 96). Initially, the membrane scaffold protein (MSP), which encloses the lipid bilayer, was based on the human ApoA1 protein component of high density lipoprotein particles (Figure 5) (97), however, the original MSP was further optimized with regard to stability and size. As a consequence of the strong tendency of phospholipids to form bilayers and the stabilizing effect of the amphipathic helix structure provided by the scaffold protein, the MSPs self-assemble into discoidal particles due to the interaction with lipid acyl chains (98). Membrane proteins can be reconstituted into nanodiscs by mixing solubilized membrane proteins with a solubilized lipid mixture of choice and the MSP, followed by a gradual removal of detergent *via* dialysis or bead adsorption (99). This self-assembly protocol can be adjusted to the required conditions including temperature, choice of detergent, lipid composition, stoichiometric ratio, and presence of cofactors as stabilizing agents (98). By utilizing MSPs with appropriate lengths, nanodiscs of various sizes can be assembled (up to 17 nm in diameter (100)). One major advantage of nanodiscs in comparison to liposomes or other scaffold proteins, such as the inherently polydisperse styrene maleic acid (SMA) polymers (101), is the overall stability of assembled discs over a period of days to weeks (98). Over the past decade, the nanodisc technology has proven to be applicable to a variety of membrane protein classes and was utilized not only for functional, but also for structural studies, including

cryo-EM, EPR, and NMR. Examples include the structure of TRPV1 (Transient Receptor Potential cation channel subfamily V member 1) in the unliganded, agonist-bound, and antagonist-bound states at resolutions of 3.2, 2.9, and 3.4 Å, respectively (98, 102). Recently, the structural basis for MsbA-mediated lipopolysaccharide recognition was elucidated by delineating the conformational transitions of nanodisc-embedded MsbA by cryo-EM (18).

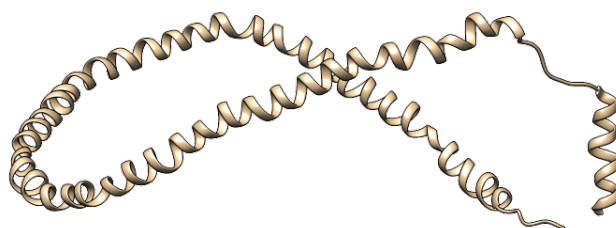


Figure 5: **Structure of apolipoprotein A-I.** 4.0-Å resolution X-ray structure of one molecule of truncated (Δ 1-43) human apolipoprotein (apo) A-I (residues 44-243). The apo Δ (1-43)A-I monomer consists primarily of a pseudo-continuous amphipathic α -helix that is punctuated by kinks at regularly spaced proline residues. Because of the curvature of the molecule, the apo Δ (1-43)A-I monomer adopts a sharply curved horseshoe-like shape, placing the N- and C-termini near one another (103).

Besides to MSPs, saposins were established as alternative scaffold proteins. In contrast to the classical nanodisc system with defined diameters dictated by the length of the MSP, saposins do not have any size limitations, but adapt to the size of the inserted membrane protein (91). Saposins are small, membrane-active proteins that exist in both soluble and lipid-bound states. Thus, saposins can form lipoprotein particles and were used to solubilize membrane proteins (91, 93, 104). In 2016, Frauenfeld *et al.* have presented a saposin-lipoprotein nanoparticle system, called Salipro, that is based on saposin A as scaffold protein (91). Frauenfeld and co-workers provided a protocol for the reconstitution of fragile membrane protein complexes into saposin-lipoprotein particles for functional and structural studies. Saposin A, a member of the saposin-like protein family (105), is composed of amphipathic helices and six invariable cysteine residues that form disulfide bridges (Figure 6). Utilizing the Salipro system, Frauenfeld *et al.* determined the structure of the homotetrameric proton-coupled oligopeptide transporter (POT) complex to subnanometer resolution. Since the POT complex harbors almost no structural features sticking out of the plane of the membrane, structure determination may have been facilitated by the saposin-lipid scaffold, which is relatively small and enhances the contrast in cryo-conditions (91). In the beginning of 2018, the importance of saposin-lipid-particles for membrane protein research was further highlighted by Flayhan *et al.* By utilizing saposin A as scaffold and analyzing different lipid compositions, Flayhan and co-workers presented the

successful reconstitution and stabilization of various membrane proteins harboring up to 56 transmembrane helices (93). A further advantage of saposin A as scaffold protein was demonstrated by Nguyen *et al.* (106). Nguyen *et al.* determined the structure of a mitochondrial calcium uniporter orthologue from *Neosartorya fischeri* (NfMCU) reconstituted into saposin-lipoprotein particles by phase-plate cryo-EM to 3.8 Å resolution. Former efforts of structure determination failed due to the channel's flexibility in nanodiscs, orientation bias in amphipols, and because of protein instability in detergent during the freezing process. The intrinsic property of saposin A to adapt to inserted membrane proteins, and thus maintaining inserted membrane proteins in an artificial lipid bilayer with a diameter being proportional to the transmembrane domains, allowed for successful high-resolution structure determination of NfMCU, which was encircled by six saposin A molecules, each forming a C-shaped clamp at an angle of approximately 45° to the central axis (106).

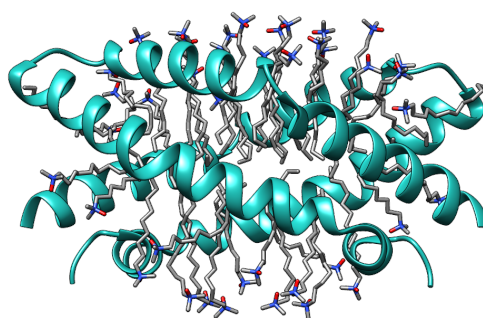


Figure 6: **Structure of saposin A.** 1.9-Å resolution X-ray structure of the open conformation of saposin A crystallized in the presence of LDAO (PDB: 4DDJ). The structure reveals two chains of saposin A in an open conformation encapsulating 40 internally bound detergent molecules organized in a highly ordered bilayer-like hydrophobic core (104).

4.3 Conformational trapping of membrane proteins

During substrate translocation, ABC transporters cycle between inward- and outward-open conformations, which are accompanied by various intermediary states. To gain further insights into the different conformational states, which are essential for a comprehensive understanding of the transport cycle, it is important to reduce the conformational flexibility by locking unique native conformations. One promising approach to stabilize distinct conformations is to lock and inhibit ABC transporters with immunoglobulin fragments. Various studies have shown that antibodies can serve as chaperones to enhance protein stability. More frequently, antibodies

are used as auxiliary agents to improve the crystallizability of membrane proteins by increasing the hydrophilic surface and by decreasing conformational flexibility (107).

In 2017, Taylor *et al.* presented the first high-resolution structure of a human multidrug transporter complexed by two antigen-binding fragments (108). This 3.8-Å resolution reconstruction of nanodisc-embedded human ABCG2 was determined with two 5D3-Fabs bound to extracellular loops of the ABC transporter, clamping the ABCG2 monomers together to preclude the formation of an outward-facing state. The Fabs did not only have an inhibitory effect, but also facilitated data processing by serving as an alignment tool. A similar approach has been already employed in 2015 for TmrAB, when Kim *et al.* identified five Fabs from a human naïve B-cell Fab phage-displayed library that formed stable complexes with TmrAB. These Fabs allowed the authors to determine three-dimensional reconstructions of TmrAB/Fab complexes to sub-nanometer resolution by cryo-EM (14).

4.3.1 Synthetic antibody fragments

The group of Anthony Kossiakoff (University of Chicago) has successfully established a general approach for the high-throughput screening and generation of synthetic antibody fragments (sABs) with high affinity, which can serve as stabilizing chaperones for structure determination of highly dynamic and unstable membrane proteins (Figure 7a). The advantage of this fully synthetic system is the opportunity to produce and select high-performance antibodies with customized properties (109). It was previously demonstrated that antibody fragments can serve as efficient stabilizing chaperones, hence the major difference of this strategy is not only the use of a synthetic phage-displayed library, but also of a functional minimalist library with restricted codon diversity (110). Since it is known that residues at certain complementarity-determining region (CDR) positions are preferentially involved in antigen binding and that certain types of amino acids enable productive binding contacts (111, 112), the library was designed using a restricted binary amino acid code of tyrosine and serine embedded in the highly stable humanized 4D5 Fab framework (109). Different libraries with increasing complexity and diversity based on the novel *reduced genetic code* concept were synthesized to obtain synthetic antibodies, which bind their antigen with affinities in the nanomolar range (110). The simplest library was diversified using the binary Tyr/Ser code only on paratope residues comprising the three heavy chain CDRs and solvent accessible paratopes in CDR-H1 as well as CDR-H2 (110). Chemical variability of the most complex and diverse library was greatly increased by diversifying CDR-H3 with an increased chance for the incorporation of tyrosine, serine, and glycine, and

exclusion of cysteine. The effectiveness of the different libraries was compared by the selection of antibodies against human vascular endothelial growth factor (hVEGF), resulting in high-affinity antibodies obtained from the most diversified library (110).

In 2016, Dominik *et al.* combined the previously described libraries with a novel antibody selection procedure to generate synthetic antibodies, which stabilize transient functional states of membrane proteins in a native-like lipid environment (113). To overcome the limitations of detergent-solubilized samples, such as loss of membrane protein stability and function, conformational bias, and insufficient biotinylation efficiency, Dominik *et al.* presented a nanodisc-based approach: Dominik and co-workers embedded membrane proteins in lipid-filled biotinylated nanodiscs, which were captured on streptavidin-coated magnetic beads for phage-displayed library sorting. The phage display selection approach is based on the incorporation of antibody-encoding genes into the phage chromosome, initially described by George P. Smith in 1985 (114) and further developed by McCafferty *et al.* in 1990 (115). For display of the antibodies on the surface, different bacteriophage systems can be utilized (e.g. T4, lambda, M13). Antibodies are mostly fused to the P3 coat protein of filamentous M13 phages. Since P3 is present in 3-5 copies per phage, the display system was designed as a *minimal plasmid* system to avoid multivalence effects. This *minimal plasmid* system is based on a phagemid vector, which only contains the genes encoding an antibiotic marker, the antibody-coat protein fusion, and the regions of the M13 chromosome required for rolling circle amplification and the production of the (+) DNA strand, which is capable of being packed into a phage. To produce new phages, *E. coli* cells harboring the phagemid vector are infected with a helper phage, which contains the complete M13 genome and is essential for phage assembly. Thus, the vast majority of the phages does not display any fusion protein, and the ones that display the fusion will only contain a single copy (116, 117). In general, phage-displayed library sorting is divided into 5 steps: phage addition, binding, washing, elution, and amplification. In case of the selection of synthetic antibodies, membrane protein-containing nanodiscs were captured, and library-displaying phages were added. Non-binding phages were removed by several washing steps. By the addition of detergent, nanodiscs were disrupted and phages were eluted for infection of *E. coli* cells and phage amplification. To avoid the enrichment of lipid- and MSP-binding synthetic antibodies, empty nanodiscs were added as soluble competitors (typically in a 5-10-fold molar excess). Upon sorting, single clones were produced and screened to determine the initial binding properties. By applying this approach for two different membrane proteins (a small YidC homolog from *Methanocaldococcus jannaschii*, Mj0480, and a pentameric magnesium ion channel from *Thermotoga maritima*, CorA), Dominik *et al.* obtained 14 and 10 unique synthetic

antibodies, respectively, with nanomolar affinities for their respective targets and virtually no affinity for empty nanodiscs (113). One of the high-affinity synthetic antibodies generated against biotinylated nanodisc-reconstituted *Mj0480* facilitated the formation of crystals that diffracted to 3.5 Å (118).

4.3.2 Nanobodies

Besides the conventional heterotetrameric IgG antibodies, which are composed of two identical heavy-chain and two identical light-chain polypeptides connected by disulfide bridges, a peculiar exception was found in sera of Camelidae (119). In addition to conventional IgGs, camelids (camels, llamas, vicuñas) have evolved antibodies composed only of heavy chains. Remarkably, a further type of heavy chain-only antibodies was found in nurse shark, wobbegong, and perhaps spotted ratfish, termed Ig-NAR (immunoglobulin new antigen receptor). In both cases, the antigen-binding domain is composed of just one variable domain, designated V_HH (variable chain of a heavy chain-only antibody) or nanobody for camels and V-NAR for cartilaginous fish (119, 120). In comparison to conventional antibodies, nanobodies possess an extended CDR3 to compensate for the loss of the light chain. Thus, nanobodies have acquired a higher structural complexity by involving more residues in antigen binding (120). As an important side effect of the extended CDR3, nanobodies exhibit a unique three-dimensional structure, allowing the binding of specific epitopes that cannot be reached by the concave antigen-binding region of conventional antibodies (121). In general, the CDRs of nanobodies are typically longer, more protruding, and lack steric interference from the light chain (120). By immunization of Camelidae with an antigen of choice, followed by cloning of the gene repertoire from peripheral blood lymphocytes and selection by a display system, such as phage or yeast display, high-affinity antigen-specific nanobodies can be easily obtained (119). Due to the small size (encoded by a gene fragment of roughly 360 base pairs, Figure 7b), nanobodies are easily cloned and expressed as recombinant proteins that are highly soluble, robust, and can be engineered into multivalent and multispecific formats (120). Due to the above-mentioned structural advantage as well as the high stability and affinity, nanobodies represent an auspicious research tool to develop future diagnostic and therapeutic applications. One recent example for nanobodies as diagnostic tools is the development of a nanobody-based luminescence sandwich assay (named DepID: Dual epitopes protein Identification) for the quantification of the soluble form of CD38 (sCD38) in the plasma of patients suffering from multiple myeloma (122).

In addition to diagnostic and therapeutic approaches, nanobodies find broad application as research tools in structural biology. Besides antibody fragments derived from conventional heterotetrameric antibodies, nanobodies were successfully used as crystallization chaperones (123-125). The Steyaert lab (University of Brussels) has established the use of nanobodies as research tools in structural biology (126), recently shown by the nanobody-dependent stabilization of the agonist-bound, active state of human β_2 AR (β_2 adrenergic receptor) (123, 124). This nanobody was selected *via* phage display from a nanobody library based on the B-cell repertoire of an immunized *Lama glama*. For the generation of the nanobody library, 100 μ g of agonist-bound G protein-coupled receptor (GPCR) reconstituted at high density into liposomes were injected weekly over a time period of six weeks intravenously into the llama. After the immunization procedure, lymphocytes were isolated, total RNA was prepared, reverse transcribed and nanobody-coding sequences were amplified and cloned into a phage display vector (123). Two selection rounds of phage-displayed library sorting were performed and GPCR-conformation-specific nanobodies were isolated. One of the selected nanobodies (Nb80) increased the β_2 AR affinity for its agonist isoproterenol 100-fold, indicating that Nb80 exhibits G protein-like behavior. This particular nanobody finally facilitated crystallization of the agonist-bound, active state of human β_2 AR (123, 124).

In 2013, the crystal structure of mouse ABCB1 in its inward-facing state complexed with a nanobody (Nb592) was published, revealing a unique mechanism of inhibition of ABC transporters (127). By binding to NBD1 of ABCB1, the nanobody hindered the formation of an ATP hydrolysis-competent dimer sandwich, resulting in an almost complete inhibition of the ATPase activity, highlighting the potential of nanobodies as arrestors of selected functional states of membrane proteins.

4.3.3 Cyclic peptides

In the past decades, biologists and chemists have explored the various properties and biological roles of peptides and related natural products in nature, including hormones, neurotoxins and antimicrobial peptides (128). These efforts have led to the development of new antibiotics, hormonal drugs such as vasopressin and oxytocin as well as the economical production of recombinant insulin (129), making this class of molecules a fundamental cornerstone in pharmaceutical industry today. Due to the sheer size of the chemical space of peptide natural products, the majority of peptide drugs on the market to date are either natural products or natural product derivatives. However new technologies for *de novo* peptide discovery have

emerged, such as phage display or mRNA display, allowing the generation of peptides against virtually any protein of interest (130). In 2014, Kodan *et al.* elucidated a novel peptide (Figure 7c), which allosterically locks a eukaryotic homolog of P-glycoprotein, CmABCB1, from *Cyanidioschyzon merolae* in the inward-facing state by clamping the transmembrane helices from the extracellular side (131). Co-crystallization of CmABCB1 with the macrocyclic peptide inhibitor prevented the transition to the outward-facing state, thus enhancing crystallization. The final structure could be solved with a resolution of 2.4 Å, showing that the inhibitor binds adjacent to the lipid bilayer. The peptide inhibitor was discovered from an artificial, ribosomally expressed cyclic peptide library using the FIT-RaPID (Flexible *in vitro* Translation - Random nonstandard Peptide Integrated Discovery) technology developed by Suga and co-workers (132). In essence, the FIT-RaPID platform combines genetic code reprogramming, allowing incorporation of non-standard amino acids with mRNA display of the *in vitro* translated peptides. Using the FIT-RaPID platform, up to 10¹³ different peptides can be analyzed in parallel for target binding. This diversity allows for robust identification of tightly binding macrocyclic peptides with K_D values in the lower nanomolar range and ring sizes typically ranging between 10-17 amino acids (132). In the FIT system, specific tRNAs are pre-aminoacylated with the amino acid of choice and supplemented to a reconstituted *in vitro* translation system. Aminoacylation of tRNAs with non-standard amino acids has been achieved either chemically, enzymatically or in the case of FIT by means of ribozymes. These so called Flexizymes have been discovered by SELEX and further engineered to catalyze the reaction of activated amino acids (e.g. cyano-methyl ester or 3,5-dinitrobenzyl ester) with the 3' hydroxyl group of tRNAs. These ribozymes specifically recognize the CCA-overhang of tRNAs, however with regard to the amino acid substrate the only requirement is an aromatic moiety either in the side-chain or the activating group. As thus, flexizymes are highly versatile, accepting a broad range of activated amino acids, including N-modified amino acids, D-amino acids, β-amino acids and various side chain modifications (133, 134). Reconstituted *in vitro* translation systems are composed of individually purified parts of the translation machinery (including ribosomes, initiation factors, elongation factors, release and recycling factors, and aminoacyl tRNA synthetases, in addition to an energy recycling system, tRNAs, amino acids, nucleoside triphosphates (132, 135)). Therefore, such *in vitro* translation systems can be readily customized for desired applications, especially genetic code reprogramming by omitting the reprogrammed amino acid or aminoacyl tRNA synthetase as well as mRNA display by excluding a release factor. A hallmark of bioactive peptide natural products is macrocyclization, which rigidifies the three-dimensional structure of the peptide leading to improved binders as well as decreased susceptibility to proteases. In the case of FIT, various chemistries have been explored for macrocyclization, however incorporation of

2-chloroacetyl amino acids in the initiator position together with a downstream cysteine has been shown to be a highly robust and convenient strategy for cyclization *via* thioether formation, and has become the dominant strategy within the RaPID system (132). A RaPID selection typically includes five steps: (I) a DNA library is transcribed into mRNA, which is subsequently ligated to a puromycin oligonucleotide at the 3' end, (II) FIT *in vitro* translation ultimately leads to a covalent linkage between the nascent peptide and the cognate mRNA *via* puromycin, (III) the mRNA display constructs are reverse transcribed, (IV) putative binders are isolated through affinity panning using the immobilized protein of interest and (V) the cDNA of binding peptides is isolated and amplified by PCR. This process can be repeated in an iterative fashion, leading to significant enrichment of binding peptides (136). The major advantage of this technique is the extremely rapid generation (days to weeks) of peptides with very high target affinities and specificities displaying non proteinogenic amino acid functionalities. (132). Besides the above-mentioned example, many more studies exist, highlighting the outstanding possibilities of tailor-made peptides prepared using the RaPID technology. One further example with regards to structure determination of membrane proteins is the generation of macrocyclic peptides that bind to the bacterial multidrug and toxic compound extrusion (MATE) transporter from *Pyrococcus furiosus* (137, 138). Hipolito and Tanaka *et al.* have presented structures of the H⁺-driven PfMATE transporter in complex with three thioether-macrocyclic peptides (MaD5, MaD3S, MaL6) determined to resolutions of 3.0, 2.6, and 2.5 Å, respectively. Based on their inhibitory bioactivity, the peptides presented in this study may represent new scaffolds for the development of potent inhibitors of MATE transporters from bacteria and eukaryotes (137).

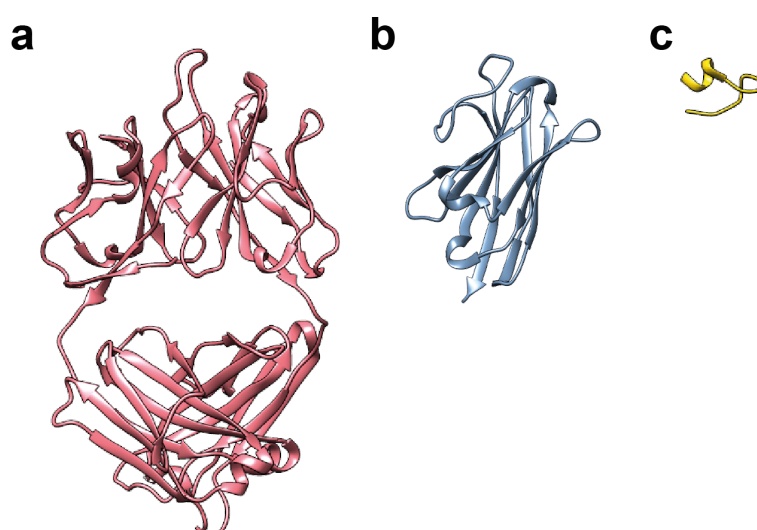


Figure 7: **Tools to lock specific conformations of dynamic membrane proteins.** **a**, anti-MBP sAB (PDB: 5BK1, (139)). **b**, Nanobody against a soluble trimeric envelope protein derived from HIV-1 subtype C (PDB: 5U65, (140)). **c**, Macrocyclic peptide aCAP generated against CmABCB1 and utilized for co-crystallization (PDB: 3WMG, (131)).

5. Aims and motivation

ABC transporters translocate a multitude of chemically diverse substrates across biological membranes. Malfunctioning ABC transporters are thus the root cause of a variety of human pathologies, including hypercholesterolemia, lipid trafficking disorders, and immune deficiency. Furthermore, ABC transporters confer multidrug resistance, an emerging global public health threat. Since the fundamental catalytic principles are thought to be shared among all ABC transporters, insights into the architecture and structural rearrangements during substrate translocation will not only deepen our understanding of human physiology, but are also of immediate clinical relevance. During ATP-driven substrate translocation, ABC transporters cycle between inward-open and outward-open states accompanied by conformational rearrangements within the NBDs and TMDs, suggesting a trajectory of numerous transient intermediates. Over the last few decades, several structures of ABC transporters determined either by X-ray crystallography or electron cryo-microscopy were reported. While these structures provided new insights into the structural dynamics of ABC transporters, the connection of different structural states of transporters during the catalytic cycle remains to be fully elucidated to understand the key events and conformational transitions that couple ATP binding and hydrolysis to substrate translocation. This is specifically true for heterodimeric ABC transporters, which are predominant in humans and for which only limited structural information is available.

One prime example of such heterodimeric human ABC transporters is the transporter associated with antigen processing (TAP) exhibiting two non-equivalent NBDs, with one half-transporter contributing to a catalytically inactive ATP-binding site. Recently, a heterodimeric ABC export system from a thermophilic eubacterium called TmrAB (*Thermus thermophilus* multidrug resistance proteins A and B) was identified, which does not only share structural homology with TAP, but is intriguingly also able to fully restore antigen presentation in human TAP-deficient cells. Moreover, it has been shown that TmrAB is an exceptionally versatile export system with an extremely broad substrate specificity that covers the substrate spectrum of the antigen translocation complex TAP. Thus, TmrAB is a biochemically well-characterized ABC exporter that can be regarded as a functional ortholog of TAP and serves as a model system for (heterodimeric) human ABC export systems in general.

In 2016, the 4.0-Å resolution structure of inward-facing TAP in complex with the viral inhibitor ICP47 was determined by cryo-EM, revealing the molecular basis of one immune evasion

mechanism employed by Herpesviridae (16). Recently, the crystal structure of TmrAB at 2.7 Å resolution in a unique asymmetric inward-facing conformation was published (15). Together with the subnanometer-resolution cryo-EM structure of TmrAB previously presented by Kim *et al.* in 2015 (14), these structures represent snapshots of inward-facing states of both ABC transporters. Nonetheless, for a complete understanding of the conformational rearrangements of TAP and TmrAB during their catalytic cycle, additional structures of catalytic intermediates are needed. A promising approach for the characterization of transient conformational states, essential for the understanding of mechanistic properties, is the conformational trapping by stabilizing chaperones.

Thus, to illuminate the molecular basis of substrate translocation of TAP and TmrAB by single-particle cryo-EM, synthetic antibodies, nanobodies, and macrocyclic peptides will be generated and analyzed with respect to stable complex formation, conformational trapping, and the ability to serve as fiducial marker/alignment tool (synthetic antibodies/nanobodies). Additionally, to enable optimal EM-imaging, TAP and TmrAB samples will be optimized with regards to contrast (signal-to-noise), stability, and homogeneity by screening different detergents, exchanging detergents for amphipols, adding fixation reagents, and embedding the transporters into a native lipid environment utilizing either the classical membrane scaffold protein MSP1D1 or saposin A.

Besides the generation of antibodies/cyclic peptides as stabilizing chaperones, various ligands will be added to nanodisc-embedded TmrAB to elucidate the conformational rearrangements during ATP hydrolysis and peptide translocation in a native-like lipid environment. Altogether, this study will provide a general transport mechanism, which is applicable to all heterodimeric (type IV) ABC exporters, and answer the controversial and in the ABC transporter field heavily discussed question, which step of the hydrolysis cycle provides the power stroke for substrate translocation.

6. Material

6.1 Antibodies and antibody fragments

Table 1: Antibodies used for immunoblotting.

Antibody	Reactivity	Host	Supplier	Dilution
Anti-TAP1 (clone 148.3)	Human	Mouse	(141)	1:20
Anti-TAP2 (clone 435.3)	Human	Mouse	(141)	1:20
Monoclonal anti-His (clone HIS-1)	-	Mouse	Sigma-Aldrich	1:3,000
CaptureSelect™ Biotin anti-C-tag conjugate	-	-	Life technologies	1:4,000
Anti-mouse IgG peroxidase conjugate	Mouse	Goat	Sigma-Aldrich	1:10,000
Anti-mouse IgG, alkaline phosphatase-conjugated	Mouse	Goat	Sigma-Aldrich	1:1,000
HRP-conjugated streptavidin	-	-	Thermo Scientific	1:4,000

6.2 Bacterial strains

Table 2: *Escherichia coli* strains.

Name	Genotype	Supplier
DH5α	F- φ80/ <i>lacZ</i> Δ <i>M15</i> Δ(<i>lacZYA-argF</i>) U169 <i>recA1 endA1 hsdR17</i> (r _k ⁻ , m _k ⁺) <i>phoA supE44 thi-1 gyrA96 relA1 λ</i> ⁻	Life technologies
BL21(DE3)	<i>FompT hsdSB</i> (r _B ⁻ , m _B ⁻) <i>galdcmm</i> 131 (DE3) pLysS (Cam ^R)	Life technologies
Rosetta-gami™ 2(DE3)	Δ(<i>ara-leu</i>)7697 Δ <i>lacX74</i> Δ <i>phoA PvuII phoR araD139 ahpC gale galk rpsL</i> (DE3) F' [<i>lac</i> ⁺ <i>lac1</i> ^q <i>pro</i>] <i>gor522::Tn10 trxB</i> pLysSRARE2 (Cam ^R , Str ^R , Tet ^R)	Novagen
TG1	[F' <i>traD36 proAB lac1</i> ^q Δ <i>M15</i>] <i>supE thi-1 Δ(lac-proAB) Δ(mcrB-hsdSM)5(rK - mK -)</i>	Lucigen
XL1-blue	<i>recA1 endA1 gyrA96 thi-1 hsdR17 supE44 relA1 lac</i> [F' <i>proAB lac1</i> ^q Δ <i>M15</i> Tn10 (Tet ^r)]	Stratagene

6.3 Buffers

Table 3: Summary of commonly used buffers.

Buffers	Composition	
AEBSF solution	PBS, pH 7.5	1x
	AEBSF (protease inhibitor; Carl Roth)	4 mg/ml
Blocking (ELISA, phage display)	PBS, pH 7.5	1x
	skimmed milk powder/BSA	2% (w/v)
	(biotin)	5 mM
Blocking (immunoblot)	PBS-T, pH 7.5	1x
	skimmed milk powder	2% (w/v)
Coomassie staining solution	methanol	40% (v/v)
	glacial acetic acid	10% (v/v)
	Coomassie Brilliant Blue G-250	0.1% (w/v)
ECL I	Tris-HCl, pH 8.0	100 mM
	luminol	2.5 mM
	coumaric acid	0.4 mM
ECL II	Tris-HCl, pH 8.0	100 mM
	H ₂ O ₂	0.02% (v/v)
Ficoll gradient (0%)	HEPES-NaOH, pH 7.5	20 mM
	NaCl	140 mM
	glycerol	5% (v/v)
Ficoll gradient (10%)	HEPES-NaOH, pH 7.5	20 mM
	NaCl	140 mM
	glycerol	5% (v/v)
	Ficoll	10% Ficoll
GraFix 10% solution	HEPES-NaOH, pH 7.4	20 mM
	NaCl	200 mM
	KCl	50 mM
	GDN	0.05% (w/v)
	glycerol	10% (v/v)

GraFix 30% solution	HEPES-NaOH, pH 7.4	20 mM
	NaCl	200 mM
	KCl	50 mM
	GDN	0.05% (w/v)
	glycerol	30% (v/v)
	glutaraldehyde	0.2% (v/v)
Liposome lysis	PBS, pH 7.5	1x
	SDS	1% (w/v)
Liposome stop	PBS, pH 7.5	1x
	EDTA	10 mM
MSP lysis	Tris-HCl, pH 8.0	40 mM
	NaCl	300 mM
	Triton X-100	1% (v/v)
MSP storage	Tris-HCl, pH 8.0	40 mM
	NaCl	300 mM
	glycerol	10% (v/v)
NAV binding	NaHCO ₃ , pH 8.2	100 mM
Nb lysis	Tris-HCl, pH 8.0	20 mM
	NaCl	100 mM
Nb purification	Tris-HCl, pH 8.0	20 mM
	NaCl	300 mM
	imidazole	300 mM
Nb storage	HEPES-NaOH, pH 7.5	20 mM
	NaCl	150 mM
Nb wash	Tris-HCl, pH 8.0	20 mM
	NaCl	300 mM
	imidazole	50 mM
Peptide binding	PBS, pH 7.4	1x
	GDN	0.05% (w/v)
Peptide elution	PBS, pH 7.4	1x
	SDS	1% (w/v)
Phosphate buffered saline (PBS)	Na ₂ HPO ₄	0.8 mM
	NaH ₂ PO ₄	0.1 mM
	NaCl	13.7 mM
	KCl	0.3 mM

PBS-T	PBS, pH 7.5	1x
	Tween-20	0.05% (v/v)
Reconstitution	HEPES-NaOH, pH 7.5	20 mM
	NaCl	140 mM
	glycerol	5% (v/v)
sABs lysis	Na ₃ PO ₄ , pH 7.4	20 mM
	NaCl	500 mM
	PMSF	1 mM
	DNase	2 mM
sABs storage	HEPES-NaOH, pH 7.5	20 mM
	NaCl	150 mM
sABs wash	Na ₃ PO ₄ , pH 7.4	20 mM
	NaCl	500 mM
Sapoin lysis/SEC	HEPES-NaOH, pH 7.5	20 mM
	NaCl	150 mM
Silver staining developing solution	ddH ₂ O	60 ml
	Na ₂ CO ₃	1.2 g
	formaldehyde	25 µl (37%)
	Na ₂ S ₂ O ₃ 5 H ₂ O	25 µl (20%, w/v)
Silver staining fixation solution	acetone	60 ml
	trichloroacetic acid	1.5 ml (50%, w/v)
	formaldehyde	25 µl (37%)
Silver staining impregnation solution	ddH ₂ O	60 ml
	AgNO ₃	0.8 ml (20%, w/v)
	formaldehyde	0.6 ml (37%)
Silver staining pre-treatment solution	ddH ₂ O	60 ml
	Na ₂ S ₂ O ₃ 5 H ₂ O	100 µl (20%, w/v)
SDS-PAGE anode	Tris-HCl, pH 8.9	1 M
SDS-PAGE cathode	Tris	1 M
	Tricine	1 M
	SDS	1% (w/v)
SDS-PAGE gel (3x)	Tris-HCl, pH 8.45	3 M
	SDS	0.3% (w/v)

SDS-PAGE sample (4x)	Tris-HCl, pH 6.8	200 mM
	glycerol	40% (v/v)
	SDS	8% (w/v)
	bromophenol blue	0.4% (w/v)
	(DTT)	400 mM
TAE	Tris	40 mM
	EDTA	20 mM
	acetic acid	1 mM
TAP IMAC elution	HEPES-NaOH, pH 7.4	20 mM
	NaCl	200 mM
	KCl	50 mM
	glycerol	15% (v/v)
	imidazole	200 mM
	GDN	0.05% (w/v)
TAP IMAC wash	HEPES-NaOH, pH 7.4	20 mM
	NaCl	200 mM
	KCl	50 mM
	glycerol	15% (v/v)
	imidazole	40 mM
	GDN	0.05% (w/v)
TAP lysis	KH ₂ PO ₄ , pH 7.4	50 mM
	EDTA	1 mM
	aminocaproic acid	5 mM
	glycerol	5% (v/v)
	benzamidin	2.5 mM
	PMSF	1 mM
TAP strep elution	HEPES-NaOH, pH 7.4	20 mM
	NaCl	200 mM
	KCl	50 mM
	glycerol	15% (v/v)
	D-desthiobiotin	10 mM
	GDN	0.05% (w/v)

TAP strep wash	HEPES-NaOH, pH 7.4	20 mM
	NaCl	200 mM
	KCl	50 mM
	glycerol	15% (v/v)
	GDN	0.05% (w/v)
TAP storage	HEPES-NaOH, pH 7.4	20 mM
	NaCl	200 mM
	KCl	50 mM
	glycerol	15% (v/v)
TFB I	CH ₃ CO ₂ K, pH 5.8	30 mM
	RbCl	100 mM
	MnCl ₂	50 mM
	CaCl ₂	10 mM
	glycerol	15% (v/v)
TFB II	MOPS, pH 6.8	10 mM
	RbCl	10 mM
	CaCl ₂	75 mM
	glycerol	15% (v/v)
TmrAB lysis	HEPES-NaOH, pH 7.5	20 mM
	NaCl	300 mM
	lysozyme	50 µg/ml
	PMSF	0.2 mM
	(β-mercaptoethanol)	1 mM
TmrAB purification	HEPES-NaOH, pH 7.5	20 mM
	NaCl	300 mM
	PMSF	0.2 mM
	β-DDM	0.05% (w/v)
	(β-mercaptoethanol)	1 mM
TmrAB SEC	HEPES-NaOH, pH 7.5	20 mM
	NaCl	150 mM
	β-DDM	0.05% (w/v)
	(β-mercaptoethanol)	1 mM
Transfer	Tris-HCl, pH 8.0	25 mM
	glycine	192 mM
	methanol	20% (v/v)

6.4 Chemicals and reagents

Table 4: List of chemicals and reagents, which were not ordered from Sigma-Aldrich or Roth.

Chemical/reagent	Supplier
1,2-dioleoyl- <i>sn</i> -glycero-3-phosphocholine	Avanti Polar Lipids
1,2-dioleoyl- <i>sn</i> -glycero-3-phospho (1'- <i>rac</i> -glycerol)	Avanti Polar Lipids
Acetic acid	VWR Chemicals
Agarose	Biozym
Ammonium molybdate	Fluka
Coomassie Brilliant Blue G250	Serva
D-desthiobiotin	IBA
Dimethylformamide	VWR Chemicals
Dimethyl sulfoxide	Thermo Scientific
dNTP-mix (10 mM)	Fermentas
Dynabeads® M-280 Streptavidin	Invitrogen
<i>E. coli</i> polar lipid extract	Avanti Polar Lipids
EZ-Link™ NHS-PEG4-Biotin	Thermo Scientific
Gene Ruler 100 bp Ladder Plus	Fermentas
Gene Ruler 1 kb Ladder	Fermentas
Hydrochloric acid	Fisher Chemical
Hydrogen peroxide	Merck
InstantBlue™	Expedeon
Ouabain	Fluka
Page Ruler Prestained Protein Ladder	Fermentas
Sulfuric acid	Merck
Trifluoroacetic acid	Merck
Zeocin	InvivoGen

6.5 Consumables and lab equipment

Table 5: List of consumables and lab equipment.

Equipment	Supplier
Agilent 1200 HPLC System	Agilent
ÄKTApurifier	GE Healthcare
Amicon Ultra Centrifugal Filters, 3 K, 30 K, 50 K, 100 K	Merck
Autoclave VE-150	Systec
Avanti J-26XP Centrifuge	Beckman Coulter
Cary 50 Bio UV/VIS spectrophotometer	Varian
CLARIOstar microplate reader	BMG Labtech
Ettan LC	GE Healthcare
Heraeus Megafuge 16R	Thermo Scientific
Lumi-Imager F1	Roche
Micro Bio-Spin [®] 30 Columns	Bio-Rad
Mini-extruder	Avestin
NanoDrop ND-1000	PeqLab
Optima [™] L-90K Ultracentrifuge	Beckman Coulter
Optima [™] TLX Ultracentrifuge	Beckman Coulter
Optima [™] XE-90 Ultracentrifuge	Beckman Coulter
PD-10 desalting columns	GE Healthcare
Shimadzu HPLC	Shimadzu
Zeba Spin Desalting Columns, 7K	Thermo Scientific

6.6 Detergents

Table 6: List of detergents used either for solubilization, purification, destabilization or washing purposes.

Detergent	Supplier
n-Dodecyl β -D-maltoside (β -DDM)	Roth
Fos-choline-12 (FC-12)	Anatrace
Glyco-diosgenin (GDN)	Anatrace
2,2-didecylpropane-1,3-bis- β -D-maltopyranoside (LMNG)	Anatrace
Sodium dodecyl sulfate (SDS)	Roth

Triton X-100	Roth
Tween-20	Roth

6.7 Enzymes

Table 7: Enzymes used for molecular biology.

Enzyme	Supplier
<i>DpnI</i> (10 U/ μ l)	Thermo Scientific
<i>HindIII</i> (10 U/ μ l)	Thermo Scientific
Pfu DNA polymerase (2.5 U/ μ l)	Thermo Scientific
Phusion high fidelity polymerase (2 U/ μ l)	Thermo Scientific
<i>Sall</i> (10 U/ μ l)	Thermo scientific
T4 ligase (5 U/ μ l)	Thermo Scientific

6.8 Media

Table 8: Summary of commonly used media.

Media	Composition	
2xYT medium	yeast extract	1% (w/v)
	NaCl	0.5% (w/v)
	tryptone	1.6% (w/v)
Basal salts	(NH ₄) ₂ SO ₄	68.1 mM
	CaSO ₄	5.4 mM
	K ₂ SO ₄	104.4 mM
	MgSO ₄	60.5 mM
	glycerol	4% (w/v)
Lysogeny broth (LB) medium (high salt)	yeast extract	0.5% (w/v)
	NaCl	1% (w/v)
	tryptone	1% (w/v)
Lysogeny broth (LB) medium (low salt)	yeast extract	0.5% (w/v)
	NaCl	0.5% (w/v)
	tryptone	1% (w/v)

Lysogeny broth (LB) agar (low salt)	yeast extract	0.5% (w/v)
	NaCl	0.5% (w/v)
	tryptone	1% (w/v)
	agar-agar	1.5% (w/v)
MGY medium	10x yeast nitrogen base (YNB) (34 g YNB + 100 g (NH ₄) ₂ SO ₄ /l)	10% (v/v)
	10x glycerol (100 g glycerol/l)	10% (v/v)
	500x biotin (200 mg/100 ml)	0.2% (v/v)
MMY medium	10x yeast nitrogen base (YNB) (34 g YNB + 100 g (NH ₄) ₂ SO ₄ /l)	10% (v/v)
	10x methanol (50 ml methanol/l)	10% (v/v)
	500x biotin (200 mg/100 ml)	0.2% (v/v)
PTM trace salts	FeSO ₄	233.8 mM
	CuSO ₄	24.03 mM
	NaI	0.53 mM
	MnSO ₄	17.8 mM
	Na ₂ MoO ₄	8.3 mM
	H ₃ BO ₃	0.32 mM
	CoCl ₂	2.1 mM
	ZnCl ₂	146.7 mM
	biotin	0.82 mM
H ₂ SO ₄	0.49% (v/v)	
Terrific broth (TB) medium	yeast extract	2.4% (w/v)
	tryptone	1.2% (w/v)
	glycerol	0.5% (w/v)
	10x TB salts	10% (v/v)
10x TB salts	KH ₂ PO ₄	0.17 M
	K ₂ HPO ₄	0.72 M

6.9 Oligonucleotides

Table 9: Oligonucleotides used for cloning of sAB-encoding genes into an expression plasmid (pIPTG) for protein production and cloning of TmrAB alanine substitutions. All oligonucleotides were purchased from MWG Eurofins in High Purity Salt Free (HPSF) grade.

Name	Sequence (5'-3')	Purpose
pIPTG_HindIII_fw	gccgaagcttctgattactcgcatcc	sAB expression
pIPTG_Sall_rev	tctgtcgaccttgggtgtgctgg	sAB expression
sAB_HindIII_fw	tctgattactcgcatccagcctc	sAB expression
sAB_Sall_rev	tcgacctgggtgtgctgggcttg	sAB expression
sAB_Col_PCR_rev	ttagtggtggtgggtggtgtctagatta	sAB expression
TmrB_D184A_fw	cggctcattgccctcgctaccgggaggcc	D184A ^{TmrB}
TmrB_D184A_rev	gtagcgacgggcaatgagccgcaggaggaa	D184A ^{TmrB}

6.10 Peptides

Table 10: Amino acid (aa) sequences of peptides used for functional studies. Y=L-Tyr, y=D-Tyr.

Peptide	Amino acid sequence
C4F	RRY ^F CKSTEL
R9LQK	RRYQKSTEL
Cyclic peptide VD3	yVTPLSVFDIWACG
Cyclic peptide VD3 ^F	yVTPLSVFDIWACGSGSGS ^F K
Cyclic peptide VD3 ^{biotin}	yVTPLSVFDIWACGSGSGS ^{biotin} K

7. Methods

7.1 Molecular biology and microbiology

7.1.1. Preparation of competent *E. coli* cells

For the preparation of competent cells, 3 ml Lysogeny broth (LB) low salt medium were inoculated with 100 μ l of *E. coli* cells (DH5 α cells for cloning, BL21 and Rosetta-gami™ 2(DE3) cells for protein production) and incubated overnight at 37 °C and 180 rpm. 2 ml of the overnight culture were used to inoculate 200 ml LB low salt medium. Cells were grown at 37 °C and 180 rpm. At an OD₆₀₀ of 0.4, cells were cooled down on ice. After 1 h incubation, cells were pelleted for 10 min at 2,000 x g, 0 °C. Subsequently, the pellet was resuspended in 35 ml TFB-I buffer. After a further incubation for 1 h on ice, cells were pelleted for 10 min at 3,000 x g, 0 °C and resuspended in 6 ml TFB-II buffer. Competent *E. coli* cells were divided into 50-150 μ l aliquots, snap frozen in liquid nitrogen, and stored at -80 °C.

7.1.2 Design of DNA constructs

7.1.3.1 DNA amplification

Restriction sites for endonucleases were introduced by polymerase chain reaction (PCR). Standard PCR conditions are summarized in Table 11. Pfu and Phusion high fidelity DNA polymerase were utilized according to the manufacturer's instructions. Oligonucleotides used for cloning and insertion of sAB-encoding sequences into a plasmid applicable for protein production are summarized in Table 9.

Table 11: Standard PCR conditions for cloning of sABs constructs.

Step	Time	Temperature	Cycles
Initial denaturation	2 min	95 °C	1x
Denaturation	30 s	95 °C	24x
Annealing	50 s	55 °C	24x
Elongation	1.5 min	72 °C	24x
Final elongation	3 min	72 °C	1x

Table 12: Standard PCR conditions for cloning of TmrAB alanine substitutions.

Step	Time	Temperature	Cycles
Initial denaturation	5 min	98 °C	1x
Annealing	1 min	63-72 °C	1x
Elongation	4 min	72 °C	1x
Denaturation	1 min	98 °C	25x
Annealing	1 min	63-72 °C	25x
Elongation	4 min	72 °C	25x
	30 s/kb (Phusion high fidelity polymerase)		
Final elongation	10 min	72 °C	1x

PCR products were analyzed by agarose gel electrophoresis using a 1.5% (w/v) agarose gel in TAE buffer. DNA amplicates were separated at 110 V and visualized by incubation with ethidium bromide for 30 min. Desired DNA products were cut out of the agarose gel and purified using the QIAquick Gel extraction kit (Qiagen). After purification, the isolated DNA products and corresponding target plasmids were either digested using the endonucleases summarized in Table 7 following the manufacturer's instructions or used directly for transformation. After further purification using the QIAquick Gel extraction kit, restricted DNA products and plasmids were ligated utilizing T4 ligase (Table 7) according to the manufacturer's protocol. For DNA amplification, 5 µl of the ligation approach were incubated with competent *E. coli* cells according to 7.1.3.2.

For cloning of TmrAB alanine mutants, the PCR-amplified DNA (30 µl) was incubated for 10 min at 37 °C with 1 µl *DpnI* (fast digest) and 3 µl 10x HF buffer.

7.1.3.2 Amplification and isolation of plasmid DNA

For DNA amplification or protein production, 100 µl of competent *E. coli* cells were incubated with 1 µl of plasmid DNA (100 ng/µl) for at least 10 min on ice. For DNA uptake, a heat shock was performed for 45 s at 42 °C, followed by a 2 min incubation on ice. Subsequently, 200-500 µl of LB low salt medium were added and cells were incubated at 37 °C and gentle shaking. After 1 h, cells were spread out onto LB low salt agar plates supplemented with the desired antibiotic as selection marker and grown overnight at 37 °C.

For plasmid isolation, 5 ml of LB low salt medium supplemented with the desired antibiotic were inoculated with a single *E. coli* colony and incubated overnight at 37 °C and 180 rpm. Plasmid DNA was isolated using the NucleoSpin® Plasmid EasyPure kit (MACHEREY-NAGEL) according to the manufacturer's instructions.

7.1.3.3 DNA sequencing

Every nucleotide replacement (e.g. for cloning of TmrAB alanine mutants) or the insertion of an open reading frame into an expression plasmid for protein production (e.g. cloning of sAB-encoding sequences into the pIPTG expression plasmid for sAB production) was confirmed by sequencing (sequencing was done by Eurofins Genomics).

7.2 Biochemistry

7.2.1 Protein production and purification

7.2.1.1 Production and purification of TAP

For the heterologous production of human TAP, the methylotrophic yeast *Pichia pastoris* was grown according to Schözl *et al.* (94).

For small-scale production, 20 ml MGY medium were inoculated with 100 µl of a *P. pastoris* glycerol stock harboring the respective TAP-encoding plasmid, kindly provided by David Parcej, and grown at 28 °C for 16-18 h. The starter culture was transferred into 400 ml MGY medium and grown at 30 °C for further 16-18 h. At an OD₆₀₀ of 2-6, cells were transferred into MMY medium. Protein production was allowed at 30 °C for 24 h.

For large-scale production, 10 ml MGY medium supplemented with 10 µl Zeocin (100 mg/ml) were inoculated with 100 µl of the *P. pastoris* glycerol stock, kindly provided by David Parcej, and grown at 30 °C overnight. This starter culture was transferred into 100 ml MGY medium and grown overnight at 30 °C until an OD₆₀₀ of 10 was reached. The cells were transferred into a 7.5-liter Labfors4 reactor (Infors-HT) filled with 1.6 l basal salts (142) supplemented with 9 ml PTM trace salts and 200 ml of 1.6 M sodium hexametaphosphate. Cells were grown at 30 °C and 1,000 rpm agitation. During a high-density growth period, induced by glycerol feeding, the pH

and pO₂ level were kept constant at 4.5 and 30%, respectively. TAP production was induced by methanol feeding. Over 24 h, the methanol concentration was kept constant at 1%. Cells were harvested at 4,500 x g and 4 °C for 20 min, snap frozen in liquid nitrogen, and stored at -80 °C.

For membrane preparation, TAP-containing *P. pastoris* cells were resuspended in TAP lysis buffer. Per 30 ml membranes, 15 ml of ice-cold glass beads pre-treated with 20% (v/v) hydrochloric acid were added. Cells were disrupted using a FastPrep[®] system (Millipore) for 45 s at 6 m/s for at least 3 cycles with 2 min breaks on ice between each cycle. Membranes were separated by two centrifugation steps: 1. 4,500 x g for 10 min at 4 °C, 2. 100,000 x g for 45 min at 4 °C. The pelleted membranes were resuspended in TAP storage buffer and homogenized. The total protein concentration of TAP-containing membranes was determined with a Bradford assay and adjusted to a total protein concentration of 20 mg/ml with TAP storage buffer.

TAP-containing membranes (20 mg/ml total protein) were solubilized for 1.5 h at 4 °C using 2% (w/v) glyco-diosgenin (GDN). After centrifugation at 100,000 x g for 45 min at 4 °C, the supernatant was loaded onto Ni Sepharose 6 Fast Flow medium (GE Healthcare) equilibrated with TAP lysis buffer. TAP was purified by an orthogonal purification strategy first utilizing the C-terminal His₁₀-tag of TAP1 and in a second purification step the C-terminal StrepII-tag of TAP2. After incubation for either 2 h at 4 °C or overnight, the beads were poured into a gravity flow column and washed with 30 ml of TAP IMAC wash buffer and eluted with 10 ml of TAP IMAC elution buffer. TAP-containing fractions were combined and loaded onto high-capacity Strep-Tactin[®] Sepharose (IBA). The C-terminally StrepII-tagged TAP2 was captured for 3 to 4 h at 4 °C. The beads were washed with 10 ml TAP strep wash buffer and eluted with 5 ml of TAP strep elution buffer containing D-desthiobiotin. If not used immediately for structural or functional studies, TAP was snap frozen in liquid nitrogen and stored at -80 °C. Due to its instability, repeated freeze and thawing of TAP-containing aliquots was avoided. For functional and structural studies, TAP was diluted in TAP storage buffer with 0.05% GDN.

7.2.1.2 Production and purification of TmrAB

Production and purification of TmrAB was performed according to Zutz *et al.* (83). In brief, 2 l LB high salt medium supplemented with ampicillin (100 µg/ml) were inoculated with 20 ml of an *E. coli* BL21 overnight culture and grown at 37 °C and 180 rpm. At an OD₆₀₀ of 0.6, protein production was induced with 0.5 mM IPTG. Harvested cells were resuspended in TmrAB lysis buffer and disrupted by sonication (output control 5, duty cycle 50). Membranes were pelleted

at 100,000 x g for 45 min at 4 °C. To extract TmrAB, crude membranes were solubilized with 1 % β -DDM in TmrAB purification buffer. The C-terminally His₁₀-tagged TmrAB was captured using Ni-NTA agarose (Qiagen) for 60 min at 4 °C, followed by a size exclusion chromatography step on either a Superdex™ 200 Increase 10/300 GL column (GE Healthcare) or a TSKgel® G3000SW_{XL} column (Tosoh Bioscience LLC) in TmrAB SEC buffer. Peak fractions were pooled for functional and structural studies. For cysteine cross-linking experiments with the double-cysteine mutant TmrA^{C416A, E523Q, S527C}/TmrB^{S503C}, 1 mM of β -mercaptoethanol was added to all buffers to prevent oxidation. Oxidative cysteine cross-linking was induced by buffer exchange to TmrAB SEC buffer.

7.2.1.3 Production and purification of synthetic antibodies

Synthetic antibodies (sABs) were produced and purified similar to Borowska *et al.* (118). sABs were produced in *E. coli* BL21 cells grown in 1 l 2xYT medium supplemented with 50 μ g/ml ampicillin. At an OD₆₀₀ of 0.8-1, protein production was induced by the addition of 1 mM IPTG. After 4 h at 37 °C and 220 rpm shaking, cells were harvested by centrifugation at 4,500 x g for 15 min at 4 °C. For purification, cells were resuspended in sABs lysis buffer and disrupted by sonication. To precipitate proteins that are less heat stable, the lysate was incubated for 30 min at 60 °C. After a further centrifugation step to clear the lysate, the sample was loaded onto a HiTrap MabSelect SuRe 5 ml column (GE Healthcare). The column was washed with 10 cv of sAB wash buffer. sABs were eluted with 0.1 M acetic acid. sABs-containing fractions were loaded onto an ion exchange Resource S 1 ml column (GE Healthcare). The column was washed with 50 mM sodium acetate (NaAc), pH 5.0, and sABs were eluted with a 50 mM NaAc pH 5.0/2 M NaCl gradient (0-100%). Immediately after elution, sAB-containing fractions were neutralized by the addition of 50 mM HEPES-NaOH, pH 7.5. The buffer was exchanged to sAB storage buffer and the sABs were snap frozen in liquid nitrogen and stored at -80 °C.

7.2.1.4 Production and purification of nanobodies

For nanobody production, *E. coli* BL21 cells harboring the pMESy4 plasmid (126) containing the nanobody-encoding sequence, were grown in 25 ml 2xYT medium supplemented with 100 μ g/ml ampicillin and 2% glucose overnight at 30 °C and 190 rpm. The starter culture was transferred into 1 l 2xYT medium supplemented with 100 μ g/ml ampicillin and 0.1% glucose. At an OD₆₀₀ of 0.8, protein production was induced with 1 mM IPTG. After 18 h at 30 °C and 190 rpm, cells were harvested by centrifugation at 6,000 x g and 4 °C for 15 min.

Subsequently, cells were resuspended in nanobody lysis buffer and disrupted by sonication (output control 7, duty cycle 70) for 2 min with 2 min breaks in between. After pelleting the cell debris at 100,000 x g and 4 °C for 45 min, the supernatant was incubated with Ni Sepharose 6 Fast Flow medium (GE Healthcare) utilizing the C-terminal His₆-tag for purification. After 2 h incubation at 4 °C, beads were poured into a gravity flow column and washed with 30 ml nanobody wash buffer. Nanobodies were eluted with 10 ml nanobody elution buffer. Nanobody-containing fractions were pooled, combined, and concentrated to a volume of 500 µl. Finally, nanobodies were purified *via* SEC using the Superdex™ 200 Increase 10/300 GL column (GE Healthcare) equilibrated with nanobody storage buffer.

7.2.1.5 Production and purification of saposin A

The saposin A-encoding plasmid was kindly provided by Jens Frauenfeld (Salipro AB, Stockholm, Sweden) within the context of a material transfer agreement.

Saposin A was expressed using *E. coli* Rosetta-gami™ 2(DE3) (Novagen) cells as described by Frauenfeld *et al.* (91). Cells were grown in TB medium supplemented with ampicillin (100 µg/ml) and kanamycin (30 µg/ml). Protein production was induced by the addition of 0.7 mM IPTG. Cells were resuspended in saposin lysis buffer, disrupted by sonication (output control 7, duty cycle 70), and the lysate centrifuged for 30 min at 26,000 x g. The supernatant was heated to 85 °C for 10 min and again centrifuged for 30 min at 26,000 x g. Saposin A was purified *via* its N-terminal His₆-tag by incubating the lysate with Ni Sepharose 6 Fast Flow medium (GE Healthcare). To remove imidazole, saposin A was dialyzed overnight against saposin SEC buffer. Finally, saposin A was purified *via* SEC (Superdex™ 200 Increase 10/300 GL column (GE Healthcare)). Peak fractions were concentrated to 5 mg/ml using Amicon® Ultra-15 ml centrifugal filters with a 3 kDa cut-off (Millipore), snap frozen in liquid nitrogen, and stored at -80 °C.

7.2.1.6 Production and purification of membrane scaffold proteins

pMSP1D1 and pMSP2N2 were a gift from Stephen Sligar (Addgene plasmids # 20061 and # 29520).

Membrane scaffold proteins (MSPs) MSP2N2 and MSP1D1 were expressed and purified as described by Roos *et al.* (143). Briefly, MSPs were expressed in *E. coli* BL21 cells grown in LB

medium supplemented with 0.5% glucose and 30 µg/ml kanamycin at 37 °C. At an OD₆₀₀ of 1, protein production was induced with 1 mM IPTG and cells were grown for 1 h at 37 °C. The temperature was subsequently lowered to 28 °C. Cells were harvested after additional 4 h and disrupted by sonication in MSP lysis buffer. The scaffold proteins were purified *via* their N-terminal His₇-tag. Stocks of purified MSP were snap frozen in liquid nitrogen and stored at -80 °C in MSP storage buffer.

7.2.2 Reconstitution

7.2.2.1 Functional reconstitution of TAP and TmrAB into LUVs

For preparation of large unilamellar liposomes (LUVs), *E. coli* polar lipid extract and DOPC (1,2-dioleoyl-*sn*-glycero-3-phosphocholine) dissolved in chloroform were mixed together in a 7:3 ratio (w/w) and dried by vacuum evaporation. The lipid film was rehydrated by the addition of reconstitution buffer (to a lipid concentration of 10 mg/ml) and sonication for 30 min at RT. For a homogenous preparation, 5 freeze and thaw cycles at -80 °C and RT respectively, were applied and the LUVs extruded 11 times through a 400 nm pore sized polycarbonate filter using a mini-extruder (Avestin). For reconstitution, LUVs (2.5 mg/ml) were destabilized with TX-100 for 30 min at 4 °C according to Geertsma *et al.* (144). Detergent-destabilized liposomes were mixed with either TAP or TmrAB in a 1:20 or 1:50 protein-to-lipid ratio (w/w) and incubated again for 30 min at 4 °C. For detergent removal, SM-2 Biobeads (Bio-Rad) were added in four consecutive steps (1 h, overnight, 2 h, 2 h) of 40 mg beads (wet weight). TAP- and TmrAB-containing proteoliposomes were harvested for 30 min at 270,000 x g at 4 °C. For functional assays, proteoliposomes were resuspended to a final lipid concentration of 5 mg/ml in reconstitution buffer and either stored at 4 °C or snap frozen in liquid nitrogen and stored at -80 °C.

For quality control of the LUV preparation, liposome size was monitored by nanoparticle tracking analysis using the NanoSight LM14 (NanoSight Ltd.).

7.2.2.1.1 Ficoll gradient fractionation

To enrich TAP-containing proteoliposomes, empty liposomes and protein aggregates were separated by centrifugation on a continuous Ficoll density gradient (0-10%) in reconstitution buffer. TAP-containing proteoliposomes were loaded onto the top of the gradient and centrifuged for 18 h at 200,000 x g and 4 °C using a SW41 Ti swing out rotor (Beckman Coulter).

Gradients were fractionated from the bottom and fractions were analyzed by immunoblotting. TAP proteoliposomes-containing fractions were isolated and washed twice with reconstitution buffer to remove residual Ficoll (270,000 x g, 20 min, 4 °C).

7.2.2.1.2 Re-solubilization

To determine the reconstitution efficiency, TAP- and TmrAB-containing proteoliposomes were solubilized with 1% β -DDM at 4 °C. After 1 h, the solubilizate was centrifuged for 30 min at 270,000 x g and 4 °C. Input taken prior to centrifugation and supernatant were compared by immunoblotting.

7.2.2.1.3 TEV protease cleavage

By Tobacco Etch Virus (TEV) protease cleavage of the His-tag, the orientation of TmrAB in proteoliposomes was determined. Proteoliposomes were incubated with TEV protease (TurboTEV (MoBiTec)) in a 10:1 ratio (transporter:TEV protease, w/w) and 1 mM DTT overnight at 4 °C. As control, a sample with 1% TX-100 was included. The protease cleavage pattern was analyzed by immunoblotting.

Furthermore, TEV protease cleavage was used to get rid of the His₁₀-tag of TmrAB and to remove the mVenus and mCerulean fusion proteins (and tags) from ^{ICP47}cTAP1^{mVenus-His10}/cTAP2^{mCerulean-StrepII}. TAP/TmrAB and TEV were added in a 10:1 ration and incubated with 1 mM DTT at 4 °C overnight.

7.2.2.2 Reconstitution of TAP and TmrAB in nanodiscs

Purified TmrAB and MSP were mixed with bovine brain lipid extract (Sigma-Aldrich) solubilized in 1% β -DDM at a TmrAB:MSP:lipid molar ratio of 1:8:200 for MSP2N2 and 1:7.5:100 for MSP1D1 in TmrAB SEC buffer without detergent. After incubation at 4 °C for 30 min, SM-2 Biobeads (Bio-Rad) were added in two consecutive incubation steps to remove the detergent (1 h, overnight). TmrAB-containing nanodiscs were separated from empty discs by SEC (column: KW404-4F (Shodex) or Superdex™ 200 Increase 3.2/300 (GE Healthcare)) in TmrAB SEC buffer without detergent and concentrated to 3-5 mg/ml at 1,500 x g using Amicon® Ultra-0.5 ml centrifugal filters with a 50 kDa cut-off (Millipore).

Reconstitution of TAP in nanodiscs was performed as previously published by Eggensperger *et al.* (145).

7.2.2.3 Reconstitution of TmrAB using saposin A

5 μ l of a brain lipid solution (5 mg/ml bovine brain lipid extract (Sigma-Aldrich) solubilized in 0.28% β -DDM) were incubated for 5 min at 37 °C according to Frauenfeld *et al.* (91). 6 μ l of purified TmrAB in 0.05% β -DDM (8.75 mg/ml) were added and incubated for 5 min at 37 °C. Subsequently, 20 μ l of purified saposin A (5 mg/ml) were added and incubated for 5 min at 37 °C. For detergent dilution, PBS (pH 7.5) was added in two consecutive steps (1. 35 μ l, 2. 40 μ l) followed by an incubation for 5 min at RT. TmrAB/saposin A complexes were isolated by SEC (KW404-4F column (Shodex)) in saposin SEC buffer. Fractions containing TmrAB/saposin A complexes were isolated and concentrated at 1,500 x g using Amicon[®] Ultra-0.5 ml centrifugal filters with a 50 kDa cut-off (Millipore) for immediate grid preparation or functional studies.

7.2.3 Protein labeling

7.2.3.1 Biotinylation

To immobilize proteins on a solid surface or on beads for antibody/peptide selection using display techniques, target proteins (MSP, TAP, TmrAB) were biotinylated using EZ-Link NHS-PEG₄-Biotin (Thermo Scientific). A 5-fold molar excess of the biotinylation reagent was added and incubated for 2 h on ice. The reaction was stopped by the addition of 10 mM Tris-HCl, pH 8.0. Unbound reagent was removed using Zeba[™] Spin Desalting columns (7 kDa cut-off, Thermo Scientific).

The biotinylation efficiency was determined by a pull-down assay using streptavidin-coated Dynabeads[®] M-280. 100 μ l beads per reaction were washed three times with 100 μ l of the respective protein purification buffer to equilibrate the system. 50 μ l of sample (700 nM concentration) were applied and incubated for 1 h at 4 °C. The supernatant was removed and collected. After three washing steps with 50 μ l of the respective protein purification buffer, the third wash was collected, and the beads were resuspended in 1x SDS sample buffer and incubated for 10 min at 65 °C (TAP, TmrAB) or 95 °C (MSP). The biotinylation efficiency was determined by comparison of the band intensities of input (I), flow-through (FT), wash (W), and beads (B) upon immunoblotting.

7.2.4 Selection of synthetic antibodies

7.2.4.1 Library sorting by phage display

The selection of sABs was performed within the context of a research visit at the Kossiakoff laboratory at the Department of Biochemistry and Molecular Biology, The University of Chicago, Chicago, IL, USA. The phage-displayed library was kindly prepared by Pawel Dominik (Kossiakoff laboratory, Department of Biochemistry and Molecular Biology, The University of Chicago, Chicago, IL, USA).

The sAB selection was performed similar to Dominik *et al.* (113). In short, the sAB selection *via* phage display was performed semi-automated magnetic bead-based utilizing a KingFisher[®] instrument (Thermo Scientific). First, streptavidin-coated magnetic beads were equilibrated in target storage buffer and the biotinylated target added in nanomolar concentrations and incubated for 30 min at 4 °C under constant shaking. The supernatant was removed, and beads were washed three times with the respective target storage buffer. Free binding sites were blocked by incubation with blocking buffer for 10 min at 4 °C. Subsequently, the phage-displayed library was added and incubated for up to 1 h at 4 °C under gentle shaking. For removal of unbound phages, beads were washed again. Specifically bound phages were either eluted by incubation with target protein storage buffer containing 1% FC-12 (for biotinylated nanodiscs) or by a pH shock (for chemically biotinylated targets). For phage amplification, *E. coli* XL1-blue cells grown to mid-log phase were infected with the eluted phages. In total, 5 rounds of library sorting were performed. Within the context of a material transfer agreement, sABs-encoding plasmids were transferred to Frankfurt for further analyses.

The following constructs were used for sABs selection:

cTAP1/cTAP2 nanodiscs

^{ICP47}cTAP1/cTAP2 nanodiscs

TmrA^{C416A, E523Q, S527C}B^{S503C} in 0.05% β-DDM

Additives, such as MgAMP-PNP, were added into all buffers and solutions during all incubation steps within the selection procedure.

7.2.4.2 Enzyme-linked immunosorbent assay (ELISA)

For immobilization of biotinylated targets, 100 μ l of a 2 μ g/ml neutravidin (NAV) solution in NAV binding buffer were added into the wells of a 96-well MaxiSorp™ plate (NUNC) and incubated overnight at 4 °C. Prior to the addition of blocking buffer to diminish unspecific binding (200 μ l, 2 h at 4 °C, gentle shaking), wells were washed three times with 200 μ l of 1x PBS to remove unbound NAV. After blocking, a further washing step was performed (three times, 200 μ l 1x PBS). Subsequently, 100 μ l of biotinylated target protein diluted in the appropriate protein standard buffer were added and incubated for 1 h at 4 °C under gentle shaking. Usually, nanomolar concentrations of biotinylated target protein were immobilized to screen for high affinity binders.

Various combinations of detection reagents were applied:

For single clone screening using phages, 50 μ l of a 10-fold dilution of precipitated phages were added and incubated for 30 min at 4 °C under gentle shaking. After three times washing with 200 μ l of the standard buffer of the respective target protein, an anti-M13 HRP-conjugated antibody was added in a 1:5,000 dilution and incubated for 30 min at 4 °C. The ELISA was developed by the addition of 50 μ l TMB Signal+ solution (3,3',5,5'-tetramethylbinzidine; Bio-Rad, former AbD Serotec). To stop the colorimetric reaction, 50 μ l of 0.2 M sulphuric acid were added. For quantification, the absorbance at 450 nm was measured using a microplate reader (CLARIOstar®, BMG LABTECH).

For single clone analysis, selected nanobodies were produced in small-scale and 100 μ l of a 5-fold dilution of the periplasmic extract were incubated with the captured target protein for 1 h at 4 °C. For detection of bound nanobody, an anti-His antibody (1:3,000) was added followed by an anti-mouse antibody with an alkaline phosphatase conjugated (1:10,000) and incubated for 1 h at 4 °C (each). For development, TMB Signal+ solution was used.

7.2.4.3 Complex formation and isolation

Transporter/antibody complexes were isolated by SEC utilizing either a TSKgel® G3000SW_{XL} column (Tosoh Bioscience LLC), a Superdex™ 200 Increase 3.2/300 column (GE Healthcare), or a KW404-4F column (Shodex) equilibrated in the respective protein storage buffer. sABs or nanobodies were added in a 1.25-fold molar excess and incubated for 15 min on ice prior to injection.

7.2.5 Selection of nanobodies

7.2.5.1 Immunization

The nanobody selection was performed within the context of a research visit at the Steyaert laboratory at the VIB-VUB Center for Structural Biology, Vrije Universiteit Brussel, Brussels, Belgium. Llama Immunization and nanobody library generation were performed and the library kindly provided by the group of Jan Steyaert (VIB-VUB Center for Structural Biology, Vrije Universiteit Brussel, Brussels, Belgium).

Nanobodies were generated as described previously by Pardon *et al.* (126). In brief, nanobody clones were obtained from two llamas (*Lama glama*) immunized over a time span of 6 weeks with TAP/TmrAB proteoliposomes (first injection: 200 µg protein, following injections: 100 µg protein).

The following constructs were used for immunization:

cTAP1/cTAP2 proteoliposomes

^{ICP47}cTAP1/cTAP2 proteoliposomes

TmrA^{C416A, E523Q, S527C}B^{S503C} proteoliposomes

7.2.5.2 Library sorting by phage display

TAP/TmrAB-binding nanobodies were isolated *via* phage-displayed library sorting. Before each round of library sorting, nanobody-displaying phages were rescued and amplified according to Pardon *et al.* (126). 60 ml of 2xYT medium supplemented with 100 µg/ml ampicillin and 2% glucose (w/v) were inoculated and grown at 37 °C, 200 rpm until an OD₆₀₀ of 0.5 was reached. Subsequently, 10 ml of the TG1 cells were infected with 4x10¹⁰ plaque-forming units (pfu) of VCSM13 helper phage and incubated for 30 min at 37 °C. The infected cells were centrifuged for 10 min at 2,800 x g, RT, the supernatant was discarded, and the pellet was resuspended in 50 ml of 2xYT medium supplemented with 100 µg/ml ampicillin and 25 µg/ml kanamycin. Cells were grown overnight at 37 °C, 200 rpm. For phage rescue, cells were centrifuged at 3,200 x g for 15 min and the supernatant was mixed with 10 ml of 20% (w/v) PEG6000/2.5 M NaCl. Phages were precipitated for 30 min on ice and, subsequently, pelleted for 10 min at 3,200 x g at 4 °C. To remove residual bacteria, phages were resuspended in 1 ml 1x PBS and centrifuged again for

1 min at 20,000 x g at 4 °C. Phages were re-precipitated from the supernatant by the addition of 250 µl ice-cold 20% (w/v) PEG6000/2.5 M NaCl. Removal of bacterial contaminants was repeated, and the phages were resuspended in 1x PBS and used for panning.

For phage selection, corresponding wells of a MaxiSorp™ 96-well plate (NUNC) were incubated overnight with 100 µl of 2 µg/ml NAV in NAV binding buffer for biotinylated target proteins. NAV-coated wells were washed three times with 250 µl of 1x PBS. Upon removal of unbound NAV, wells were incubated at 4 °C for 2 h and 700 rpm with blocking buffer to avoid unspecific binding. After blocking, wells were washed 5 times with 1x PBS. Subsequently, 100 µl of biotinylated TAP/TmrAB were added and incubated for 1 h at 4 °C and 700 rpm. After a further washing step (5 times with 250 µl of standard buffer of the particular target protein), 100 µl of the rescued phage library were added to the captured target and incubated for 2 h at 4 °C and 700 rpm. Unbound phages were removed by washing with 250 µl of the target standard buffer (15x). For phage elution, wells were incubated for 30 min at 4 °C and 700 rpm with 100 µl of a 0.25 mg/ml trypsin solution. To inhibit further protease activity, eluted phages were transferred into tubes filled with 5 µl of a 4 mg/ml AEBSF solution. For recovery and amplification of phages, 3 ml of TG1 cells grown to mid-log phase were infected with 50 µl of the eluted phages. After 30 min at 37 °C without shaking, LB medium supplemented with ampicillin (100 µg/ml) and glucose (2% w/v) was added and cells were grown overnight at 37 °C and 170 rpm. A serial dilution of infected TG1 cells was performed to follow enrichment of target-specific binding phages. In case of insufficient enrichment, a further round of panning was performed.

Additives, such as the high-affinity peptide R9LQK or ATP-Mg²⁺, were added to all buffers and solutions during all incubation steps within the selection procedure.

The following constructs were used during phage display to generate conformation-specific nanobodies:

Reconstituted into biotinylated nanodiscs:

cTAP1/cTAP2

^{ICP47}cTAP1/cTAP2

Biotinylated protein in detergent (0.05% GDN/β-DDM):

cTAP1/cTAP2

^{ICP47}cTAP1/cTAP2

TmrA^{C416A, E523Q, S527C}B^{S503C}

Reconstituted protein in proteoliposomes:

cTAP1/cTAP2

^{ICP47}cTAP1/cTAP2

TmrA^{C416A, E523Q, S527C}B^{S503C}

7.2.5.3 Single clone screening

For single clone screening, serial dilutions of infected TG1 cells were spread out on LB agar supplemented with 100 µg/ml ampicillin and 2% (w/v) glucose and grown overnight at 37 °C. To produce nanobodies in small-scale, wells of a 96-well culture plate were inoculated with one single colony per well and grown overnight at 37 °C. 1 ml of 2xYT medium supplemented with 100 µg/ml ampicillin and 0.1% glucose were inoculated with 10 µl of the overnight culture and grown at 37 °C, 200 rpm. At an OD₆₀₀ of 0.6, nanobody production was induced by the addition of 1 mM IPTG. After 4 h at 37 °C and 200 rpm, cells were pelleted at 3,200 x g for 10 min. Cells were disrupted by freeze and thawing, resuspended in 1x PBS and the cell debris was pelleted again. The supernatant contained the nanobodies extracted from the periplasm and was used for single clone screening *via* an ELISA.

Positive clones were sequenced, the DNA was isolated, and *E. coli* BL21 cells were transformed for large-scale nanobody production. Within the context of a material transfer agreement, nanobody-encoding plasmids were transferred to Frankfurt for further analyses.

7.2.5.4 Determination of binding constants by switchSENSE

The basic principle of the *switchSENSE* technology are immobilized DNA nanolevers, which are electrically actuated at high-frequency on microelectrodes, while the orientation is monitored by time-resolved single photon counting (146, 147). Upon binding of proteins, the switching dynamics are altered. When the DNA levers tilt towards the gold surface of the chip, the fluorescence from attached Cy3 dyes is gradually quenched what allows for gauging the distance of the DNA to the surface and, thus, monitoring changes in DNA orientation in real time (147).

This system was utilized to study TmrAB-nanobody interactions. Nanobodies 268, 296, and 300 were covalently conjugated to the DNAs top ends *via* lysines according to Langer *et al.* (147). Within the first step, nanobody-conjugated single-stranded DNA was hybridized with single-stranded nanolevers immobilized on the chip surface. Upon removal of unbound DNA, TmrAB

was added in increasing concentrations (1.2, 3.7, 11.1, 33.3, and 100 nM). As a consequence of TmrAB binding to immobilized nanobodies, the DNA lever motions slowed down. This change in motion was used to follow binding kinetics in real time and to calculate k_{on} and k_{off} values to determine the dissociation constant K_D .

7.2.6 Binding Assays

7.2.6.1 Filter binding

Substrate binding of purified TAP was explored by a filter-based binding assay using the fluorescently-labeled high-affinity peptide C4 (referred to as C4F, Table 10). 4 μ g of purified TAP in 0.05% GDN were incubated for 15 min at 4 °C with 1 μ M C4F peptide in peptide binding buffer in a total volume of 50 μ l. To proof specificity of peptide binding, a control sample with a 250-fold molar excess (250 μ M) of the unlabeled competitor peptide R9LQK (Table 10) was included. The samples were transferred onto 96-well MultiScreen[®] microfilter plates (0.65 μ m diameter, Millipore) pre-treated with 0.3% (w/v) polyethyleneimine and washed twice with 250 μ l of ice-cold peptide binding buffer. Next, 250 μ l of peptide elution buffer were added and incubated for 10 min at RT. 200 μ l of the sample were incubated for 10 min at 95 °C prior to fluorescence measurement to exclude interference of the mVenus fusion. Bound peptide was quantified using a microplate reader (CLARIOstar[®], BMG LABTECH) at $\lambda_{ex/em}=485/520$ nm.

7.2.6.2 Fluorescence anisotropy

Binding of fluorescently-labeled peptides to TmrAB was analyzed by fluorescence anisotropy measurements. Increasing amounts of TmrAB were incubated with 50 nM cyclic peptide VD3 or C4F (Table 10) in a total volume of 20 μ l for 10 min on ice. Subsequently, fluorescence anisotropy was measured using a microplate reader (CLARIOstar[®], BMG LABTECH) at $\lambda_{ex/em}=485/520$ nm.

7.2.7 Peptide transport

To analyze ATP-dependent substrate translocation, TAP proteoliposomes (50 μ g) were incubated with 1 μ M of the fluorescently-labeled high-affinity peptide C4 (Table 10) in reconstitution buffer. Upon addition of 5 mM MgCl₂ and 3 mM ATP in a total volume of 50 μ l, peptide transport was measured for 15 min at 37 °C and stopped by the addition of 200 μ l ice-

cold stop buffer. To remove excess of C4F, proteoliposomes were transferred onto 96-well MultiScreen[®] microfilter plates (0.65 μm diameter, Millipore) pre-treated with 0.3% (w/v) polyethyleneimine and washed twice with 250 μl of ice-cold stop buffer. 250 μl of liposome lysis buffer were added and incubated for 10 min to disrupt the liposomes. cTAP1^{mVenus-His10}/cTAP2^{mCerulean-StrepII} proteoliposomes were incubated for 10 min at 95 °C prior to fluorescence measurement to exclude interference of the mVenus fusion. The ATP-dependent peptide translocation was quantified using a microplate reader (CLARIOstar[®], BMG LABTECH) at $\lambda_{\text{ex/em}}=485/520$ nm. As control, either 3 mM ADP or reconstitution buffer were added instead of ATP.

Substrate translocation by TmrAB was determined according to the previously described protocol either for 5 min at 68 °C or 10 min at 45 °C.

7.2.8 ATPase assays

7.2.8.1 Malachite-Green based assay

To proof functionality of TmrAB upon purification and reconstitution, ATPase activity was determined by following the release of inorganic phosphate (P_i) (83, 148). 200 nM TmrAB in 0.05% β -DDM or reconstituted were incubated with 3 mM MgCl_2 and 1 mM ATP in TmrAB SEC buffer in a total volume of 25 μl . Release of inorganic phosphate was monitored for 5 min at 68 °C and stopped by the addition of 175 μl 20 mM H_2SO_4 . ATP hydrolysis was visualized by a colorimetric reaction based on the complex formation of Malachite Green, ammonium molybdate, and P_i . Therefore, 50 μl of Malachite Green solution were added. After 5-10 min incubation at RT, the absorbance at 620 nm was measured using a microplate reader (CLARIOstar[®], BMG LABTECH). For quantification, KH_2PO_4 samples ranging from 0.4 nmol to 4.8 nmol diluted in 20 mM H_2SO_4 were measured.

A similar protocol was applied to determine the peptide-stimulated ATPase activity of purified or reconstituted TAP. 500 nM TAP were incubated with 1 μM of the high affinity peptide R9LQK (Table 10), 3 mM MgCl_2 , and 1 mM ATP in TAP storage buffer supplemented with 1 mM ouabain, 50 μM EGTA, and 5 mM NaN_3 in a total volume of 25 μl . The ATPase activity was measured at 37 °C for 30 min. The reaction was stopped by the addition of 175 μl 20 mM H_2SO_4 . Detection and quantification were performed as described above.

7.2.8.2 Radioactive assay

200 nM TmrAB in 0.05% β -DDM or reconstituted into either saposin A complexes or nanodiscs were incubated with 3 mM MgCl₂ and 1 mM ATP (supplemented with tracer amounts of [γ -³²P]ATP) in TmrAB SEC buffer with and without detergent, respectively. Release of inorganic phosphate was monitored at specific time points or over a time course of 20 min at 68 °C. Reaction mixtures were analyzed by thin layer chromatography on polyethyleneimine cellulose. Background corrected data were fitted according to the Michaelis-Menten equation (Equation 1) to determine v_{max} and K_M values. The concentration of ATP is represented by [S] and the velocity of the hydrolysis reaction is represented by v .

$$v = \frac{v_{max} * [S]}{K_M + [S]} \quad \text{equation 1}$$

7.2.9 Nucleotide occlusion

Occluded nucleotides were identified by trapping experiments according to Zutz *et al.* (83). In brief, TmrAB (5 μ M) was incubated with 3 mM MgCl₂, 1 mM ATP (supplemented with tracer amounts of [α -³²P]ATP), and 5 mM orthovanadate for 3.5 min at 68 °C. Subsequently, to proof occlusion of nucleotides, 2 mM ATP were added and incubated for 2 min at RT. Unbound nucleotides were removed by buffer exchange by a Micro Bio-Spin[®] 30 gel filtration column by centrifugation for 2 min at 1,000 x g and 4 °C (Bio-Rad). The identity of bound nucleotides was analyzed by thin layer chromatography on polyethyleneimine cellulose.

7.2.10 SDS-PAGE

As quality control of protein purification, reconstitution efficiency, co-migration, and complex formation, proteins were separated regarding their molecular mass by sodium dodecyl sulfate polyacrylamide gel electrophoresis (SDS-PAGE). Samples were incubated with 1x SDS sample buffer for 10 min at 95 °C (for antibodies) and 65 °C (for membrane proteins). For all gels shown in this thesis, a PageRuler™ Prestained Protein Ladder (Thermo Scientific) was used. Gel electrophoresis was performed at 135 volt (V) for 1.5-2 h. Straight after performing the SDS-PAGE, proteins were visualized either by a Coomassie-blue/silver staining or by an immunoblot.

Table 13: Composition of SDS-stacking and -separating gel. Volumes are calculated for 6 gels using the Bio-Rad system.

Compound	Separating gel (11%)	Stacking gel (3%)
Rotiphorese [®] Gel 40 (19:1)	7 ml	1.9 ml
gel buffer (3x)	8.5 ml	6.4 ml
glycerol	2.5 g	-
H ₂ O	7.9 ml	11 ml
APS (10%, w/v)	192 μ l	96 μ l
TEMED	38 μ l	19 μ l

7.2.11 Coomassie staining

To visualize separated proteins by a Coomassie-blue staining, the polyacrylamide gels were incubated with Coomassie staining solution for at least 30 min at RT. Excessive dye was removed by a gentle de-staining procedure using ddH₂O and heating the gel until only protein bands were visible. Alternatively, InstantBlue[™] Protein stain was used instead of Coomassie-blue. The polyacrylamide gels were incubated with InstantBlue[™] staining solution for 15-30 min at RT according to the manufacturer's instructions.

7.2.12 Silver staining

For fixation, polyacrylamide gels were incubated for 5 min at RT in 60 ml fixation solution. After 3x 5 s rinsing the gel in ddH₂O, a wash step of 5 min at RT with ddH₂O was applied. Followed by another rinsing step and pre-treatment with 60 ml acetone (50% v/v) for 5 min at RT. Acetone was removed, and 60 ml of pre-treatment solution were added and incubated for 1 min at RT. After a third rinsing in ddH₂O, the gel was incubated with impregnation solution for 8 min at RT. The impregnation solution was removed, the gel rinsed for a fourth time and protein bands detected by the addition of developing solution for 10-20 s. Depending on the intensity of the silver stained protein bands, the developing solution was removed and 1% glacial acetic acid (v/v) added to stop the reaction.

7.2.13 Immunoblotting

To detect low protein amounts (nM concentrations) and specific proteins (e.g. using cell lysate or membranes), proteins were transferred onto polyvinylidene difluoride (PVDF) membranes

(Thermo Scientific) for immunostaining with protein-specific primary and species-specific secondary antibodies conjugated with the horseradish peroxidase (HRP). For semi-dry blotting, PVDF membranes were first activated in methanol. Subsequently, the polyacrylamide gel, PVDF membrane, and two Whatman papers were equilibrated with transfer buffer for 1-2 min and arranged in the following order (from anode to cathode) using the semi-dry setup from Bio-Rad: Whatman paper, PVDF membrane, polyacrylamide gel, Whatman paper. Blotting was performed for 30 min at 25 V. To avoid unspecific binding of the antibodies, the PVDF membrane was incubated with blocking buffer for 30 min at RT. After three washing steps of 5 min each with PBS-T, the primary antibody was added and either incubated for 1 h at RT or overnight at 4 °C. Antibodies used within this study are summarized in Table 1. Before adding the secondary antibody, PVDF membranes were washed three times with PBS-T for 5 min each. Mostly, as secondary antibody, the anti-mouse IgG peroxidase-conjugate (Sigma-Aldrich) was used and incubated for 1 h at RT. After a third washing procedure, protein bands were detected by the addition of ECL solution 1 and 2 mixed in a 1:1 ratio using a Lumi Imager F1™ system (Roche).

For nanobody detection, the PVDF membranes were incubated with the CaptureSelect™ Biotin anti-C-tag conjugate (Life technologies) and a Streptavidin-HRP conjugate (Thermo Scientific) mixed in a 1:1 ratio (1:4,000 dilution) and incubated for 1 h at RT. The CaptureSelect™ Biotin anti-C-tag conjugate binds to the C terminal EPEA-tag of the nanobodies.

7.2.14 Bradford assay

As an alternative to determining the protein concentration by measuring the absorption at 280 nm using a Nanodrop spectrophotometer ND-1000 (PeqLab), a Bradford assay was performed. 10 µl of protein sample were mixed with 290 µl of the Coomassie Plus™ Protein Assay reagent (Thermo Scientific). As protein standard for quantification, BSA dilutions from 0.125 to 1 mg/ml were prepared. After 5-10 min incubation at RT, the absorbance at 600 nm was measured by a microplate reader (CLARIOstar®, BMG LABTECH).

7.2.15 Size exclusion chromatography

For detergent and buffer exchange, purification, and to analyze homogeneity of purified protein samples, a size exclusion chromatography was performed. Table 14 summarizes all fast protein liquid chromatography (FPLC) and high-performance liquid chromatography (HPLC) columns used in this study.

Table 14: FPLC and HPLC columns.

Column	Supplier	Flow rate	System
KW404-4F	Shodex	0.3 mg/ml	Shimadzu
TSKgel [®] G3000SW _{XL}	Tosoh Bioscience LLC	0.5 mg/ml	Shimadzu ÄKTApurifier
Superdex [™] 200 Increase 10/300 GL	GE Healthcare	0.5 mg/ml	ÄKTApurifier
Superdex [™] 200 Increase 3.2/300	GE Healthcare	0.08 mg/ml	Ettan LC

7.2.16 Detergent exchange to amphipols

For structural studies of TAP by single-particle electron microscopy, GDN was replaced by an amphiphilic polymer, amphipol A8-35. TAP and A8-35 were mixed in a protein-to-amphipol ratio of 1:5 (w/w) and incubated for 30 min at 4 °C. For detergent removal, SM-2 Biobeads (Bio-Rad) were added and incubated for at least 3 h at 4 °C. For complete detergent removal, a dilution (at least 5-fold) and concentration step using Amicon[®] Ultra-0.5 ml centrifugal filters with a 100 kDa cut-off (Millipore) was applied. To remove unbound polymers, the sample was applied onto a TSKgel[®] G3000SW_{XL} column (Tosoh Bioscience LLC) equilibrated with TAP storage buffer without detergent. The TAP-containing peak fraction was used for immediate grid preparation.

7.2.17 GraFix

Gradient Fixation (GraFix), developed by Kastner *et al.* (149), is a method for a mild and slow fixation of protein complexes by intramolecular cross-linking (150). 60 pmol ¹³C⁴⁷cTAP1/cTAP1 were applied onto a continuous glycerol gradient (10-30%) with increasing concentrations of glutaraldehyde (0.2% as highest concentration) and centrifuged for 18 h at 200,000 x g and 4 °C using an SW41 Ti swing out rotor (Beckman Coulter). The gradient was fractionated from the bottom and TAP-containing fractions were pooled. To decrease the glycerol content for single-particle electron microscopy, a buffer exchange to TAP storage buffer was performed using Zeba[™] Spin Desalting columns (7 kDa cut-off, Thermo Scientific).

7.3 Biophysics

7.3.1 Electron microscopy (EM)

All EM work presented in this thesis was performed in collaboration with the Kühlbrandt laboratory/Möller laboratory at the Department of Structural Biology, Max Planck Institute of Biophysics, Frankfurt.

7.3.1.1 Single-particle negative-stain EM

2 μ l of purified protein (3-10 μ g/ml) were applied to a glow-discharged carbon-coated copper grid (400 mesh) and stained with 2% uranyl formate. Data were collected on a Tecnai-Spirit transmission electron microscope (Thermo Fisher, former FEI), operated at 120 kV and equipped with a Gatan 4x4k CCD camera. Images were automatically collected on a CCD camera using the Legion software package (151) at a nominal magnification of x42,000, corresponding to a pixel size of 2.68 Å. For automated particle selection, the Appion software package was used (152). Stacks containing roughly 30,000-80,000 preselected particles were subjected to a reference-free 2D classification utilizing the Relion 1.3 software package (153). As an alternative, the cisTEM software package was applied for particle selection and reference-free 2D classification (154).

7.3.1.2 Cryo-EM sample preparation, data acquisition, and image processing

All cryo-EM work and analysis were done by Dovile Janulienė and Arne Möller (Möller laboratory, Department of Structural Biology, Max Planck Institute of Biophysics, Frankfurt).

For cryo-EM grid preparation, 3 μ l of 0.8-1.2 mg/ml TmrAB^{WT}-Nb or TmrA^{EQ}B-Nb complexes (with or without nucleotides and substrate) were applied onto freshly glow-discharged Quantifoil grids with gold support (R2/2 or R1.2/1.3) and plunge-frozen in liquid ethane using a Vitrobot Mark IV (Thermo Fisher) with the environmental chamber set to 100% humidity and 4 °C. For the turnover experiment, TmrAB^{WT}-Nb was incubated at 45°C with 6 mM MgCl₂, 5 mM ATP, and 50 μ M C4F for 1 min and immediately plunge-frozen. For the TmrA^{EQ}B_{ATP} experiment, 1 mM of ATP was used and activation at 45 °C was extended to 5 min. The same ATP concentration and incubation time was used in the TmrAB_{ATP-Vi} experiment with addition of

orthovanadate (1 mM). TmrA^{EQ}_{B_{ATP-ADP}} experiment was carried out in an identical manner same with addition of 1 mM ATP and 1 mM ADP.

Micrographs were recorded automatically with EPU, using a Titan Krios microscope operated at 300 kV (Thermo Fisher), equipped with a BioQuantum energy filter and a K2 camera (Gatan) at a nominal magnification of x130,000, corresponding to a pixel size of 1.077 Å. Dose-fractionated movies were acquired at an electron flux of 9-9.5 e-/pixel/s over 8 s with 0.2 s exposures per frame (40 frames in total), corresponding to a total electron dose of ~62 e-/Å². Images were recorded in the defocus range from -0.8 to -2.8 μm. Data collection quality was monitored through Warp.

Frame-based motion correction was performed using Relion3 (155) implementation of MotionCor2 (156) with a dose filter of 1.5 or 1.6 e-/Å²/frame. The contrast transfer function (CTF) was estimated from non-dose weighted images, using Gctf (157) within Relion3. Initially, images were pre-processed either in *cis*TEM (154) or in Warp and the particles, obtained from one of these softwares, were subjected to likelihood based 2D classification in Relion3. The best 2D-classes were used to generate templates for automated particle selection in Relion3. Picked particles were extracted at a box size of 64 pixels with 4.308 Å/pixel and directly subjected to a single round of multi-model 3D classification to eliminate particles of poor quality. The cryo-EM map of TmrAB in IF conformation (EMDB 6085) was used as a starting reference. Selected maps at 8.6 Å resolution (Nyquist for the binned data) readily revealed multiple conformations. The selected particles from each conformation were re-centered and re-extracted at full pixel size. Each conformation was refined individually. Particles were polished and ctf refined as implemented in Relion3. To further sort out conformational variability, refined particles were subjected to the next round of 3D classification using local searches. Particles from the best classes were further refined and post-processed, resulting in final maps. In cases where high flexibility was observed, especially for IF conformation, none uniform-refinement in CryoSPARC (158) was used. No symmetry was applied at any step of processing.

7.3.2 Model building

Initial models were prepared and kindly provided by Ahmad Reza Mehdipour (Hummer laboratory, Department of Theoretical Biophysics, Max Planck Institute of Biophysics, Frankfurt). Final models were kindly provided by Christoph Thomas (Tampé laboratory, Institute of Biochemistry, Goethe-University, Frankfurt).

In order to build structural models of TmrAB, three initial models were used: 1) the equilibrated X-ray structure taken from previously published data (15), which was used for fitting of the inward-facing maps. 2) An OF-occluded model obtained from targeted MD based on the McjD structure (43). This model was used for the OF-occluded maps. 3) An OF-open model obtained from targeted MD based on the Sav1866 structure (33). This model was used for the OF-open maps.

In the initial fitting, cascade molecular dynamics flexible fitting (cMDFF) simulations was used (159). The MDFF plugin v0.4 in VMD1.9.2 was used to perform MD simulations guided by the cryo-EM density maps. The cMDFF simulations were performed in vacuum and with a gscale factor of 0.3, which describes the strength of the external potential derived from the EM density map. In cMDFF, the EM maps were smoothed by applying a series of Gaussian blurs with increasing half-widths to obtain a set of theoretical maps with gradually decreasing resolution; $\sigma = 0 \text{ \AA}$ corresponds to the actual map, and $\sigma > 0 \text{ \AA}$ corresponds to a smoothed one. Here, the following settings were used: $0.5 \geq \sigma \geq 5.0 \text{ \AA}$. Primarily, the models were docked rigidly into the EM maps with Situs 2.7.2. Afterwards, the initial docked model was fitted to the smoothest map (i.e. the one with the largest σ value). Then, the resulting fitted model was flexibly fitted to the next higher-resolution map in the series. These fitting and fitted model refreshment steps were repeated through the series of maps in order of decreasing σ , until the model was finally fitted to the actual EM map. At each step, 200 ps MDFF simulation was performed followed by 1000 steps of minimization. Secondary structure, chirality, and *cis*-peptide restraints were used during the MDFF simulation in order to enforce the original secondary structure, chirality, and isomerism.

The OF-occluded structure of McjD (PDB: 4PLO, (43)) was used to construct an OF-occluded model of TmrAB. A pairwise sequence alignment of TmrAB with McjD was generated using CLUSTALW (160). An OF-occluded model of TmrAB was constructed using the X-ray structure of McjD as template using MODELLER 9v14 (161), based on the sequence alignment. Among 100 models, the one with the highest MODELLER score and best PROCHECK profile was selected for further analysis. This model was used as the target structure in a targeted MD simulations using NAMD v2.9 (162). A bias potential acting on the $C\alpha$ RMSD pushed the initial structure, the POPE-membrane embedded IF structure of TmrAB, toward the target structure, the OF-occluded state. The targeted MD run was 10 ns. After the targeted MD run, 2 ATP molecules and 2 Mg^{2+} were placed in the nucleotide-binding site and the system was equilibrated in a 10 ns run with restraints on the $C\alpha$ positions to relax the lipids and water molecules around the protein.

Afterwards, a 50 ns unbiased production run was performed. The OF-open model of TmrAB was generated using the previously described protocol based on the OF-open structure of Sav1866 (PDB: 2ONJ, (33)).

All-atom explicit solvent MD simulation was performed for lipid-membrane embedded TmrAB. According to MCCE (163) electrostatics calculations for neutral pH, all Asp, Glu, Arg and Lys residues were charged. All His residues were neutral, protonated at either the N δ or N ϵ atoms according to the network of hydrogen bonds. Both TmrAB structures were embedded in a mixed bilayer of POPE and POPG lipids (164). The IF, OF-occluded and OF-open systems were containing 253PE/253PE, 298PE/298PE and 250PE/252PG, respectively. All systems were hydrated with 150 mM KCl electrolyte, resulting of $\sim 13 \times 13 \times 17$. The modified all-atom CHARMM36 force field (165) was used for protein, lipids, and ions, and TIP3P was used for water molecules. The MD trajectories were analyzed with Visual Molecular Dynamics (VMD) (166). All simulations were performed using GROMACS 5.0.6 (167). The starting systems were energy minimized for 5,000 steepest-descent steps and equilibrated initially for 500 ps of MD in an NVT ensemble and later for 8 ns in an NPT ensemble under periodic boundary conditions. During equilibration, the restraints on the positions of non-hydrogen protein atoms of initially 4000 kJ mol⁻¹ nm² were gradually released. Particle-mesh Ewald summation with cubic interpolation and a 0.12 nm grid spacing was used to treat long-range electrostatic interactions. The time step was initially 1 fs and then increased to 2 fs. The LINCS algorithm was used to fix all bond lengths. Constant temperature was set with a Berendsen thermostat with a coupling constant of 1.0 ps. A semi isotropic Berendsen barostat was used to maintain a pressure of 1 bar. During the production run, the Berendsen thermostat and barostat were replaced by a Nosé-Hoover thermostat and a Parrinello-Rahman barostat. Analysis was carried out on unconstrained simulations.

The models were refined using Coot (168) and phenix.real_space_refine (169). Models were validated with built-in functions of Coot, with MolProbity (170), and PROCHECK (171).

8. Results and Discussion

8.1 Structural analysis of human cTAP

8.1.1 Purified cTAP is functional in peptide binding and translocation

In order to determine the structure of unique conformations of TAP, human cTAP1^{mVenus-His10}/cTAP2^{mCerulean-StrepII} and the ICP47-TAP fusion construct ^{ICP47}cTAP1^{mVenus-His10}/cTAP2^{mCerulean-StrepII} were investigated regarding stability, homogeneity, and function. Both constructs carry two fluorescent fusion proteins (mVenus and mCerulean) followed by two purification tags (His₁₀-tag fused to cTAP1 and StrepII-tag fused to cTAP2) to allow for the stoichiometric purification of both half-transporters (145). cTAP and ^{ICP47}cTAP were produced using the methylotrophic yeast *Pichia pastoris*. After membrane preparation and solubilization in 1% GDN, both constructs were purified *via* an orthogonal affinity purification strategy by Ni²⁺-NTA and a StrepTactin matrix to guarantee the isolation of stoichiometrically well-defined, heterodimeric TAP complexes (Figure 8). Homogeneity and 1:1 stoichiometry of TAP1 and TAP2 were shown by multicolor fluorescence-detection size-exclusion chromatography (MC-FSEC) utilizing the two fluorescent fusion proteins (Figure 8a and c), and SDS-PAGE gel analysis (Figure 8b and d).

In 2011, Schölz *et al.* emphasized the importance of a native lipid environment for restoring TAP function (94). Thus, purified cTAP was reconstituted into LUVs composed of *E. coli* polar lipids and DOPC in a 7:3 ratio and peptide translocation was measured (Figure 9). Additionally, as an alternative approach to embed TAP into a native-like environment with defined lipid composition, TAP was reconstituted into nanodiscs utilizing the membrane scaffold protein MSP1D1. By MC-FSEC, TAP-containing nanodiscs were separated from lipid-only particles. Exemplarily, the reconstitution of ^{ICP47}cTAP into MSP1D1 nanodiscs is shown (Figure 8e). SDS-PAGE analysis of the peak fraction revealed a stoichiometric TAP/MSP1D1 complex (Figure 8f).

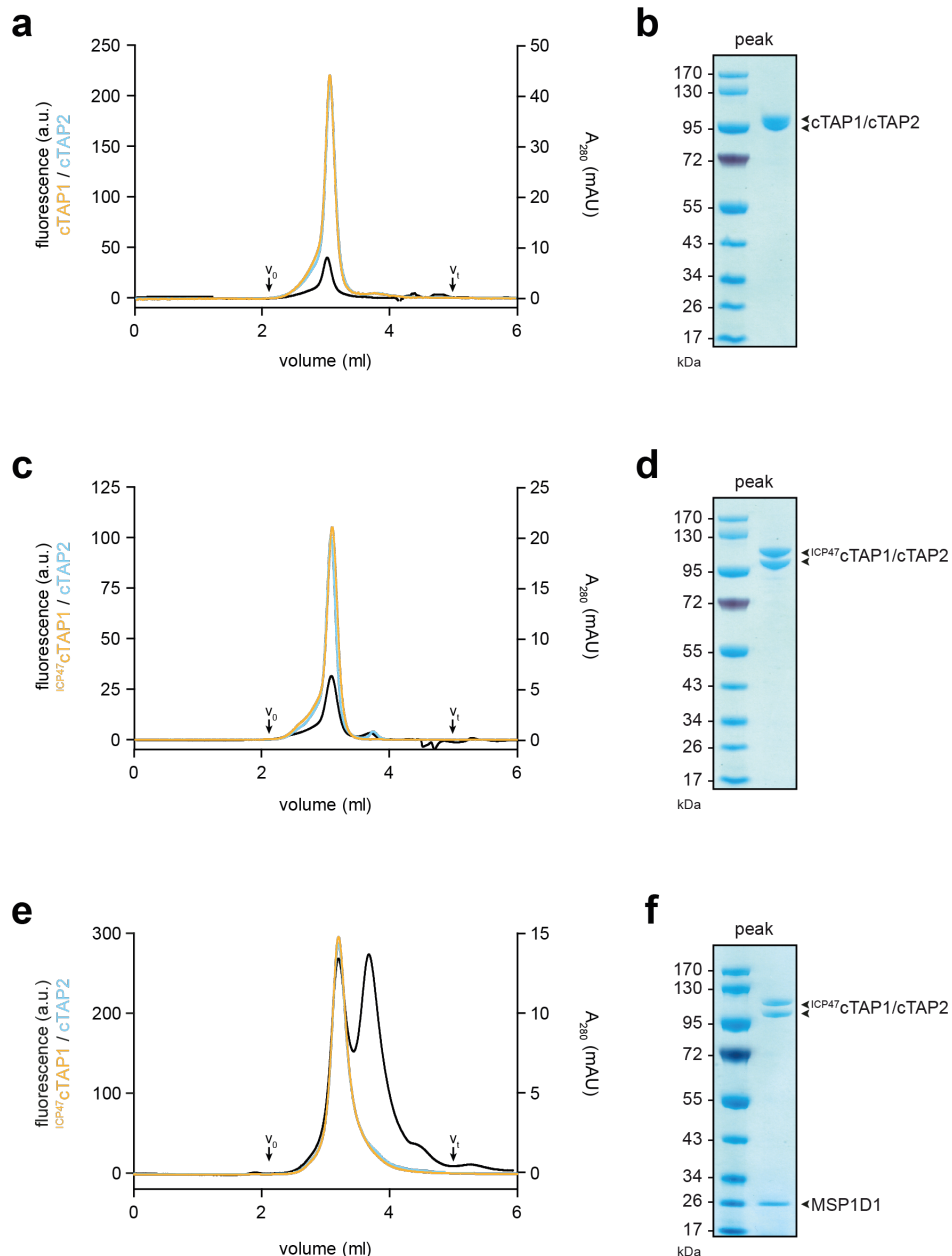


Figure 8: **Purification of TAP variants.** **a**, MC-FSEC elution profile of cTAP upon solubilization in 1% GDN (w/v) and tandem affinity purification *via* His₁₀- (cTAP1) and StrepII-tag (cTAP2). **b**, InstantBlue™-stained SDS-PAGE gel of the sample isolated by SEC. **c**, MC-FSEC elution profile of ICP47 cTAP. **d**, InstantBlue™-stained SDS-PAGE gel of the sample isolated by SEC. **e**, ICP47 cTAP reconstituted into MSP1D1 nanodiscs. By MC-FSEC, ICP47 cTAP-containing nanodiscs (front peak) were separated from empty nanodiscs. **f**, Reconstitution efficiency and stoichiometry were determined by an InstantBlue™-stained SDS-PAGE gel of purified ICP47 cTAP nanodiscs. **a**, **c**, **e**, Column: KW404-4F (Shodex). Void and total column volume are indicated by v_0 and v_t , respectively.

Functionality and stability of cTAP were shown by peptide binding, peptide transport, and ATP hydrolysis activity measurements (Figure 9). In agreement with previously published data (145), purified TAP was capable of binding the fluorescently-labeled high-affinity substrate C4F revealing $29.3 \pm 0.4\%$ of cTAP showing peptide binding (Figure 9a). Additionally, a 3-fold

stimulated ATPase activity with a turnover of $2.5 \text{ ATP min}^{-1} \text{ cTAP}^{-1}$ was observed upon addition of the high affinity substrate R9LQK (Figure 9b). To follow peptide translocation, cTAP-containing proteoliposomes were enriched by centrifugation on a continuous Ficoll density gradient (Figure 9d) and ATP-dependent transport of the high-affinity peptide C4F was measured. Specificity of transport was proven since transport could be competed by the addition of a 100-fold excess of unlabeled competitor peptide R9LQK (Figure 9c).

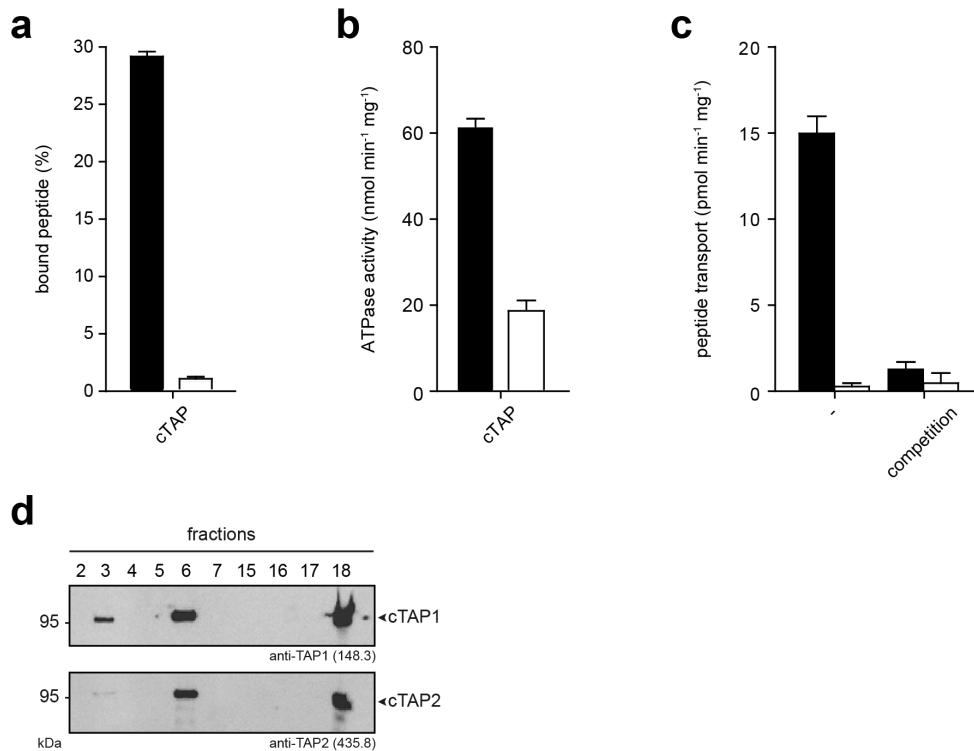


Figure 9: Purified cTAP is active in peptide binding and translocation. **a**, Substrate binding of cTAP was explored by a filter-based binding assay. $4 \mu\text{g}$ cTAP were incubated with $1 \mu\text{M}$ C4F (RRY^FCKSTEL, black bar) for 15 min at 4°C . C4F binding was competed by the addition of $250 \mu\text{M}$ of unlabeled peptide R9LQK (RRYQKSTEL, white bar). Data were measured in triplicates. Error bars indicate SD. **b**, ATPase activity of cTAP was determined by a malachite-green based ATPase assay. 500 nM cTAP were incubated with 3 mM MgCl_2 , 1 mM ATP, and with (black bar) or without (white bar) $1 \mu\text{M}$ R9LQK peptide for 30 min at 37°C . Data were measured in triplicates. Error bars indicate SD. **c**, ATP-dependent substrate translocation of cTAP in proteoliposomes composed of *E. coli* polar lipids and DOPC (7:3). Reconstituted cTAP was incubated with $1 \mu\text{M}$ C4F peptide, 3 mM MgCl_2 , and 3 mM ATP (black bars) or 3 mM ADP (white bars) and transport measured for 15 min at 37°C . To proof specificity of transport, $100 \mu\text{M}$ of unlabeled competitor peptide R9LQK were added. Data were measured in triplicates. Error bars indicate SD. **d**, cTAP-containing proteoliposomes (fraction 6) were enriched and separated from protein aggregates (fraction 18) by Ficoll density gradient centrifugation (0-10%).

These data show that isolated TAP complexes fulfill all quality criteria (purity, stoichiometry of the two ABC half-transporters, and functionality) and can be used for antibody selection and structural studies.

8.1.2 Antibodies as stabilizing chaperones of selected functional states of TAP

In order to stabilize certain functional states of TAP, synthetic antibodies and nanobodies were generated in collaboration with Pawel Dominik (Kossiakoff laboratory, Department of Biochemistry and Molecular Biology, The University of Chicago, Chicago, IL, USA) and Els Pardon (Steyaert laboratory, VIB-VUB Center for Structural Biology in Brussels, Vrije Universiteit Brussel, Brussels, Belgium). The antibody selection was performed within the context of research visits at the Kossiakoff laboratory and the Steyaert laboratory.

8.1.2.1 Selection of synthetic antibodies

In order to immobilize TAP-containing nanodiscs on streptavidin-coated beads for antibody selection, the MSP was chemically biotinylated. The advantage of scaffold protein-labeling is the generation of biotinylated nanodiscs without affecting the inserted membrane protein. A pull-down experiment using streptavidin-coated magnetic beads revealed an immobilization efficiency of 80% (Figure 10; exemplarily shown for ^{ICP47}cTAP nanodiscs).

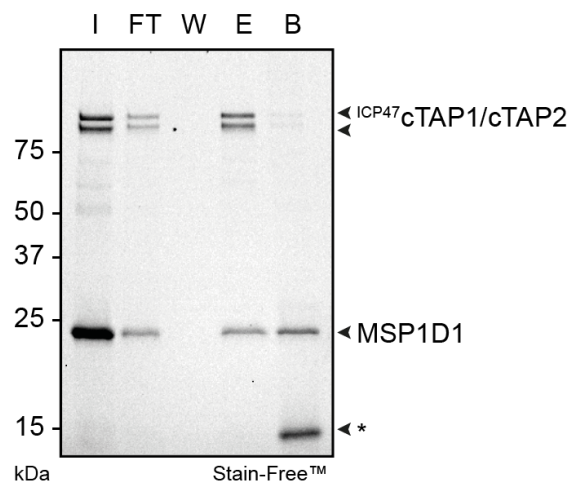


Figure 10: **Immobilization efficiency of ^{ICP47}cTAP nanodiscs.** Chemically biotinylated ^{ICP47}cTAP-containing nanodiscs were incubated with streptavidin-coated magnetic beads (Dynabeads[®] M-280 Streptavidin; Invitrogen). After 1 h incubation at 4 °C, unbound nanodiscs were removed by several washing steps. For elution, 1% FC-12 was added to disrupt the nanodiscs. Beads were resuspended in 1x SDS sample buffer. I: input; FT: flow-through; W: wash; E: elution, B: beads. *: streptavidin.

In total, five consecutive rounds of phage-displayed library sorting were performed with gradually decreased TAP concentrations (starting with 1 μ M to a final concentration of 90 nM in the fifth round). Prior to the selection, TAP was treated with TEV protease for removal of the fluorescent tags to avoid the enrichment of mVenus/mCerulean-binding antibodies. Additionally, empty non-biotinylated nanodiscs were added as soluble competitors during incubation with the phage-displayed library. According to Dominik *et al.*, the sorting process was monitored by comparing the enrichment of eluted phages after each sorting round (Figure 11) (113). A 12-fold enrichment was observed for ^{ICP47}cTAP-containing nanodiscs (Figure 11a) and a 5-fold enrichment for cTAP-containing nanodiscs (Figure 11b).

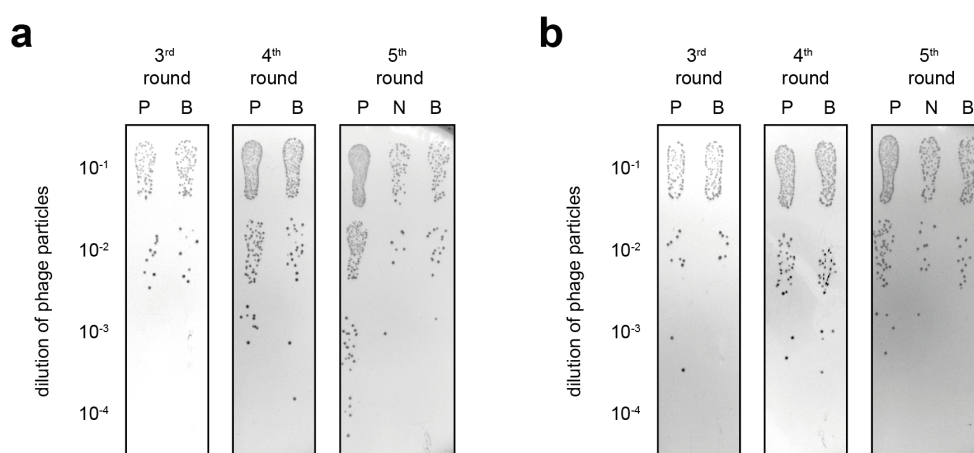


Figure 11: Enrichment of eluted phage particles after 3rd, 4th, and 5th round of phage-displayed library sorting against TAP. After each sorting round, *E. coli* XL-1 cells were infected with eluted phage particles and plated in serial dilutions on LB agar plates supplemented with ampicillin. By comparing the number of colonies of either the TAP-containing sample (P: protein), beads only (B: beads; indicator for stickiness of eluted phage particles) or empty nanodiscs (N: negative control) after each round, the enrichment was determined. **a**, ^{ICP47}cTAP-containing nanodiscs. **b**, cTAP-containing nanodiscs.

After sorting, individual clones from round four to five (127 individual clones selected against ^{ICP47}cTAP nanodiscs, 63 clones selected against cTAP nanodiscs) were picked and phages were produced in *E. coli* XL-1 cells to perform single-point phage enzyme-linked immunosorbent assays (ELISA). ELISA analysis revealed >95% of all tested synthetic antibodies as strong and specific TAP-binders (Figure 12 and Figure 13). Based on the ELISA results, the DNA of 140 clones was isolated, amplified, and sequenced, resulting in 17 and 23 unique antibody clones, which bound specific to ^{ICP47}cTAP and cTAP, respectively.

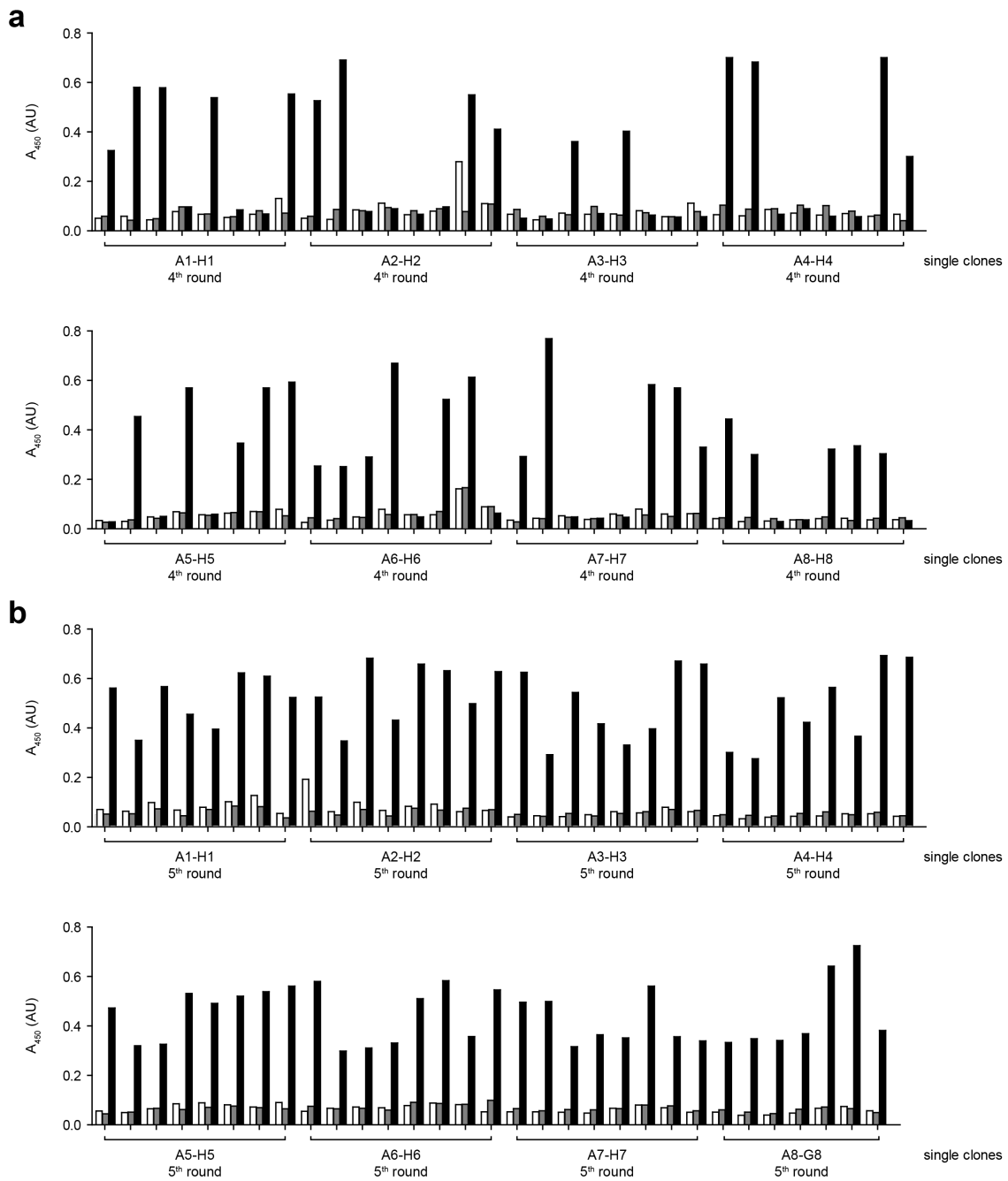


Figure 12: **Specificity of putative ICP47cTAP-binding single clones tested by phage ELISA.** Phages amplified and produced in *E. coli* XL-1 cells were added to neutraavidin-captured biotinylated ICP47cTAP-nanodiscs (45 nM, black bars). Bound phages were detected with an anti-phage antibody directed against filamentous M13 phages. As negative control, phages were incubated with neutraavidin only (white bars) and empty nanodiscs (45 nM, grey bars). Bars (white/grey/black) indicate single measurements. **a**, Single clones after 4th sorting round. **b**, Single clones after 5th sorting round.

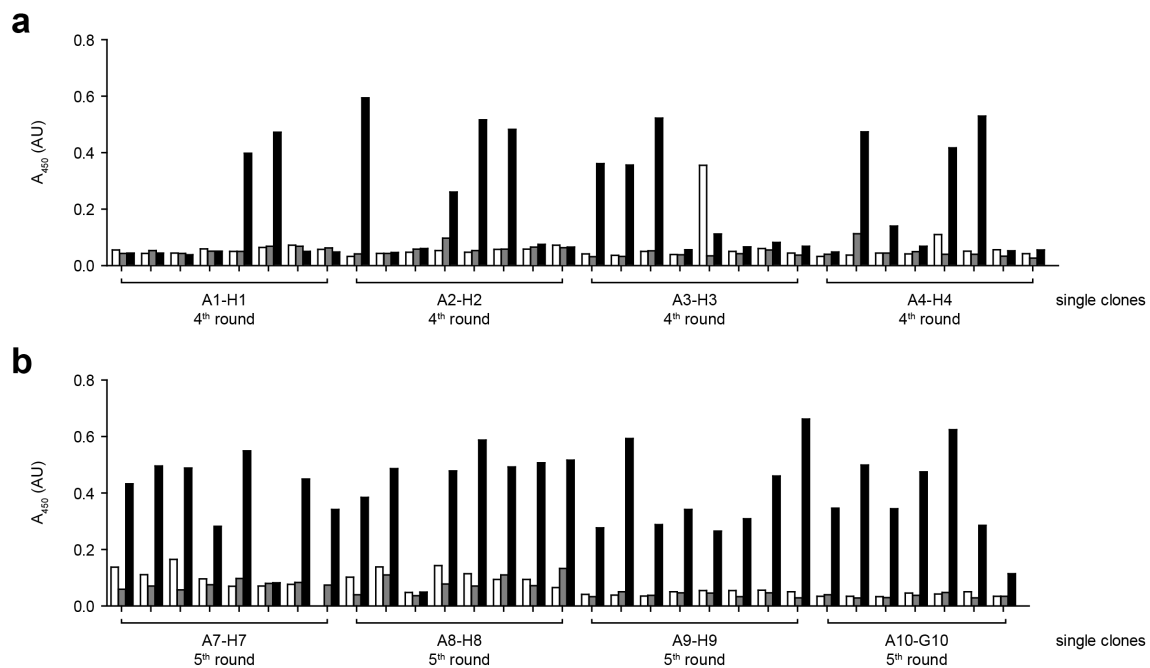


Figure 13: **Specificity of putative cTAP-binding single clones tested by phage ELISA.** Phages amplified and produced in *E. coli* XL-1 cells were added to neutravidin-captured biotinylated cTAP-nanodiscs (90 nM, black bars). Bound phages were detected with an anti-phage antibody directed against filamentous M13 phages. As negative control, phages were incubated with neutravidin only (white bars) and empty nanodiscs (90 nM, grey bars). Bars (white/grey/black) indicate single measurements. **a**, Single clones after 4th sorting round. **b**, Single clones after 5th sorting round.

Taken together, after five rounds of phage-displayed library sorting, 40 unique single clones were identified that were capable of binding specific to TAP. To further characterize the TAP-antibody interaction, initially 10 synthetic antibodies (4 clones binding to ^{ICP47}cTAP and 6 clones binding to cTAP) were chosen based on their abundance and diversity of CDR3. The antibody-encoding sequences were cloned into a bacterial expression plasmid and produced utilizing *E. coli* BL21 cells. Out of 1 l bacterial expression culture, milligram quantities of >99% pure antibody were obtained after a two-step purification *via* protein A (HiTrap MabSelect SuRe column; GE Healthcare) with subsequent cation exchange chromatography.

To analyze stable TAP/antibody complex formation, a gel filtration shift assay was performed. Synthetic antibodies C2, E2, and F8 formed stable complexes with detergent solubilized ^{ICP47}cTAP (Figure 14). Only for synthetic antibody A6 no shift of the retention volume was observed upon incubation with ^{ICP47}cTAP. For putative cTAP-binding synthetic antibodies, no complex formation was observed at all (data not shown).

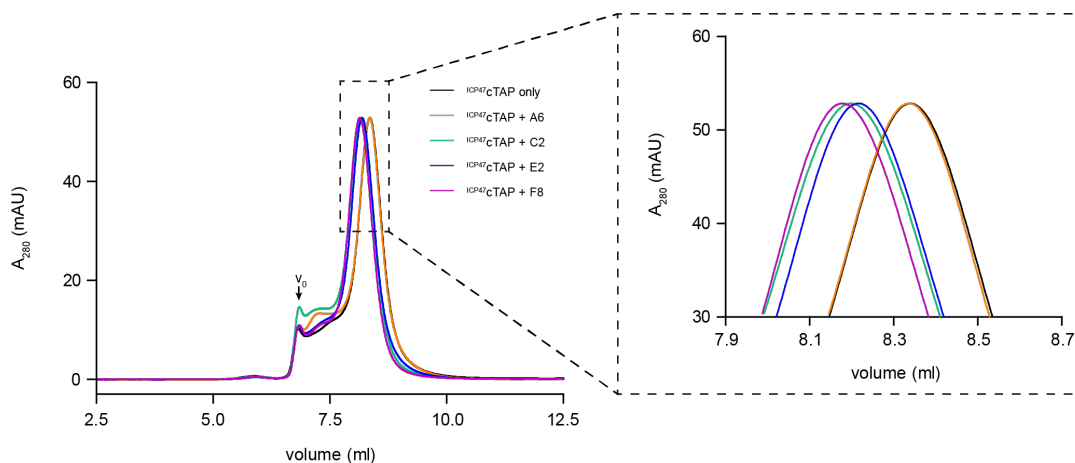


Figure 14: **Synthetic antibodies C2, E2, and F8 form stable complexes with ICP47cTAP.** ICP47cTAP/sAB complex formation. TEV-treated ICP47cTAP was incubated with a 1.25-fold molar excess of sAB for 15 min on ice prior to gel filtration (column: TSKgel® G3000SW_{XL}; Tosoh Bioscience LLC). Void volume is indicated by v_0 . In order to illustrate stoichiometric binding, data were normalized to the ICP47cTAP run without sAB (ICP47cTAP only).

Taken together, these data demonstrate the generation of highly specific anti-ICP47cTAP antibodies (C2, E2, and F8), which form stable and stoichiometric TAP/antibody complexes for further investigation by single-particle EM.

8.1.2.2 Selection of nanobodies

For llama immunization, proteoliposomes were shown to serve as a stable system to maintain the native conformation of membrane proteins (126, 172). Therefore, ICP47cTAP and cTAP were reconstituted into proteoliposomes and were injected weekly over a time period of 6 weeks with starting concentrations of 200-300 μg of reconstituted protein to stimulate the llama's immune response. After the immunization process, B-cells were isolated, the total RNA was prepared and reverse transcribed. The cDNA repertoire was used to amplify the nanobody-encoding sequences and reformatted into a phage display vector for selection (126).

For the phage-displayed library sorting, either biotinylated TAP in GDN, in proteoliposomes or TAP reconstituted in biotinylated nanodiscs were immobilized on a solid phase (50 nM). In comparison to the fully synthetic antibody library, two selection rounds were sufficient to achieve a strong enrichment of TAP-binding nanobodies. Additionally, ligands like R9LQK peptide or ATP-Mg²⁺ were added during the sorting procedure. For most of the selection conditions, a strong enrichment was achieved after the first sorting round (Table 15). Surprisingly, for ICP47cTAP in nanodiscs, even after the second round of phage-displayed library sorting, no enrichment was achieved.

Table 15: Enrichment results after two rounds of library sorting.

Antigen	Enrichment		Comments
	1 st sorting round	2 nd sorting round	
^{ICP47}cTAP			ligands
nanodiscs	no enrichment	no enrichment	ICP47-fusion
proteoliposomes	300-fold	-	ICP47-fusion
GDN	90-fold	-	ICP47-fusion
cTAP			
nanodiscs	no enrichment	-	-
nanodiscs	no enrichment	-	R9LQK, ATP-Mg ²⁺
proteoliposomes	no enrichment	210-fold	-
GDN	75-fold	-	-
GDN	131-fold	-	R9LQK, ATP-Mg ²⁺

To screen for TAP-binding clones, 624 single clones were picked and *E. coli* periplasmic extract containing nanobodies was prepared to perform a single-point phage ELISA (216 single clones selected against ^{ICP47}cTAP and 408 single clones selected against cTAP). The majority of single clones bound specifically to ^{ICP47}cTAP and cTAP in GDN or proteoliposomes (Figure 15a and b). No TAP-binding clones were selected for nanodiscs. Although empty nanodiscs were added as soluble competitors in excess during the nanobody selection, only MSP-binding nanobodies were identified (Figure 15c).

However, based on the phage ELISA results, the DNA of 286 clones was amplified by PCR and sequenced, resulting in 145 unique nanobody clones. Based on the similarity in their CDR3 sequence, these nanobody clones were grouped into 29 nanobody families (a nanobody family is defined as a group of nanobodies with identical CDR3 length and >80% sequence identity (126)).

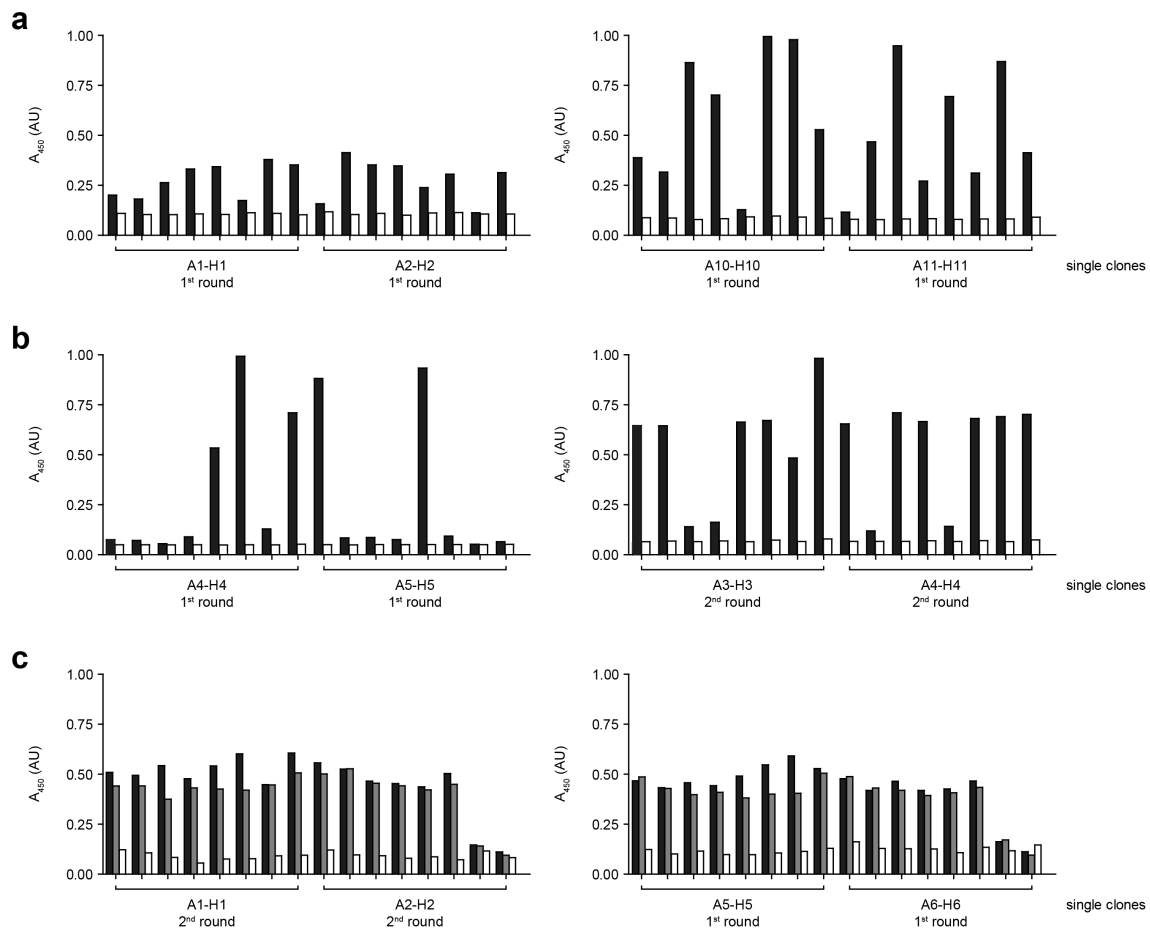


Figure 15: **Specificity of TAP-binding nanobodies.** The periplasmic extract (PE) of nanobody-producing *E. coli* cells (1:5 dilution) was added to neutravidin-captured biotinylated TEV-treated TAP (45 nM, black bars). For detection of bound nanobody, an anti-His antibody (1:3,000) was added followed by an anti-mouse antibody with an alkaline phosphatase conjugated (1:10,000). As negative control, PE was incubated with neutravidin only (white bars) or empty nanodiscs (grey bars). Bars (black/grey/white) indicate single measurements. **a**, ICP47 cTAP in GDN (left panel), cTAP in GDN (right panel). **b**, ICP47 cTAP in proteoliposomes (left panel), cTAP in proteoliposomes (right panel). **c**, ICP47 cTAP-containing nanodiscs (left panel), cTAP-containing nanodiscs (right panel).

Initially, out of 29 nanobody families, 13 nanobody clones selected against ICP47 cTAP were chosen to be further characterized regarding the TAP-nanobody interaction. For nanobody production, nanobody-encoding sequences were expressed in *E. coli* BL21 cells using the original display plasmid. Out of 1 l bacterial culture, milligram quantities of >99% pure nanobodies were obtained after a two-step purification *via* IMAC and subsequent gel filtration.

Specific binding of all purified nanobodies to ICP47 cTAP was shown by an ELISA (Figure 16a). To further investigate the ICP47 cTAP-nanobody interaction, complex formation was analyzed by SEC. Unexpectedly, only for nanobody 244 coelution with ICP47 cTAP was observed (20%). No stable ICP47 cTAP/nanobody complexes could be isolated (Figure 16b and c).

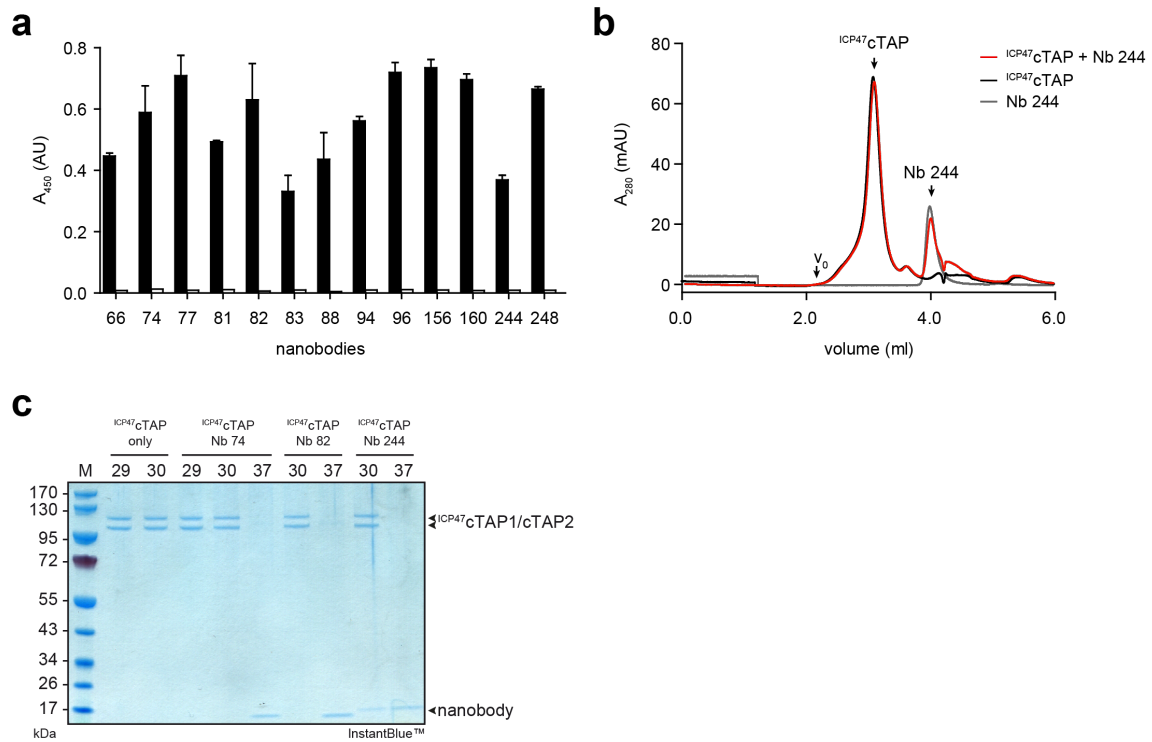


Figure 16: **ICP47cTAP-nanobody interaction.** **a**, Specific binding of nanobodies to ICP47cTAP in GDN. 1 μ M of nanobody was added to neutravidin-captured biotinylated TEV-treated ICP47cTAP (45 nM, black bars) and incubated for 1 h at 4 $^{\circ}$ C. For nanobody detection, an anti-His antibody (mouse, 1:3,000 dilution) was added followed by an anti-mouse HRP conjugate (1:10,000 dilution). TAP samples were measured in triplicates. White bars represent background binding (single measurements). Error bars indicate SD. **b**, ICP47cTAP/nanobody complex formation. ICP47cTAP was incubated with a 1.25-fold molar excess of nanobody for 15 min on ice prior to gel filtration. Column: KW404-4F (Shodex). Void volume is indicated by V_0 . **c**, InstantBlueTM-stained SDS-PAGE gel of TAP/nanobody samples upon gel filtration.

8.1.3 Electron microscopy of human ^{ICP47}cTAP

In order to perform electron microscopy, ^{ICP47}cTAP was chosen for first trials due to the higher stability in comparison to cTAP and the conformational locking by ICP47. To gain first insights into the stability and homogeneity of purified ^{ICP47}cTAP, TAP samples were applied to negative-stain EM. All EM work was performed in collaboration with either Simone Prinz (Kühlbrandt laboratory, Department of Structural Biology, Max Planck Institute of Biophysics, Frankfurt) or Arne Möller and Dovile Janulienė (Möller laboratory, Department of Structural Biology, Max Planck Institute of Biophysics, Frankfurt) at the Max Planck Institute of Biophysics.

Upon the orthogonal affinity purification, ^{ICP47}cTAP1^{mVenus-His10}/^{cTAP2^{mCerulean-StrepII}} was TEV treated to remove the C-terminal fluorescence- and purification-tags. TEV protease and tags were separated from TAP by SEC (Figure 17a). In order to avoid background signal caused by excess of detergent micelles, detergent concentration was reduced to 0.01% GDN during SEC. Immediately after SEC, ^{ICP47}cTAP was applied to glow discharged carbon-coated copper grids and stained with 2% uranyl formate. Micrographs were collected on a Tecnai-Spirit transmission electron microscope (Thermo Fisher, former FEI), operating at 120 kV and equipped with a Gatan 4x4k CCD camera (Figure 17b).

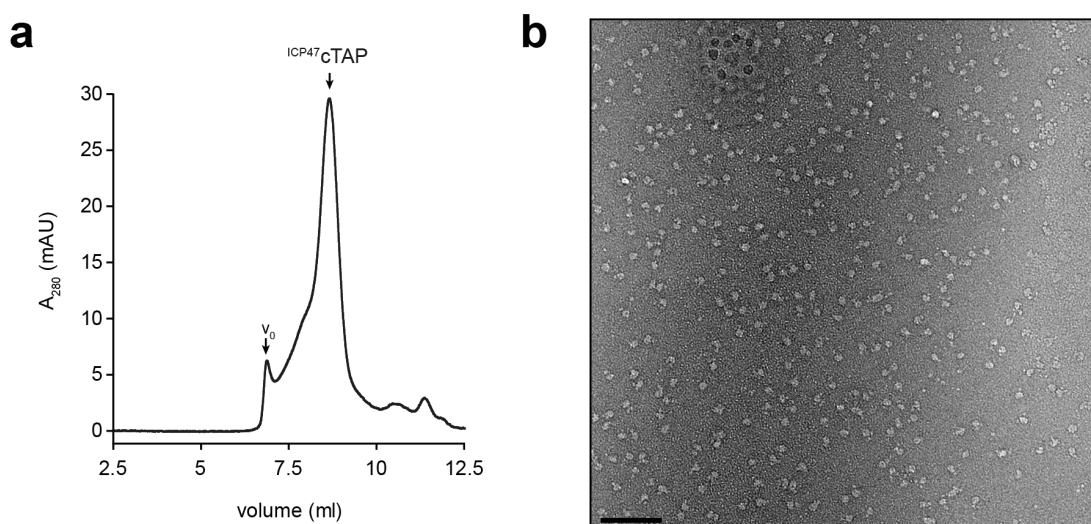


Figure 17: **Negative-stain EM analysis of ^{ICP47}cTAP in GDN.** **a**, For removal of fluorescence- and purification-tags and buffer exchange to 0.01% GDN, ^{ICP47}cTAP was subjected to gel filtration. Column: TSKgel[®] G3000SW_{XL} (Tosoh Bioscience LLC). Void volume is indicated by v_0 . **b**, The peak fraction was applied to glow discharged carbon-coated grids and stained with 2% uranyl formate. Micrographs were collected on a Tecnai-Spirit transmission electron microscope (Thermo Fisher, former FEI), operated at 120 kV and equipped with a Gatan 4x4k CCD camera. Scale bar: 100 nm. (Micrographs were collected by Simone Prinz (Kühlbrandt laboratory, Department of Structural Biology, Max Planck Institute of Biophysics, Frankfurt)).

Upon gel filtration, $^{13}\text{C}^{47}\text{cTAP}$ migrated as a symmetric peak indicating a monodisperse and homogeneous sample. In accordance with this result, negative-stain EM revealed a homogeneous distribution of particles with a similar size (diameter of roughly 10 nm). Upon analysis of the data, classical features of an ABC transporter, such as NBDs protruding from the detergent micelle, were not detected. Based on this result, it was speculated that either the intrinsic dynamic of the NBDs of $^{13}\text{C}^{47}\text{cTAP}$ is too high or the choice of detergent might be reconsidered. Thus, the cross-linking reagent glutaraldehyde was added (Figure 18a). Upon analysis of the sample by negative-stain EM, no improvement was observed. In order to minimize the size of the detergent micelle, SM-2 Biobeads (Bio-Rad) were added prior to grid preparation (Figure 18b). Again, upon analysis of EM data, no difference in comparison to previous samples was observed.

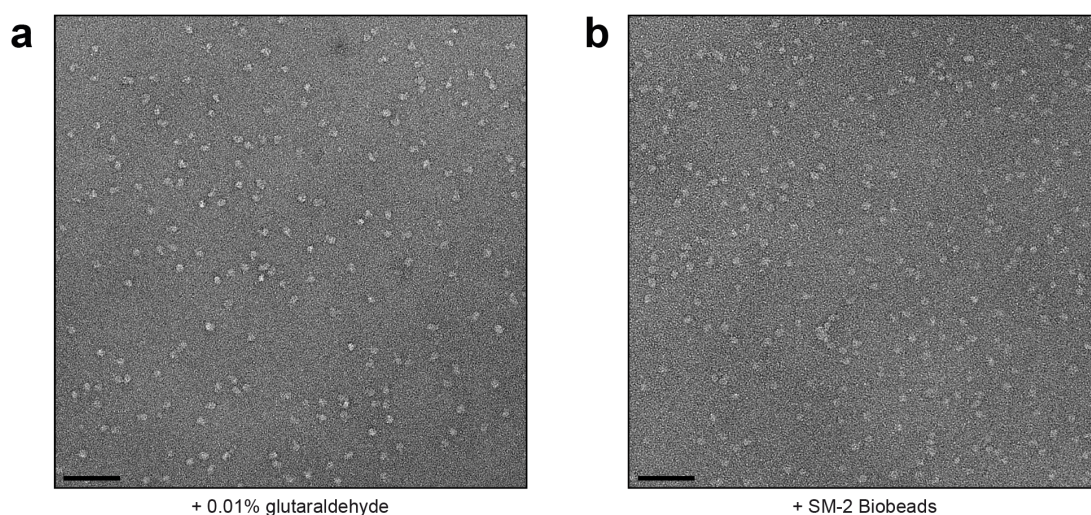


Figure 18: **EM analysis of $^{13}\text{C}^{47}\text{cTAP}$ upon fixation and detergent removal.** **a**, Upon SEC of TEV-treated $^{13}\text{C}^{47}\text{cTAP}$, 0.01% glutaraldehyde were added, and the sample incubated for 30 min on ice. For EM, the protein sample was applied to glow discharged carbon-coated grids and stained with 2% uranyl formate. Micrographs were collected on a Tecnai-Spirit transmission electron microscope (Thermo Fisher, former FEI), operated at 120 kV and equipped with a Gatan 4x4k CCD camera. Scale bar: 100 nm. **b**, For detergent removal, SM-2 Biobeads (Bio-Rad) were added and incubated for 1 h on ice prior to grid preparation. Scale bar: 100 nm. (Micrographs were collected by Simone Prinz (Kühlbrandt laboratory, Department of Structural Biology, Max Planck Institute of Biophysics, Frankfurt)).

Next, a method called GraFix was applied (gradient fixation). GraFix combines the sedimentation of protein complexes into a glycerol density gradient with chemical fixation by glutaraldehyde (149). Hence, $^{13}\text{C}^{47}\text{cTAP}$ was subjected to a 10-30% glycerol gradient supplemented with 0-0.2% glutaraldehyde and 0.01% GDN. After centrifugation, fractions were collected and analyzed by negative-stain EM (Figure 19). $^{13}\text{C}^{47}\text{cTAP}$ was found in fractions 4 to 7. In contrast to an improvement of the overall sample quality, particles were less well-behaved and even clustered.

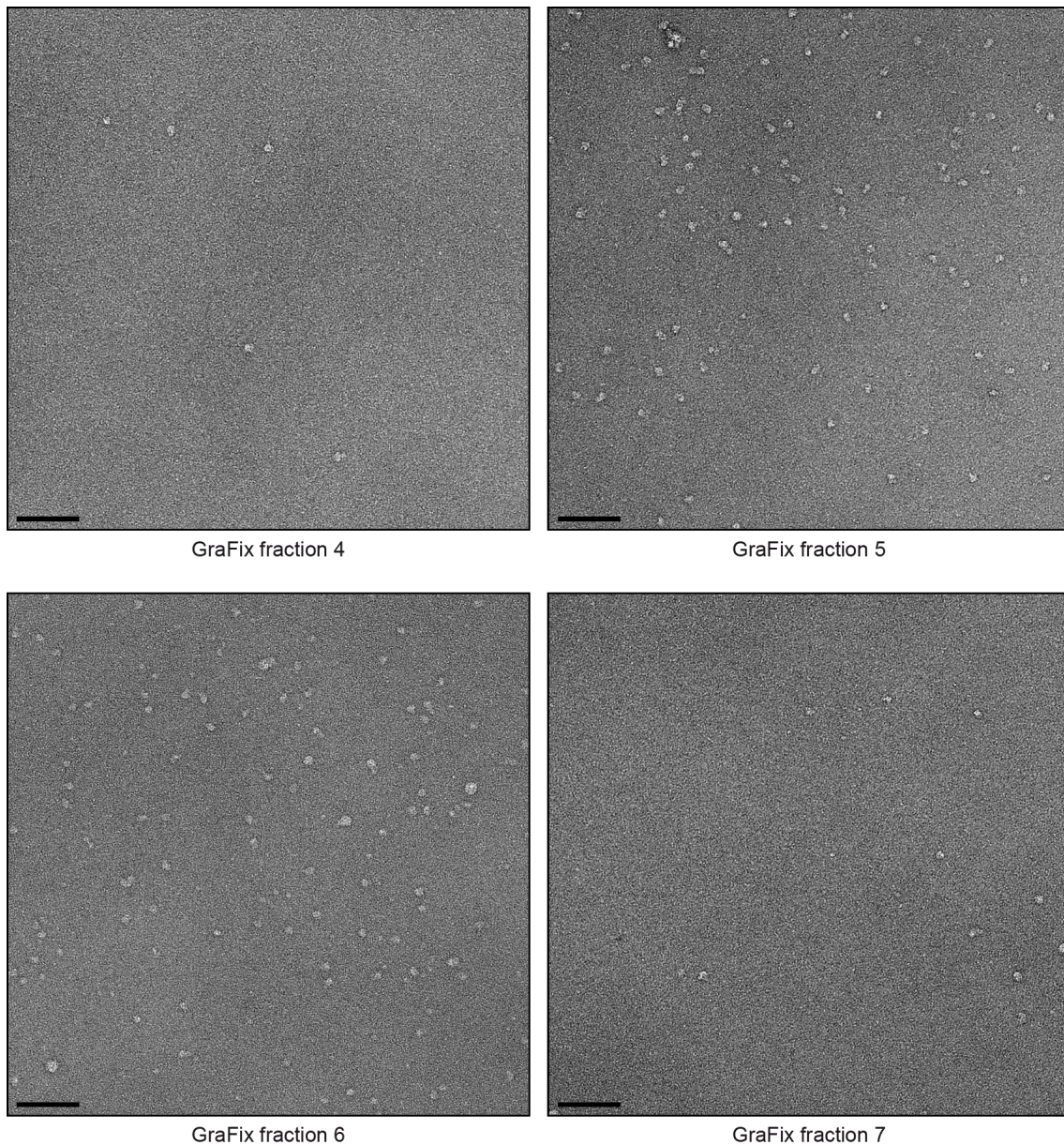


Figure 19: **GraFix treatment of ^{ICP47}cTAP**. Negative-stain EM analysis of fraction 4, 5, 6, and 7. 3 μ l of sample were applied to glow discharged carbon-coated grids and stained with 2% uranyl formate. Micrographs were collected on a Tecnai-Spirit transmission electron microscope (Thermo Fisher, former FEI), operated at 120 kV and equipped with a Gatan 4x4k CCD camera. Scale bar: 100 nm. (Micrographs were collected by Simone Prinz (Kühlbrandt laboratory, Department of Structural Biology, Max Planck Institute of Biophysics, Frankfurt)).

So far, all analyzed particles did not contain adequate features for image alignment. Within this study, two different types of antibodies (synthetic antibodies and nanobodies) were generated to trap selected functional states of TAP and to serve as a tool for image alignment. Therefore, ^{ICP47}cTAP/synthetic antibody complexes were isolated by SEC and were immediately used for grid preparation (Figure 20). The unprocessed EM micrographs showed individual particles with (presumably) bound antibody. Anyhow, upon 2D classification no classes were obtained showing transporter-like features.

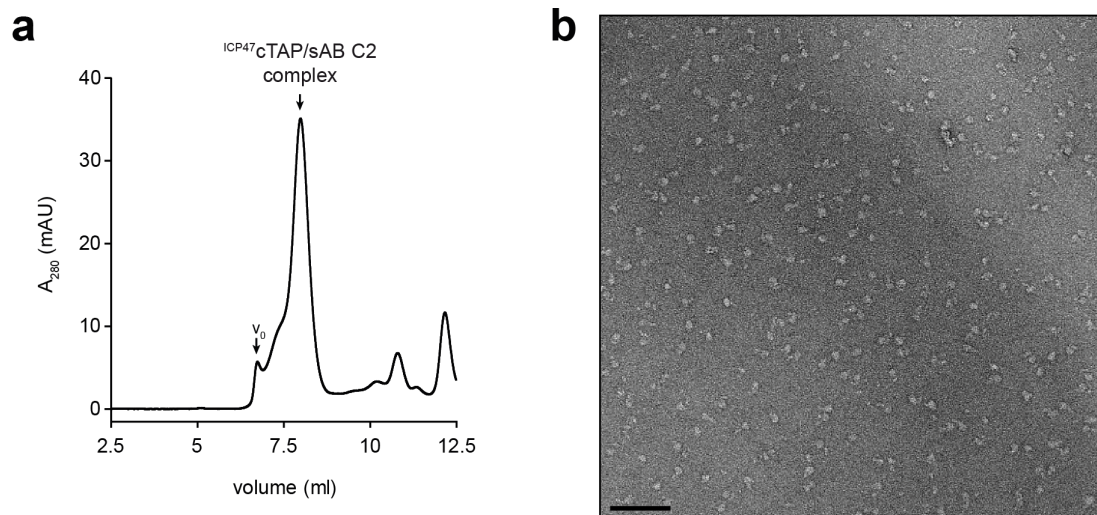


Figure 20: **Synthetic antibody C2 as fiducial marker for EM.** **a**, ^{125}I -ICP47cTAP/antibody complex isolated by SEC. Synthetic antibody C2 was added in a 1.25-fold molar excess and preincubated with TEV-treated ^{125}I -ICP47cTAP for 15 min on ice. Column: TSKgel[®] G3000SW_{XL} (Tosoh Bioscience LLC). Void volume is indicated by V_0 . **b**, The peak fraction was applied to glow discharged carbon-coated grids and stained with 2% uranyl formate. Micrographs were collected on a Tecnai-Spirit transmission electron microscope (Thermo Fisher, former FEI), operated at 120 kV and equipped with a Gatan 4x4k CCD camera. Scale bar: 100 nm. (Micrographs were collected by Simone Prinz (Kühlbrandt laboratory, Department of Structural Biology, Max Planck Institute of Biophysics, Frankfurt)).

In line with the stabilization of membrane proteins is the usage of amphipols, a class of amphipathic polymers (173). One of the most commonly utilized amphipols is A8-35. The major advantage of amphipols besides the biochemical stabilization of proteins is the possibility to work with membrane proteins in detergent-free solutions. Thus, GDN was exchanged for A8-35 and amphipol-solubilized TAP-complexes were isolated by gel filtration (Figure 21). Exchange of detergent for A8-35 did not disrupt the antigen translocation complex, but TAP was kept soluble in detergent-free solution (Figure 21a). The excess of A8-35 was separated by SEC. Amphipol A8-35 self-assembles into globular particles with an apparent MW of ~40 kDa (174). Despite an improvement of the signal-to-background-ratio by the removal of detergent, still no ABC transporter-like features were observed.

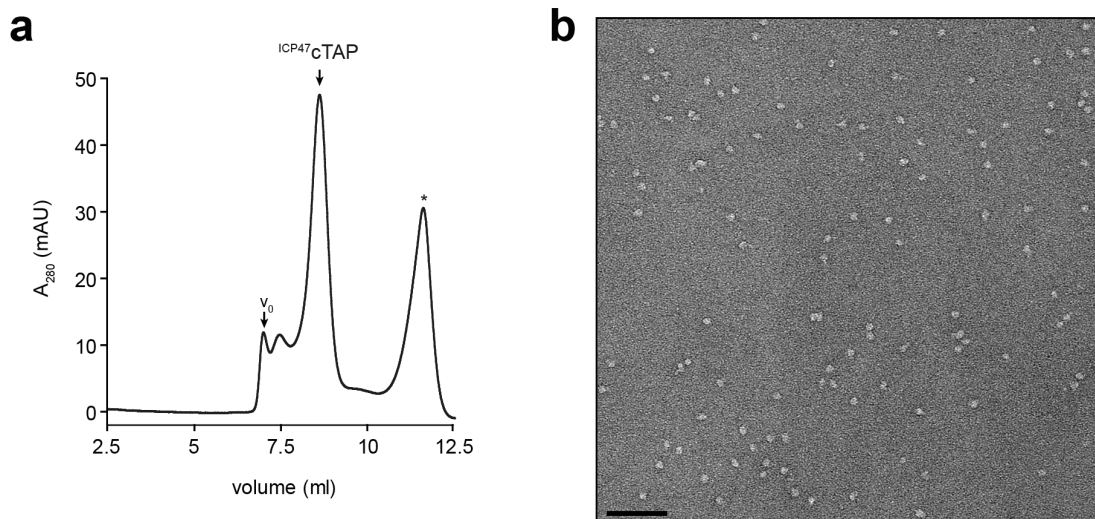


Figure 21: **Detergent exchange for amphipols.** **a**, ^{135}I -ICP47cTAP and A8-35 were mixed in a protein-to-amphipol ratio of 1:5 (w/w) and incubated for 30 min at 4 °C. After detergent removal with SM-2 Biobeads (Bio-Rad), the sample was applied to a TSKgel® G3000SW_{XL} column (Tosoh Bioscience LLC). Asterisk: amphipol A8-35. **b**, The peak fraction was applied to glow discharged carbon-coated grids and stained with 2% uranyl formate. Micrographs were collected on a Tecnai-Spirit transmission electron microscope (Thermo Fisher, former FEI), operated at 120 kV and equipped with a Gatan 4x4k CCD camera. Scale bar: 100 nm. (Micrographs were collected by Simone Prinz (Kühlbrandt laboratory, Department of Structural Biology, Max Planck Institute of Biophysics, Frankfurt)).

In summary, various methods were applied to improve the overall quality of TAP for EM. To inhibit the intrinsic dynamics of TAP, the ^{135}I -ICP47cTAP fusion construct was used and different fixation methods were applied. Moreover, different detergent concentrations were tested and GDN replaced by amphipols. Additionally, ^{135}I -ICP47cTAP/antibody complexes were isolated and subjected to EM analysis. But none of the approaches did improve the overall sample quality.

8.1.4 Discussion

8.1.4.1 Selection of state-specific antibody fragments

During ATP-driven substrate translocation, ABC transporters cycle between inward-open and outward-open states, suggesting a trajectory of numerous transient intermediates (9, 12, 175). Within the last few years, the number of high-resolution membrane transporter structures, determined either by X-ray crystallography or by single-particle cryo-EM, has increased exponentially. Especially recent advances in single particle cryo-EM, such as the development of direct electron detectors, better microscopes, and improved image processing software, resulted in structural insights of proteins that were refractory to crystallization (9, 42, 176-178). A number of structures of ABC transporters haven been deposited, all presenting

physiologically-relevant and unique conformational states. Nevertheless, these structures represent only snapshots within the multitude of conformational states a highly dynamic ABC transporter can adopt during substrate translocation (175). To be able to fully understand the underlying mechanism of transport across membranes, it is of vital importance to elucidate the full translocation cycle by structural, but also biochemical means. Thus, the aim of this project was the stabilization of intermediates along the peptide translocation pathway to get insights into the structural organization of TAP. When starting the project, the only high-resolution structural information about TAP was based on the crystal structure of a Walker B/D-loop double mutant of the NBD of rat TAP1 (27). Further high-resolution information about TAP was missing and was eagerly awaited due to its important role as key player in the adaptive immune response.

A promising approach for a conformational locking of TAP was the generation of state-specific antibodies. Thus, within this project, two types of antibodies with very different properties were generated: synthetic antibodies (based on a Fab scaffold) and nanobodies (126, 179). Because of their size of approximately 50 kDa and the ability to form stable antibody/antigen complexes, Fabs were proven to serve as perfect tools for particle alignment in single-particle cryo-EM previously (14). The synthetic antibody approach used here combines this feature with a *reduced genetic code* concept allowing for the generation of high-affinity antibodies, which form stable complexes with highly dynamic membrane proteins (179). Nanobodies, in contrast, have a much smaller size (~15 kDa), but possess an extended CDR-3 loop. This unique three-dimensional structure allows for binding of epitopes, which cannot be reached by the concave antigen-binding region of conventional antibodies and therefore implements a high potential for nanobodies to trap selected functional states (126).

The selection of synthetic antibodies was performed against TAP (^{ICP47}cTAP and cTAP) reconstituted in biotinylated nanodiscs. Upon five rounds of phage-displayed library sorting, 40 unique antibodies were identified. Out of ten synthetic antibodies, which were produced and purified in a large scale, synthetic antibodies C2, E2, and F8 were shown to form stable, stoichiometric complexes with ^{ICP47}cTAP (Figure 14). Surprisingly, no cTAP/antibody complexes could be isolated *via* SEC. Since this result differs strongly from what was observed by ELISA upon single clone screening (Figure 13), it is tempting to speculate that selected anti-cTAP antibodies did bind, but with rather low affinity. Previously, only a few examples of successful *in vitro* selections against membrane proteins were shown (113, 131, 180, 181). Often, the

diversity covered by phage display (10^8 - 10^{10}) might be insufficient to enrich high-affinity binders and thus can lead to poorly enriched binder pools resulting in weak binding affinities (181, 182).

The nanobody selection, in contrast, offered the advantage of an *in vivo* maturation of the antibody pool prior to phage-displayed library sorting (126). Upon a maximum number of two sorting rounds and single clone screening, 29 nanobody families were identified, binding to detergent-solubilized TAP and TAP in proteoliposomes. However, upon large scale nanobody production and purification, no TAP/nanobody complexes could be isolated *via* SEC (Figure 16). Within the context of this study, a Master thesis was designed and supervised, analyzing the kinetics of nanobody binding to ^{ICP47}cTAP investigated by surface plasmon resonance (Conformation-specific nanobodies for functional studies of the heterodimeric ABC exporters TmrAB and TAP, Lisa Marie Gottron, 2015). For all tested nanobodies, relatively fast *off*-rates were determined (ranging from $1-6 \times 10^{-3} \text{ s}^{-1}$), which might explain the SEC results (Figure 16).

Unexpectedly, no enrichment of putative binding nanobodies was observed for TAP in nanodiscs. In contrast, only MSP binding was observed (Figure 15). This differs fundamentally from results obtained for the selection of synthetic antibodies. In theory, reconstitution of TAP into a more native-like lipid environment should strongly increase the stability of the transport complex (94, 145). This result indicates a strong selection bias, which could neither be tackled by the immunization strategy applied, nor by the addition of empty nanodiscs as soluble competitors.

Collectively, these results demonstrate the generation of specific high-affinity antibodies against ^{ICP47}cTAP, but not cTAP (Figure 14, Figure 16). Many factors were considered that have an impact on TAP stability and function, such as temperature, choice of detergent or importance of lipids, before starting the antibody selection (55, 81, 94). To this end, stability and functionality of cTAP was proven by various biochemical methods. cTAP eluted as a defined peak in gel filtration (Figure 8) and was shown to bind and translocate peptides (Figure 9). Additionally, due to the importance of lipids for TAP function, cTAP was reconstituted in nanodiscs (Figure 8) and proteoliposomes (Figure 9). However, even though the whole antibody selection was performed strictly on ice and incubation times were kept as short as possible, the procedure comprises steps, such as extensive washing, that cannot be avoided and might result in a loss of protein function or even protein precipitation and thus impair the outcome of the antibody selection. Additionally, it is difficult to select for conformational states induced by the addition of non-covalent ligands, because the risk of ligand dissociation during immunization or washing is

extremely high. To overcome these limitations, a very elegant and novel approach for the generation of single domain antibodies against distinct conformational states of membrane proteins was presented in 2018 by Zimmermann *et al.* (181). Within this study, Zimmermann and co-workers developed an *in vitro* selection platform combining ribosome and phage display based on synthetic single domain antibodies named sybodies. To cover the natural shape diversity of camelid nanobodies, three sybody libraries were designed based on prototypical nanobody structures representing a concave, loop, and convex binding mode (181). Besides the library design, also binding and selection mode were optimized with regards to an optimized high-throughput screening process. Zimmermann and co-workers combined ribosome display with phage-displayed library sorting to allow for processing of very large diversities. In the initial round starting with ribosome display, 10^{12} different library members can be displayed (in comparison to phage display with a starting diversity of 10^8 - 10^{10} binder candidates) (181-183). Thus, Zimmermann *et al.* developed a selection procedure built as a selection cascade, which starts with one round of ribosome display and is followed by two rounds of phage display with varying immobilizations chemistries in every selection round (181). This selection approach should be considered for a repetition of the selection of high-affinity state-specific cTAP-binding antibodies.

8.1.4.2 Structural analysis of TAP by single-particle EM

When starting the project in 2015, the *resolution revolution* had just begun and new advances in single-particle cryo-EM have enabled the determination of high-resolution structures of proteins below 200 kDa (184, 185). For the structural analysis of TAP by single-particle cryo-EM, ^{ICP47}cTAP was chosen due to the conformational locking by ICP47 and thus higher stability of the TAP complex (81). First attempts by negative-stain EM revealed a homogenous distribution of particles (Figure 17). Surprisingly, no transporter-like features, such as the NBDs protruding from the detergent micelle, were observed. Various attempts were applied to increase the overall sample quality. Systematically different detergents concentrations were tested (Figure 18), glutaraldehyde as cross-linking reagent was added (Figure 19), and a detergent exchange for amphipols was performed to stabilize the complex (Figure 21). To introduce an alignment feature, synthetic antibodies were added and the ^{ICP47}cTAP/C2 complex was isolated *via* SEC. Even though the antibody was visible in the negative-stain micrographs, antibody addition did not improve particle quality (Figure 20). Since there was no apparent difference between all sample preparations independent of the addition of fixation reagent or detergent exchange, the

data might be explained by a folding defect or loss of structural integrity of the complex induced by fusion of ICP47 to TAP.

Notably, in 2016 Oldham and co-workers presented the structure of ICP47-trapped TAP determined to 4.0 Å by single-particle cryo-EM (16, 17). Within this study, purified ICP47 was added to TAP-containing *P. pastoris* membranes and the stably-formed ICP47/TAP complex was solubilized with β -DDM. Upon affinity purification using a protein A affinity tag fused to TAP1, homogenous ICP47/TAP complexes were isolated by SEC and used for cryo-EM. A new sample, which was prepared according to the protocol published by Oldham *et al.* (solubilization and purification in β -DDM, buffer exchange to β -DDM and C12E8 (1 mM each) immediately before grid preparation), did not show an improvement compared to all previous experiments. Since the published results could not be reproduced with the ^{ICP47}cTAP fusion construct, the decision made to change the emphasis of the study and focus on the TAP ortholog TmrAB.

8.2 Conformational cycle of TmrAB resolved by cryo-EM

In 2017, Nöll *et al.* presented the 2.7-Å X-ray structure of TmrAB in an unprecedented inward-facing state (15). This structure, together with biochemical data, provided first insights into the rearrangements of TmrAB during substrate translocation. However, for a complete understanding of the events and conformational transitions that couple ATP binding and hydrolysis to substrate translocation, structural information on intermediates was needed. Therefore, one of the major objectives of this thesis was to stabilize conformational intermediates to elucidate the complete catalytic cycle of TmrAB by cryo-EM.

8.2.1 Purification of TmrAB in catalytically active form

Production, purification, and reconstitution of TmrAB was carried out according to Nöll *et al.* (15). After purification by IMAC, TmrAB eluted as a defined peak during gel filtration (Figure 22a). Functionality of TmrAB was proven by ATP hydrolysis and peptide-transport assays. In agreement with data published by Zutz *et al.*, TmrAB hydrolyzed ATP with a turnover rate of $3.0 \pm 0.1 \text{ ATP s}^{-1}$ (Figure 22b) (83).

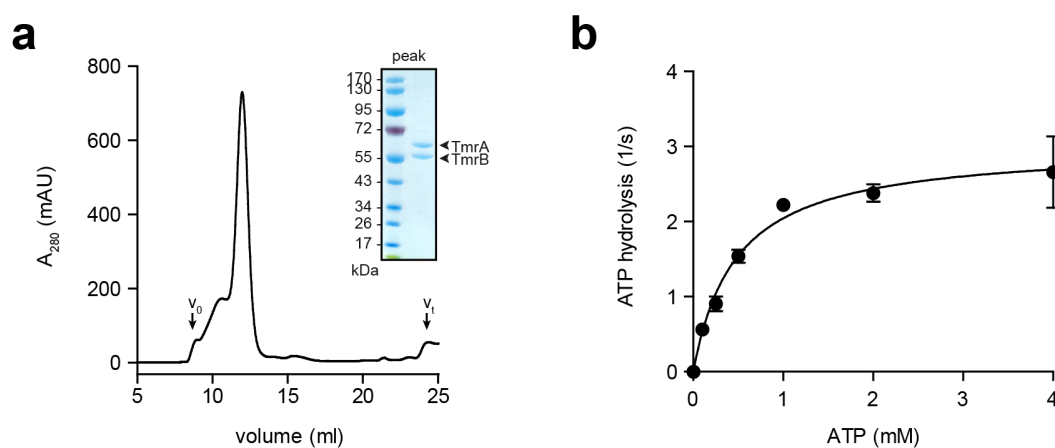


Figure 22: **Purified TmrAB is active in ATP hydrolysis.** **a**, Upon solubilization in 1% β -DDM and IMAC, TmrAB was further purified by SEC. Column: Superdex™ 200 Increase 10/300 GL (GE Healthcare). Void and total column volume are indicated by v_0 and v_t , respectively. The peak fraction was analyzed by SDS-PAGE and Coomassie staining. **b**, ATPase activity of TmrAB in β -DDM. 200 nM TmrAB were incubated for 5 min at 68 °C with 3 mM MgCl_2 and increasing concentrations of ATP. The Michaelis-Menten equation (Equation 1) was fitted to the data. Samples were measured in triplicates. Error bars indicate SD.

To further examine transporter function, ATP-dependent substrate accumulation within TmrAB proteoliposomes was tested (Figure 23a). Re-solubilization of TmrAB upon reconstitution in proteoliposomes revealed a reconstitution efficiency of >95%. (Figure 23b). The orientation of TmrAB was determined by cleavage of the C-terminal His₁₀-tag. Quantitative immunoblotting of TEV-treated TmrAB revealed that >80% of all transport complexes were inserted in the right orientation, with the NBDs pointing outwards (Figure 23c).

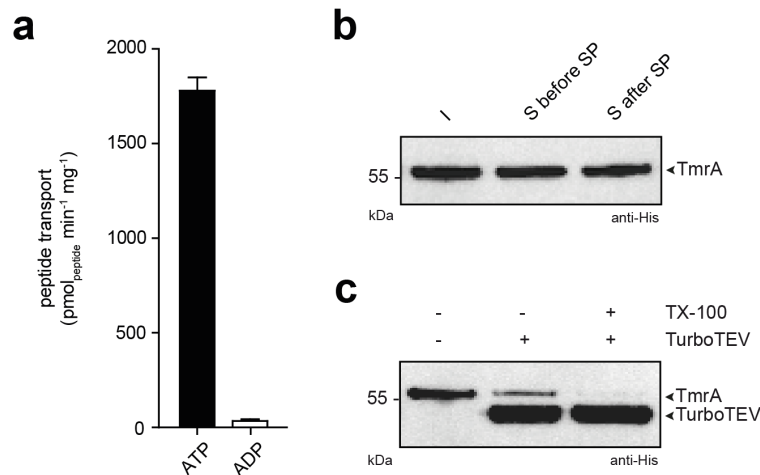


Figure 23: **TmrAB in proteoliposomes transports peptide substrates.** **a**, Substrate translocation of TmrAB in proteoliposomes composed of *E. coli* polar lipids/DOPC (7:3). 50 μ g proteoliposomes were incubated with 1 μ M C4F peptide (RRY^FCKSTEL), 3 mM MgCl₂, and 3 mM ATP (black bar) or 3 mM ADP (white bar). Transport was measured for 5 min at 68 °C. Data were measured in triplicates. Error bars indicate SD. **b**, Re-solubilization of TmrAB with 1% β -DDM for 1 h at 4 °C. Input (I): TmrAB proteoliposomes prior to addition of β -DDM. Supernatant before spin down (S before SP): Sample after incubation with 1% β -DDM for 1 h at 4 °C. Supernatant after spin down (S after SP): Sample after centrifugation for 30 min at 270,000 x g. **c**, TEV cleavage of His₁₀-tag of TmrA in proteoliposomes. Proteoliposomes were incubated with TEV protease in a 10:1 ratio at 4 °C overnight. Control sample was treated with 1% TX-100.

In summary, purified TmrAB was catalytically active, showing turnover numbers in the range of previously published data.

8.2.2 Generation of antibodies to trap selected functional states of TmrAB

For antibody selection, a catalytically inactive double cysteine variant of TmrAB (TmrA^{C416A, E523Q, S527C}B^{S503C}) was utilized to enrich synthetic antibodies/nanobodies against a conformation different from the inward-facing state. This construct harbors two serine to cysteine mutations at positions 527 (TmrA) and 503 (TmrB), which allow for disulfide cross-linking within the D-loop of the NBDs to induce NBD dimerization. Solubilization and purification of TmrA^{C416A, E523Q,}

S527C_B^{S503C} was performed in presence of 1 mM β-mercaptoethanol to prevent oxidation. Oxidative cysteine cross-linking was induced by a buffer exchange to SEC buffer without reducing agent. SDS-PAGE analysis revealed a cross-link efficiency of ~70% (Figure 24).

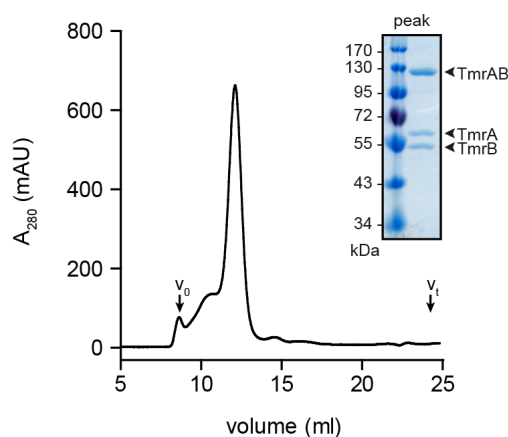


Figure 24: **Purification of TmrA^{C416A, E523Q, S527C}B^{S503C}**. Double cysteine cross-link formation of TmrA^{C416A, E523Q, S527C}B^{S503C} was induced by buffer exchange to SEC buffer without reducing agent *via* SEC. Column: Superdex™ 200 Increase 10/300 GL (GE Healthcare). Void and total column volume are indicated by v_0 and v_t , respectively. The peak fraction was analyzed by a Coomassie-stained SDS-PAGE gel. Single subunits and cross-linked TmrAB are indicated.

8.2.2.1 Selection of synthetic antibodies

The selection of synthetic antibodies was performed as described previously. Biotinylated TmrA^{C416A, E523Q, S527C}B^{S503C} was immobilized on streptavidin-coated beads *via* EZ-Link™ NHS-PEG4-Biotin. A pull-down experiment revealed a labeling efficiency of 30% (Figure 25).

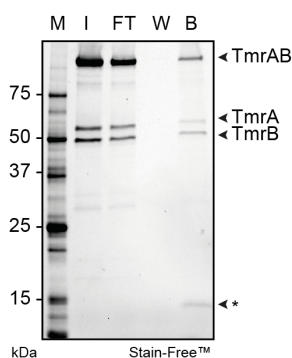


Figure 25: **Immobilization efficiency of TmrA^{C416A, E523Q, S527C}B^{S503C}**. Biotinylated TmrA^{C416A, E523Q, S527C}B^{S503C} was incubated for 1 h at 4 °C with streptavidin-coated magnetic beads. Unbound TmrA^{C416A, E523Q, S527C}B^{S503C} was removed by several washing steps. Beads were resuspended in 1x SDS sample buffer. M: marker; I: input; FT: flow-through; W: wash; B: beads. *: streptavidin.

Five rounds of phage-displayed library sorting were performed with gradually decreased TmrA^{C416A, E523Q, S527C}B^{S503C} concentrations (500 nM to 30 nM). To enrich synthetic antibodies against conformations different from the apo state, 5 mM MgCl₂ and 5 mM AMP-PNP were added throughout the whole selection procedure. By comparing the number of eluted phages, a 15-fold enrichment upon the 5th round of library sorting was observed (Figure 26).

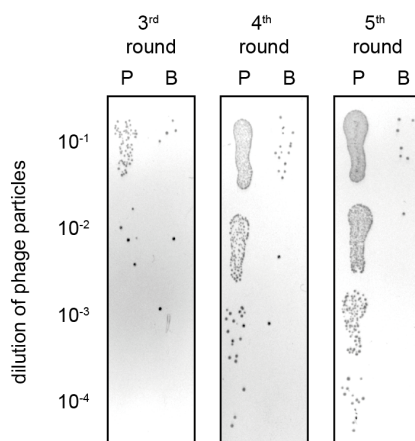


Figure 26: **Enrichment of eluted phage particles after round 3 to 5 of phage-displayed library sorting against TmrA^{C416A, E523Q, S527C}B^{S503C}.** After each sorting round, *E. coli* XL-1 cells were infected with eluted phage particles and plated in serial dilutions on LB agar plates supplemented with ampicillin. By comparing the number of colonies of either the TmrA^{C416A, E523Q, S527C}B^{S503C}-containing sample (P:protein) or beads only (B: beads; indicator for stickiness of eluted phage particles) after each round, enrichment was determined.

After sorting, 96 individual clones from round three to five were picked and phages were produced in *E. coli* XL-1 cells to perform single-point phage ELISAs. The majority of single clones bound specific to TmrA^{C416A, E523Q, S527C}B^{S503C} upon round four (Figure 27). Based on these data, the DNA of 73 clones was isolated, amplified, and sequenced, resulting in 17 unique antibodies.

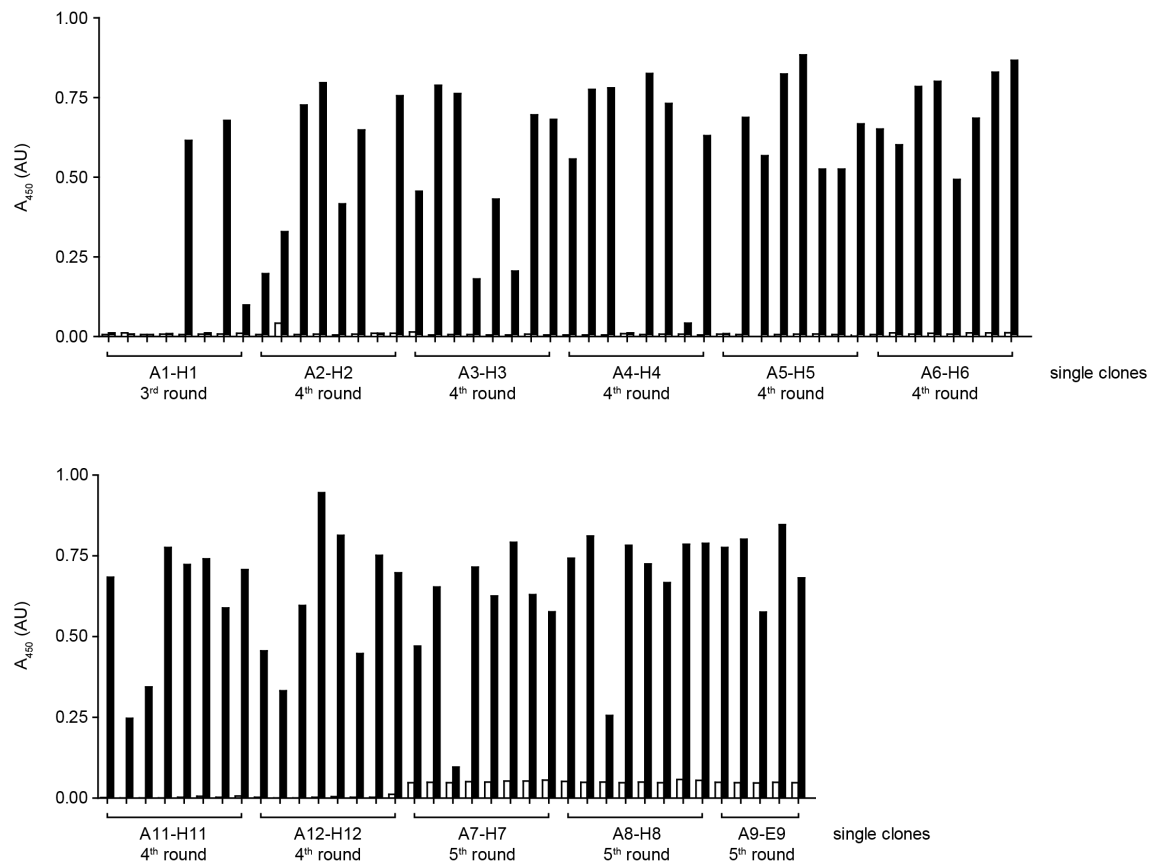


Figure 27: **Specificity of putative TmrA^{C416A, E523Q, S527C}B^{S503C}-binding single clones tested by phage ELISA.** Phages amplified and produced in *E. coli* XL-1 cells were added to neutravidin-captured biotinylated TmrA^{C416A, E523Q, S527C}B^{S503C} (20 nM, black bars). Bound phages were detected with an anti-phage antibody directed against filamentous M13 phages. As negative control, phages were incubated with neutravidin only (white bars). Bars (black/white) indicate single measurements.

To characterize the TmrAB-antibody interaction, six synthetic antibodies were produced and purified in a large scale, yielding milligram quantities of >99% pure antibody. All six synthetic antibodies formed stable stoichiometric TmrA^{C416A, E523Q, S527C}B^{S503C}/antibody complexes, which could be isolated by SEC (Figure 28). Importantly, although Mg²⁺ and AMP-PNP were added during selection and single clone screening, all antibodies bound TmrAB without the addition of any ligand. To test whether antibody binding is specific for TmrA^{C416A, E523Q, S527C}B^{S503C}, the shift assay was repeated using TmrAB^{WT}. All six synthetic antibodies formed stable complexes with TmrAB^{WT} (data not shown). Collectively, these results show the generation of TmrAB-specific high-affinity antibodies, but suggest that antibody binding is either not conformation-specific or that the antibodies were raised against the 30% un-crosslinked TmrAB in the inward-facing state.

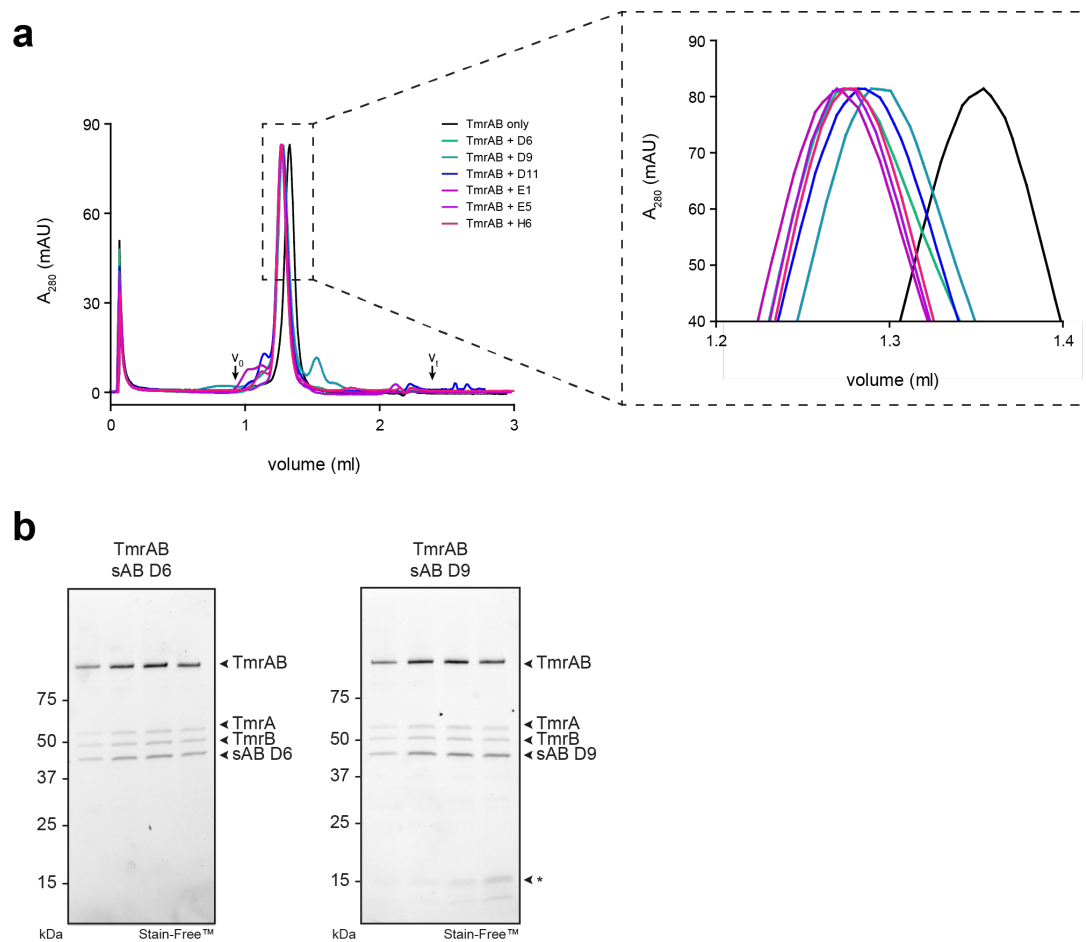


Figure 28: **Synthetic antibodies form stable complexes with TmrA^{C416A, E523Q, S527C}B^{S503C}**. **a**, Isolation of TmrAB/sAB complexes by SEC. Prior to gel filtration, synthetic antibodies were added to TmrAB in a 1.25-fold molar excess and incubated for 15 min on ice. Column: Superdex™ 200 Increase 3.2/300 (GE Healthcare). Void and total column volume are indicated by V_0 and V_t , respectively. In order to illustrate stoichiometric binding, data were normalized to the TmrAB run without sAB (*TmrAB only*). **b**, Representative SDS-PAGE gels of TmrAB/sAB complexes isolated by SEC.

8.2.2.2 Selection of nanobodies

Nanobodies were selected by phage-displayed library sorting against neutravidin-captured biotinylated TmrA^{C416A, E523Q, S527C}B^{S503C} in β -DDM or TmrA^{C416A, E523Q, S527C}B^{S503C} proteoliposomes (20 nM). In contrast to the previously described selection of synthetic antibodies, ATP instead of the non-hydrolysable ATP analogue AMP-PNP was added throughout the nanobody selection procedure. Upon two rounds of library sorting, a strong enrichment (>1000-fold) of putative TmrA^{C416A, E523Q, S527C}B^{S503C}-binding nanobodies was achieved. By phage ELISA, 144 single clones were analyzed to screen for putative TmrA^{C416A, E523Q, S527C}B^{S503C}-binding clones (Figure 29). Especially for proteoliposomes, the majority of single clones bound specific to TmrA^{C416A, E523Q, S527C}B^{S503C} (Figure 29b).

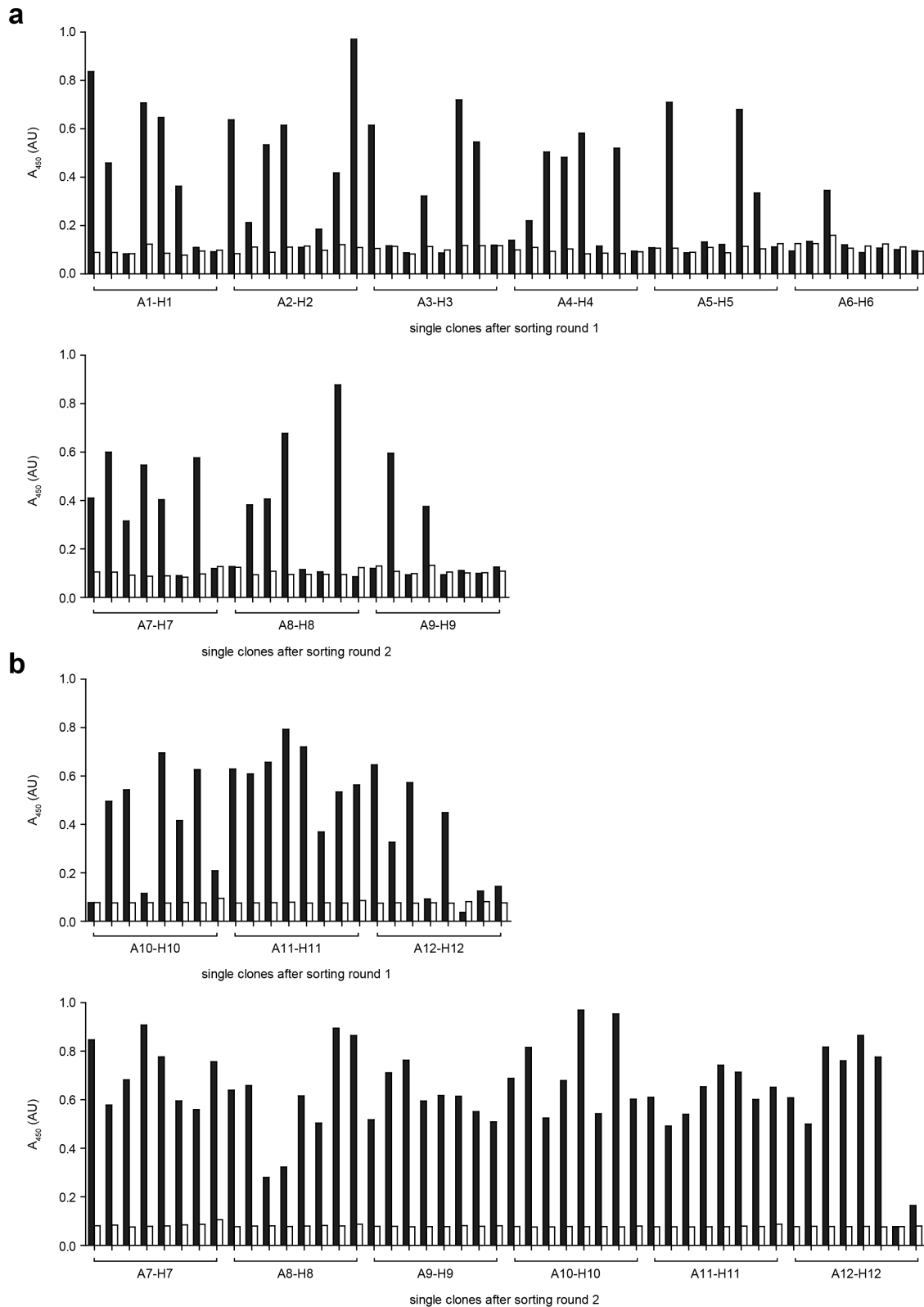


Figure 29: **Specificity of putative TmrA^{C416A, E523Q, S527CB5503C}-binding single clones tested by phage ELISA.** The periplasmic extract (PE) of nanobody-producing *E. coli* cells (1:5 dilution) was added to neutravidin-captured biotinylated TEV-treated TmrA^{C416A, E523Q, S527CB5503C} (20 nM, black bars). For detection of bound nanobody, an anti-His antibody (1:3,000) was added followed by an anti-mouse antibody, which was conjugated to alkaline phosphatase (1:10,000). As negative control, PE was incubated with neutravidin only (white bars). Bars (black/white) indicate single measurements. **a**, TmrAB in β -DDM. **b**, TmrAB proteoliposomes.

Based on the ELISA results, the DNA of 80 clones was PCR-amplified and sequenced, resulting in 53 unique nanobody clones. These 53 nanobody clones were classified into 12 nanobody families (by definition, nanobodies from the same family derive from the same B-cell lineage and, thus, bind to the same epitope on the antigen (126)). For further analysis of the TmrAB/nanobody interaction (Figure 30), ten single clones were produced and purified in a large scale (nanobodies 265, 268, 269, 272, 293, 294, 295, 296, 299, and 300). All ten nanobodies bound specific to TmrAB (Figure 30a) and formed stable TmrAB/nanobody complexes (Figure 30c). Additionally, by immunoblotting utilizing the purified nanobodies as detection reagents the epitope was narrowed down to either the A (nanobody 268) or B (nanobody 272, 293, 295, 296, 299, and 300) subunit (Figure 30b). Interestingly, nanobodies 265, 269, and 294 recognized both subunits. For nanobodies 268, 296, and 300, binding affinities were determined using the *switchSENSE* technology. *Via* an amine coupling kit, nanobodies were conjugated with single-stranded DNA nanolevers and immobilized on the chip surface (147, 186). For all three nanobodies, affinities in the low nanomolar range were determined (Nb268: 1.3 ± 0.1 nM, Nb296: 2.7 ± 0.1 nM, Nb300: 2.1 ± 0.1 nM; exemplarily shown for Nb296 in Figure 30d). Collectively, these results demonstrate the generation of specific, high-affinity anti-TmrAB nanobodies.

However, all purified nanobodies bound to the same extent to TmrA^{C416A, E523Q, S527C}B^{S503C} (with and without addition of ATP-Mg²⁺) and TmrAB^{WT}. Just like in case of the synthetic antibodies, these results indicate that nanobody binding is either not conformation-specific or both variants represent the inward-facing state.

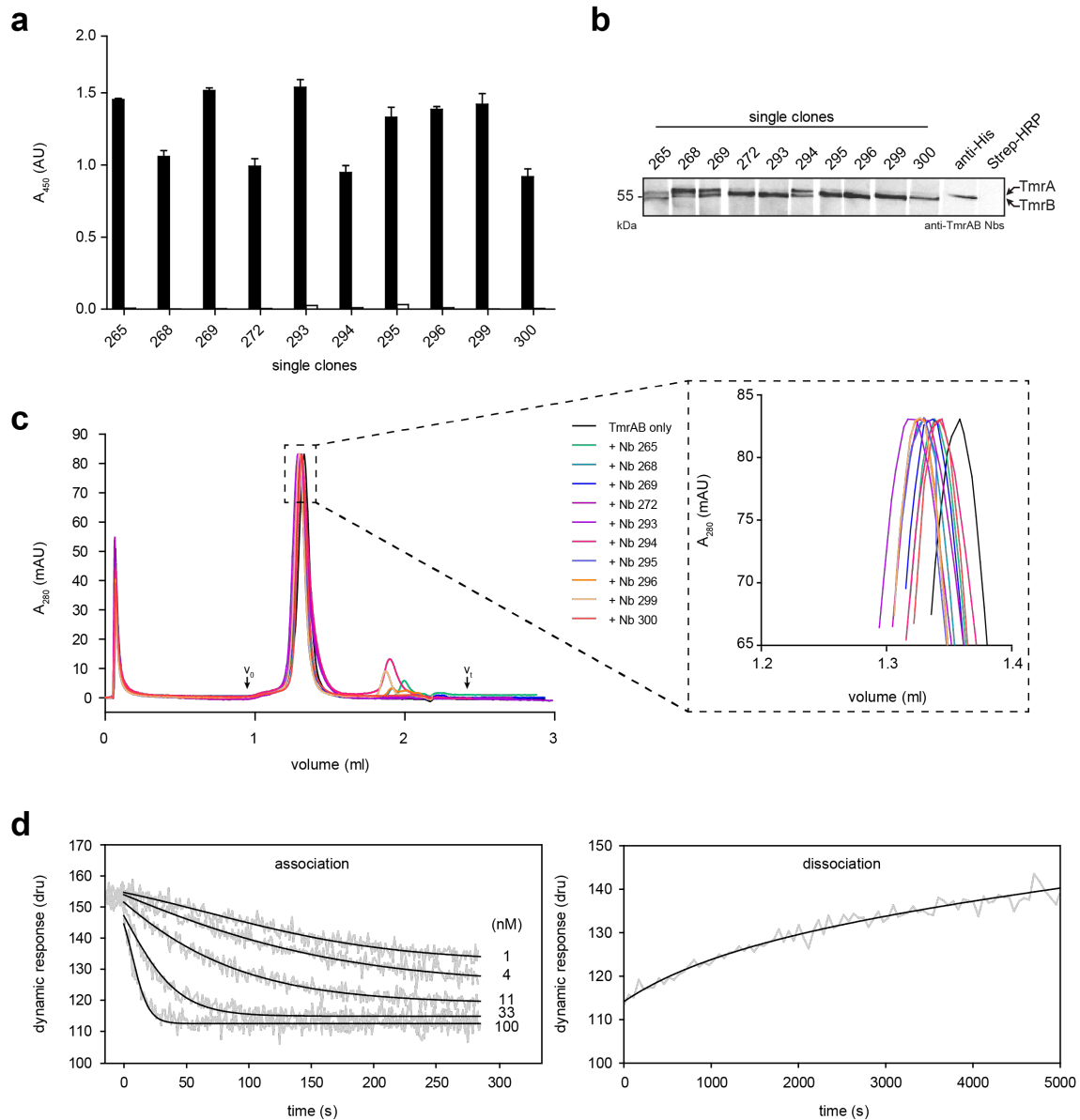


Figure 30: Characterization of anti-TmrAB nanobodies. **a**, Specific binding of nanobodies to TmrAB shown by ELISA. 1 μ M of nanobody were added to neutravidin-captured biotinylated TEV-treated TmrAB (20 nM, black bars) and incubated for 1 h at 4 $^{\circ}$ C. For detection, an anti-His antibody (mouse, 1:3,000 dilution) and an anti-mouse HRP conjugate (1:10,000 dilution) were added successively and incubated for 1 h at 4 $^{\circ}$ C each. Protein samples were measured in triplicates. White bars represent background binding. **b**, Immunoblot analysis using nanobodies as detection reagents. For detection (1 μ g TmrAB per lane), 1 μ g/ml nanobody was added and incubated for 1 h at 4 $^{\circ}$ C. Next, a CaptureSelectTM Biotin anti-C-tag conjugate (Life technologies)/HRP-conjugated streptavidin (Thermo Scientific) mixture (1:1 ratio, 1:4,000 dilution) was added to detect bound nanobodies. **c**, TmrAB/nanobody complex formation. TmrAB was incubated with a 1.25-fold molar excess of nanobody for 15 min prior to gel filtration. Column: SuperdexTM 200 Increase 3.2/300 (GE Healthcare). Void and total volume are indicated by V_0 and V_t , respectively. In order to illustrate stoichiometric binding, data were normalized to the TmrAB run without nanobody (*TmrAB only*). **d**, Binding of Nb 296 to TmrAB determined by *switchSENSE*.

8.2.3 Structural analysis of TmrAB by single-particle cryo-EM

To explore the entire trajectory of conformational rearrangements TmrAB undergoes during substrate translocation by cryo-EM, various environments were tested with regards to TmrAB stability, functionality, and homogeneity. First, SEC-purified TmrAB in β -DDM was subjected to negative-stain EM analysis to gain insights about the overall quality of the sample (Figure 31). Unprocessed EM micrographs of negatively-stained β -DDM-solubilized TmrAB clearly showed individual particles in one preferred orientation. 2D class averaging revealed TmrAB in one distinct conformation, with the NBDs well separated, which is referred to as the inward-facing state (IF) and is consistent with previously published EM micrographs of TmrAB (14).

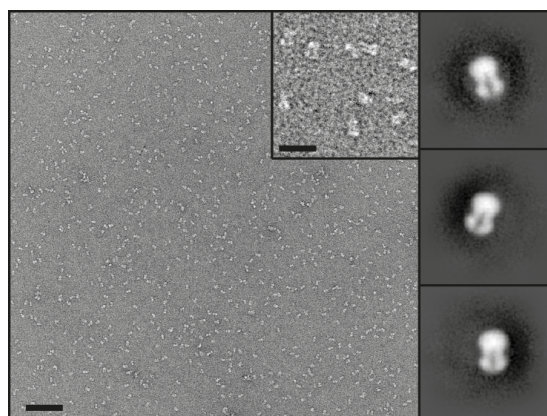


Figure 31: **Negative-stain EM analysis of TmrAB in β -DDM.** Representative micrograph and 2D class averages. Micrographs were collected on a Tecnai-Spirit transmission electron microscope (Thermo Fisher, former FEI), operated at 120 kV and equipped with a Gatan 4x4k CCD camera. Scale bar for original micrograph: 100 nm. Scale bar for inset (4x4 magnified): 25 nm. (Electron microscopy was performed in collaboration with the Kühlbrandt laboratory, Department of Structural Biology, Max Planck Institute of Biophysics, Frankfurt).

However, when performing single-particle cryo-EM with detergent-solubilized proteins, the presence of an excess of detergent micelles might create severe background noise and affects the surface tension of the thin buffer film, which is vitrified during cryo-EM sample preparation (187). To overcome this limitation and to allow for the investigation of TmrAB function in a native-like lipid environment, TmrAB was reconstituted into the following scaffold proteins: saposin A, MSP1D1, and MSP2N2. TmrAB:scaffold protein:lipid ratios were systematically screened. For reconstitution, TmrAB was mixed with bovine brain lipids and the respective scaffold protein, followed by detergent exchange *via* rapid dilution and addition of polystyrene beads, respectively. Reconstituted TmrAB enclosed by two or more copies of scaffold protein was separated from lipid-only particles by SEC, resulting in a monodisperse and homogenous sample for EM imaging (Figure 32).

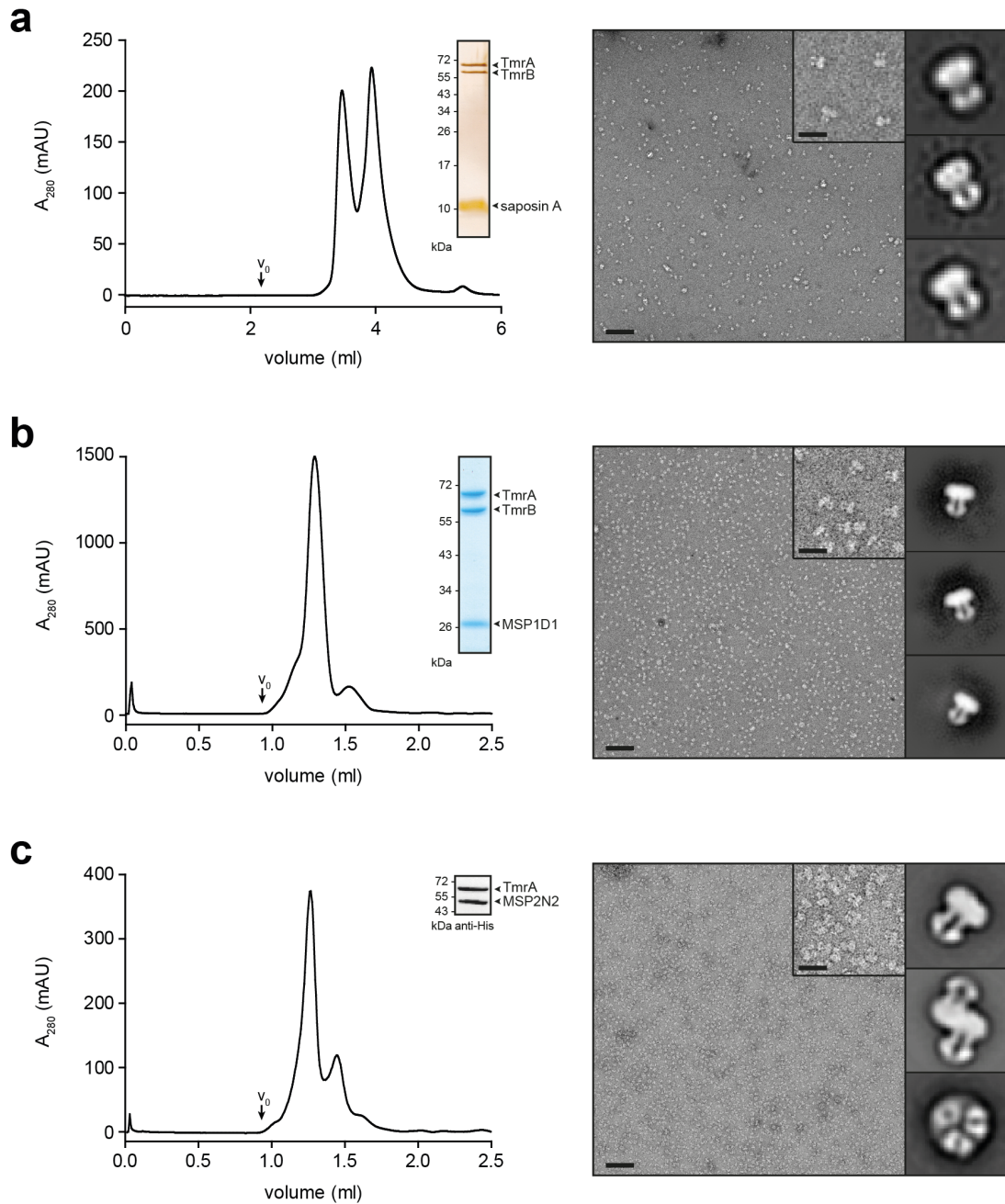


Figure 32: **Negative-stain EM analysis of reconstituted TmrAB.** **a**, Reconstitution of TmrAB into saposin A-enclosed discs. Reconstituted TmrAB (front peak) was separated from lipid-only discs (2nd peak) by SEC, as confirmed by a silver-stained SDS-PAGE gel. Column: KW404-4F (Shodex). Void volume is indicated by v_0 . The peak fraction (front) was applied to glow discharged carbon-coated grids and stained with 2% uranyl formate. Micrographs were collected on a Tecnai-Spirit transmission electron microscope (Thermo Fisher, former FEI), operated at 120 kV and equipped with a Gatan 4x4k CCD camera. A representative micrograph with corresponding 2D class averages of negatively-stained TmrAB/saposin A-discs is shown. Scale bar for original micrograph: 100 nm. Scale bar for inlet (4x magnified): 25 nm. **b**, Reconstitution of TmrAB into small (MSP1D1) nanodiscs. Column: Superdex™ Increase 3.2/300 (GE Healthcare). Void volume is indicated by v_0 . Peak fraction was analyzed by a Coomassie-stained SDS-PAGE gel. **c**, Reconstitution of TmrAB into large (MSP2N2) nanodiscs. Column: Superdex™ Increase 3.2/300 (GE Healthcare). Void volume is indicated by v_0 . Peak fraction was analyzed by immunoblotting. (Electron microscopy was performed in collaboration with the Kühlbrandt laboratory, Department of Structural Biology, Max Planck Institute of Biophysics, Frankfurt).

Negative-stain EM analysis confirmed the assembly of disk-like particles. 2D class averaging verified the insertion of one transport complex per disc for saposin A (Figure 32a) and MSP1D1 (Figure 32b). Due to the large diameter of roughly 17 nm, MSP2N2-discs were shown to accommodate one, two, or even three transport complexes per disc (Figure 32c). Based on these results and the overall sample quality, all further cryo-EM samples were prepared using MSP1D1 as scaffold protein.

Besides sample homogeneity, TmrAB function upon reconstitution was investigated and compared to detergent-solubilized protein. Using a radioactive assay, release of inorganic phosphate (P_i) from ATP at 68 °C over a time span of 20 min was monitored, yielding the same ATPase activity for reconstituted (either scaffold) and detergent-solubilized protein, while an ATPase-deficient transport complex harboring the E523Q mutation did not show any hydrolysis activity (Figure 33).

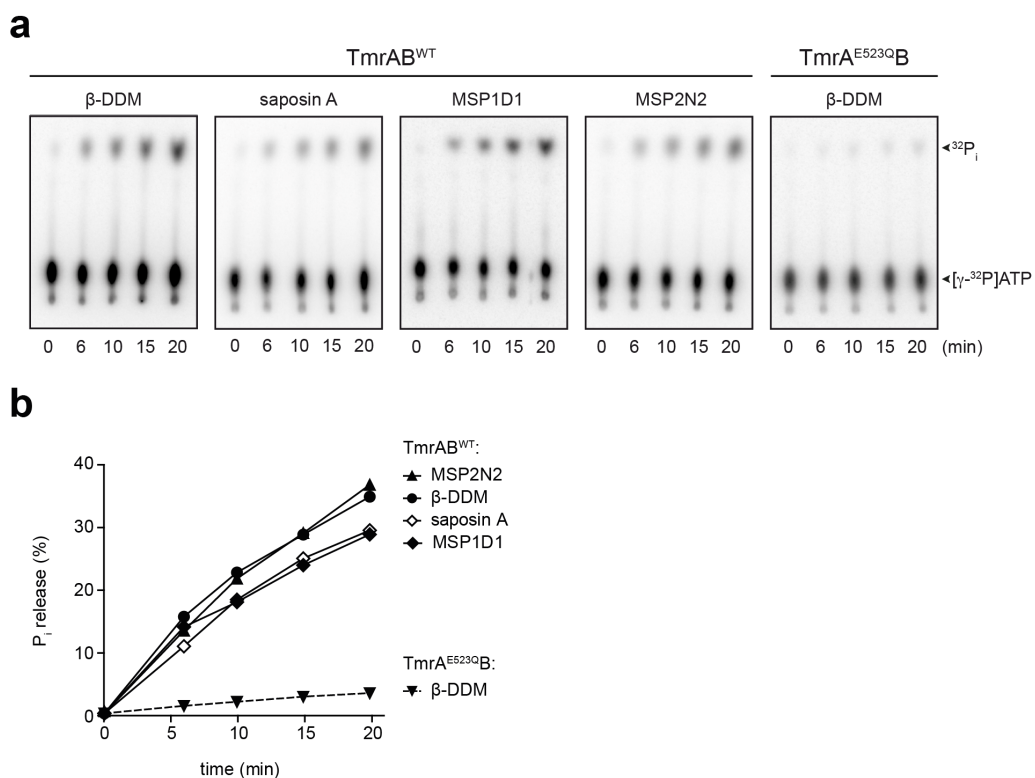


Figure 33: **ATPase activity of TmrAB in nanodiscs.** **a**, ATPase activity of TmrAB (200 nM; in β-DDM or reconstituted) in the presence of 3 mM MgCl₂ and 1 mM ATP (supplemented with tracer amounts of [γ-³²P]ATP) measured for 20 min at 68 °C. Reaction mixtures were analyzed by thin layer chromatography on polyethyleneimine cellulose. **b**, Kinetic data from **(a)** were blotted. The ATPase activity of detergent-solubilized TmrAB^{WT} was normalized to 100%.

Recent technological breakthroughs in the field of single-particle cryo-EM have enabled structure determination of medium-sized membrane proteins at resolutions between 3.3 and 4.0 Å (16, 34, 40, 41). However, due to its pseudo-symmetric domain organization, structure determination of TmrAB is technically challenging. Therefore, synthetic antibodies and nanobodies were selected to be used as fiducial markers and, furthermore, to trap TmrAB in distinct functional states. Negative-stain EM analysis of TmrAB/sAB and TmrAB/Nb complexes yielded 2D class averages, which clearly showed the antibody bound to TmrAB (Figure 34). Especially 2D class averages of TmrAB/sAB complexes revealed characteristic features of Fabs (Figure 34a-b). Unexpectedly, further analysis led to the conclusion that binding of synthetic antibodies and nanobodies occurs state-specific, but for the inward-facing state. Upon antibody binding, conformational transitions to the outward-facing conformation were impeded. Conversely, upon trapping of TmrAB in the outward-facing state, antibody binding was disabled (data not shown).

Based on these results, the nanobody selection was repeated by Benedikt Kuhn (Geertsma laboratory, Institute of Biochemistry, Goethe-University, Frankfurt) and Stefan Brüchert (Tampé laboratory, Institute of Biochemistry, Goethe-University, Frankfurt). Briefly, MNG-3-solubilized TmrAB was used for alpaca immunization. Upon two rounds of phage-displayed library sorting using neutravidin-captured biotinylated TmrAB, nanobody 9F10 was identified, which forms a rigid complex with the NBD of TmrB, independent of the respective conformational state (Figure 34d-f). Nanobody 9F10 was therefore used as alignment tool for cryo-EM of TmrAB.

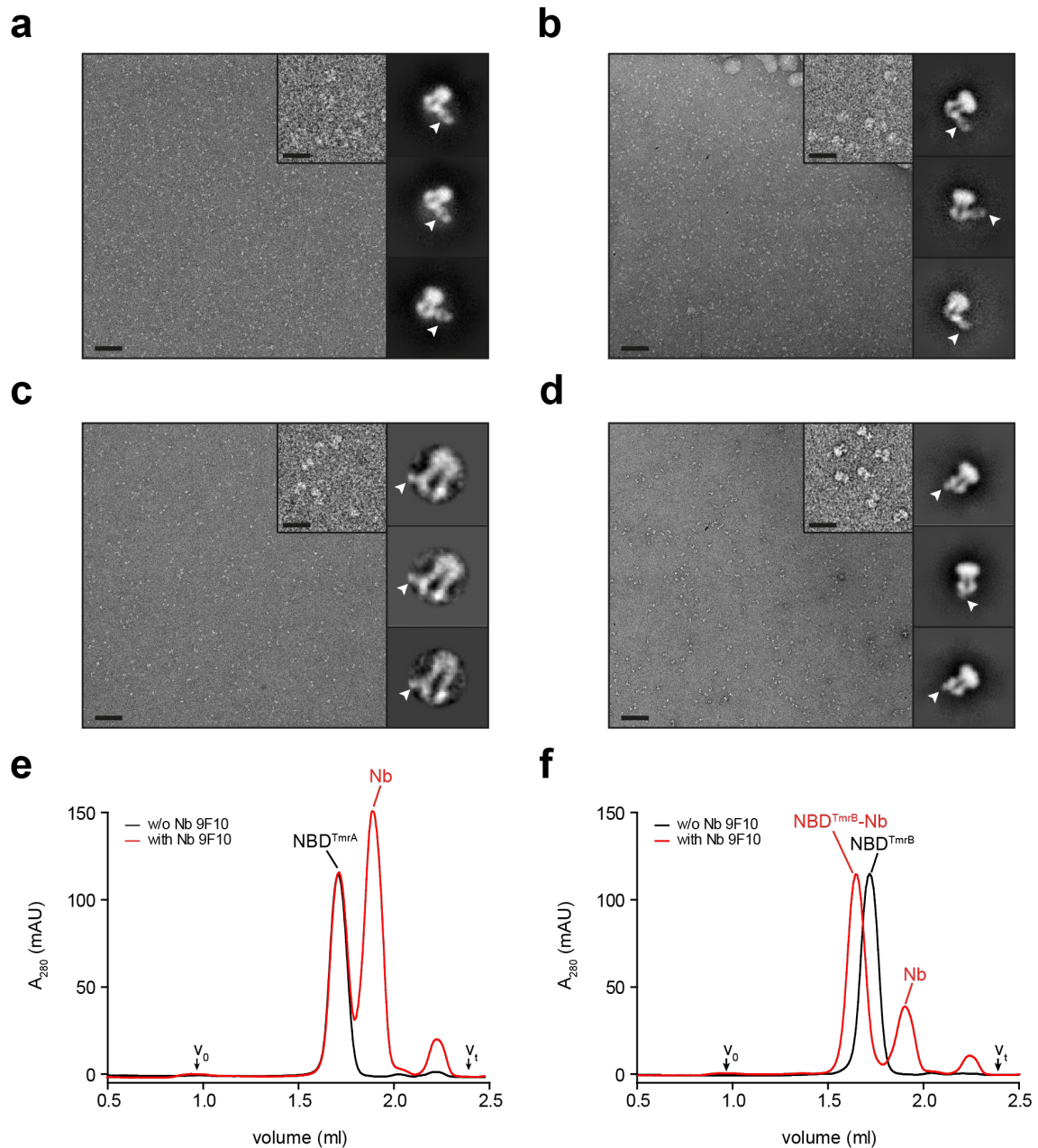


Figure 34: Antibodies as fiducial marker proteins. **a-d**, Representative negative-stain micrographs and 2D class averages of TmrAB/antibody complexes. TmrAB/antibody complexes were isolated by SEC and applied to glow discharged carbon-coated grids and stained with 2% uranyl formate. Micrographs were collected on a Tecnai-Spirit transmission electron microscope (Thermo Fisher, former FEI), operated at 120 kV and equipped with a Gatan 4x4k CCD camera. Bound antibodies are indicated by a white arrowhead. Scale bar for original micrograph: 100 nm. Scale bar for inlet (4x4 magnified): 25 nm. **a**, sAB D9. **b**, sAB D11. **c**, Nb 268. **d**, Nb 9F10 (provided by Stefan Brüchert (Tampé laboratory, Institute of Biochemistry, Goethe-University, Frankfurt) and Benedikt Kuhn (Geertsma laboratory, Institute of Biochemistry, Goethe-University, Frankfurt)). **e-f**, Nb 9F10/NBD complex formation. TmrAB NBDs were incubated with a 1.25-fold molar excess of Nb 9F10 for 15 min on ice prior to gel filtration. Column: Superdex™ 200 Increase 3.2/300 (GE Healthcare). Void and total volume are indicated by v_0 and v_t , respectively. In order to illustrate stoichiometric binding and monodispersity, data were normalized to NBD of TmrA. **e**, NBD of TmrA. **f**, NBD of TmrB. NBD^{TmrA}-/NBD^{TmrB}-encoding plasmids were provided by Benedikt Kuhn (Geertsma laboratory, Institute of Biochemistry, Goethe-University, Frankfurt). (Electron microscopy was performed in collaboration with the Kühlbrandt laboratory, Department of Structural Biology, Max Planck Institute of Biophysics, Frankfurt).

In order to map the conformational space of TmrAB under turnover conditions by cryo-EM, the nanodisc-embedded TmrAB^{WT}/Nb complex was isolated *via* SEC and incubated with ATP-Mg²⁺ and substrate to initiate the translocation cycle (6 mM MgCl₂, 5 mM ATP, 50 μM C4F peptide, 1 min incubation at 45 °C). All EM work shown and discussed in this chapter was performed in collaboration with Arne Möller and Dovile Janulienė (Möller laboratory, Department of Structural Biology, Max Planck Institute of Biophysics, Frankfurt). Cryo-EM analysis of lipid-embedded TmrAB^{WT} under turnover conditions (TmrAB_{turnover}) provided a comprehensive view onto the conformational flexibility of the translocation complex and revealed two major populations, captured simultaneously on a single EM-object carrier (Figure 35). One population (~50%) comprised inward-facing (IF) conformations with clearly separated NBDs, while the second major population (~50%) of particles showed NBD-dimerized conformations.



Figure 35: **Cryo-EM analysis of nanodisc-embedded TmrAB^{WT} under turnover conditions.** Representative cryomicrograph and 2D class averages showing different conformational states of TmrAB_{turnover}. Scale bar: 100 nm. (Cryo-EM data collection and analysis were performed by Arne Möller and Dovile Janulienė (Möller laboratory, Department of Structural Biology, Max Planck Institute of Biophysics, Frankfurt)).

8.2.3.1 Conformational plasticity in IF conformations

Upon 3D classification, the IF particles were separated into two distinct conformations (IF^{narrow} and IF^{wide}), which displayed an uncoupled movement of TMDs and NBDs (Figure 36, Figure 47). While the inter-NBD distance of both conformations changed only marginally, transmembrane helix six (TM6) of both subunits swings out to open the intracellular gate by 4.4 Å, thereby dilating the cavity from 4,650 to 5,900 Å³ in IF^{wide} (corresponding to the volume of about 40 additional water molecules) (Figure 36c). Both IF conformations show nucleotides at the binding sites; however, the occupancy by ADP or ATP could not be defined due to the free nucleotide exchange. To elucidate the impact of substrate binding onto conformational rearrangements of TmrAB, a 3D classification of all IF particles focused on the TMDs was performed. Intriguingly, a weak additional density close to residues M139^{TmrB}, D184^{TmrB}, H246^{TmrB}, and W297^{TmrB} was observed in IF^{wide}, which displayed a wider opening of the intracellular gate, indicating the presence of substrate (Figure 36d). No such density was found for IF^{narrow}, where, due to the inward movement of TM6, the smaller volume of the cavity prevents binding of bulky substrates. In order to investigate the involvement of these residues in specific substrate interactions, a mutational analysis was performed. Mutation of M139^{TmrB} and W297^{TmrB} into alanine led to a strong reduction in substrate binding in comparison to wild-type TmrAB (Figure 36e). In contrast, the H246^{TmrB} alanine mutant displayed a similar activity as wild-type TmrAB, in accordance to previously published data (15). Substitution of both residues (M139/W297^{TmrB} double mutant) reduced the activity by 90%, indicating a synergistic effect. A direct involvement of M139^{TmrB} and W297^{TmrB} in substrate binding was further confirmed by substrate translocation studies (Figure 36f). Transport kinetics of wild-type and M139/W297^{TmrB} revealed a K_m value of $6.0 \pm 2.3 \mu\text{M}$ and $>40 \mu\text{M}$, respectively. To exclude a folding or assembly defect of the double mutant, purified M139/W297^{TmrB} was subjected to negative-stain EM analysis. No differences regarding complex assembly, stability and homogeneity were observed in comparison to wild-type TmrAB (Figure 36g). In accordance, a significant extra density was found at the same position in a control experiment with a ten-fold higher substrate concentration (500 μM C4F peptide), but was absent in a cryo-EM experiment without addition of any ligand (data not shown). The equal occurrence of two distinct IF conformations in the 500 μM C4F (TmrAB_{C4F}) and apo control (TmrAB_{apo}) experiments and the observation that significant extra density was found in IF^{wide} only indicates that substrate binding is conformation specific, but does not induce a conformational change.

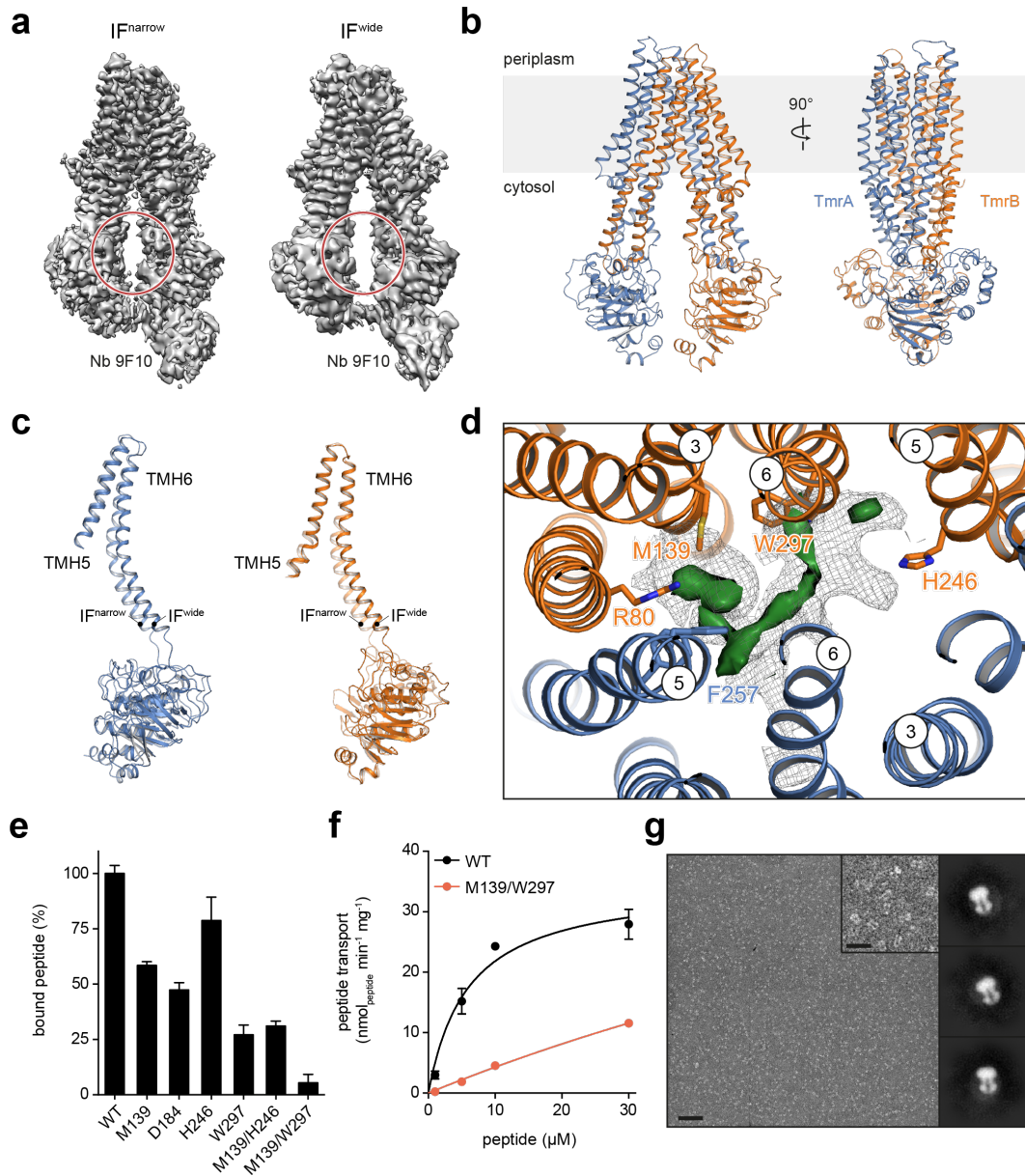


Figure 36: Conformational plasticity in IF conformations translates to substrate binding. **a**, Cryo-EM density maps of IF TmrAB_{turnover} filtered to a resolution of 3.8 Å (IF^{narrow}) and 4.2 Å (IF^{wide}), respectively. **b**, IF^{wide} (cartoon representation) viewed from within the plane of the membrane. **c**, The flexibility of TM6 is illustrated by individual superposition of TmrA (A258-R594, blue) and TmrB (A237-K574, orange) in IF^{narrow} and IF^{wide}. **d**, Focused top view around TM5^{TmrA} and TM3/TM5/TM6^{TmrB} with cryo-EM density (grey mesh) and positive difference density (green surface) in the binding site of IF^{wide} (TmrAB_{C4F}), as also identified in TmrAB_{turnover}, but not in TmrAB_{apo}. Nearby residues are depicted as sticks colored by heteroatoms. Color scheme as in (c). **e**, Impact of alanine substitutions onto substrate binding. TmrAB (2 μM) was incubated with C4F peptide (RRY^FCKSTEL; 50 nM) for 15 min on ice. Fluorescence anisotropy was measured at λ_{ex/em}=485/520 nm. Data were measured in triplicates. All data are given as mean ± SD. (M139^{TmrB-}, H246^{TmrB-}, W297^{TmrB-}, M139/H246^{TmrB}, and M139/W297^{TmrB-}-encoding plasmids were kindly provided by Stefan Brüchert (Tampé laboratory, Institute of Biochemistry, Goethe-University, Frankfurt)). **f**, Transport kinetics of TmrAB wild-type and double alanine mutant. 50 μg TmrAB-containing proteoliposomes (wild-type: black curve, M139/W297^{TmrB} mutant: red curve) were incubated with 1, 5, 10 and 30 μM C4F peptide (RRY^FCKSTEL), 3 mM MgCl₂ and 3 mM ATP. Transport was analyzed for 6 min at 68 °C. Data were measured in triplicates. All data are given as mean ± SD. **g**, TmrAB double alanine mutant (M139/W297^{TmrB}) was applied to glow discharged carbon-coated grids

and stained with 2% uranyl formate. Micrographs were collected on a Tecnai-Spirit transmission electron microscope (Thermo Fisher, former FEI), operated at 120 kV and equipped with a Gatan 4x4k CCD camera. Scale bar for original micrograph: 100 nm. Scale bar for inlet (4x4 magnified): 25 nm. (Cryo-EM data collection and analysis were performed by Arne Möller and Dovile Janulienė (Möller laboratory, Department of Structural Biology, Max Planck Institute of Biophysics, Frankfurt). Initial models were prepared by Ahmad Reza Mehdipour (Hummer laboratory, Department of Theoretical Biophysics, Max Planck Institute of Biophysics, Frankfurt). Final models were provided by Christoph Thomas (Tampé laboratory, Institute of Biochemistry, Goethe-University, Frankfurt)).

8.2.3.2 ATP-triggered NBD dimerization induces the transition to the OF-open conformation

The NBD-dimerized conformation observed in the TmrAB_{turnover} experiment was markedly different from what was shown previously for all other structures of ABC transporters with dimerized NBDs (Figure 37a and b, Figure 47). Intriguingly, in this new asymmetric unlocked-return conformation (UR^{asym}), the intracellular gate is unlocked by a separation of TM3 and TM4 by 1.5 Å. Further sub classification revealed a second population of particles, which displayed an even wider separation of TM3 and TM4 by 3.0 Å (UR^{asym*}), indicating a progressive return to the IF conformation (Figure 37c). In UR^{asym} and UR^{asym*}, the canonical site is slightly wider breaking the two-fold pseudo-symmetric organization of the sandwiched NBD dimer and contains ADP, while ATP is still bound at the non-canonical site, demonstrating an asymmetric post-hydrolysis state (Figure 37d).

Although the opening and closure of the extracellular gate are key steps of the substrate translocation cycle, no OF-open conformations were detected in the turnover experiment, suggesting that this opening must be highly transient. In order to stabilize the OF-open state, a new cryo-EM analysis was performed using a catalytically inactive mutant of TmrAB, harboring the E523Q^{TmrA} mutation that allows ATP binding but not hydrolysis (83).

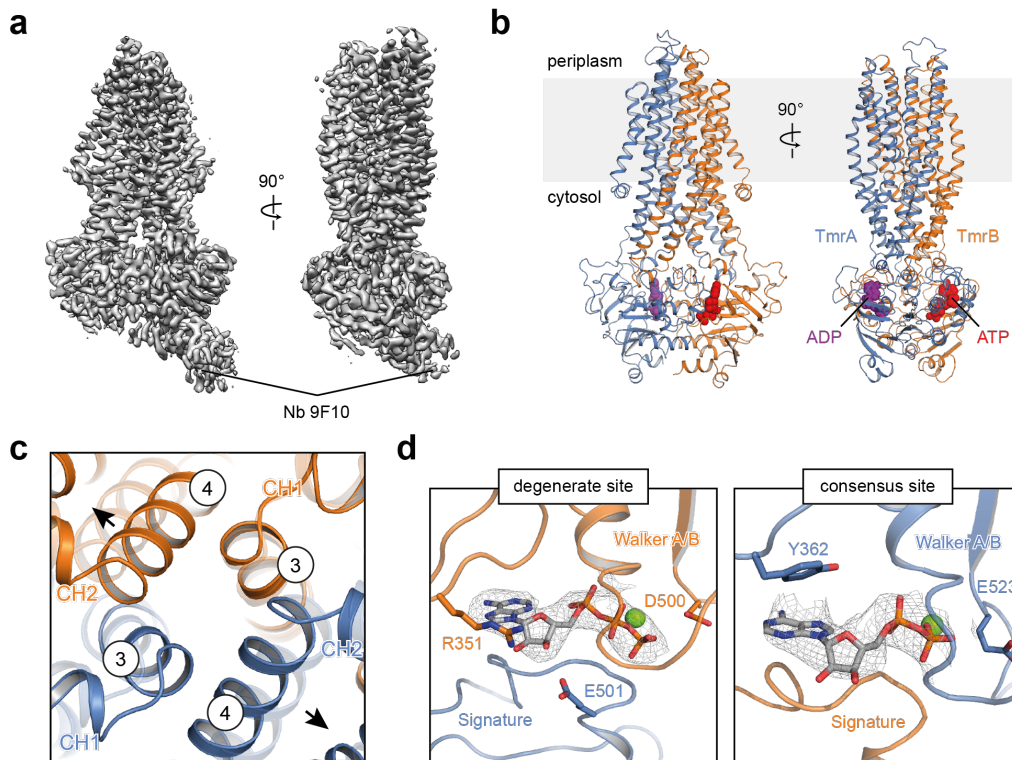


Figure 37: Asymmetric post-hydrolysis state. **a**, Cryo-EM map of UR^{asym} filtered to a resolution of 3.5 Å. **b**, Overall structure of the asymmetric post-hydrolysis state of TmrAB_{turnover} viewed from within the plane of the membrane. Color scheme as in Figure 36. **c**, After P_i release, the intracellular gate lined by TM4 and TM3 of each subunit is unlocked, forming the asymmetric turnover state UR^{asym}/UR^{asym*} (indicated by black arrows). **d**, Close-up views of the degenerate and consensus NBSs. Interacting motifs are shown in cartoon representation with selected side chains shown as sticks. The nucleotides are represented by grey sticks colored by heteroatoms. Mg²⁺ is shown as green sphere. (Cryo-EM data collection and analysis were performed by Arne Möller and Dovile Janulienė (Möller laboratory, Department of Structural Biology, Max Planck Institute of Biophysics, Frankfurt). Initial models were prepared by Ahmad Reza Mehdipour (Hummer laboratory, Department of Theoretical Biophysics, Max Planck Institute of Biophysics, Frankfurt). Final models were provided by Christoph Thomas (Tampé laboratory, Institute of Biochemistry, Goethe-University, Frankfurt)).

The nanodisc-embedded TmrA^{EQ}B/Nb complex was incubated with ATP-Mg²⁺ to lock the transporter in the ATP-bound conformation (3 mM MgCl₂, 1 mM ATP, 5 min incubation at 45 °C). Remarkably, within the same dataset, two different OF conformations were resolved, OF-open and OF-occluded, both in an ATP-bound state (Figure 38, Figure 47). 40% of the particles displayed a wide opening of the TMDs to the extracellular space, resembling an OF-open conformation (Figure 38a), which shares some similarities with the OF X-ray structures of Sav1866 (32, 33). The other 60% of the particles were found in an OF-occluded conformation (Figure 38b), which is comparable to the previously reported structure of McjD in the presence of the non-hydrolysable ATP-analog AMP-PNP, however, with a significantly smaller cavity (188).

Both maps were of sufficient quality to build a model of TmrA^{EQ}B_{ATP} in the OF-open (Figure 38c) and OF-occluded conformation (Figure 38d).

In both OF conformations (open/occluded), the NBDs are rotated towards each other to form a closed, *sandwich*-like dimer in a head-to-tail fashion (Figure 38e), as observed in previously reported nucleotide-bound structures of ABC transporters (32, 33, 35, 47, 188). The NBD dimerization is tightly coupled to reorganizations within the transmembrane region of TmrA^{EQ}B_{ATP}. Thus, the cytosolic gate is closed and the cavity accessible from the cytosol to accommodate a potential substrate is sealed. These data agree with the notion that substrate binding of TmrA^{EQ}B is impaired upon ATP-triggered NBD dimerization (Figure 38h).

Both EM maps allowed positioning of two ATP molecules occluded at the dimer interface. Each ATP molecule was shown to interact with a number of conserved motifs such as the Walker A/B motifs, which coordinate the phosphate groups, and signature motif, which aligns ATP for hydrolysis (Figure 38g). Notably, pronounced differences between the ATP coordination within the degenerate and consensus NBS were observed. Besides the presence of an aspartate residue (D500^{TmrB}) instead of a glutamate in the expected position of the catalytic base in the degenerate site, the coordination of the purine base differs strongly between both NBSs. In the consensus site, a conserved tyrosine residue of the aromatic (A)-loop (Y362^{TmrA}) makes π - π stacking contacts to the purine base of bound ATP, while in the degenerate site, the sugar moiety is positioned by R351^{TmrB} and E501^{TmrA}.

With regards to NBD dimerization and ATP binding, no difference between the OF-open and OF-occluded conformation of ATP-Mg²⁺-bound TmrA^{EQ}B was found. This observation, and the co-existence of these two conformations at nearly similar ratios in the ATP-bound state, indicates that the transporter is able to fluctuate between the different conformers (OF-open/OF-occluded) without the need of ATP hydrolysis or release.

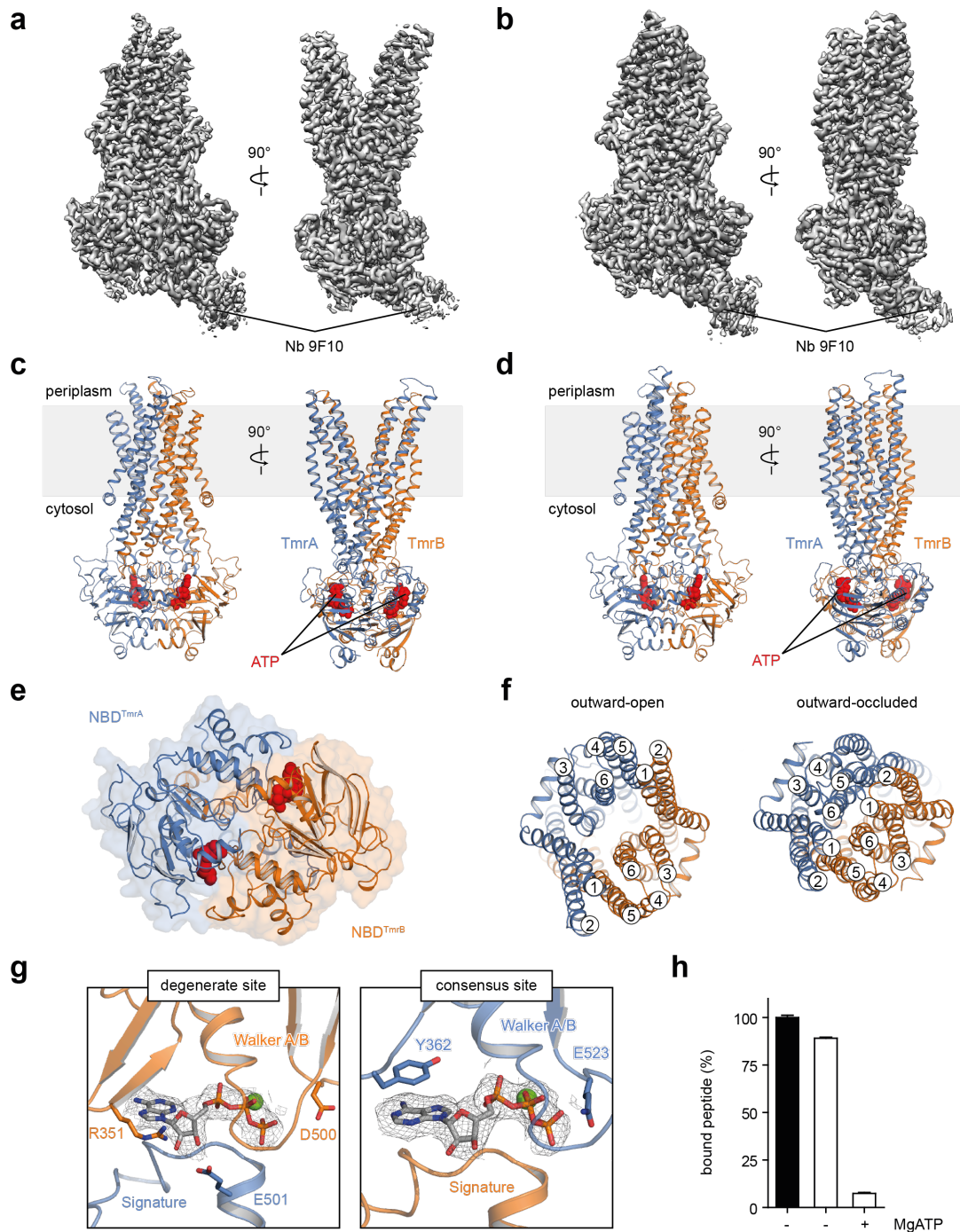


Figure 38: ATP binding induces the IF-OF-open transition. **a** and **b**, Cryo-EM map of OF-open (**a**) and OF-occluded (**b**) TmrA^{EQB}_{ATP-ADP} filtered to a resolution of 2.8 Å and 2.9 Å, respectively. **c** and **d**, Overall structure of TmrA^{EQB}_{ATP-ADP} in the OF-open (**c**) and OF-occluded (**d**) conformation viewed from within the plane of the membrane. **e**, View onto the NBD dimer of OF-occluded TmrA^{EQB}_{ATP-ADP} from the intracellular side. The NBDs are shown both as transparent surface and in cartoon representation. ATP is shown as red spheres. **f**, Extracellular view onto the TMDs of OF-open and OF-occluded TmrA^{EQB}_{ATP-ADP}. TMH numbers are indicated. **g**, Close-up views of the degenerate and consensus NBSs of OF-open TmrA^{EQB}_{ATP-ADP}. Interacting motifs are shown in cartoon representation with selected side chains represented by sticks. ATP is represented by grey sticks colored by heteroatoms. Mg²⁺ is shown as green sphere. **h**, Peptide binding activity of TmrAB^{WT} (black bar) and TmrA^{EQB} (white bar) in the presence and absence of ATP-Mg²⁺ (3 mM MgCl₂ and 1 mM ATP). 4 μM TmrAB were incubated for 5 min at 45 °C (with and without ATP-Mg²⁺). Subsequently, 50 nM C4F peptide (RRY^FCKSTEL) were added and incubated for 10 min on ice. Fluorescence anisotropy

was measured at $\lambda_{\text{ex/em}}=485/520$ nm. Data were measured in triplicates. All data are given as mean \pm SD. (Cryo-EM data collection and analysis were performed by Arne Möller and Dovile Janulienė (Möller laboratory, Department of Structural Biology, Max Planck Institute of Biophysics, Frankfurt). Initial models were prepared by Ahmad Reza Mehdipour (Hummer laboratory, Department of Theoretical Biophysics, Max Planck Institute of Biophysics, Frankfurt). Final models were provided by Christoph Thomas (Tampé laboratory, Institute of Biochemistry, Goethe-University, Frankfurt)). Of note, due to the high resolution of 2.8 Å and 2.9 Å, respectively, the OF-open and OF-occluded maps/models of TmrA^{EQ}B_{ATP-ADP} instead of TmrA^{EQ}B_{ATP} are shown. In both datasets, the OF-open and OF-occluded states were identical.

8.2.3.3 ATP hydrolysis and nucleotide release are necessary to reset TmrAB back into the IF conformation

To understand the conditions and conformational changes required to reset the transporter to an IF conformation, the hydrolysis-transition state was characterized by orthovanadate (V_i)-induced trapping of TmrAB^{WT} (TmrAB_{ATP- V_i}). To this end, a cryo-EM data set of the nanodisc-embedded TmrAB^{WT}/Nb complex in presence of ATP-Mg²⁺ and V_i was determined (3 mM MgCl₂, 1 mM ATP, 1 mM V_i , 5 min at 45 °C). Again, two populations of particles were observed, representing the OF-open and OF-occluded conformation. Single-particle cryo-EM analysis resulted in two three-dimensional reconstructions at overall resolutions of 3.5 Å (OF-open, Figure 39a, Figure 47) and 3.3 Å (OF-occluded, Figure 39b, Figure 47). Interestingly, both conformations (OF-open and OF-occluded) were found in comparable ratios as observed for the TmrA^{EQ}B_{ATP} experiment. Likewise, the OF-open conformation displays a wide opening of the extracellular gate similar to OF Sav1866 (32, 33). In the OF-occluded conformation, the NBDs are tightly dimerized and both, the cytoplasmic and extracellular gate are closed (Figure 39c and d). The existence of an OF-open conformation and its degree of opening in the presence of ATP-Mg²⁺ and V_i are consistent with previously published EPR data (15, 89). A comparison of all four OF models (open/occluded) showed that the ATP-bound (TmrA^{EQ}B_{ATP}) and ATP-hydrolysis transition state (TmrAB_{ATP- V_i}) are equivalent. The only significant difference observed between both preparations was the identity of nucleotide occluded at the consensus side. In contrast to TmrA^{EQ}B_{ATP} (ATP at both NBSs of both conformations), stoichiometric occlusion of ATP at the degenerate site and ADP at the consensus site of TmrAB_{ATP- V_i} was observed, what was additionally proven by a radioactivity-based trapping experiment using [α -³²P]ATP (Figure 39e and f). Importantly, the data show that the sandwiched NBD dimer does not have to be disrupted to allow for release of the inorganic phosphate and entry of vanadate.

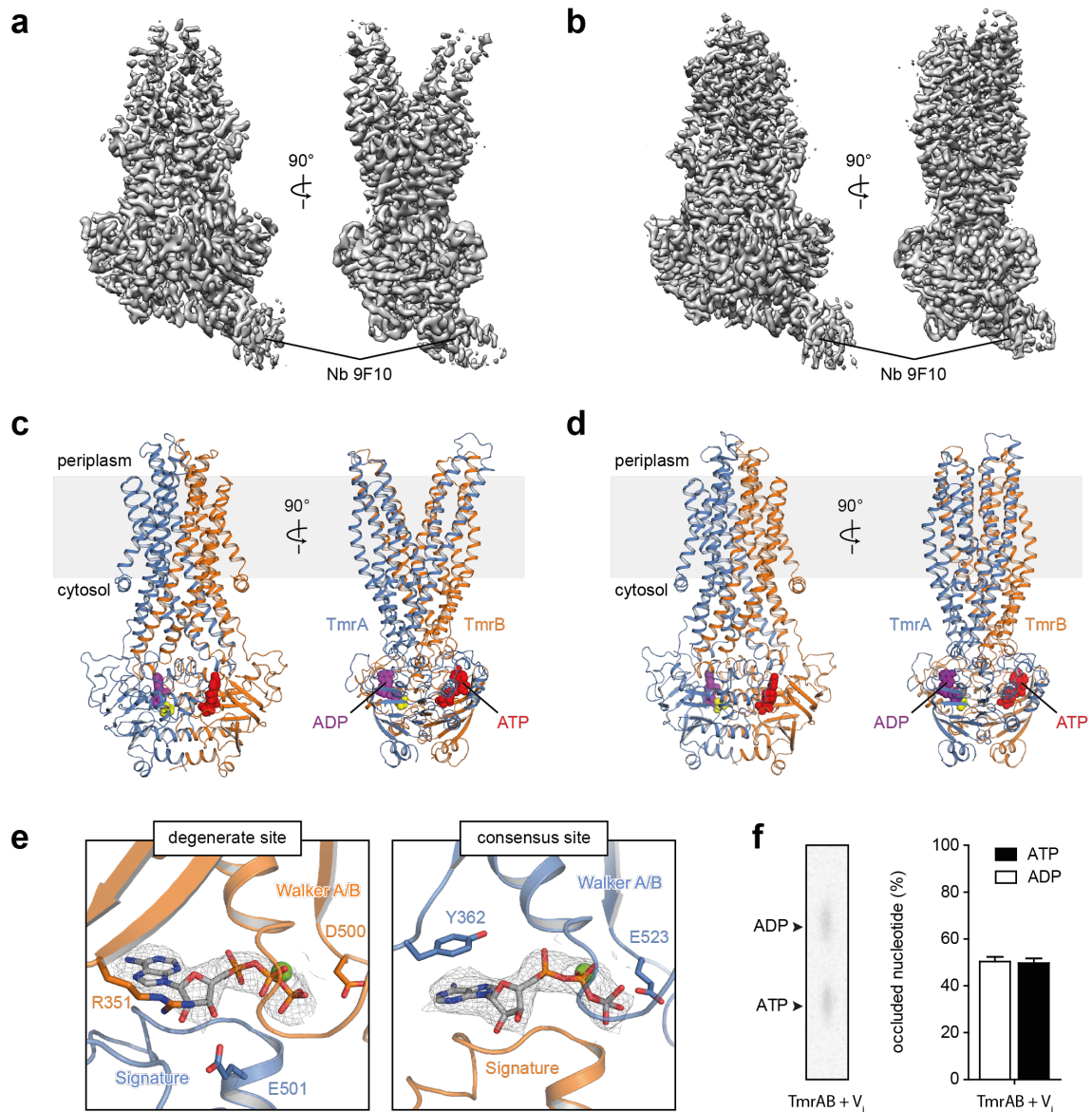


Figure 39: TmrAB_{ATP-V_i} and TmrA^{EQ}B_{ATP} are equivalent. **a** and **b**, Cryo-EM density map of TmrAB_{ATP-V_i} in the OF-open (**a**) and OF-occluded (**b**) conformation filtered to a resolution of 3.5 Å and 3.3 Å, respectively. **c** and **d**, Overall structure of TmrAB_{ATP-V_i} in the OF-open (**c**) and OF-occluded (**d**) conformation viewed from within the plane of the membrane. **e**, Close-up views of the degenerate and consensus ATPase sites of TmrAB_{ATP-V_i} (OF-occluded). Interacting motifs are shown in cartoon representation with selected side chains represented by sticks. Nucleotide and V_i are represented by grey sticks colored by heteroatoms. Mg²⁺ is shown as green sphere. **f**, Nucleotide occlusion upon V_i-induced trapping of TmrAB^{WT}. Trapping experiments were performed according to Zutz *et al.* (83). The identity of occluded nucleotides (either [α -³²P]ATP or [α -³²P]ADP) was analyzed by thin layer chromatography followed by phosphorus imaging. (Cryo-EM data collection and analysis were performed by Arne Möller and Dovile Janulienė (Möller laboratory, Department of Structural Biology, Max Planck Institute of Biophysics, Frankfurt). Initial models were prepared by Ahmad Reza Mehdipour (Hummer laboratory, Department of Theoretical Biophysics, Max Planck Institute of Biophysics, Frankfurt). Final models were provided by Christoph Thomas (Tampé laboratory, Institute of Biochemistry, Goethe-University, Frankfurt)).

The above described results from the TmrAB_{ATP-VI} dataset and the existence of the asymmetric post-hydrolysis state in the turnover experiment demonstrated that one single ATP molecule seems to be sufficient to maintain the NBD dimer. Thus, resetting to the IF conformation has to occur through the release of nucleotide. In order to investigate this notion, the nanodiscs-embedded TmrA^{EQB}/Nb complex was incubated with an equal ratio of ADP and ATP (3 mM MgCl₂, 1 mM ATP, 1 mM ADP, 5 min at 45 °C) to probe whether the asymmetric state can be induced through a backward reaction by simultaneous binding of ATP and ADP (TmrA^{EQB}_{ATP-ADP}). Cryo-EM analysis revealed four conformations: two ATP-bound OF conformations (open and occluded) and two IF conformations (Figure 40, Figure 47). All conformations were equal to the IF and OF conformations already described in this chapter. In neither of the conformations, an asymmetric nucleotide-bound state was detected, proving that this state can only be achieved by a forward reaction through ATP hydrolysis at the canonical site.

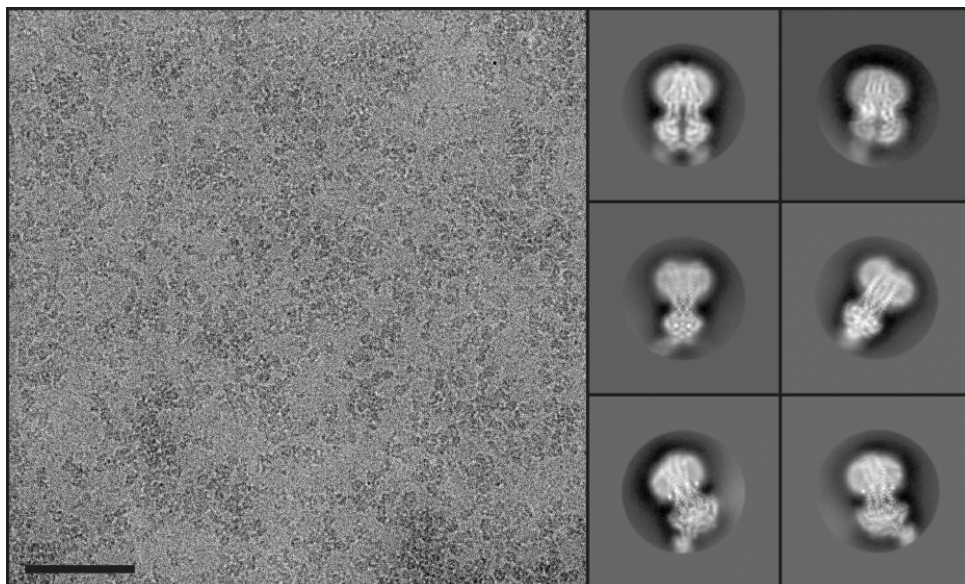


Figure 40: **Cryo-EM analysis of nanodisc-embedded TmrA^{EQB}_{ATP-ADP}**. Representative cryomicrograph and 2D class averages showing different conformational states of TmrA^{EQB}_{ATP-ADP}. Scale bar: 100 nm. (Cryo-EM data collection and analysis were performed by Arne Möller and Dovile Janulienė (Möller laboratory, Department of Structural Biology, Max Planck Institute of Biophysics, Frankfurt)).

8.2.3.4 Global conformational changes and helical shifts within the TMDs during the translocation cycle of TmrAB

During the ATP-triggered conversion from IF to OF-open, TmrAB undergoes large-scale conformational transitions within the TMDs, which involve successive closure of the intracellular and opening of the extracellular gate in a stepwise manner. Extracellular gate closure follows the same rationale to ensure gate opening to only one side of the membrane at a time avoiding potential leakage in the OF-open state. In detail, upon closure of the intracellular gate, the upper half of the TMDs split into two in a *wing*-like manner. This opening is mainly driven by TM helices 1-2 and 5-6 of both monomers, which bend widely towards the outside to open the exit pathway of a bound substrate to the extracellular space. As indicated by Figure 41 and Figure 42, both ABC half-transporters contribute equally to these ATP-driven changes within the TMDs. Intriguingly, within the scope of extracellular gate opening, TM helix 3 of both subunits collapses into the binding cavity. This collaborative movement of TM bundles 1-2/5-6 and TM helix 3 seems to be necessary to ensure substrate release to the opposite side of the membrane and to prevent substrate re-entry from the extracellular space. The transition from the OF-open to the OF-occluded conformation is induced by TM helices 1-2 and 5-6, which switch back in order to initiate extracellular gate closure. In contrast to extracellular gate opening, re-opening of the intracellular gate occurs asymmetrically and is mainly driven by TmrA. Once this point of no return is reached, the transition to the IF conformation is initiated.

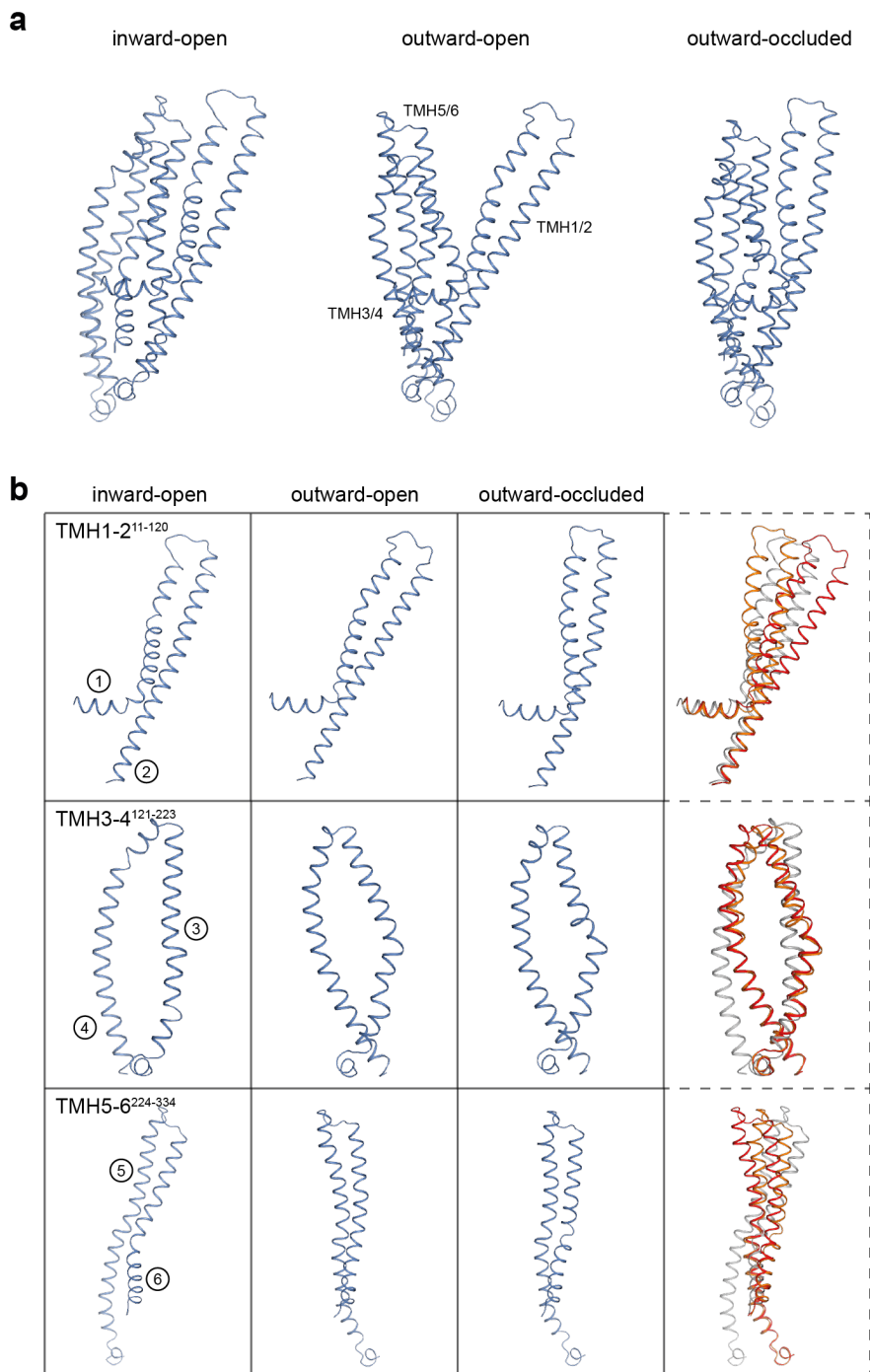
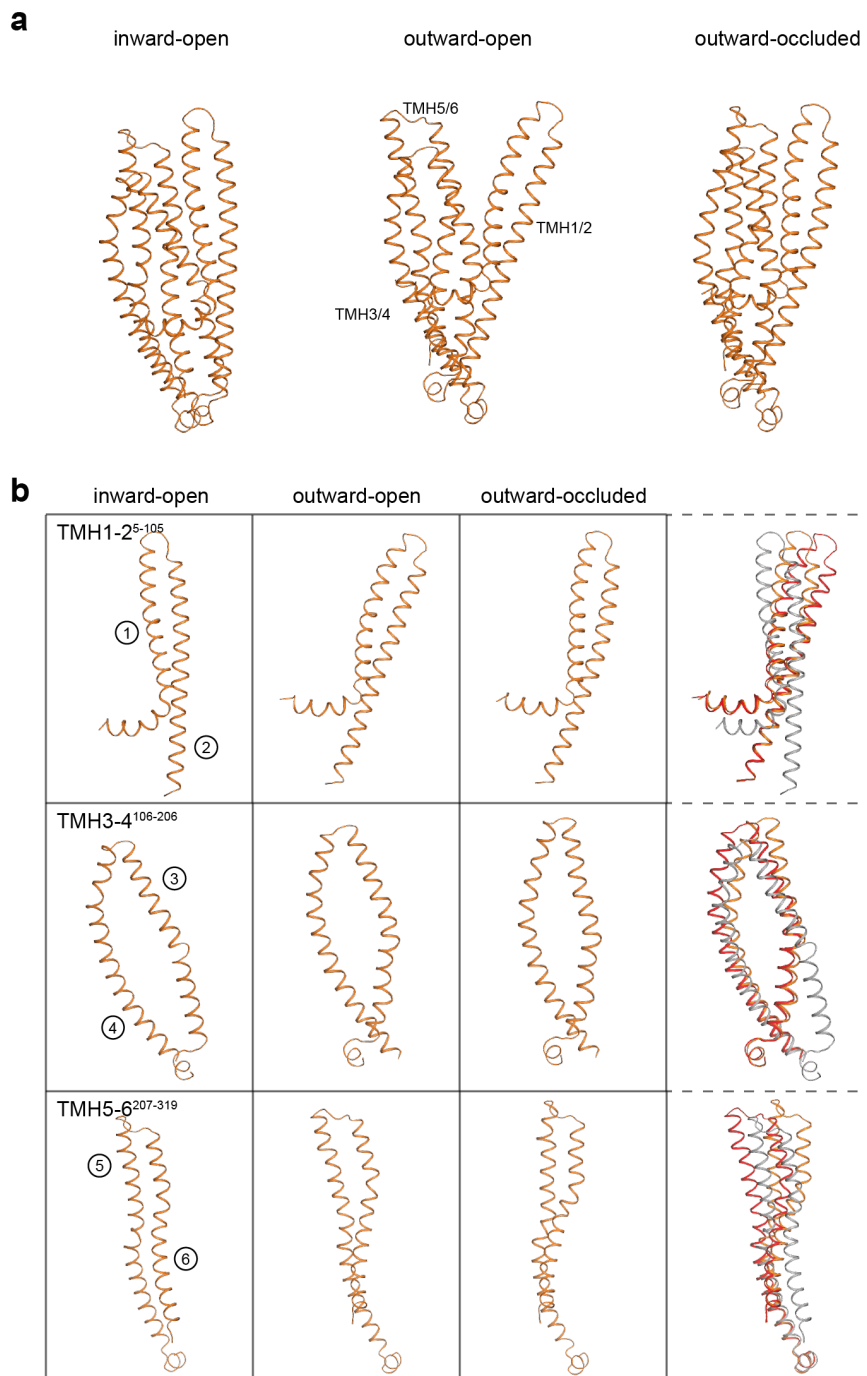


Figure 41: **Helical shifts within the TMD of TmrA during substrate translocation.** **a**, TMD^{TmrA} in the IF, OF-open, and OF-occluded conformation. Coloring scheme as in Figure 36. Helical bundles are indicated. **b**, Dissection of the TMD^{TmrA} into bundles of two helices to illustrate helical shifts during the IF-OF-conversion. Single helices are numbered. For comparison, an overlay of all three conformational states is shown (IF: grey, OF-open: red, OF-occluded: orange). (Initial models were prepared by Ahmad Reza Mehdipour (Hummer laboratory, Department of Theoretical Biophysics, Max Planck Institute of Biophysics, Frankfurt). Final models were provided by Christoph Thomas (Tampé laboratory, Institute of Biochemistry, Goethe-University, Frankfurt)).



8.2.4 Discussion

Over the last few decades, significant progress has been made in unveiling the translocation mechanism of ABC transporters. High-resolution structures, especially fueled by cryo-EM, have significantly advanced the understanding of ABC exporter function (189). However, the available data is incomprehensive and heavily biased as available structures are dominated by homodimeric ABC exporters in an IF-open conformation, which reflects only a snapshot out of a plethora of conformational rearrangements ABC transporters undergo during their catalytic cycle. This paucity poses a significant bottleneck in understanding the substrate translocation and ATP hydrolysis cycle of heterodimeric ABC exporters. Thus, within this study, three key aspects of ABC transporter action were investigated:

- (1) How do specific substrate interactions influence the conformational spectrum of an ABC transporter?
- (2) How are ATP binding and hydrolysis allosterically coupled to substrate translocation?
- (3) Which step(s) of the hydrolysis cycle provide(s) the power stroke(s) for substrate translocation?

In 2017, the crystal structure of TmrAB at 2.7 Å resolution was published. Together with the subnanometer-resolution cryo-EM structure previously presented by Kim *et al.* in 2015, these structures represented highly accurate snapshots of the IF-open state and provided new insights into the structural dynamics of TmrAB. However, for a complete understanding of the conformational space during the catalytic cycle, additional structures of intermediates were needed. In a first approach to illuminate the molecular basis of substrate translocation of TmrAB by single-particle cryo-EM, synthetic antibodies and nanobodies were generated aiming for stable complex formation and conformational trapping, which is a well-established strategy as recently exemplified by the structure of human ABCG2 in complex with two antigen-binding fragments of the human-specific antibody 5D3 (108) or nucleotide-free ABCB1 bound to the antigen-binding fragment of human-specific antibody UIC2 (46).

All synthetic antibodies and nanobodies generated in this study formed stable high-affinity complexes with TmrAB, which could be isolated by SEC, suggesting the formation of sufficiently rigid complexes for cryo-EM (Figure 28 and Figure 30). Negative-stain EM analysis revealed 2D class averages, which showed synthetic antibodies/nanobodies bound to the NBDs of TmrAB, making them a perfect alignment tool by breaking the pseudo-symmetric organization of the

heterodimeric transport complex (Figure 34). However, all tested antibodies bound to TmrAB only in the IF conformation and impeded the transition to the OF state by prevention of NBD dimerization. This result agrees with a study published in 2013 by Ward *et al.* presenting the structure of mouse ABCB1 in complex with a nanobody (127). The nanobody bound to the C-terminal side of the first NBD and therefore prevented the formation of an NBD-NBD dimer, which is essential for the IF to OF conversion. A similar result was presented by Perez *et al.* in 2017. Perez and co-workers presented the structure of PglK complexed by one single nanobody, which bound to both NBDs and induced a unique IF conformation impeding the IF-OF conversion (190).

As an alternative approach to decipher the conformational spectrum of TmrAB during catalysis, cryo-EM analyses were performed under turnover conditions. In the field of structural biology, the physiological relevance of some crystal structures has been questioned in recent years due to the absence of nucleotide (and substrate), detergent solubilization, and crystallization conditions, which could potentially lead to artefactual results (2, 189). For many ABC exporters, it was demonstrated that an alteration of the membrane environment has profound effects on their biochemical properties. MsbA in nanodiscs for example displayed a substantially higher ATPase activity than MsbA in DDM (18, 191, 192). For ABCB1, it was even shown that the inhibitors tariquidar, elacridar, and zosuquidar inhibit P-gp-mediated ATP hydrolysis in native membranes, but stimulate the ATP hydrolysis mediated by detergent-solubilized ABCB1 (193). The turnover numbers determined for TmrAB-catalyzed ATP hydrolysis were equal for membrane-embedded and detergent-solubilized protein (Figure 33). Yet, since the biophysical properties of the membrane may play a key role in ABC transporter function (189), TmrAB was reconstituted into lipid nanodiscs and all EM experiments were performed in a native-like lipid environment in presence of nucleotide (and substrate). Although reconstitution in nanodiscs requires an initial detergent solubilization step, it is generally accepted that nanodiscs provide a more native environment in comparison to detergent micelles (189, 194, 195).

Cryo-EM analysis of nanodiscs-embedded TmrAB under turnover conditions revealed distinct IF conformations (IF^{narrow} and IF^{wide}), one of them (IF^{wide}) with bound peptide substrate, and previously undescribed asymmetric post-hydrolysis states with dimerized NBDs and a closed extracellular gate ($UR^{\text{asym}}/UR^{\text{asym}*}$). IF^{narrow} and IF^{wide} were found in three datasets (TmrAB_{turnover}, TmrAB_{apo}, and TmrA^{EQ}_{B_{ATP-ADP}}) in a nearly equal ratio indicating that both conformations are in a fast equilibrium with each other. The only exception was found in the TmrAB_{C4F} dataset with a 10-fold higher C4F concentration in comparison to TmrAB_{turnover}. Here, IF^{wide} was populated to a

significant extent in comparison to IF^{narrow}. This observation and the notion that significant extra density within the substrate binding cavity was found only in IF^{wide} suggest that substrate binding to TmrAB occurs conformation specific, but binding of C4F itself does not induce a conformational change. Once C4F has entered the substrate binding cavity, it locks TmrAB in the IF^{wide} conformation.

Although the extra density could clearly be attributed to C4F, the occupancy was very low. Additionally, due to the high conformational flexibility of the peptide backbone, the density was less clear and did not represent the complete peptide. In a recent study published by Alam *et al.*, the 3.5 Å cryo-EM structure of substrate-bound human ABCB1 reconstituted in lipid nanodiscs was shown (196). Here, it was demonstrated that the chemotherapeutic compound paclitaxel (Taxol) induces an occluded conformation and a concomitant closure of the inter NBD-gap (196). The density of interacting residues was well defined. However, the density contributed to the Taxol molecule was less clear, which also suggest the possibility of multiple binding modes – similar to C4F and TmrAB. For further studies of the TmrAB-substrate interaction a more rigid substrate with a higher affinity should be considered. Although within this study no evidence was found that binding of C4F induces a conformational shift, it cannot be excluded that binding of a more physiological substrate – such as a lipid – might induce certain conformational changes.

Since substrate release requires the opening of the extracellular gate, the absence of an OF-open conformation in TmrAB_{turnover} indicates the transient nature of this state vulnerable to substrate re-entry. For capturing an OF-open conformation, a slow-down in ATP hydrolysis was required and the TmrA^{EQ}_{B_{ATP}} and TmrAB_{ATP-VI} experiments were performed. In both experiments, the co-existence of OF-open and OF-occluded conformations was discovered. In previous studies it was shown, that orthovanadate-induced trapping of TmrAB led to the closed conformation at the NBSs and an open conformation at the extracellular gate (15, 89). This unexpected equivalence of the ATP-bound and -hydrolysis transition state directly resolves previously conflicting data on the onset of the extracellular gate opening and addresses the controversy in the field regarding the first power-stroke of ABC exporters with asymmetric ATP-binding sites and provides proof that binding of two ATP molecules is sufficient to drive the large-scale conformational change from IF to OF-open.

The discovery of a previously undescribed post-hydrolysis state with asymmetric nucleotide binding and unlocked intracellular gate (asymmetric UR^{asym}/UR^{asym*} conformations of

TmrAB_{turnover}) suggests that the trigger to reset the transporter to an IF conformation is P_i release, not ATP hydrolysis. The dilation of the intracellular gate in UR^{asym} and UR^{asym*} prohibits the opening of the extracellular gate and sets the transporter on path to the IF conformations. This state marks the synergetic process of P_i release and separation of the nucleotide binding domains as the rate-limiting step of the cycle.

Based on the insights gained from the cryo-EM analysis of TmrAB_{turnover}, TmrAB_{C4F}, TmrAB_{apo}, TmrA^{EQ}_{B_{ATP}}, TmrA^{EQ}_{B_{ATP-ADP}}, and TmrAB_{ATP-Vi} the following mechanism was proposed (Figure 43): In the IF-conformation, TM6 acts as a gatekeeper, controlling volume and access to the intracellular cavity for conformation-specific substrate uptake. Upon ATP binding in both NBDs, they dimerize, close the intracellular gate, and allow opening of the extracellular gate. In this state, the transporter can transition between OF-open and OF-occluded conformations until the release of P_i from the canonical site weakens the NBD interactions. In turn, the intracellular gate unlocks, and the transporter transitions from an OF to an IF conformation *via* UR^{asym}/UR^{asym*}. The high abundance of the asymmetric ADP/ATP-bound UR^{asym}/UR^{asym*} state under turnover conditions with excess of ATP suggests that the separation of the sandwiched NBD dimer, which requires dissociation of the ATP-bound non-canonical site, constitutes the rate-limiting step during the transport cycle.

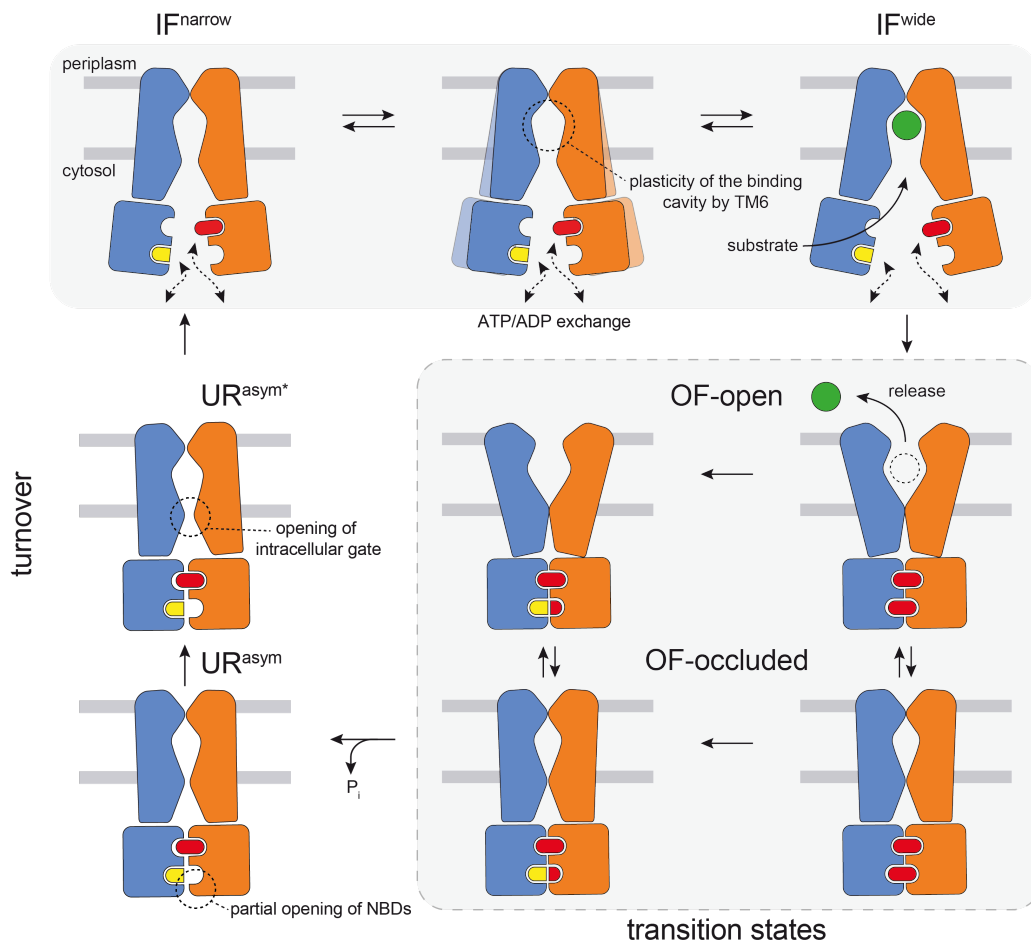


Figure 43: **Transport cycle of the heterodimeric ABC exporter TmrAB.** TmrAB fluctuates between IF^{narrow} and IF^{wide} with TM6 acting as gatekeeper, controlling access and volume of the substrate-binding cavity. Therefore, bulky substrates can only bind to the IF^{wide} conformation. ATP binding to both NBDs induces NBD dimerization, which triggers closure of the intracellular gate and opening of the extracellular gate. After substrate release, TmrAB can isomerize between OF-open and OF-occluded conformations in the ATP-bound state until P_i is discharged from the canonical site. P_i release *via* a phosphate channel results in an asymmetric UR^{asym} (and UR^{asym*}) conformation and triggers partial opening of the NBDs and the intracellular gate, which advances the exporter towards the IF conformation. Separation of the NBD dimer by dissociation of the ATP-bound non-canonical site represents the rate-limiting step during the cycle. TmrA and TmrB are shown in blue and orange, respectively.

8.3 Alternative attempts to stabilize the outward-facing state of TmrAB

8.3.1 Selection of macrocyclic peptides as conformational arrestors

In collaboration with Richard Obexer (Suga laboratory, Department of Chemistry, The University of Tokyo, Japan), bioactive cyclic peptides were generated against TmrAB aiming for allosteric locking of the transport complex to further elucidate key events leading to extracellular gate opening and closing. Based on pulsed electron-electron double resonance spectroscopy (PELDOR/DEER) measurements (15, 89) and the above described cryo-EM data, which have revealed a strong population of the OF-open state upon V_i -trapping, the selection of cyclic peptides was performed against streptavidin-captured, biotinylated V_i -trapped TmrAB using the RaPID system (132).

For peptide selection, an RNA library with a diversity of $\sim 2 \times 10^{12}$ members was created allowing for 8-15 *NNK* codons ($K = G$ or T). In total, six consecutive selection rounds were performed. Peptide selection and synthesis were done by Richard Obexer at the University of Tokyo in Japan. For a biochemical characterization of the TmrAB/peptide interaction, biotin- and FITC-labeled cyclic peptides were kindly provided.

Out of the selected putative TmrAB-binding peptide candidates, cyclic peptide VD3 was of particular interest (aa sequence is shown in Table 10; Figure 44). In absence of nucleotide, no binding of FITC-labeled VD3 was observed by MC-FSEC (Figure 44a). Upon addition of ATP-Mg²⁺, however, FITC-labeled VD3 bound to TmrAB in a stoichiometric ratio of 1:0.8 (TmrAB:VD3^F) as revealed by coelution of TmrAB and peptide (Figure 44b). Previous studies have provided proof that TmrAB is a very versatile translocation systems with a broad substrate specificity (15, 83). Among other substrates, binding and translocation of fluorescein by TmrAB was shown (15). In order to elucidate specific binding of the peptide, but not the fluorescence label, a pull-down assay was performed using biotin-conjugated VD3. First, TmrAB was incubated with a 2-fold molar excess of VD3^{biotin} (in the absence or presence of nucleotide). Subsequently, the TmrAB/VD3^{biotin} complex was added to streptavidin-coated magnetic beads and binding was analyzed by an InstantBlueTM-stained SDS-PAGE gel. In accordance to the MC-FSEC data, binding of VD3^{biotin} was overserved only in the presence of nucleotide (Figure 44d).

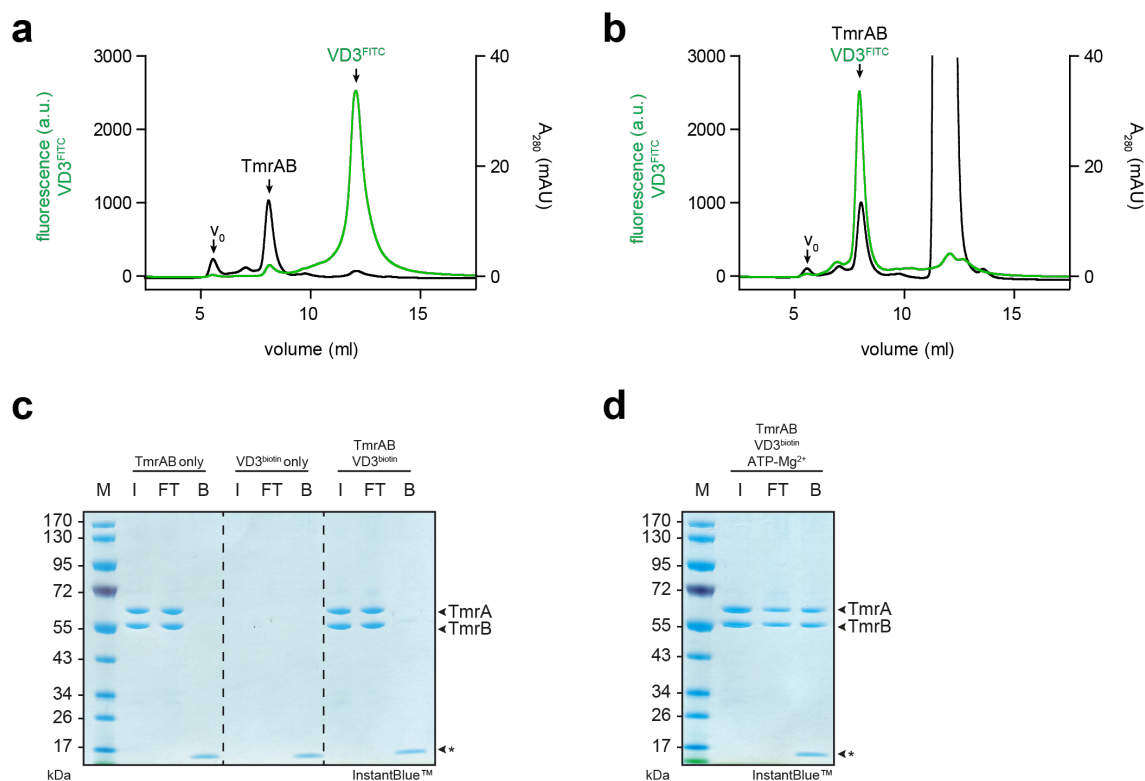


Figure 44: **Cyclic peptide VD3 binds specific to nucleotide-bound TmrAB.** **a** and **b**, MC-FSEC of TmrAB (2 μM) and $VD3^F$ (1.6 μM) in absence (**a**) or presence of ATP-Mg²⁺ (**b**). Column: TSKgel® G3000SW_{XL} (Tosoh Bioscience). Void volume is indicated by V_0 . **c** and **d**, TmrAB (1 μM) pull down using streptavidin-coated magnetic beads upon incubation with $VD3^{biotin}$ (2 μM) in absence (**c**) or presence of ATP-Mg²⁺ (**d**) analyzed by an InstantBlue™-stained SDS-PAGE gel. M: marker; I: input; FT: flow-through; W: wash; B: beads. *: streptavidin.

Interestingly, 40% of TmrAB were found in the flow-through (Figure 44). This results implies that either 40% of TmrAB were not complex with $VD3^{biotin}$ or 40% of TmrAB/ $VD3^{biotin}$ complexes did not bind to streptavidin.

To get further insights into the TmrAB/ $VD3$ interaction, the equilibrium binding constant was determined by fluorescence anisotropy measurements using FITC-labeled $VD3$. In presence of ATP-Mg²⁺, $VD3^F$ bound to TmrAB with an affinity in the low nanomolar range (K_D : 18.1 ± 2.8 nM; Figure 45a). Addition of a 1000-fold molar excess of unlabeled competitor peptide diminished binding of $VD3^F$ completely. Owing to the exploration of putative conformational locking of TmrAB induced by cyclic peptide binding, the ATPase activity in presence of increasing concentrations of $VD3$ (0-1 μM) was investigated showing an 80% reduction of the ATPase activity upon addition of 1 μM $VD3$ (Figure 44b).

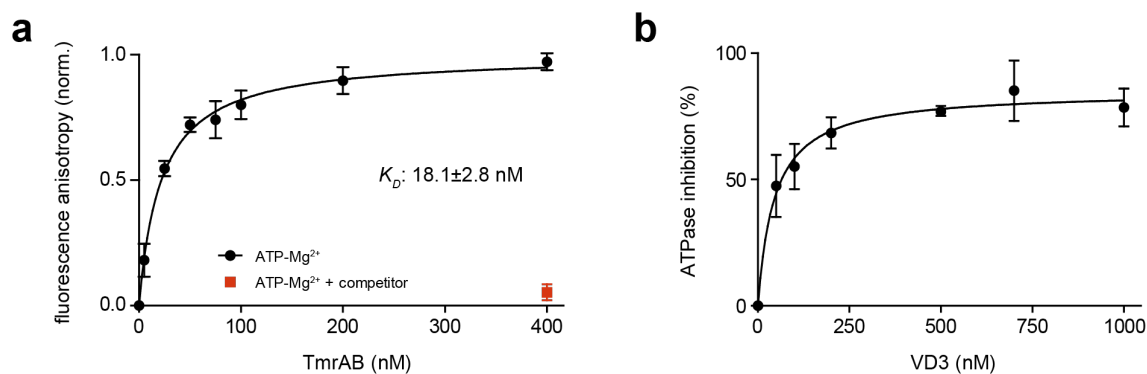


Figure 45: **Cyclic peptide VD3 as potent and highly selective inhibitor.** **a**, Binding of VD3^F to TmrAB in presence of nucleotide analyzed by fluorescence anisotropy. 0, 5, 25, 50, 75, 100, 200, and 400 nM TmrAB in β -DDM were incubated with 50 nM VD3^F peptide and 10 mM ATP-Mg²⁺ for 15 min on ice. To proof specificity of binding, a 1000-fold molar excess of unlabeled VD3 (competitor) peptide was added. Fluorescence anisotropy was analyzed at $\lambda_{ex/em}=485/520$ nm. Data were measured in triplicates. All data are given as mean \pm SD. **b**, Impact of VD3-binding onto the ATPase activity of TmrAB. ATP hydrolysis of β -DDM-solubilized TmrAB (200 nM) in the presence of 3 mM MgCl₂, 1 mM ATP (supplemented with tracer amounts of [γ -³²P]ATP), and increasing concentrations of VD3 peptide (0, 50, 100, 200, 500, 700, 1000 nM) was measured for 10 min at 68 °C. Data were measured in triplicates. All data are given as mean \pm SD.

To gain insights into the mode of inhibition, particularly the conformational state of TmrAB upon VD3 binding, a negative-stain EM analysis of nucleotide-bound VD3-complexed TmrAB was performed. 2D class averaging revealed no difference to previous preparations of TmrAB without addition of any ligand, suggesting that cyclic peptide VD3 does not allosterically lock TmrAB in the OF, but in the IF-state (data not shown). Notably, a different degree of NBD separation, a restriction of the intrinsic dynamics of TmrAB in the IF state or minor changes at the extracellular gate induced by VD3 binding cannot be distinguished or excluded by this analysis. Owing to a further exploration of the TmrAB/VD3 interaction, the VD3-binding site was narrowed down by the addition of monovalent streptavidin as a fiducial marker to unambiguously identify binding of VD3 to the intra- or extracellular side of TmrAB (Figure 46). In the presence of nucleotide, TmrAB/VD3^{biotin}/streptavidin complexes were isolated by SEC and subjected to negative-stain EM analysis (Figure 46b). 2D class averaging revealed two major populations as already indicated by a peak broadening during SEC: TmrAB complexed with streptavidin and TmrAB without streptavidin bound (Figure 46c). Streptavidin density was only found at the periplasmic side of TmrAB, suggesting that cyclic peptide VD3 acts as a surface clamp at the extracellular gate of TmrAB. To increase the EM density at this region, β -DDM was exchanged for LMNG. In comparison to DDM, LMNG forms larger micelles as reported previously (197). In agreement, the detergent belt formed by LMNG seemed much larger in comparison β -DDM solubilized TmrAB. Additionally, bound streptavidin was found in one orientation, whereas

2D class averages of β -DDM-solubilized TmrAB showed a higher degree of flexibility (Figure 46d). Of note, as a further tool to differentiate between the intra- and extracellular side of TmrAB, nanobody 9F10 was added (indicated by a white arrowhead).

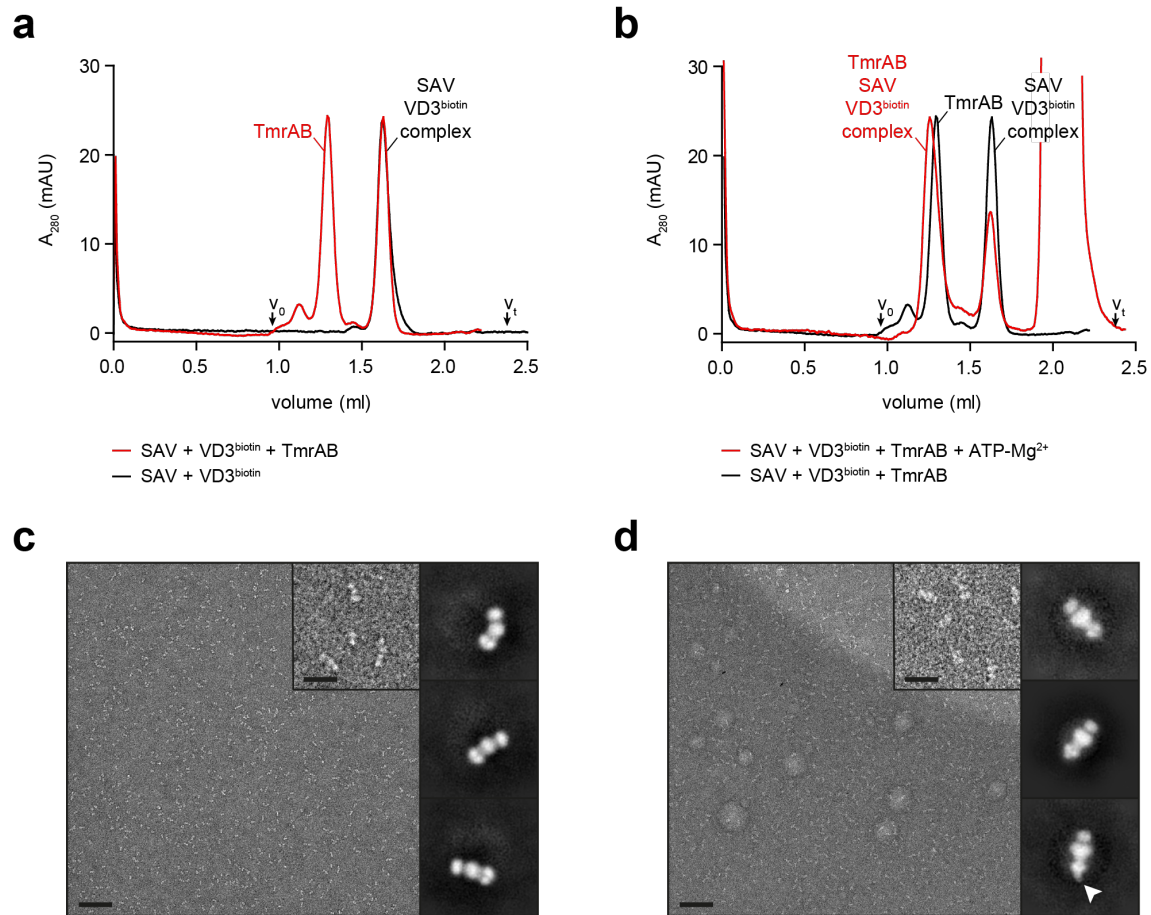


Figure 46: VD3 binds to the periplasmic side of TmrAB. **a** and **b**, TmrAB/VD3^{biotin}/streptavidin complex formation analyzed in absence (**a**) and presence (**b**) of nucleotide (10 mM MgCl₂ and 10 mM ATP, incubation for 10 min at 4 °C). TmrAB, VD3^{biotin}, and monovalent streptavidin were added in stoichiometric amounts (0.5 μ M each). Column: Superdex™ 200 Increase 3.2/300 (GE Healthcare). Void and total volume are indicated by v_0 and v_t , respectively. (Monovalent streptavidin was kindly provided by Nita Chang (Geertsma laboratory, Institute of Biochemistry, Goethe-University, Frankfurt)). **c**, Representative negative-stain micrograph and 2D class averages of β -DDM-solubilized TmrAB/VD3^{biotin}/streptavidin complexes stained with 2% uranyl formate. Micrographs were collected on a Tecnai-Spirit transmission electron microscope (Thermo Fisher, former FEI), operated at 120 kV and equipped with a Gatan 4x4k CCD camera. Scale bar for original micrograph: 100 nm. Scale bar for inlet (4x4 magnified): 25 nm. **d**, Representative negative-stain micrograph and 2D class averages of LMNG-solubilized TmrAB/VD3^{biotin}/streptavidin complexes stained with 2% uranyl formate. Micrographs were collected on a Tecnai-Spirit transmission electron microscope (Thermo Fisher, former FEI), operated at 120 kV and equipped with a Gatan 4x4k CCD camera. Scale bar for original micrograph: 100 nm. Scale bar for inlet (4x4 magnified): 25 nm.

8.3.2 Discussion

In the previous chapter, the complete conformational spectrum of TmrAB in a native lipid environment was mapped allowing for a detailed understanding of the catalytic cycle of the NBDs. Extensive analysis of the EM data provided proof that ATP-triggered dimerization of the NBDs is sufficient to drive the conformational change from an IF-open to an OF-open conformation allowing a potential substrate to exit the binding pocket. To further unleash the molecular events occurring at the extracellular gate of TmrAB for a full understanding of the allosteric coupling of substrate translocation and ATP binding/hydrolysis, cyclic peptides were generated against V_i -trapped TmrAB to lock the highly transient OF-open conformation. Using the RaPID system (132), cyclic peptides were generated against putatively OF-open TmrAB. Out of the selected candidates, cyclic peptide VD3 was of particular interest, because it was shown that VD3 binds specific with high affinity to TmrAB, but only in the presence of nucleotide (Figure 44). Additionally, VD3 was shown to almost completely diminish the ATPase activity of TmrAB (Figure 45). Both results indicated that TmrAB might be conformationally locked in the ATP-bound state corresponding to the OF-open conformation. Yet, negative-stain EM analysis revealed IF particles exclusively. This result agrees with the highly transitory nature of the OF-open state. It seems that the lifespan of the OF-open state induced by V_i -trapping is too short to allow for the selection of stabilizing chaperones. Of note, this result agrees with previous attempts to analyze the V_i -trapped state by cryo-EM after SEC (to remove the trapping reagents): after SEC, no OF-open particles were observed, but a mixture of IF-open and OF-occluded particles. For a further understanding of the binding and inhibition mechanism of VD3, the VD3 binding site was mapped. By the addition of monovalent streptavidin to ATP-bound $VD3^{biotin}$ -complexed TmrAB and subsequent negative-stain EM analysis, binding to the periplasmic side of TmrAB was shown (Figure 45). Hence, it seems that VD3 binds at the interface between the outer surface of TmrAB and the outer leaflet of the membrane bilayer and thus restricts the conformational dynamics, similar as it was shown for aCAP and CmABCB1 (131).

Although none of the selected peptides locked TmrAB in the OF conformation, with VD3 a highly selective and potent cyclic peptide inhibitor of TmrAB was generated. Nevertheless, for a detailed understanding of this allosteric coupling of nucleotide-triggered conformational changes allowing VD3 to bind, further investigation is necessary.

9. Conclusion

One crucial part of this study was the generation and comparison of three different tools for the conformational arrest of the ABC export systems TAP and TmrAB: synthetic antibodies, nanobodies, and cyclic peptides. With a size of about 50 kD, synthetic antibodies, which are based on a Fab scaffold, form stable and rigid complexes with their respective target protein and thus provide a defined feature for accurate image alignment in single-particle cryo-EM. Nanobodies, in contrast, are much smaller in size, but based on the structural organization of their CDR3-loop, nanobodies are more suitable for stable locking of distinct conformational states. Macrocytic peptides have proven to be a particularly useful tool for the inhibition or stimulation of membrane protein function and thus offer a great potential for the reduction of the conformational heterogeneity of ABC transport complexes. Although none of the generated binding molecules was used to map the conformational space of TmrAB by cryo-EM in the end, the synthetic antibodies and nanobodies generated here proved to be valuable tools to break the pseudo-symmetric organization of TmrAB and the cyclic peptides represented important tools to modulate TmrAB function and might prove useful in future crystallization approaches.

Within the last years, several structures of ABC transporters have been published, and the number of deposited structures is constantly increasing – especially due to recent advances in the field of single-particle cryo-EM. But mostly, these structures represent snapshots of the most abundant conformational states of an ABC transporter, which could be stabilized and selected in crystallization or cryo-EM approaches. However, the full mechanochemical cycle of a heterodimeric ABC transport system has not been mapped yet, and thus many aspects, such as the power strokes driving the interconversion of conformational states or the coupling of the conformational plasticity in the TMDs to the pair of nucleotides in the transiently sandwiched NBD dimer are poorly understood. Therefore, this study provides a general template for (heterodimeric) ABC exporter-catalyzed substrate translocation and sheds light onto fundamental mechanistic details. In one single experiment the complete conformational space of TmrAB under turnover conditions was mapped illustrating the global changes TmrAB undergoes during substrate translocation. Missing gaps were filled by the analysis of strategic positioned ligand combinations and mutations of TmrAB. The way this experiment was designed provides a template for future studies on ABC transporter structure and exemplifies the importance of gaining a temporal relation between individual conformers within the transport cycle to significantly advance the understanding of ABC transporter function.

Since TmrAB is an exceptionally versatile export system with an extremely broad substrate specificity, one very important task for future studies will be the discovery of physiological substrates of TmrAB to further elucidate the impact of substrate binding. Besides to peptides and dyes, an involvement of TmrAB in glycolipid translocation is discussed, an aspect that was not part of this study, but is essential for a complete understanding of TmrAB function.

10. References

1. Rees DC, Johnson E, & Lewinson O (2009) ABC transporters: the power to change. *Nat Rev Mol Cell Biol* 10(3):218-227.
2. Locher KP (2016) Mechanistic diversity in ATP-binding cassette (ABC) transporters. *Nat Struct Mol Biol* 23(6):487-493.
3. Davidson AL & Chen J (2004) ATP-binding cassette transporters in bacteria. *Annu Rev Biochem* 73:241-268.
4. Higgins CF (2007) Multiple molecular mechanisms for multidrug resistance transporters. *Nature* 446(7137):749-757.
5. Parcej D & Tampé R (2010) ABC proteins in antigen translocation and viral inhibition. *Nat Chem Biol* 6(8):572-580.
6. Higgins CF (1992) ABC transporters: from microorganisms to man. *Annu Rev Cell Biol* 8:67-113.
7. Dean M, Rzhetsky A, & Allikmets R (2001) The human ATP-binding cassette (ABC) transporter superfamily. *Genome Res* 11(7):1156-1166.
8. Schmitt L & Tampé R (2002) Structure and mechanism of ABC transporters. *Curr Opin Struct Biol* 12(6):754-760.
9. Thomas C & Tampé R (2018) Multifaceted structures and mechanisms of ABC transport systems in health and disease. *Curr Opin Struct Biol* 51:116-128.
10. Korkhov VM, Mireku SA, & Locher KP (2012) Structure of AMP-PNP-bound vitamin B12 transporter BtuCD-F. *Nature* 490(7420):367-372.
11. Oldham ML, Khare D, Quioco FA, Davidson AL, & Chen J (2007) Crystal structure of a catalytic intermediate of the maltose transporter. *Nature* 450(7169):515-521.
12. Seyffer F & Tampé R (2015) ABC transporters in adaptive immunity. *Biochim Biophys Acta* 1850(3):449-460.
13. Xu K, *et al.* (2013) Crystal structure of a folate energy-coupling factor transporter from *Lactobacillus brevis*. *Nature* 497(7448):268-271.
14. Kim J, *et al.* (2015) Subnanometre-resolution electron cryomicroscopy structure of a heterodimeric ABC exporter. *Nature* 517(7534):396-400.
15. Nöll A, *et al.* (2017) Crystal structure and mechanistic basis of a functional homolog of the antigen transporter TAP. *Proc Natl Acad Sci U S A* 114(4):E438-E447.
16. Oldham ML, Grigorieff N, & Chen J (2016) Structure of the transporter associated with antigen processing trapped by herpes simplex virus. *Elife* 5: e21829.

17. Oldham ML, *et al.* (2016) A mechanism of viral immune evasion revealed by cryo-EM analysis of the TAP transporter. *Nature* 529(7587):537-540.
18. Mi W, *et al.* (2017) Structural basis of MsbA-mediated lipopolysaccharide transport. *Nature* 549(7671):233-237.
19. Bi Y, Mann E, Whitfield C, & Zimmer J (2018) Architecture of a channel-forming O-antigen polysaccharide ABC transporter. *Nature* 553(7688):361-365.
20. Luo Q, *et al.* (2017) Structural basis for lipopolysaccharide extraction by ABC transporter LptB2FG. *Nat Struct Mol Biol* 24(5):469-474.
21. Fitzpatrick AWP, *et al.* (2017) Structure of the MacAB-TolC ABC-type tripartite multidrug efflux pump. *Nat Microbiol* 2:17070.
22. Smith PC, *et al.* (2002) ATP binding to the motor domain from an ABC transporter drives formation of a nucleotide sandwich dimer. *Mol Cell* 10(1):139-149.
23. Kim IW, *et al.* (2006) The conserved tyrosine residues 401 and 1044 in ATP sites of human P-glycoprotein are critical for ATP binding and hydrolysis: evidence for a conserved subdomain, the A-loop in the ATP-binding cassette. *Biochemistry* 45(24):7605-7616.
24. Leippe DD, Koonin EV, & Aravind L (2003) Evolution and classification of P-loop kinases and related proteins. *J Mol Biol* 333(4):781-815.
25. Saraste M, Sibbald PR, & Wittinghofer A (1990) The P-loop - a common motif in ATP- and GTP-binding proteins. *Trends Biochem Sci* 15(11):430-434.
26. Gaudet R & Wiley DC (2001) Structure of the ABC ATPase domain of human TAP1, the transporter associated with antigen processing. *EMBO J* 20(17):4964-4972.
27. Grossmann N, *et al.* (2014) Mechanistic determinants of the directionality and energetics of active export by a heterodimeric ABC transporter. *Nat Commun* 5:5419.
28. Nikaido K & Ames GF (1999) One intact ATP-binding subunit is sufficient to support ATP hydrolysis and translocation in an ABC transporter, the histidine permease. *J Biol Chem* 274(38):26727-26735.
29. Zaitseva J, Jenewein S, Jumpertz T, Holland IB, & Schmitt L (2005) H662 is the linchpin of ATP hydrolysis in the nucleotide-binding domain of the ABC transporter HlyB. *EMBO J* 24(11):1901-1910.
30. Oancea G, *et al.* (2009) Structural arrangement of the transmission interface in the antigen ABC transport complex TAP. *Proc Natl Acad Sci U S A* 106(14):5551-5556.
31. Procko E, Ferrin-O'Connell I, Ng SL, & Gaudet R (2006) Distinct structural and functional properties of the ATPase sites in an asymmetric ABC transporter. *Mol Cell* 24(1):51-62.

32. Dawson RJ & Locher KP (2006) Structure of a bacterial multidrug ABC transporter. *Nature* 443(7108):180-185.
33. Dawson RJ & Locher KP (2007) Structure of the multidrug ABC transporter Sav1866 from *Staphylococcus aureus* in complex with AMP-PNP. *FEBS Lett* 581(5):935-938.
34. Johnson ZL & Chen J (2017) Structural basis of substrate recognition by the multidrug resistance protein MRP1. *Cell* 168(6):1075-1085 e1079.
35. Kim Y & Chen J (2018) Molecular structure of human P-glycoprotein in the ATP-bound, outward-facing conformation. *Science* 359(6378):915-919.
36. Hohl M, Briand C, Grutter MG, & Seeger MA (2012) Crystal structure of a heterodimeric ABC transporter in its inward-facing conformation. *Nat Struct Mol Biol* 19(4):395-402.
37. Shintre CA, *et al.* (2013) Structures of ABCB10, a human ATP-binding cassette transporter in apo- and nucleotide-bound states. *Proc Natl Acad Sci U S A* 110(24):9710-9715.
38. Lee JY, Yang JG, Zhitnitsky D, Lewinson O, & Rees DC (2014) Structural basis for heavy metal detoxification by an Atm1-type ABC exporter. *Science* 343(6175):1133-1136.
39. Srinivasan V, Pierik AJ, & Lill R (2014) Crystal structures of nucleotide-free and glutathione-bound mitochondrial ABC transporter Atm1. *Science* 343(6175):1137-1140.
40. Liu F, Zhang Z, Csanady L, Gadsby DC, & Chen J (2017) Molecular structure of the human CFTR ion channel. *Cell* 169(1):85-95 e88.
41. Taylor NMI, *et al.* (2017) Structure of the human multidrug transporter ABCG2. *Nature* 546(7659):504-509.
42. Seeger MA (2018) Membrane transporter research in times of countless structures. *Biochim Biophys Acta* 1860(4):804-808.
43. Choudhury HG, *et al.* (2014) Structure of an antibacterial peptide ATP-binding cassette transporter in a novel outward occluded state. *Proc Natl Acad Sci U S A* 111(25):9145-9150.
44. Lin DY, Huang S, & Chen J (2015) Crystal structures of a polypeptide processing and secretion transporter. *Nature* 523(7561):425-430.
45. Perez C, *et al.* (2015) Structure and mechanism of an active lipid-linked oligosaccharide flippase. *Nature* 524(7566):433-438.
46. Alam A, *et al.* (2018) Structure of a zosuquidar and UIC2-bound human-mouse chimeric ABCB1. *Proc Natl Acad Sci U S A* 115(9):E1973-E1982.

47. Johnson ZL & Chen J (2018) ATP binding enables substrate release from multidrug resistance protein 1. *Cell* 172(1-2):81-89 e10.
48. Szakacs G, Paterson JK, Ludwig JA, Booth-Genthe C, & Gottesman MM (2006) Targeting multidrug resistance in cancer. *Nat Rev Drug Discov* 5(3):219-234.
49. El-Awady R, *et al.* (2016) The role of eukaryotic and prokaryotic ABC transporter family in failure of chemotherapy. *Front Pharmacol* 7:535.
50. Everett H & McFadden G (1999) Apoptosis: an innate immune response to virus infection. *Trends Microbiol* 7(4):160-165.
51. Blees A, *et al.* (2017) Structure of the human MHC-I peptide-loading complex. *Nature* 551(7681):525-528.
52. Trowitzsch S & Tampé R (2018) ABC transporters in dynamic macromolecular assemblies. *J Mol Biol* 430(22):4481-4495.
53. Dick TP (2004) Assembly of MHC class I peptide complexes from the perspective of disulfide bond formation. *Cell Mol Life Sci* 61(5):547-556.
54. Abele R & Tampé R (2004) The ABCs of immunology: structure and function of TAP, the transporter associated with antigen processing. *Physiology (Bethesda)* 19:216-224.
55. Herget M, *et al.* (2009) Purification and reconstitution of the antigen transport complex TAP: a prerequisite for determination of peptide stoichiometry and ATP hydrolysis. *J Biol Chem* 284(49):33740-33749.
56. Abele R & Tampé R (2011) The TAP translocation machinery in adaptive immunity and viral escape mechanisms. *Essays Biochem* 50(1):249-264.
57. Blees A, *et al.* (2015) Assembly of the MHC I peptide-loading complex determined by a conserved ionic lock-switch. *Sci Rep* 5:17341.
58. Koch J, Guntrum R, Heintke S, Kyritsis C, & Tampé R (2004) Functional dissection of the transmembrane domains of the transporter associated with antigen processing (TAP). *J Biol Chem* 279(11):10142-10147.
59. Procko E, Raghuraman G, Wiley DC, Raghavan M, & Gaudet R (2005) Identification of domain boundaries within the N-termini of TAP1 and TAP2 and their importance in tapasin binding and tapasin-mediated increase in peptide loading of MHC class I. *Immunol Cell Biol* 83(5):475-482.
60. Koch J, Guntrum R, & Tampé R (2005) Exploring the minimal functional unit of the transporter associated with antigen processing. *FEBS Lett* 579(20):4413-4416.
61. van Endert PM, *et al.* (1994) A sequential model for peptide binding and transport by the transporters associated with antigen processing. *Immunity* 1(6):491-500.

62. Koopmann JO, Post M, Neefjes JJ, Hammerling GJ, & Momburg F (1996) Translocation of long peptides by transporters associated with antigen processing (TAP). *Eur J Immunol* 26(8):1720-1728.
63. Uebel S, *et al.* (1997) Recognition principle of the TAP transporter disclosed by combinatorial peptide libraries. *Proc Natl Acad Sci U S A* 94(17):8976-8981.
64. Uebel S, *et al.* (1995) Requirements for peptide binding to the human transporter associated with antigen processing revealed by peptide scans and complex peptide libraries. *J Biol Chem* 270(31):18512-18516.
65. Momburg F, Armandola EA, Post M, & Hammerling GJ (1996) Residues in TAP2 peptide transporters controlling substrate specificity. *J Immunol* 156(5):1756-1763.
66. Herget M, *et al.* (2011) Conformation of peptides bound to the transporter associated with antigen processing (TAP). *Proc Natl Acad Sci U S A* 108(4):1349-1354.
67. Lehnert E, *et al.* (2016) Antigenic peptide recognition on the human ABC transporter TAP resolved by DNP-enhanced solid-state NMR spectroscopy. *J Am Chem Soc* 138(42):13967-13974.
68. Ahn K, *et al.* (1996) Molecular mechanism and species specificity of TAP inhibition by herpes simplex virus ICP47. *EMBO J* 15(13):3247-3255.
69. Galocha B, *et al.* (1997) The active site of ICP47, a herpes simplex virus-encoded inhibitor of the major histocompatibility complex (MHC)-encoded peptide transporter associated with antigen processing (TAP), maps to the NH₂-terminal 35 residues. *J Exp Med* 185(9):1565-1572.
70. Früh K, *et al.* (1995) A viral inhibitor of peptide transporters for antigen presentation. *Nature* 375(6530):415-418.
71. Ahn K, *et al.* (1997) The ER-luminal domain of the HCMV glycoprotein US6 inhibits peptide translocation by TAP. *Immunity* 6(5):613-621.
72. Hengel H, *et al.* (1997) A viral ER-resident glycoprotein inactivates the MHC-encoded peptide transporter. *Immunity* 6(5):623-632.
73. Lehner PJ, Karttunen JT, Wilkinson GW, & Cresswell P (1997) The human cytomegalovirus US6 glycoprotein inhibits transporter associated with antigen processing-dependent peptide translocation. *Proc Natl Acad Sci U S A* 94(13):6904-6909.
74. Hewitt EW, Gupta SS, & Lehner PJ (2001) The human cytomegalovirus gene product US6 inhibits ATP binding by TAP. *EMBO J* 20(3):387-396.

75. Koppers-Lalic D, *et al.* (2005) Varicelloviruses avoid T cell recognition by UL49.5-mediated inactivation of the transporter associated with antigen processing. *Proc Natl Acad Sci U S A* 102(14):5144-5149.
76. Koppers-Lalic D, *et al.* (2008) Varicellovirus UL 49.5 proteins differentially affect the function of the transporter associated with antigen processing, TAP. *PLoS Pathog* 4(5):e1000080.
77. Loch S, *et al.* (2008) Signaling of a varicelloviral factor across the endoplasmic reticulum membrane induces destruction of the peptide-loading complex and immune evasion. *J Biol Chem* 283(19):13428-13436.
78. Rensing ME, *et al.* (2005) Impaired transporter associated with antigen processing-dependent peptide transport during productive EBV infection. *J Immunol* 174(11):6829-6838.
79. Lin J, *et al.* (2014) A negative feedback modulator of antigen processing evolved from a frameshift in the cowpox virus genome. *PLoS Pathog* 10(12):e1004554.
80. Aller SG, *et al.* (2009) Structure of P-glycoprotein reveals a molecular basis for poly-specific drug binding. *Science* 323(5922):1718-1722.
81. Herbring V, Bäucker A, Trowitzsch S, & Tampé R (2016) A dual inhibition mechanism of herpesviral ICP47 arresting a conformationally thermostable TAP complex. *Sci Rep* 6:36907.
82. Choi CH (2005) ABC transporters as multidrug resistance mechanisms and the development of chemosensitizers for their reversal. *Cancer Cell Int* 5: 30.
83. Zutz A, *et al.* (2011) Asymmetric ATP hydrolysis cycle of the heterodimeric multidrug ABC transport complex TmrAB from *Thermus thermophilus*. *J Biol Chem* 286(9):7104-7115.
84. Lubelski J, Konings WN, & Driessen AJ (2007) Distribution and physiology of ABC-type transporters contributing to multidrug resistance in bacteria. *Microbiol Mol Biol Rev* 71(3):463-476.
85. Oshima T & Imahori K (1974) Physicochemical properties of deoxyribonucleic acid from an extreme thermophile. *J Biochem* 75(1):179-183.
86. Henne A, *et al.* (2004) The genome sequence of the extreme thermophile *Thermus thermophilus*. *Nat Biotechnol* 22(5):547-553.
87. Bechara C, *et al.* (2015) A subset of annular lipids is linked to the flippase activity of an ABC transporter. *Nat Chem* 7(3):255-262.

88. Hohl M, *et al.* (2014) Structural basis for allosteric cross-talk between the asymmetric nucleotide binding sites of a heterodimeric ABC exporter. *Proc Natl Acad Sci U S A* 111(30):11025-11030.
89. Barth K, *et al.* (2018) Conformational coupling and trans-Inhibition in the human antigen transporter ortholog TmrAB resolved with dipolar EPR spectroscopy. *J Am Chem Soc* 140(13):4527-4533.
90. Wallin E & von Heijne G (1998) Genome-wide analysis of integral membrane proteins from eubacterial, archaean, and eukaryotic organisms. *Protein Sci* 7(4):1029-1038.
91. Frauenfeld J, *et al.* (2016) A saposin-lipoprotein nanoparticle system for membrane proteins. *Nat Methods* 13(4):345-351.
92. Overington JP, Al-Lazikani B, & Hopkins AL (2006) How many drug targets are there? *Nat Rev Drug Discov* 5(12):993-996.
93. Flayhan A, *et al.* (2018) Saposin lipid nanoparticles: a highly versatile and modular tool for membrane protein research. *Structure* 26(2):345-355 e345.
94. Schölz C, *et al.* (2011) Specific lipids modulate the transporter associated with antigen processing (TAP). *J Biol Chem* 286(15):13346-13356.
95. Denisov IG, Grinkova YV, Lazarides AA, & Sligar SG (2004) Directed self-assembly of monodisperse phospholipid bilayer Nanodiscs with controlled size. *J Am Chem Soc* 126(11):3477-3487.
96. Bayburt TH & Sligar SG (2002) Single-molecule height measurements on microsomal cytochrome P450 in nanometer-scale phospholipid bilayer disks. *Proc Natl Acad Sci U S A* 99(10):6725-6730.
97. Brouillette CG, Anantharamaiah GM, Engler JA, & Borhani DW (2001) Structural models of human apolipoprotein A-I: a critical analysis and review. *Biochim Biophys Acta* 1531(1-2):4-46.
98. Denisov IG & Sligar SG (2017) Nanodiscs in membrane biochemistry and biophysics. *Chem Rev* 117(6):4669-4713.
99. Bayburt TH & Sligar SG (2010) Membrane protein assembly into Nanodiscs. *FEBS Lett* 584(9):1721-1727.
100. Grinkova YV, Denisov IG, & Sligar SG (2010) Engineering extended membrane scaffold proteins for self-assembly of soluble nanoscale lipid bilayers. *Protein Eng Des Sel* 23(11):843-848.
101. Knowles TJ, *et al.* (2009) Membrane proteins solubilized intact in lipid containing nanoparticles bounded by styrene maleic acid copolymer. *J Am Chem Soc* 131(22):7484-7485.

102. Gao Y, Cao E, Julius D, & Cheng Y (2016) TRPV1 structures in nanodiscs reveal mechanisms of ligand and lipid action. *Nature* 534(7607):347-351.
103. Borhani DW, Rogers DP, Engler JA, & Brouillette CG (1997) Crystal structure of truncated human apolipoprotein A-I suggests a lipid-bound conformation. *Proc Natl Acad Sci U S A* 94(23):12291-12296.
104. Popovic K, Holyoake J, Pomès R, & Privé GG (2012) Structure of saposin A lipoprotein discs. *Proc Natl Acad Sci U S A* 109(8):2908-2912.
105. Bruhn H (2005) A short guided tour through functional and structural features of saposin-like proteins. *Biochem J* 389(Pt 2):249-257.
106. Nguyen NX, *et al.* (2018) Cryo-EM structure of a fungal mitochondrial calcium uniporter. *Nature* 559(7715):570-574.
107. Griffin L & Lawson A (2011) Antibody fragments as tools in crystallography. *Clin Exp Immunol* 165(3):285-291.
108. Taylor NMI, *et al.* (2017) Structure of the human multidrug transporter ABCG2. *Nature* 546(7659):504-509.
109. Paduch M, *et al.* (2012) Generating conformation-specific synthetic antibodies to trap proteins in selected functional states. *Methods* 60(1):3-14.
110. Fellouse FA, *et al.* (2007) High-throughput generation of synthetic antibodies from highly functional minimalist phage-displayed libraries. *J Mol Biol* 373(4):924-940.
111. Davies DR & Cohen GH (1996) Interactions of protein antigens with antibodies. *Proc Natl Acad Sci U S A* 93(1):7-12.
112. Mian IS, Bradwell AR, & Olson AJ (1991) Structure, function and properties of antibody binding sites. *J Mol Biol* 217(1):133-151.
113. Dominik PK, *et al.* (2016) Conformational chaperones for structural studies of membrane proteins using antibody phage display with nanodiscs. *Structure* 24(2):300-309.
114. Smith GP (1985) Filamentous fusion phage: novel expression vectors that display cloned antigens on the virion surface. *Science* 228(4705):1315-1317.
115. McCafferty J, Griffiths AD, Winter G, & Chiswell DJ (1990) Phage antibodies: filamentous phage displaying antibody variable domains. *Nature* 348(6301):552-554.
116. Hoogenboom HR, *et al.* (1998) Antibody phage display technology and its applications. *Immunotechnology* 4(1):1-20.
117. Ledsgaard L, Kilstrup M, Karatt-Vellatt A, McCafferty J, & Laustsen AH (2018) Basics of antibody phage display technology. *Toxins (Basel)* 10(6) pii: E236.

118. Borowska MT, Dominik PK, Anghel SA, Kosiakoff AA, & Keenan RJ (2015) A YidC-like protein in the archaeal plasma membrane. *Structure* 23(9):1715-1724.
119. Muyldermans S (2013) Nanobodies: natural single-domain antibodies. *Annu Rev Biochem* 82:775-797.
120. Stortelers C, Pinto-Espinoza C, Van Hoorick D, & Koch-Nolte F (2018) Modulating ion channel function with antibodies and nanobodies. *Curr Opin Immunol* 52:18-26.
121. Muyldermans S (2001) Single domain camel antibodies: current status. *J Biotechnol* 74(4):277-302.
122. Li T, *et al.* (2018) Nanobody-based dual epitopes protein identification (DepID) assay for measuring soluble CD38 in plasma of multiple myeloma patients. *Anal Chim Acta* 1029:65-71.
123. Steyaert J & Kobilka BK (2011) Nanobody stabilization of G protein-coupled receptor conformational states. *Curr Opin Struct Biol* 21(4):567-572.
124. Rasmussen SG, *et al.* (2011) Structure of a nanobody-stabilized active state of the beta(2) adrenoceptor. *Nature* 469(7329):175-180.
125. Korotkov KV, Pardon E, Steyaert J, & Hol WG (2009) Crystal structure of the N-terminal domain of the secretin GspD from ETEC determined with the assistance of a nanobody. *Structure* 17(2):255-265.
126. Pardon E, *et al.* (2014) A general protocol for the generation of Nanobodies for structural biology. *Nat Protoc* 9(3):674-693.
127. Ward AB, *et al.* (2013) Structures of P-glycoprotein reveal its conformational flexibility and an epitope on the nucleotide-binding domain. *Proc Natl Acad Sci U S A* 110(33):13386-13391.
128. Moran BM, McKillop AM, & O'Harte FP (2016) Development of novel ligands for peptide GPCRs. *Curr Opin Pharmacol* 31:57-62.
129. Lau JL & Dunn MK (2018) Therapeutic peptides: Historical perspectives, current development trends, and future directions. *Bioorg Med Chem* 26(10):2700-2707.
130. Obexer R, Walport LJ, & Suga H (2017) Exploring sequence space: harnessing chemical and biological diversity towards new peptide leads. *Curr Opin Chem Biol* 38:52-61.
131. Kodan A, *et al.* (2014) Structural basis for gating mechanisms of a eukaryotic P-glycoprotein homolog. *Proc Natl Acad Sci U S A* 111(11):4049-4054.
132. Passioura T & Suga H (2017) A RaPID way to discover nonstandard macrocyclic peptide modulators of drug targets. *Chem Commun (Camb)* 53(12):1931-1940.
133. Saito H & Suga H (2001) A ribozyme exclusively aminoacylates the 3'-hydroxyl group of the tRNA terminal adenosine. *J Am Chem Soc* 123(29):7178-7179.

134. Saito H, Watanabe K, & Suga H (2001) Concurrent molecular recognition of the amino acid and tRNA by a ribozyme. *RNA* 7(12):1867-1878.
135. Murakami H, Ohta A, Goto Y, Sako Y, & Suga H (2006) Flexizyme as a versatile tRNA acylation catalyst and the application for translation. *Nucleic Acids Symp Ser (Oxf)* (50):35-36.
136. Roberts RW & Szostak JW (1997) RNA-peptide fusions for the in vitro selection of peptides and proteins. *Proc Natl Acad Sci U S A* 94(23):12297-12302.
137. Tanaka Y, *et al.* (2013) Structural basis for the drug extrusion mechanism by a MATE multidrug transporter. *Nature* 496(7444):247-251.
138. Hipolito CJ, Tanaka Y, Katoh T, Nureki O, & Suga H (2013) A macrocyclic peptide that serves as a cocrystallization ligand and inhibits the function of a MATE family transporter. *Molecules* 18(9):10514-10530.
139. Mukherjee S, *et al.* (2018) Engineered synthetic antibodies as probes to quantify the energetic contributions of ligand binding to conformational changes in proteins. *J Biol Chem* 293(8):2815-2828.
140. Koch K, *et al.* (2017) Selection of nanobodies with broad neutralizing potential against primary HIV-1 strains using soluble subtype C gp140 envelope trimers. *Sci Rep* 7(1):8390.
141. Meyer TH, van Endert PM, Uebel S, Ehring B, & Tampé R (1994) Functional expression and purification of the ABC transporter complex associated with antigen processing (TAP) in insect cells. *FEBS Lett* 351(3):443-447.
142. Lerner-Marmarosh N, Gimi K, Urbatsch IL, Gros P, & Senior AE (1999) Large scale purification of detergent-soluble P-glycoprotein from *Pichia pastoris* cells and characterization of nucleotide binding properties of wild-type, Walker A, and Walker B mutant proteins. *J Biol Chem* 274(49):34711-34718.
143. Roos C, *et al.* (2012) Characterization of co-translationally formed nanodisc complexes with small multidrug transporters, proteorhodopsin and with the *E. coli* MraY translocase. *Biochim Biophys Acta* 1818(12):3098-3106.
144. Geertsma ER, Nik Mahmood NA, Schuurman-Wolters GK, & Poolman B (2008) Membrane reconstitution of ABC transporters and assays of translocator function. *Nat Protoc* 3(2):256-266.
145. Eggensperger S, Fiset O, Parcej D, Schäfer LV, & Tampé R (2014) An annular lipid belt is essential for allosteric coupling and viral inhibition of the antigen translocation complex TAP (transporter associated with antigen processing). *J Biol Chem* 289(48):33098-33108.

146. Knezevic J, *et al.* (2012) Quantitation of affinity, avidity, and binding kinetics of protein analytes with a dynamically switchable biosurface. *J Am Chem Soc* 134(37):15225-15228.
147. Langer A, *et al.* (2013) Protein analysis by time-resolved measurements with an electro-switchable DNA chip. *Nat Commun* 4:2099.
148. Henkel RD, VandeBerg JL, & Walsh RA (1988) A microassay for ATPase. *Anal Biochem* 169(2):312-318.
149. Kastner B, *et al.* (2008) GraFix: sample preparation for single-particle electron cryomicroscopy. *Nat Methods* 5(1):53-55.
150. Stark H (2010) GraFix: stabilization of fragile macromolecular complexes for single particle cryo-EM. *Methods Enzymol* 481:109-126.
151. Suloway C, *et al.* (2005) Automated molecular microscopy: the new Legimon system. *J Struct Biol* 151(1):41-60.
152. Lander GC, *et al.* (2009) Appion: an integrated, database-driven pipeline to facilitate EM image processing. *J Struct Biol* 166(1):95-102.
153. Scheres SH (2015) Semi-automated selection of cryo-EM particles in RELION-1.3. *J Struct Biol* 189(2):114-122.
154. Grant T, Rohou A, & Grigorieff N (2018) cisTEM, user-friendly software for single-particle image processing. *Elife* 7 pii: e35383.
155. Zivanov J, *et al.* (2018) New tools for automated high-resolution cryo-EM structure determination in RELION-3. *Elife* 7 pii: e42166.
156. Zheng SQ, *et al.* (2017) MotionCor2: anisotropic correction of beam-induced motion for improved cryo-electron microscopy. *Nat Methods* 14(4):331-332.
157. Zhang K (2016) Gctf: Real-time CTF determination and correction. *J Struct Biol* 193(1):1-12.
158. Punjani A, Rubinstein JL, Fleet DJ, & Brubaker MA (2017) cryoSPARC: algorithms for rapid unsupervised cryo-EM structure determination. *Nat Methods* 14(3):290-296.
159. Singharoy A, *et al.* (2016) Molecular dynamics-based refinement and validation for sub-5 Å cryo-electron microscopy maps. *Elife* 5 pii: e16105.
160. Larkin MA, *et al.* (2007) Clustal W and Clustal X version 2.0. *Bioinformatics* 23(21):2947-2948.
161. Sali A & Blundell TL (1993) Comparative protein modelling by satisfaction of spatial restraints. *J Mol Biol* 234(3):779-815.
162. Phillips JC, *et al.* (2005) Scalable molecular dynamics with NAMD. *J Comput Chem* 26(16):1781-1802.

163. Alexov EG & Gunner MR (1997) Incorporating protein conformational flexibility into the calculation of pH-dependent protein properties. *Biophys J* 72(5):2075-2093.
164. Wu EL, *et al.* (2014) CHARMM-GUI membrane builder toward realistic biological membrane simulations. *J Comput Chem* 35(27):1997-2004.
165. Best RB, *et al.* (2012) Optimization of the additive CHARMM all-atom protein force field targeting improved sampling of the backbone phi, psi and side-chain chi(1) and chi(2) dihedral angles. *J Chem Theory Comput* 8(9):3257-3273.
166. Humphrey W, Dalke A, & Schulten K (1996) VMD: Visual molecular dynamics. *J Mol Graph Model* 14(1):33-38.
167. Abraham MJ, *et al.* (2015) GROMACS: High performance molecular simulations through multi-level parallelism from laptops to supercomputers. *SoftwareX* 1-2:19-25.
168. Emsley P, Lohkamp B, Scott WG, & Cowtan K (2010) Features and development of Coot. *Acta Crystallogr D Biol Crystallogr* 66(Pt 4):486-501.
169. Adams PD, *et al.* (2010) PHENIX: a comprehensive Python-based system for macromolecular structure solution. *Acta Crystallogr D Biol Crystallogr* 66(Pt 2):213-221.
170. Chen VB, *et al.* (2010) MolProbity: all-atom structure validation for macromolecular crystallography. *Acta Crystallogr D Biol Crystallogr* 66(Pt 1):12-21.
171. Laskowski RA, Rullmannn JA, MacArthur MW, Kaptein R, & Thornton JM (1996) AQUA and PROCHECK-NMR: programs for checking the quality of protein structures solved by NMR. *J Biomol NMR* 8(4):477-486.
172. Smirnova I, *et al.* (2015) Transient conformers of LacY are trapped by nanobodies. *Proc Natl Acad Sci U S A* 112(45):13839-13844.
173. Tribet C, Audebert R, & Popot JL (1996) Amphipols: polymers that keep membrane proteins soluble in aqueous solutions. *Proc Natl Acad Sci U S A* 93(26):15047-15050.
174. Gohon Y, *et al.* (2006) Well-defined nanoparticles formed by hydrophobic assembly of a short and polydisperse random terpolymer, amphipol A8-35. *Langmuir* 22(3):1281-1290.
175. Moeller A, *et al.* (2015) Distinct conformational spectrum of homologous multidrug ABC transporters. *Structure* 23(3):450-460.
176. Bai XC, McMullan G, & Scheres SH (2015) How cryo-EM is revolutionizing structural biology. *Trends Biochem Sci* 40(1):49-57.
177. Cheng Y (2015) Single-particle cryo-EM at crystallographic resolution. *Cell* 161(3):450-457.

178. Frank J (2017) Advances in the field of single-particle cryo-electron microscopy over the last decade. *Nat Protoc* 12(2):209-212.
179. Paduch M, *et al.* (2013) Generating conformation-specific synthetic antibodies to trap proteins in selected functional states. *Methods* 60(1):3-14.
180. Seeger MA, *et al.* (2012) Tuning the drug efflux activity of an ABC transporter in vivo by in vitro selected DARPIn binders. *PLoS One* 7(6):e37845.
181. Zimmermann I, *et al.* (2018) Synthetic single domain antibodies for the conformational trapping of membrane proteins. *Elife* 7 pii: e34317.
182. Yan J, Li G, Hu Y, Ou W, & Wan Y (2014) Construction of a synthetic phage-displayed nanobody library with CDR3 regions randomized by trinucleotide cassettes for diagnostic applications. *J Transl Med* 12:343.
183. Zahnd C, Amstutz P, & Plückthun A (2007) Ribosome display: selecting and evolving proteins in vitro that specifically bind to a target. *Nat Methods* 4(3):269-279.
184. Kühlbrandt W (2014) Biochemistry. The resolution revolution. *Science* 343(6178):1443-1444.
185. Lu P, *et al.* (2014) Three-dimensional structure of human gamma-secretase. *Nature* 512(7513):166-170.
186. Cléry A, Sohler TJM, Welte T, Langer A, & Allain FHT (2017) switchSENSE: A new technology to study protein-RNA interactions. *Methods* 118-119:137-145.
187. Singh SK & Sigworth FJ (2015) Cryo-EM: spinning the micelles away. *Structure* 23(9):1561.
188. Bountra K, *et al.* (2017) Structural basis for antibacterial peptide self-immunity by the bacterial ABC transporter McjD. *EMBO J* 36(20):3062-3079.
189. Wright J, Muench SP, Goldman A, & Baker A (2018) Substrate polyspecificity and conformational relevance in ABC transporters: new insights from structural studies. *Biochem Soc Trans* 46(6):1475-1484.
190. Perez C, *et al.* (2017) Structural basis of inhibition of lipid-linked oligosaccharide flippase PglK by a conformational nanobody. *Sci Rep* 7:46641.
191. Doerrler WT & Raetz CR (2002) ATPase activity of the MsbA lipid flippase of *Escherichia coli*. *J Biol Chem* 277(39):36697-36705.
192. Kawai T, Caaveiro JM, Abe R, Katagiri T, & Tsumoto K (2011) Catalytic activity of MsbA reconstituted in nanodisc particles is modulated by remote interactions with the bilayer. *FEBS Lett* 585(22):3533-3537.

193. Shukla S, Abel B, Chufan EE, & Ambudkar SV (2017) Effects of a detergent micelle environment on P-glycoprotein (ABCB1)-ligand interactions. *J Biol Chem* 292(17):7066-7076.
194. Denisov IG & Sligar SG (2016) Nanodiscs for structural and functional studies of membrane proteins. *Nat Struct Mol Biol* 23(6):481-486.
195. Hardy D, Bill RM, Jawhari A, & Rothnie AJ (2016) Overcoming bottlenecks in the membrane protein structural biology pipeline. *Biochem Soc Trans* 44(3):838-844.
196. Alam A, Kowal J, Broude E, Roninson I, & Locher KP (2019) Structural insight into substrate and inhibitor discrimination by human P-glycoprotein. *Science* 363(6428):753-756.
197. Vahedi-Faridi A, Jastrzebska B, Palczewski K, & Engel A (2013) 3D imaging and quantitative analysis of small solubilized membrane proteins and their complexes by transmission electron microscopy. *Microscopy (Oxf)* 62(1):95-107.

11. Appendix

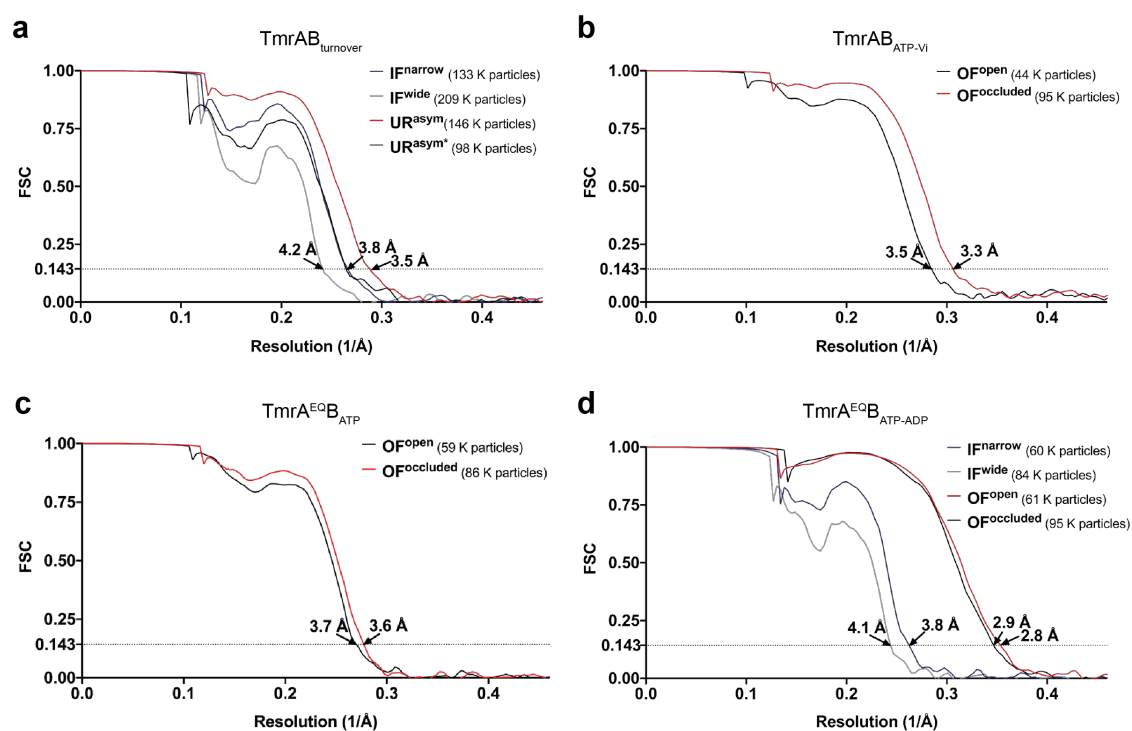


Figure 47: **Fourier shell correlation (FSC) curves.** **a**, FSC curves for TmrAB_{turnover} show a resolution of 3.8 Å for I^Fnarrow, 4.2 Å for I^Fwide, and 3.5 Å for the asymmetric U^Rasym state as judged from the 0.143 threshold. **b**, FSC curves for TmrAB_{ATP-VI} show a resolution of 3.5 Å for O^F-open and 3.3 Å for O^F-occluded. **c**, FSC curves for TmrA^{EQB}_{ATP} show a resolution of 3.7 Å for O^F-open and 3.6 Å for O^F-occluded. **d**, FSC curves for TmrA^{EQB}_{ATP-ADP} show a resolution of 3.8 Å for I^Fnarrow, 4.1 Å for I^Fwide, 2.8 Å for O^F-open and 2.9 Å for O^F-occluded. (FSC analysis and angular assignment was performed by Arne Möller and Dovile Janulienė, Möller laboratory, Department of Structural Biology, Max Planck Institute of Biophysics, Frankfurt).

12. Abbreviations

Abbreviation	Description
β -DDM	dodecyl- β -D-maltoside
μ	micro
Å	Ångström
aa	amino acid
ABC	ATP-binding cassette
APS	ammonium persulfate
ATP	adenosine triphosphate
B	beads
BSA	bovine serum albumin
C	Celsius
CDR	complementarity determining region
CCD	charge-coupled device
CMC	critical micelle concentration
cryo-EM	electron cryo-microscopy
cv	column volumes
Da	Dalton
dd	double distilled
DMSO	dimethyl sulfoxide
DNA	deoxyribonucleic acid
dNTP	deoxynucleotide triphosphate
DOPC	1,2-dioleoyl- <i>sn</i> -glycero-3-phosphocholine
DTT	dithiothreitol
ECL	enhanced chemiluminescence
EDTA	ethylenediaminetetraacetic acid
ELISA	enzyme-linked immunosorbent assay
EM	electron microscopy
EPR	electron paramagnetic resonance
ER	endoplasmic reticulum
Fab	fragment antigen binding
Fc	fragment crystallizable
FPLC	fast protein liquid chromatography

FSEC	fluorescence-detection size exclusion chromatography
FT	flow-through
fw	forward
g	gravity
GDN	glyco-diosgenin
GPCR	G protein-coupled receptor
GraFix	gradient fixation
h	hour
HPLC	high performance liquid chromatography
HRP	horseradish peroxidase
hVEGF	human vascular endothelial growth factor
I	input
ICP47	infected cell peptide 47
IF	inward-facing
Ig	immunoglobulin
IMAC	immobilized metal affinity chromatography
IPTG	isopropyl- β -thiogalactopyranoside
kDa	kilo Dalton
LB	lysogeny broth
LUVs	large unilamellar vesicles
M	molar
mAb	monoclonal antibody
mCerulean	monomeric enhanced cyan fluorescent protein
MD	molecular dynamics
MHC I	major histocompatibility complex class I
min	minutes
ml	milliliter
MOPS	3-(N-Morpholino)propanesulfonic acid
MSP	membrane scaffold protein
mVenus	monomeric enhanced yellow fluorescent protein
MW	molecular weight
n	nano
NAV	neutravidin
NBD	nucleotide-binding domain

NBS	nucleotide-binding site
Nbs	nanobodies
NfMCU	mitochondrial calcium uniporter orthologue from <i>Neosartorya fischeri</i>
NMR	nuclear magnetic resonance
OD	optical density
OF	outward-facing
p	pico
PAGE	polyacrylamide gel electrophoresis
PBS	phosphate buffered saline
PCR	polymerase chain reaction
PDB	protein data bank
PE	periplasmic extract
PEG	polyethylene glycol
pfu	plaque-forming units
PG	phosphatidylglycerol
P _i	inorganic phosphate
PLC	peptide-loading complex
PMSF	phenylmethylsulphonyl fluoride
PVDF	polyvinylidene difluoride
RaPID	Random non-standard Peptide Integrated Discovery
rev	reverse
RMSD	root-mean-square deviation
rpm	rounds per minute
RT	room temperature
s	second
SDS	sodium dodecyl sulfate
sABs	synthetic antibodies
SEC	size exclusion chromatography
sp	single-particle
TAE buffer	Tris-acetate EDTA buffer
TAP	transporter associated with antigen processing
TB	terrific broth
TEA	triethanolamine

TEV	tobacco etch virus
TFA	trifluoro acetic acid
TMH	transmembrane helix
TMB	3,3',5,5'-tetramethylbenzidine
TMD	transmembrane domain
Tris	tris(hydroxymethyl)amino methane
V	volt
V _H H	variable region of a heavy chain-only antibody
V _i	orthovanadate
v/v	volume/volume
W	wash
w/v	weight/volume
YNB	yeast nitrogen base

13. List of figures

Figure 1: Representative bacterial ABC transporters.....	2
Figure 2: Domain organization of TAP1 NBD.....	3
Figure 3: TAP complex at atomic resolution.....	7
Figure 4: Nucleotide-free inward-facing conformation of TmrAB.....	10
Figure 5: Structure of apolipoprotein A-I.....	12
Figure 6: Structure of saposin A.....	13
Figure 7: Tools to lock specific conformations of dynamic membrane proteins.....	19
Figure 8: Purification of TAP variants.....	60
Figure 9: Purified cTAP is active in peptide binding and translocation.....	61
Figure 10: Immobilization efficiency of ^{ICP47} cTAP nanodiscs.....	62
Figure 11: Enrichment of eluted phage particles.....	63
Figure 12: Specificity of putative ^{ICP47} cTAP-binding single clones tested by phage ELISA.	64
Figure 13: Specificity of putative cTAP-binding single clones tested by phage ELISA.....	65
Figure 14: Synthetic antibodies C2, E2, and F8 form stable complexes with ^{ICP47} cTAP.....	66
Figure 15: Specificity of TAP-binding nanobodies.....	68
Figure 16: ^{ICP47} cTAP-nanobody interaction.....	69
Figure 17: Negative-stain EM analysis of ^{ICP47} cTAP in GDN.....	70
Figure 18: EM analysis of ^{ICP47} cTAP upon fixation and detergent removal.....	71
Figure 19: GraFix treatment of ^{ICP47} cTAP.....	72
Figure 20: Synthetic antibody C2 as fiducial marker for EM.....	73
Figure 21: Detergent exchange for amphipols.....	74
Figure 22: Purified TmrAB is active in ATP hydrolysis.....	79
Figure 23: TmrAB in proteoliposomes transports peptide substrates.....	80
Figure 24: Purification of TmrA ^{C416A, E523Q, S527C} B ^{S503C}	81
Figure 25: Immobilization efficiency of TmrA ^{C416A, E523Q, S527C} B ^{S503C}	81
Figure 26: Enrichment of eluted phage particles.....	82
Figure 27: Specificity of putative TmrA ^{C416A, E523Q, S527C} B ^{S503C} -binding single clones.....	83
Figure 28: Synthetic antibodies form stable complexes with TmrA ^{C416A, E523Q, S527C} B ^{S503C} ...	84
Figure 29: Specificity of putative TmrA ^{C416A, E523Q, S527C} B ^{S503C} -binding single clones.....	85
Figure 30: Characterization of anti-TmrAB nanobodies.....	87
Figure 31: Negative-stain EM analysis of TmrAB in β-DDM.....	88
Figure 32: Negative-stain EM analysis of reconstituted TmrAB.....	89

Figure 33: ATPase activity of TmrAB in nanodiscs.....	90
Figure 34: Antibodies as fiducial marker proteins.....	92
Figure 35: Cryo-EM analysis of nanodisc-embedded TmrAB ^{WT} under turnover conditions.....	93
Figure 36: Conformational plasticity in IF conformations translates to substrate binding.....	95
Figure 37: Asymmetric post-hydrolysis state.....	97
Figure 38: ATP binding induces the IF-OF-open transition.....	99
Figure 39: TmrAB _{ATP-Vi} and TmrA ^{EQ} B _{ATP} are equivalent.....	101
Figure 40: Cryo-EM analysis of nanodisc-embedded TmrA ^{EQ} B _{ATP-ADP}	102
Figure 41: Helical shifts within the TMD of TmrA during substrate translocation.....	104
Figure 42: Helical shifts within the TMD of TmrB during substrate translocation.....	105
Figure 43: Transport cycle of the heterodimeric ABC exporter TmrAB.....	110
Figure 44: Cyclic peptide VD3 binds specific to nucleotide-bound TmrAB.....	112
Figure 45: Cyclic peptide VD3 as potent and highly selective inhibitor.....	113
Figure 46: VD3 binds to the periplasmic side of TmrAB.....	114
Figure 47: Fourier shell correlation (FSC) curves.....	133

14. List of tables

Table 1: Antibodies used for immunoblotting.....	23
Table 2: <i>Escherichia coli</i> strains.....	23
Table 3: Summary of commonly used buffers.....	24
Table 4: List of chemicals and reagents.....	29
Table 5: List of consumables and lab equipment.....	30
Table 6: List of detergents.....	30
Table 7: Enzymes used for molecular biology.....	31
Table 8: Summary of commonly used media.....	31
Table 9: Oligonucleotides.....	33
Table 10: Amino acid sequences of peptides used for functional studies.....	33
Table 11: Standard PCR conditions for cloning of sABs constructs.....	35
Table 12: Standard PCR conditions for cloning of TmrAB alanine substitutions.....	36
Table 13: Composition of SDS-stacking and -separating gel.....	50
Table 14: FPLC and HPLC columns.....	54
Table 15: Enrichment results after two rounds of library sorting.....	67

15. Danksagung

Abschließend möchte ich mich bei allen Personen bedanken, die zum Gelingen dieser Arbeit beigetragen und mich währenddessen begleitet haben:

An erster Stelle danke ich meinem Doktorvater, Prof. Dr. Robert Tampé, für die Bereitstellung des spannenden Themas, das stete Interesse am Fortgang des Projektes und die kontinuierliche Unterstützung in Form wissenschaftlicher Diskussionen. Der rege Austausch und die Ideen haben maßgeblich zum Erfolg des Projektes beigetragen

Ein herzlicher Dank gilt meinen Mentoren, PD Dr. Rupert Abele, Prof. Dr. Klaas Martinus Pos und Jun. Prof. Dr. Eric Geertsma, für die Möglichkeit den Fortschritt meines Projektes in regelmäßigen Treffen zu diskutieren und zu beurteilen. Prof. Dr. Klaas Martinus Pos möchte ich außerdem für die Übernahme des Zweitgutachtens danken.

Ein großer Dank gilt außerdem meinen Kooperationspartnern, ohne die diese Arbeit nur halb so erfolgreich gewesen wäre. Bei Prof. Dr. Kühlbrandt und den Mitarbeitern der Abteilung für Strukturbiologie am Max-Planck-Institut für Biophysik möchte ich mich für die Unterstützung und die regelmäßigen Messzeiten an den Mikroskopen bedanken. Ohne diese Möglichkeit und die einmalige Ausstattung wäre es nicht möglich gewesen, das konformationelle Spektrum von TmrAB zu bestimmen. Speziell möchte ich mich hier bei Simone Prinz und Deryck Mills für die Unterstützung an den Elektronenmikroskopen bedanken.

Ein besonderer Dank gilt Dr. Arne Möller und Dr. Dovile Januliene. Das immense Kryo-EM Fachwissen, das Opfern von Messzeiten für das TmrAB Projekt, der unermüdliche Einsatz und der stete Input haben den Erfolg des Projektes erst möglich gemacht. Vielen Dank dafür!

Prof. Dr. Anthony Kossiakoff und Dr. Pawel Dominik danke ich für die Möglichkeit, die Selektion der synthetischen Antikörper am *Institute of Biochemistry and Molecular Biology* der *University of Chicago* durchzuführen. Gleiches gilt für Prof. Dr. Jan Steyaert und Dr. Els Pardon am *VIB-VUB Center for Structural Biology* in Brüssel: Vielen Dank für die Möglichkeit, die Nanobody Selektion in Brüssel durchzuführen und die Unterstützung vor Ort. Im Rahmen der Nanobody Selektion danke ich außerdem INSTRUCT (*I thank Hercules Foundation Flanders for support to the ESFRI Nanobodies4Instruct platform for nanobodies used in this study*).

Bei Prof. Dr. Gerhard Hummer und Dr. Ahmad Reza Mehdipour bedanke ich mich für die Zusammenarbeit im TmrAB Projekt, das sehr von den Erfahrungen und wissenschaftlichen Diskussionen profitiert hat. Dr. Ahmad Reza Mehdipour und Dr. Christoph Thomas danke ich in

diesem Zusammenhang auch für die Erstellung der TmrAB Modelle. Ohne die Modelle hätten wir nie so viel über den Transportmechanismus lernen können.

Danke an Prof. Dr. Hiroaki Suga und Dr. Richard Obexer für die Selektion und Synthese der zyklischen Peptide.

Bei Benedikt Kuhn und Stefan Brüchert möchte ich mich für die Bereitstellung des Nanobodies bedanken, der einen essentiellen Bestandteil für den erfolgreichen Ausgang des TmrAB Projektes dargestellt hat. Außerdem danke ich Benedikt Kuhn für die Bereitstellung der NBD-kodierenden Plasmide.

Nita Chang möchte ich für das monovalente Streptavidin danken.

Ebenso bedanke ich mich bei Dr. Jens Frauenfeld für das Saposin A Plasmid.

Bei allen Mitgliedern der Arbeitsgruppen Tampé, Abele und Hänel möchte ich mich für die kontinuierliche Unterstützung, die herzliche Arbeitsatmosphäre und die tolle Zeit im Labor im bedanken. Bei Andrea Pott und Inga Nold bedanke ich mich für die wunderbare Hilfe bei bürokratischen und organisatorischen Herausforderungen. Speziell Labor 1.23 (Nicole, Valentina, Jamina, Martina und Alina) danke ich für die tolle Zeit!

Ganz besonderer Dank gilt meiner Familie für die moralische Unterstützung während meiner gesamten Studien- und Promotionszeit. Speziell danken möchte ich meinem Vater Walter Hank und meinem Mann Patrick Hofmann für ihr Verständnis, ihre Geduld und vor allem ihre Liebe in allen Höhen und Tiefen der letzten Jahre. Diese Arbeit habe ich euch gewidmet.

16. Curriculum vitae

Personal data:

Name: Susanne Hofmann
Address: Kiesstraße 10
60486 Frankfurt
Date of birth: 03.01.1987
Place of birth: Darmstadt, Germany
Name at birth: Hank



Professional experience:

03/2013 until present **Research scientist/Ph.D. candidate** at the Institute of Biochemistry, Goethe-University, Germany (group of Prof. Dr. Robert Tampé)

- ▶ Structure determination of medical-relevant ABC exporters
- ▶ Supervision of Bachelor-/Master-students, scientific presentations and discussions

Research visits:

02/2015 to 03/2015 Vrije Universiteit Brussel, Belgium (group of Prof. Dr. Jan Steyaert)

- ▶ Generation of nanobodies as stabilizing chaperones
- ▶ Funded by scholarship from INSTRUCT

2013 and 2014 University of Chicago, USA (group of Prof. Dr. Anthony Kossiakoff)

- ▶ Generation of synthetic antibodies as stabilizing chaperones (August-October)

04/2008 to 08/2010 **Student assistant** at the Department of Cell Biology, Technical University Darmstadt, Germany

- ▶ Planning and supervision of practical courses for undergraduate students

2007 to 2011 **Employment via Randstad Inhouse Services**
Several employments in medical engineering and chemical industry in a regulated environment (Wella, BCM Kosmetik, aap Implantate AG)

Education:

- 03/2013 until present **PhD candidate**, Institute of Biochemistry, Goethe-University, Germany (group of Prof. Dr. Robert Tampé)
- 10/2006 to 11/2012 **Diploma in biology**, Technical University Darmstadt, Germany, and University of Skövde, Sweden
- ▶ Certificate: Diploma (final grade: 1.3)
 - ▶ Diploma thesis: “VHH antibodies as intracellular adapter molecules for the site-specific accumulation of enzymes” (group of Prof. Dr. Harald Kolmar) (final grade: 1.0)
- 1993 to 2006 **Abitur**, Albert-Einstein-Schule, Groß-Bieberau, Germany
Certificate: Abitur (final grade: 2.0)

Additional qualifications and extracurricular engagement:

- Language skills: German (native speaker), English (fluent oral and written communication skills), Swedish (basic knowledge), Spanish (basic knowledge)
- Training in project management, GLP/GMP, and economics *via* GRADE (Goethe Research Academy for Early Career Researchers)
- Training at the integrated research training group TRAM (graduate school of CRC 807)
- Mentee at “Mentoring Hessen - für Frauen in Naturwissenschaft und Technik“
- Former treasurer and still member of “Etudes Sans Frontières – Studieren Ohne Grenzen Deutschland e.V.“

Selected conferences and workshops:

- 03/2018 **ATP-Binding Cassette (ABC) Proteins: From Multidrug Resistance to Genetic Diseases**, 7th FEBS Special Meeting, Innsbruck, Austria
Oral presentation
- 2013 until present (annually) **International Summer School**, Institute of Biochemistry, Goethe-University Frankfurt
Oral presentation (presentation award: 2015, 2017)
- Frankfurt, 2019

17. Erklärung

Ich erkläre hiermit, dass ich mich bisher keiner Doktorprüfung im Mathematisch-Naturwissenschaftlichen Bereich unterzogen habe.

Frankfurt am Main,

18. Versicherung

Ich erkläre hiermit, dass ich die vorgelegte Dissertation mit dem Titel

**“Structure and mechanism
of the heterodimeric ABC translocation complexes
TAP and TmrAB“**

selbstständig angefertigt und mich anderer Hilfsmittel als der in ihr angegebenen nicht bedient habe, insbesondere, dass alle Entlehnungen aus anderen Schriften mit Angabe der betreffenden Schrift gekennzeichnet sind.

Ich versichere, die Grundsätze der guten wissenschaftlichen Praxis beachtet, und nicht die Hilfe einer kommerziellen Promotionsvermittlung in Anspruch genommen zu haben.

Frankfurt am Main,